TEXAS TECH UNIVERSITY
Multidisciplinary Research in Transportation

Risk Assessment Model for Wind-Induced Fatigue Failure of Cantilever Traffic Signal Structures

Authors: Christopher Letchford, Hector Cruzado

Performed in Cooperation with the Texas Department of Transportation and the Federal Highway Administration

Research Project 0-4586
Research Report 0-4586-4
http://www.techmrt.ttu.edu/reports.php

NOTICE

The United States Government and the State of Texas do not endorse products or manufacturers. Trade or manufacturers' names appear herein solely because they are considered essential to the object of this report

Technical Report Documentation Page

1. Report No.: FHWA/TX -07-4586-4	2. Government Accession No.:	3. Recipient's Catalog No.:
4. Title and Subtitle: Risk Assessment Model for Wind-Induced Fatigue Failure of Cantilever Traffic Signal Structures		5. Report Date: May 2008 6. Performing Organization Code:
7. Author(s): Christopher Letchford, Hector Cruzado		8. Performing Organization Report No. 0-4586- 4
9. Performing Organization Name and Address: Texas Tech University College of Engineering Center for Multidisciplinary Research in Transportation Box 41023 Lubbock, Texas 79409-1023		10. Work Unit No. 11. Contract or Grant No. : Project 0-4586
12. Sponsoring Agency Name and Address Texas Department of Transportation Research and Technology Implementation P. O. Box 5080 Austin, TX 78763-5080		Type of Report and Period Cover: Technical Report August 2003-October 2007 Sponsoring Agency Code:
15. Supplementary Notes: Project performed in cooperation with the Texas Department of Transportation and the Federal Highway Administration. Revision of AASHTO Fatigue Design Loadings for Signs, Luminaires, and Traffic Signal Structures for Use in Texas		

16. Abstract:

The wind-induced vibrations of the mast arm of cantilever traffic signal structures can lead to the fatigue failure of these structures. For this project, both full-scale and wind tunnel tests were conducted to study the behavior of the structures. Results of these experiments indicated that when the signals have backplates, vortex shedding can cause large-amplitude vibrations that may lead to fatigue failure. These results contradict what has been generally accepted by other researchers: that galloping is the main cause for the fatigue inducing vibrations and that vortex shedding is of no relevance in this type of structure.

As a result of this research, a methodology to estimate the fatigue life of these structures was developed. Using the climatology of the region, the methodology was applied as a risk assessment model to traffic signal structures of the City of Lubbock. Guidance is given on how life-cycle cost analysis can be applied to the structures.

17. Key Words: Cantilever, mast arm, galloping, fatigue failure, vortex shedding, backplates		Distribution Statement – No restrictions. This document is available to the public through the National Technical Information Service, Springfield, VA 22161 www.ntis.gov	
19. Security Classif. (of this report) Unclassified	20. Security Classif. (of this page) unclassified	21. No. of Pages 246	22. Price

Risk Assessment Model for Wind-Induced Fatigue Failure of Cantilever Traffic Signal Structures

by
Christopher J. Letchford
Hector Cruzado

Department of Civil and Environmental Engineering
Texas Tech University
Center for Multidisciplinary Research in Transportation

Research Report Number 0-4586-4
Research Project Number 0-4586
Revision of AASHTO Fatigue Design Loadings for Signs, Luminaires, and Traffic Signal Structures for Use in Texas

Performed in Cooperation with the Texas Department of Transportation and the Federal Highway Administration

Report No. 0-4586-4 May 2008

AUTHOR'S DISCLAIMER

The contents of this report reflect the views of the authors who are responsible for the facts and the accuracy of the data presented herein. The contents do not necessarily reflect the official view of policies of the Texas Department of Transportation or the Federal Highway Administration. This report does not constitute a standard, specification, or regulation.

PATENT DISCLAIMER

There was no invention or discovery conceived or first actually reduced to practice in the course of or under this contract, including any art, method, process, machine, manufacture, design or composition of matter, or any new useful improvement thereof, or any variety of plant which is or may be patentable under the patent laws of the United States of America or any foreign country.

ENGINEERING DISCLAIMER

Not intended for construction, bidding, or permit purposes.

TRADE NAMES AND MANUFACTURERS' NAMES

The United States Government and the State of Texas do not endorse products or manufacturers. Trade or manufacturers' names appear herein solely because they are considered essential to the object of this report.

TABLE OF CONTENTS

Title Page ii
Disclaimers iii
Table of Contents iv
List of Tables vi
List of Figures vii

Chapter 1 Introduction 1
1.1 Cantilever Traffic Signal Structures 1
1.2 Problem Statement 3
1.3 Research Objectives 5
1.4 Organization of This Report 6

Chapter 2 Literature Review 7
2.1 Introduction 7
2.2 Vibration-Inducing Mechanisms 7
2.2.1 Vortex Shedding 8
2.2.2 Galloping 10
2.2.3 Natural Wind Gusts 14
2.2.4 Truck-Induced Gusts 14
2.3 Research on Cantilever Traffic Signal Structures 15
2.3.1 Illinois Department of Transportation 15
2.3.2 Texas Tech University 20
2.3.3 Lehigh University 29
2.3.4 Missouri Department of Transportation 34
2.3.5 University of Wyoming 38
2.3.6 University of Minnesota 41
2.3.7 The University of Texas at Austin 42
2.4 Summary 43

Chapter 3 Full-Scale Experiments 45
3.1 Introduction 45
3.2 Experimental Setup 46
3.2.1 Geometry and Light Configuration 46
3.2.2 Foundations 47
3.2.3 Instrumentation 49
3.2.4 Quality Assurance Measures 56
3.2.5 Pluck Test 58
3.2.6 Experimental Program 60
3.3. Results 61
3.3.1 March 29, 2005 62
3.3.2 Mode 1100 71
3.3.3 Mode 1101 76
3.4 Conclusions 81

Chapter 4 Wind Tunnel Studies 83
4.1 Introduction 83
4.2 Dimensional Analysis 83
4.2.1 Mass Scale 84
4.2.2 Elastic Stiffness Scale 85
4.2.3 Time Scale 86
4.2.4 Froude-s Model Law 87
4.3 University of Western Ontario Experiments 87
4.3.1 Model Design and Construction 87
4.3.2 Experimental Setup and Procedure 93
4.3.3 Results 96
4.4 Texas Tech University Experiments 103
4.4.1 Model Design and Construction 103
4.4.2 Experimental Setup and Procedure 103
4.4.3 Results 106
4.5 Conclusions 117

Chapter 5 Estimation of Fatigue Life 119
5.1 Methodology for Predicting Fatigue Life 119
5.2 Example of Application of Methodology 122
5.2.1 Step 1: The W-Matrix 122
5.2.2 Step 2: The N-Matrix 127
5.2.3 Step 3: The Y-Matrix 129
5.2.4 Step 4: The Ŷ-Matrix 134
5.2.5 Step 5: The S-Matrix 136
5.2.6 Step 6: The N-Matrix 146
5.2.7 Step 7: Miner's Rule 151
5.3 Conclusions 155

Chapter 6 Life-Cycle Cost Analysis 158
6.1 Introduction 158
6.2 Life-Cycle Cost Analysis Defined 159
6.3 Example of Life-Cycle Cost Analysis 161
6.4 Recommendations 162

Chapter 7 Conclusions and Recommendations 164

References 167

Appendix A Mode 1100 Results 172
Appendix B Mode 1101 Results 183
Appendix C Justification for Elimination of the Pole from the Wind Tunnel Model . 194
Appendix D Texas Tech Wind Tunnel Results 195
Appendix E Full-Scale Experiments with Vented Backplates and Damping Plates ... 207

List of Tables

3.1 Resolution and Accuracy of Anemometer for Wind Speeds in the 0-67 mph Range 52
3.2 Content of Each Column of the Processed Files 55
3.3 Fundamental Frequency (f_o) and Damping Ratio (ζ) of Mast Arms 60
3.4 Experimental Program 61
4.1 Scale Parameters Considered in Wind Tunnel Modeling 84
4.2 Comparison Between the Actual and Required Properties of the Mast Arm Model 90
4.3 Dimensions of Grids 95
4.4 Wind Tunnel Performance 95
4.5 Results of UWO Wind Tunnel Experiments 102
4.6 Cases for Which Experiments Were Conducted 105
4.7 Vertical Fundamental Frequency (f_o) and Damping Ratio (ζ) of Models 106
4.8 TTU Results for 90° Angle of Attack 108
4.9 Calculation of Strouhal Number (St) 116
5.1 Probability of Wind Blowing and Parameters for Weibull Distribution for Given Wind Direction (Vega and Letchford 2006) 125
5.2 Portion of the W-Matrix 127
5.3 Portion of the N-Matrix 129
5.4 Portion of the Y-Matrix 133
5.5 Portion of the $\hat{Y}$-Matrix 136
5.6 Results of the Dynamic Analysis 142
5.7 Portion of the S-Matrix 146
5.8 Allowable Fatigue Stress Range (AASHTO 1996) 150
5.9 Portion of the N-Matrix 151
5.10 Damage (D) Prediction after One Day with $C = 1$ 152
5.11 Fatigue Life (in years) for Different Values of C for Structures with Backplates 154

List of Figures

1.1 Traffic Signal Structure with Straight Mast Arm 2
1.2 Cantilever Traffic Signal Structure with Bent Mast Arm 2
1.3 Fatigue Failure of Mast Arm in Lubbock, Texas 4
2.1 Schematic of von Kármán Vortex Street in the Wake of a Circular Cylinder (Kaczinski, Dexter, and Van Dien 1998) 8
2.2 Vortex Shedding Acting on Cross-Section of Mast Arm with Traffic Signal .. 9
2.3 Initiation of Galloping (Pulipaka 1995) 11
2.4 Instrumented Traffic Signal Structure at the Physical Research Laboratory in Springfield, Illinois (South 1994) 17
2.5 Models Used for Water-Table Experiments (Pulipaka, McDonald, and Mehta 1995) 21
2.6 Force Coefficient (C_{Fy}) vs. Angle of Attack for Traffic Signal Configuration Identified as Susceptible to Galloping (Pulipaka 1995) 24
2.7 Signal Light Configuration Considered Susceptible To Galloping (Pulipaka, Sarkar, and McDonald 1998) 25
2.8 Wind Tunnel Test Conducted at TTU (Pulipaka, Sarkar, and McDonald 1998) 26
2.9 Aerodynamic Damping (H_1^*) vs. Reduced Velocity (U/nB) (Pulipaka, Sarkar, and McDonald 1998) 27
2.10 Specimen A for Wind Tunnel Testing. Bold Face Indicates the Dimensions of the Prototype (Kaczinski, Dexter, and Van Dien 1998) 31
2.11 Schematic of Structure Studied by MoDOT (Chen et al. 2001) 35
2.12 Typical Arm-Post Connection used by MoDOT (Chen et al. 2001) 38
2.13 Test Cantilevered Traffic Signal Structure in Wyoming (Hamilton, Riggs, and Puckett 2000) 39
2.14 Connection Detail used in Wyoming (Hamilton, Riggs, and Puckett 2000) 39
2.15 Combination of In-Plane and Out-of-Plane Motion (Hamilton, Riggs and Puckett 2000) 40
2.16 Equipment Layout for Galloping Experiment (Florea 2005) 42
3.1 Two Cantilever Traffic Signal Structures Tested at Reese Technology Center 45
3.2 Geometry and Light Configuration of TS1 (60' mast arm) 46
3.3 Geometry and Light Configuration of TS2 (44' mast arm) 47
3.4 Dimensions of Signal Light Heads Used in Full-Scale Experiments (shown with backplates) 47
3.5 Foundation with Steel Plate 48
3.6 Dimension of Foundation Steel Plate 48
3.7 Foundation Details 49
3.8 Instrumentation 51
3.9 Infrared Target as Viewed from Top of Pole 51
3.10 Anemometer Orientation and Angle of Attack Sign Convention 52
3.11 Comparison Between Traffic Signals' Anemometers and Mesonet Wind Data 57
3.12 Comparison Between Actual and Calculated Distances Between Infrared Lights 57
3.13 Pluck Test Run for Case of 44-ft Arm Under Horizontal Vibrations 59

3.14 Wind and Displacement Data Collected on March 29, 2005 62
3.15 Time Histories of Total Wind Speed, Angle of Attack, and Tip Displacement 63
3.16 Effect of Wind Speed on Horizontal Vibrations of the Arm 65
3.17 Effect of Total Wind Speed on Vertical Vibrations of the Arm 66
3.18 Effect of Turbulence on Horizontal Vibrations of the Arm..... 66
3.19 Effect of Turbulence on Vertical Vibrations of the Arm..... 67
3.20 Effect of Wind Angle of Attack on Horizontal Vibrations..... 67
3.21 Effect of Wind Angle of Attack on Vertical Vibrations 68
3.22 Effect of Variations in Angle of Attack on Horizontal Vibrations 68
3.23 Effect of Variations in Angle of Attack on Vertical Vibrations 69
3.24 Comparison of Data Analysis Using Segments of 100 and 300 Seconds..... 70
3.25 Effect of u-Component on Vertical Vibrations of TS1 with Backplates..... 72
3.26 Effect of u-Component on Vertical Vibrations of TS2 with Backplates 73
3.27 Effect of Mean Wind Speed on Vertical Vibrations of TS1 with Backplates .. 73
3.28 Effect of Mean Wind Speed on Vertical Vibrations of TS2 with Backplates .. 74
3.29 Effect of Angle of Attack on Vertical Vibrations of TS1 with Backplates 74
3.30 Effect of Angle of Attack on Vibrations of TS2 with Backplates 75
3.31 Number of Observations per Range of Angle of Attack for Mode 1100..... 76
3.32 Effect of Mean Wind Speed on Vertical Vibrations of TS1 without Backplates 78
3.33 Effect of Mean Wind Speed on Vertical Vibrations of TS2 without Backplates 78
3.34 Effect of Angle of Attack on Vertical Vibrations of TS1 without Backplates . 79
3.35 Effect of Angle of Attack on Vertical Vibrations of TS2 without Backplates . 79
3.36 Comparison between Modes 1100 and 1101 80
3.37 Number of Observations Per Range of Angle of Attack for Mode 1101 81
4.1 Design Drawing for Wind Tunnel Model..... 91
4.2 Open Circuit Small Wind Tunnel ()CSWT) 93
4.3 Model and Laser Mounted in the OCSWT 94
4.4 Fine and Coarse Grids..... 94
4.5 Time Histories for Wind Tunnel Tests with No Grid..... 98
4.6 Time Histories for Wind Tunnel Tests with Fine Grid..... 99
4.7 Time Histories for Wind Tunnel Tests with Coarse Grid..... 99
4.8 Effect of Wind Speed on Cross-Wind Displacement of Tip with No Grid 101
4.9 Effect of Wind Speed on Cross-Wind Displacement of Tip with Fine Grid 101
4.10 Effect of Wind Speed on Cross-Wind Displacement of Tip with Coarse Grid 102
4.11 Model with Backplates Mounted in TTU Wind Tunnel..... 105
4.12 Tunnel Results for Angle of Attack of 90 Degrees..... 108
4.13 Comparison of TTU and UWO Wind Tunnel Results..... 110
4.14 Wind Tunnel Results for Angle of Attack of 55 Degrees..... 111
4.15 Wind Tunnel Results for Angle of Attack of 45 Degrees..... 111
4.16 Wind Tunnel Results for Angle of Attack of 125 Degrees..... 112
4.17 Wind Tunnel Results for Angle of Attack of 135 Degrees..... 113
4.18 Wind Tunnel Results for Angle of Attack of 270 Degrees 114
4.19 Maximum Amplitude of Vibration Observed for Full-Scale Wind Speed in the 0-15 MPH Range 115

4.20 Effect of Reduced Velocity on Amplitudes of Vibrations 116

5.1 Wind Direction Classification (Vega and Letchford 2006)..... 124

5.2 a) Three-Dimensional Histogram and (B) Directional Analysis Using Weibull Distribution of Wind Data at Reese Station, Lubbock, Texas (Vega and Letchford 2006)..... 125
5.3 Interpolation and Extrapolation for Angle of Attack of 90° 130
5.4 Interpolation and Extrapolation for Angle of Attack of 45° 132
5.5 Sample Data Collected in TTU Wind Tunnel for Smooth Flow 135
5.6 Cantilever Beam Subjected to Load p(x,t) and Having Tip Displacement q(t). 137
5.7 Finite-Element Modeling of Tapered Element (Kaczinski, Dexter, and Van Dien 1998)..... 139
5.8 Finite Element Model (M = Member, N = Node)..... 140
5.9 x vs. $p_o(x)$ 143
5.10 Loads Acting on Mast Arm..... 144
5.11 Typical S-N Curve 147
5.12 Fillet-Welded Mast-Arm-To-Column Connection (AASHTO 2001) 148
5.13 Lower-Bound S-N Curves for AASHTO's Seven Primary Fatigue Categories (Chen and Duan 2000)..... 149
5.14 Effect of Factor *C* on the Prediction of the Fatigue Life of Mast Arms with Backplates..... 155
5.15 Occurrences of Fatigue Damage..... 157

7.1 Traffic Signal Configuration Susceptible to Vortex Shedding..... 165

CHAPTER 1

INTRODUCTION

1.1 Cantilever Traffic Signal Structures

Traffic signals (or traffic lights) are used extensively around the world. The signals, as well as their supporting structures, are manufactured in many different sizes and shapes. A commonly used support for traffic signals is the cantilever traffic signal structure. Figure 1.1 shows an example of this type of structure in which the vertical component is usually referred to as the post or the pole and the horizontal element is referred to as the mast arm. Both the pole and the mast arm are usually made of hollow galvanized steel with circular or octagonal cross-section and tapered diameters.

In Texas, poles are typically 17 to 20 ft high and arms range from 20 to 48 ft in length (Pulipaka 1995), although the Texas Department of Transportation (1995) uses designs for arms that go up to 65 ft in length. Often the arms are manufactured in different shapes. To show one example, in Figure 1.1 the mast arm is straight; while Figure 1.2 shows a structure that has a bent mast arm.

Figure 1.1 Cantilever Traffic Signal Structure with Straight Mast Arm

Figure 1.2 Cantilever Traffic Signal Structure with Bent Mast Arm

The signal heads supported by the mast arm are usually either 3-signal heads or 5-signal heads. For example, in Figure 1.1 the arm supports one 5-signal head and two 3-signal heads; while in Figure 1.2 the arm supports one 5-signal head and one 3-signal

head. Signal heads can have backplates, which are flat plates that surround the signals extending half a light width. Backplates are usually black and offer drivers better visibility of the signal lights against the sun. The signal heads in Figure 1.1 have backplates, while the ones in Figure 1.2 do not. Another parameter that varies from structure to structure is how the signal heads are connected to the mast arm. In Figure 1.1 the signals are at the height of the arm; while in Figure 1.2 the signals are below the arm. In other cases the lights are mounted vertically rather than horizontally.

The mast arms usually have a low resonant frequency of about 1 Hz and a damping of less than 1% of critical damping (Dexter and Ricker 2002). Therefore, they have the propensity of vibrating under wind loading. Vibrations of mast arms can occur at wind speeds as low as 10 mph (Pulipaka, Sarkar, and McDonald 1998) or they may also be provoked by truck-induced gusts (Kaczinski, Dexter, and Van Dien 1998).

1.2 Problem Statement

According to Dexter and Ricker (2002), the span of mast arms of cantilever traffic signal structures and other similar sign and light support structures has increased because "the setback distance of the upright from the roadway has increased for safety reasons and these structures are increasingly being used on roads with more lanes." The longer the mast arm, the more flexible the structure is, therefore larger vibration amplitudes can be expected.

If the vibrations of the mast are too large, it could be difficult for drivers to see the signals and drivers may feel uncomfortable while driving under the vibrating structure

(Kaczinski, Dexter, and Van Dien 1998). Also, vibrating mast arms could create a distraction to passing motorists (Pulipaka 1995). Many drivers complain when the vibrations exceed 8 inches (Kaczinski, Dexter, and Van Dien 1998).

More importantly, vibrations of the mast can lead to fatigue failure. Figure 1.3 shows one example of such failures, which have been reported by many state DOTs. The State of Missouri had over 12 traffic signal mast arms fail in a period of six years (Hartnagel and Barker 1999). Similar failures have been reported in Wyoming, California, and Texas (Chen et al. 2001). In Lubbock, two failures occurred from 2001 to 2005 (Hart 2005).

Figure 1.3 Fatigue Failure of Mast Arm in Lubbock, Texas

Dexter and Ricker (2002) indicated there are many cases of fatigue cracks occurring in cantilevered signal, sign, and light supports and that the economic cost of inspecting, repairing, or replacing for this type of crack is substantial. They stated that

although many of the failures are caught before a collapse occurs, there are a few collapses reported each year where vehicles have collided with the fallen mast, causing injuries and deaths. They also stated the following:

> "The few collisions that occur between vehicles and collapsed cantilevered support structures are not at all significant when considered in terms of the total number of highway collisions. However, the perceived significance of these collisions between vehicles and collapsed cantilevered support structures is enhanced because the collisions are totally unexpected (i.e., the failures take place in weather that is not that unusual, and the public does not expect these support structures to be a hazard)." (Dexter and Ricker 2002)

There are four recognized mechanisms that induce mast arm vibrations on cantilever traffic signal structures: galloping, natural wind gusts, truck-induced gusts, and vortex shedding (Kaczinski, Dexter, and Van Dien 1998). It has generally been thought that galloping is the main cause of vibrations that lead to fatigue failure of mast arms, that natural wind gusts and truck-induced gusts are minor causes, and that vortex shedding does not cause significant vibrations. This has been so widely accepted in the United States that the national design guidelines do not consider vortex shedding in the fatigue design of cantilever traffic signal structures (AASHTO 2001).

1.3 Research Objectives

For the research presented in this report, the objectives are to:

1. Determine the mechanisms that lead to mast arm vibrations and how significant each is in contributing to the fatigue failure of these structures.
2. Provide a methodology for estimating the fatigue life of cantilevered traffic signal structures.

3. Provide guidelines to performing life-cycle cost analysis of cantilevered traffic signal structures.

Both wind tunnel studies and full-scale testing were conducted and their results were used to achieve the first objective. For the second objective, the local climatology of the city of Lubbock, Texas, was used in conjunction with the wind tunnel results. For the third objective, an example of life-cycle cost analysis applied to cantilever traffic signal structures was developed.

1.4 Organization of This Report

Chapter 2 presents a literature review of the research conducted on cantilever traffic signal structures. Chapters 3 and 4 describe the experimental set-up and discuss the results obtained for full-scale tests and wind tunnel studies, respectively. Chapter 5 presents a methodology for estimating the fatigue life of a cantilever traffic signal structure. Chapter 6 discusses life-cycle cost analysis as applied to cantilever traffic signal structures. Finally, the conclusions and recommendations coming out of this research are presented in Chapter 7.

CHAPTER 2

LITERATURE REVIEW

2.1 Introduction

In this chapter, the wind mechanisms that induce vibrations in cantilever traffic signal structures are introduced and the major research undertaken on vibration and fatigue failure of cantilevered traffic signal structures is discussed. Some publications that deal with the testing of damping devices are also briefly discussed, but only to cover the aspect that deals with the vibration of mast arms. The damping devices themselves are not discussed here since they fall outside the scope of this research.

2.2 Vibration-Inducing Mechanisms

Kaczinski, Dexter, and Van Dien (1998) identified vortex shedding, galloping, natural wind gusts, and truck-induced gusts as the most critical fatigue-loading mechanisms in cantilevered supports of signals, signs, and lights. Each of these mechanisms is discussed in this section.

2.2.1 Vortex Shedding

Vortex shedding occurs when vortices with alternating rotational direction are shed periodically into the wake of a bluff body. It forms as a result of the rolling-up of the separating shear layers alternately one side, then the other, and occurs on bluff bodies of all cross-sections (Holmes 2001). The series of decaying vortices that formed in the wake is known as the *von Kármán vortex street*. A sketch of the occurrence of vortex shedding and the von Kármán vortex street is shown in Figure 2.1.

The conditions for coherent vortex shedding to occur are that the approach flow be uniform with low turbulence, that the body be long with a constant cross-section, and that no shear layer attachment occurs (Letchford 2003). Turbulence in the approach flow tends to make the shedding less regular, but the strengths of the vortices are maintained, or even enhanced (Holmes 2001).

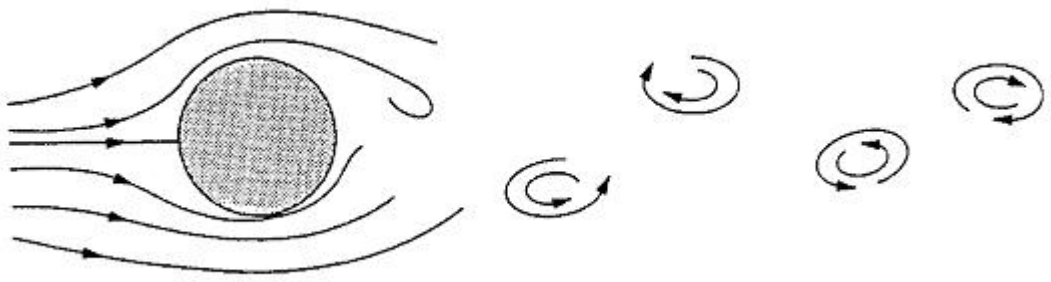

Figure 2.1 Schematic of von Kármán Vortex Street in the Wake of a Circular Cylinder (Kaczinski, Dexter, and Van Dien 1998)

Figure 2.2 Vortex Shedding Acting on Cross-Section of Mast Arm with Traffic Signal

Each vortex being shed causes a change in pressure distribution that virtually produces a cross-wind force at the point where the vortex is being shed. For vortices shed from a flat plate (e.g., a backplate) there will only be cross-wind forces induced on the structure if there are portions downwind of the plate for the alternating vortices to act upon. In the case of signal lights it is likely to be the visors, as shown in Figure 2.2.

The vortex shedding frequency is often described by the non-dimensional Strouhal number (*St*) as follows:

$$St = \frac{f_s B}{U} \tag{2-1}$$

where f_s is the vortex shedding frequency, B is the cross-wind body width, and U is the mean flow speed. From Equation (2-1), the mean velocity at which vortex shedding is expected to occur can be obtained:

$$U = \frac{f_s B}{St} \tag{2-2}$$

Alternating shedding of vortices produces periodic cross-wind forces acting on the body. These cross-wind forces may produce a nominal periodic response, but large

cross-wind vibrations can occur if the frequency of the vortex shedding (f_s) is close to one of the natural frequencies of the body (f_n). Vibrations of the body may enhance the vortex strength, and the vortex-shedding frequency may change to the frequency of vibration, in a phenomenon known as lock-in (Holmes 2001). Therefore, lock-in vibrations ($f_s = f_n$) not only occur at the above wind speed, but also at any speed U within the interval

$$\frac{f_s B}{St} - \Delta U < U < \frac{f_s B}{St} + \Delta U \tag{2-3}$$

where $\Delta U / U$ depends on cross-sectional shape and mechanical damping and is of the order of a few percent (Simiu and Miyata 2006).

2.2.2 Galloping

Galloping consists of large amplitude cross-wind vibrations that can occur to long bodies with certain cross-sections. Circular cylinders are not susceptible to galloping (Pulipaka 1995; Kaczinski, Dexter, and Van Dien 1998). For a given cross-section, the frequency of galloping-induced vibrations is much lower than the frequency of vibrations induced by vortex shedding (Simiu and Miyata 2006).

For galloping to start, there has to be an initial displacement that changes the apparent angle of attack of the wind flow with respect to the cross-section. The initial displacement could be induced by wind gusts or vortex shedding. For example, consider the case presented in Figure 2.3. A square cylinder is immersed in wind with a velocity U in the horizontal direction. Assuming a small downward displacement with a velocity

of $\dot{y}$ is induced, this would produce a wind relative velocity U_{rel} which is the result of the vector sum of U and $\dot{y}$. U_{rel} will have an angle of attack α as shown in the figure.

The lift and drag forces along the direction of relative wind velocity U_{rel} can be expressed as follows:

$$L(\alpha) = \frac{1}{2} C_L(\alpha) \rho U_{rel}^2 A \tag{2-4}$$

$$D(\alpha) = \frac{1}{2} C_D(\alpha) \rho U_{rel}^2 A \tag{2-5}$$

where ρ is the density of air, A is the area of the cylinder projected to the wind, and $C_L(\alpha)$ and $C_D(\alpha)$ are the lift and drag coefficients, respectively, which are functions of the angle of attack α.

The force component in the y-direction (F_y) is calculated as:

$$F_y(\alpha) = D(\alpha)\sin(\alpha) + L(\alpha)\cos(\alpha) \tag{2-6}$$

Another way of expressing F_y is:

$$F_y(\alpha) = \frac{1}{2} C_{Fy}(\alpha) \rho U^2 A \tag{2-7}$$

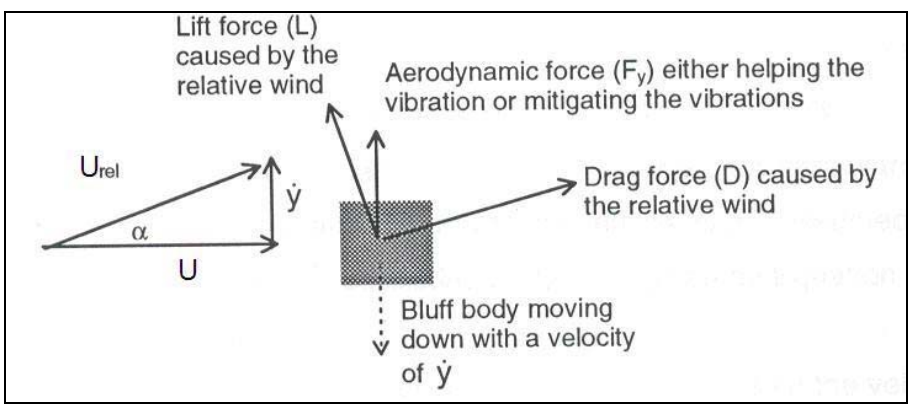

Figure 2.3 Initiation of Galloping (Pulipaka 1995)

From Equations (2-6) and (2-7):

$$\frac{1}{2}C_{Fy}(\alpha)\rho U^2 A = D(\alpha)\sin(\alpha) + L(\alpha)\cos(\alpha) \tag{2-8}$$

Substituting $U = U_{rel}\cos(\alpha)$ and Equations (2-4) and (2-5) into (2-8) and solving for C_{Fy}:

$$C_{Fy}(\alpha) = \frac{C_L(\alpha) + C_D(\alpha)\tan(\alpha)}{\cos(\alpha)} \tag{2-9}$$

Differentiating Equation (2-9) with $\alpha = 0$:

$$\left.\frac{dC_{Fy}}{d\alpha}\right|_{\alpha=0} = \left(\frac{dC_L}{d\alpha} + C_D\right)_{\alpha=0} \tag{2-10}$$

For a small α:

$$\alpha \approx \frac{\dot{y}}{U} \tag{2-11}$$

and:

$$F_y \approx \left.\frac{dF_y}{d\alpha}\right|_{\alpha=0} \alpha \tag{2-12}$$

Inserting Equations (2-7) and (2-11) into (2-12):

$$F_y \approx \frac{1}{2}\rho UA\left(\frac{dC_{Fy}}{d\alpha}\right)_{\alpha=0}(\dot{y}) \tag{2-13}$$

The equation of motion of the body can be written as:

$$m(\ddot{y} + 2\zeta\omega\dot{y} + \omega^2 y) = -F_y \tag{2-14}$$

where m is the mass per unit length, ζ is the damping ratio, ω is the natural circular frequency, y is the displacement, and $\ddot{y}$ is the acceleration. Substituting Equation (2-13) into Equation (2-14) and rearranging:

$$m\ddot{y} + \left[2m\zeta\omega + \frac{1}{2}\rho UA\left(\frac{dC_{Fy}}{d\alpha}\right)_{\alpha=0} \right]\dot{y} + m\omega^2 y = 0 \tag{2-15}$$

It is recognized that in Equation (2-15) the damping coefficient d is given by:

$$d = 2m\zeta\omega + \frac{1}{2}\rho UA\left(\frac{dC_{Fy}}{d\alpha}\right)_{\alpha=0} \tag{2-16}$$

The first term in Equation (2-16) is the mechanical damping of the structure, while the second one can be considered the aerodynamic damping. The system is stable if $d > 0$. For the system to become unstable (i.e., to have negative damping, $d < 0$), the term in parenthesis of Equation (2-16) must be negative:

$$\left(\frac{dC_{Fy}}{d\alpha}\right)_{\alpha=0} < 0 \tag{2-17}$$

Substituting Equation (2-10) into Equation (2-17):

$$\left(\frac{dC_L}{d\alpha} + C_D\right)_{\alpha=0} < 0 \tag{2-18}$$

This is known as the *Den Hartog criterion* or the *Glauert-Den Hartog criterion*, and states, “A section is dynamically unstable if the negative slope of the lift curve is greater than the ordinate of the drag curve” (Den Hartog 1985). This criterion must be satisfied for galloping to occur.

Since the damping coefficient d must be negative for galloping to occur, a critical wind velocity U_c for galloping to occur can be calculated from Equation (2-16) by making $d = 0$ and solving for U:

$$U_c = -\frac{4m\zeta\omega}{\rho A}\frac{1}{\left(\frac{dC_{Fy}}{d\alpha}\right)_{\alpha=0}} \tag{2-19}$$

For galloping to occur, the wind velocity must be greater than U_c (Dyrbye and Hansen 1997).

2.2.3 Natural Wind Gusts

Natural wind gusts occur due to turbulence - the inherent tendency of the wind to change velocity (speed and direction). These changes in velocity affect wind-loading of structures by producing changes in pressure that may induce vibrations in certain structural elements. In lightly damped structures, the structural response due to natural wind gusts is dominated by the response at the resonant frequency, but the amplitude of the response is variable and randomly distributed, unlike the almost constant amplitude harmonic response due to vortex shedding. In addition, turbulence typically causes an along-wind response.

2.2.4 Truck-Induced Gusts

The passage of trucks under cantilever support structures tends to produce gust loads on the front and underside of mast arms and their attachments (Kaczinski, Dexter, and Van Dien 1998). Truck-induced gusts may produce either horizontal or vertical vibrations, or a combination of both.

2.3 Research on Cantilever Traffic Signal Structures

2.3.1 Illinois Department of Transportation

South (1994) conducted research for the Illinois Department of Transportation (ILDOT) with the purpose of combining "pertinent wind loading and vibration theory, fatigue damage theory, and experimental data into a useable fatigue analysis method for overhead sign and signal structures." South collected wind speed data, conducted full-scale experiments on cantilever traffic signal structures, and developed a procedure to predict the fatigue life of these structures.

Wind Speed Data

South (1994) instrumented an in-service traffic signal structure to collect wind speed for about a year and a half. Only wind speed data was collected. He noticed that 91.7% of the measured wind speeds were less than or equal to 15 mph. He concluded the following:

> "…structures are subjected to constantly varying winds. Although this observation may seem naive in light of the complexity of the force calculation methods, the effort was made to reinforce the point that use of isotach charts or maximum predicted wind speeds based on empirical formulas will not account for the variations in wind speeds and applied stresses which affect the fatigue life of the structure." (South 1994)

The above quote makes reference to the fact that the AASHTO *Standard Specifications for structural supports for highway signs, luminaires and traffic signals* (from hereon the AASHTO Specifications) did not have fatigue provisions until its fourth edition published in 2001. Before that, the specifications had only an empirical equation

to calculate the wind pressure on a structure by using the wind speed taken from isotach charts.

Full-Scale Experiments

Full-scale experiments were conducted on a cantilever traffic signal structure with a 44-ft mast arm and signal heads mounted vertically, as shown in Figure 2.4. Initially the structure was tested by the Smith Emery Company in California with only the strain gages 1 through 4 shown in the figure. The structure was tested under a wind force produced by blower set to blow to the front of the signal light head mounted at the tip of the arm. South (1994) recognized that this load is not seen in practice, but indicated that it was interesting to see the behavior of the structure under constant wind. He noted that even steady winds induce variable amplitude cyclic loading.

Afterward, the same structure was installed at ILDOT's Physical Research Laboratory in Springfield, Illinois. This time it was instrumented with all 10 strain gages shown in Figure 2.4. Data was collected for four months. The structure was used to generate a histogram of applied stress range due to ambient wind load. Apparently, the wind velocity itself was not monitored while data was being collected by the strain gages. South (1994) noticed that, for the mast arm, a total of over 3 million stress cycles were measured in the horizontal direction, while almost 2.5 million stress cycles were measured in the vertical direction.

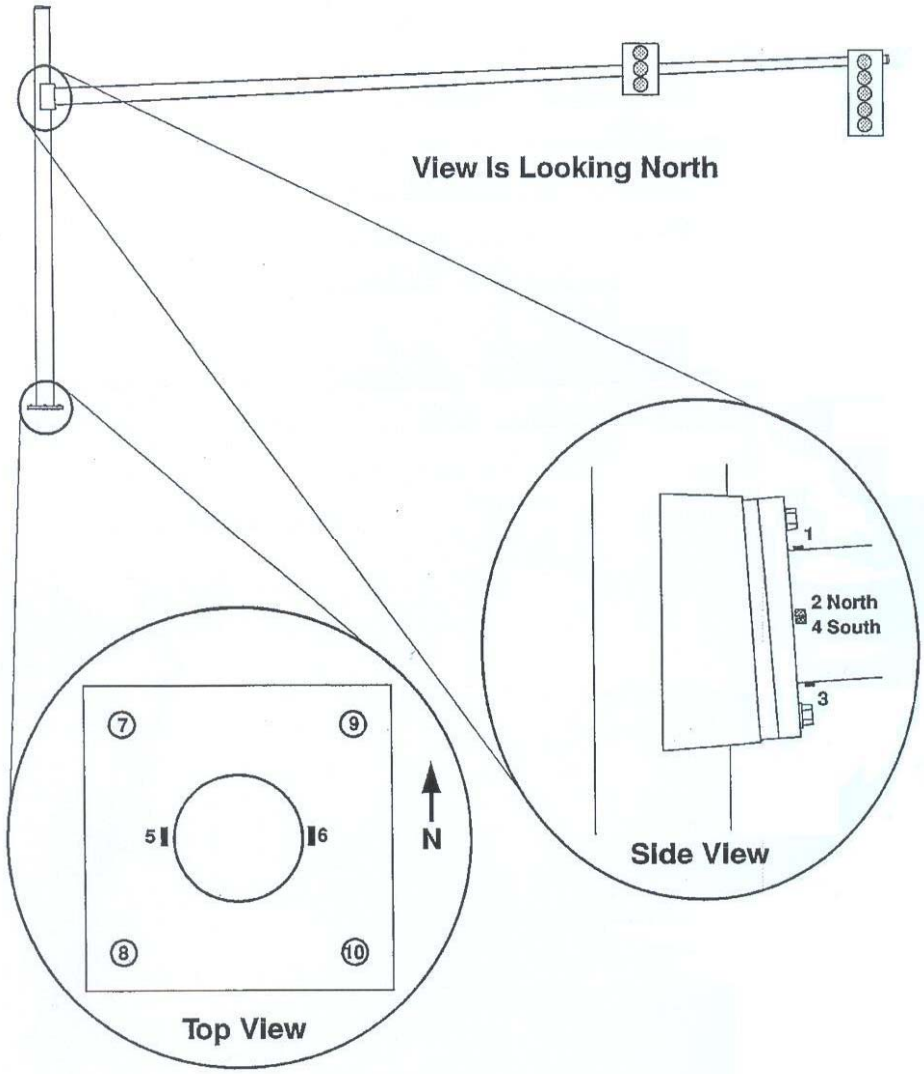

Figure 2.4 Instrumented Traffic Signal Structure at the Physical Research Laboratory in Springfield, Illinois (South 1994)

Subsequently, with the structure still installed at the Physical Research Laboratory, the frequency and amplitude of vertical vibrations of the mast arm induced by vortex shedding were measured using an accelerometer and an oscillographic chart recorder. According to South (1994), the experimental results revealed that the mast arm vibrated in synchronization with the first and second transverse modes when the wind

speed was in the 12-20 mph range. Still, no real proof was offered in the report to demonstrate that the vibrations were in fact induced by vortex shedding.

Fatigue Life Prediction

South (1994) suggested a method to estimate the fatigue life of the structures using horizontal vibrations of the mast arm because, as explained before, he noticed that more stress cycles occur horizontally than vertically. The method does not consider wind direction, only wind speed. It assumes that vortex shedding vibrations have the effect of increasing drag forces and therefore produce horizontal vibrations. A histogram of wind speed of the location of the structure is required. The method is as follows:

1. "Calculate the vortex shedding frequency for each wind speed in the histogram using [the Strouhal number] equation… [See Equation (2-1). In his sample calculations, South assumed $St = 0.2$.]

2. Calculate the drag forces for each wind speed… [For this step, South provided a series of equations which basically calculate drag forces as a product of vortex-shedding-induced vibrations.]

3. Using the drag forces, calculate the applied stresses at the detail(s) of interest… [Details of interest are welds and anchor bolts.]

4. Assume the counts in the histogram to be one-second intervals of constant winds speed application; then the histogram frequency represents the total number of seconds of application of a particular wind speed. Multiply the number of seconds by the vortex shedding frequency to estimate the total number of applied cycles at each wind speed for a year.

5. Use the results of steps 3 and 4 to construct a new histogram for each detail of interest. The result is a stress [range] versus cycles-per-year histogram.

6. Use the histogram developed above in conjunction with the methods outlined… to calculate the expected fatigue life of the detail(s) of interest." (South 1994)

Of the three methods outlined by South (1994) for step 6, he placed more emphasis in the one of applying Miner's Rule, which is the first, simplest and most widely used damage model used to predict fatigue damage for structural components subjected to variable loading conditions (Lee 2005). Miner's Rule is expressed as:

$$D = \sum \frac{n_i}{N_i} \tag{2-20}$$

where:

D = cumulative fatigue damage

n_i = number of cycles at i^{th} stress amplitude

N_i = number of cycles to failure at i^{th} stress amplitude.

Fatigue failure is expected to occur when the summation of Equation (2-20) reaches unity. In South's method, the values of n_i are given by the histogram obtained in step 5 and the values of N_i are obtained from stress range versus frequency (S-N) curves which are published by the American Welding Society for different welded tubular connections. With the calculation of D in South's method, the fatigue damage accumulated in one year is calculated and the fatigue life of the structure can be estimated.

Using a wind speed histogram generated with data collected over one year, South (1994) estimated the fatigue life of the structure used in the full-scale experiments as 24.75 years. He also used the 4-month stress range histogram generated for the same

structure in the full-scale experiments and multiplied by three to estimate a 1-year histogram. This allowed him to skip steps 1 to 5 in his methodology, going straight to step 6 and calculating a fatigue life of 19.74 years. He indicated that this second result correlated "with many actual fatigue failures of light poles and highmast structures using weathering steel."

2.3.2 Texas Tech University

Extensive research on wind loading of cantilevered traffic signal structures was conducted by researchers at Texas Tech University (TTU). These researchers observed that cantilevered traffic signal structures used by the Texas Department of Transportation (TXDOT) generally undergo large amplitude vibrations in wind speeds of 10 mph or slightly higher and that the vibrations are steady up-and-down motions perpendicular to the wind direction (Pulipaka, Sarkar, and McDonald 1998). Pulipaka (1995) indicated that the vibration amplitudes could be as high as 20-24 inches from peak to peak. He did not provide a source for these values nor indicate for what arm length these vibrations were observed. TTU researchers conducted water-table, tow-tank, and wind tunnel experiments as well as field testing.

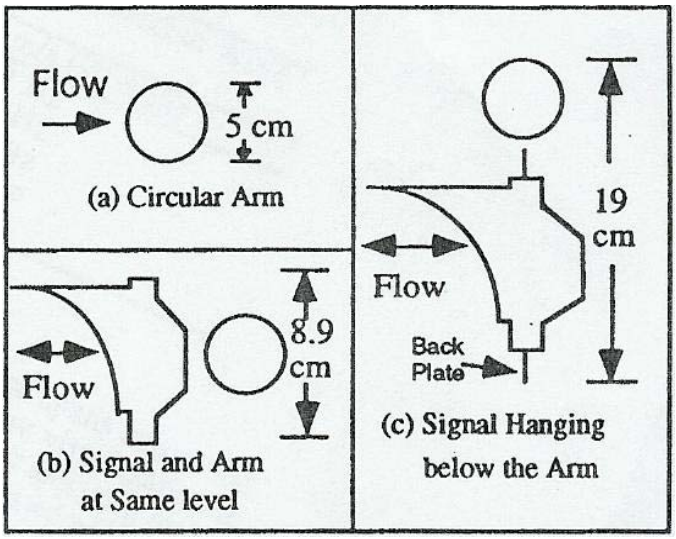

Figure 2.5 Models Used for Water-Table Experiments
(Pulipaka, McDonald, and Mehta 1995)

Water-Table Experiments

TTU researchers first conducted water-table experiments to observe for vortex shedding behavior around mast arm and signal light head cross-sections (Pulipaka, McDonald, and Mehta 1995; McDonald et al. 1995). They tested two-dimensional, one-quarter scale models of the cross-sections for various arrangements of the signal light head with respect to the mast arm, changing flow directions and adding or removing backplates, as shown in Figure 2.5.

Through Finite Element Analysis, the TTU researchers had calculated the fundamental frequency of various cantilever traffic signal structures and they estimated that “for a resonance condition, the vortex shedding frequencies need to be approximately equal to 1.0 Hz” (McDonald et al. 1995). From the water table experiments, they determined that vortex shedding frequencies of 1.0 Hz would occur at wind speeds of less than 10 mph. Since large amplitude vibrations had been observed in the wind speed range

of 10 to 30 mph, they concluded that “the water table experiments demonstrated that vortex shedding is not the cause of large amplitude vibrations cantilever traffic signal structures” (McDonald et al. 1995).

Although McDonald et al. (1995) referred in the passage above to vortex-induced vibrations as a case of resonance, in reality, vortex shedding is a complex phenomenon that involves both wind-initiated forces and self-excitation forces (Billah and Scanlan 1991).

Tow-Tank Experiments

From the tow-tank experiments the researchers tried to determine the source of aerodynamic force causing the vibrations (Pulipaka 1995). They were particularly looking at vortex shedding and galloping. An actual signal head with a portion of a mast arm was towed through the tank to simulate wind speeds in the 10-30 mph wind speed range. Experiments were conducted with the signal connected to the mast arm in different configurations. Flow visualization was used to check for vortex shedding. To check for galloping, the researchers measured drag and lift forces to determine if a signal-light configuration satisfied the Glauert-Den Hartog’s criterion. From the flow visualization, Pulipaka reported:

> “The flow was very disorganized. The variety of edges and corners on the traffic signals produced a complex turbulent flow field in which identification of a dominant shedding frequency was difficult. . . . Randomness and high frequency of vortex formation are characteristics that make vortex shedding an unlikely candidate to produce significant wind-driven oscillations of traffic signal structures.” (Pulipaka 1995)

From the measurement of forces, force coefficients in the vertical direction (C_{Fy}) as a function of angle of attack (α) were obtained. The angle of attack was measured between the horizontal axis and the relative wind speed (U_{rel}), as shown in Figure 2.3.

Figure 2.6 shows one of the configurations tested and the corresponding results. The angle of attack was induced with motion of the model in the y-direction. From Figure 2.6 it was noticed that for all angles of attack:

$$\frac{dC_{Fy}}{d\alpha} = \frac{dC_L}{d\alpha} + C_D < 0 \tag{2-21}$$

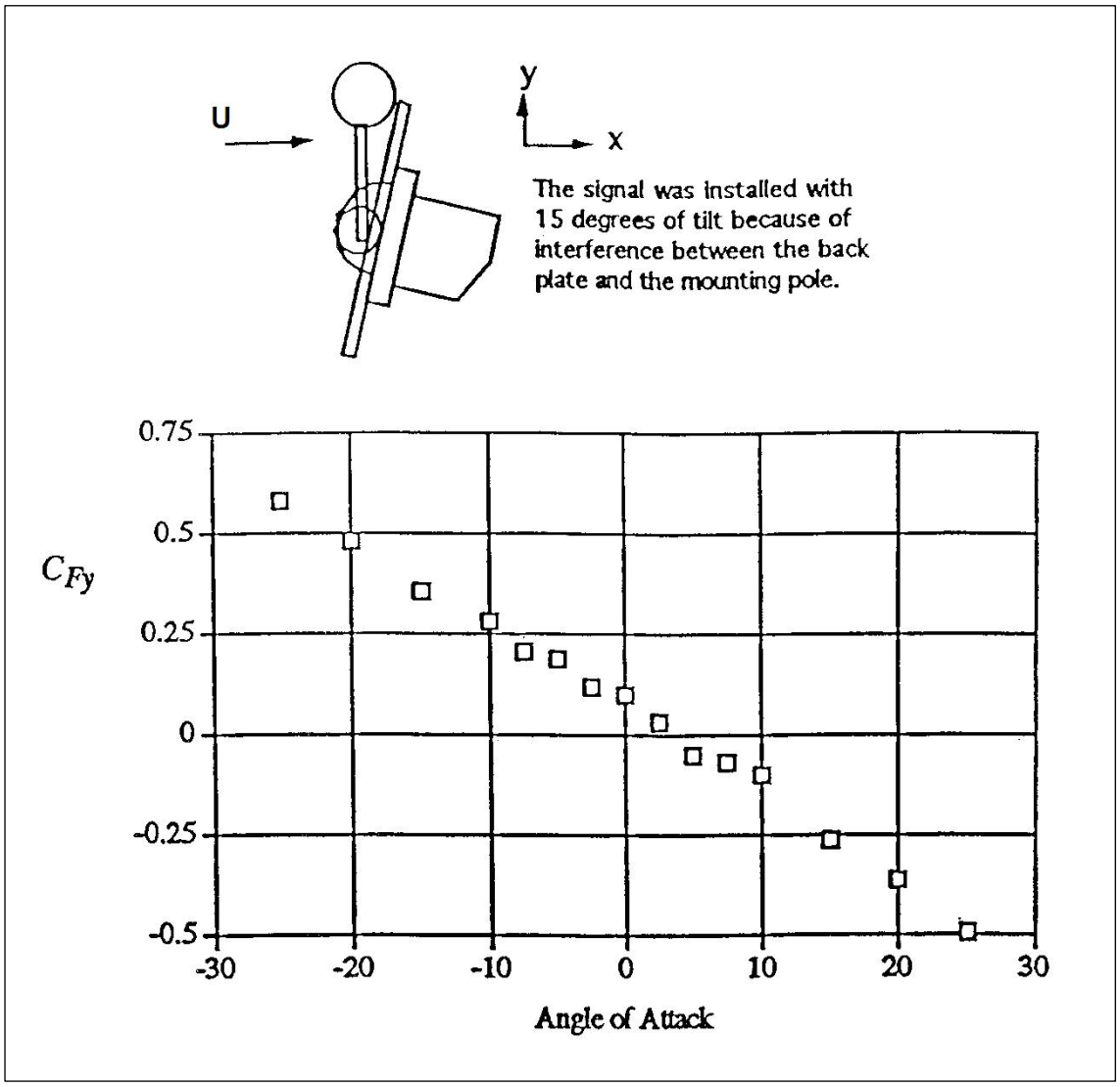

Figure 2.6 Force Coefficient (C_{Fy}) vs. Angle of Attack for Traffic Signal Configuration Identified as Susceptible to Galloping (Pulipaka 1995)

Pulipaka (1995) noticed that the configuration satisfied the Den Hartog criterion for galloping (see Equations (2-17) and (2-18)). He wrote: "The negative slope for C_{Fy} indicates that the aerodynamic forces are destabilizing and the model is susceptible to galloping oscillations." The configuration shown in Figure 2.6 was the only one for

which this was the case, therefore this was the only configuration they found to be susceptible to galloping. At this point, TTU researchers appeared to have eliminated vortex shedding as a possible source of large amplitude vibrations.

Wind Tunnel Experiments

The wind tunnel experiments at TTU started with the notion that the configuration shown in Figure 2.6 was the only one susceptible to galloping (Pulipaka, Sarkar, and McDonald 1998). It should be noted that this configuration with the signal head having a 15-degree downward tilt does not represent a real field condition. Therefore when the wind tunnel experiments were conducted, the configuration tested is the one shown in Figure 2.7.

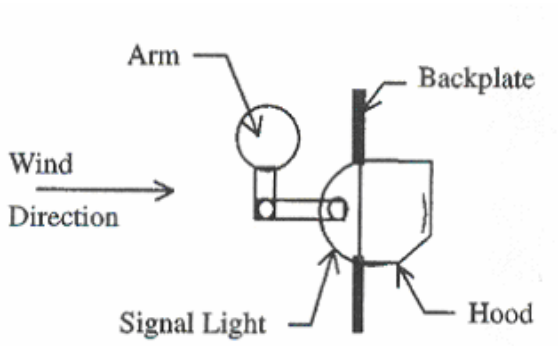

Figure 2.7 Signal Light Configuration Considered Susceptible To Galloping
(Pulipaka, Sarkar, and McDonald 1998)

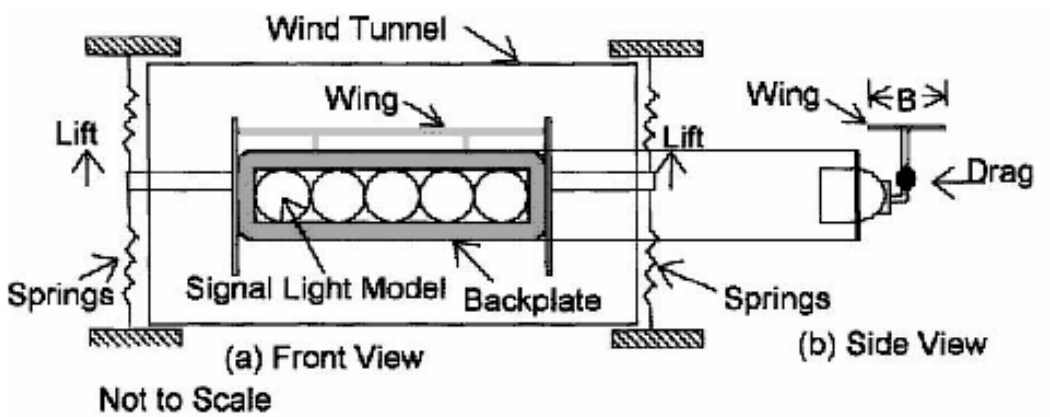

Figure 2.8 Wind Tunnel Test Conducted at TTU (Pulipaka, Sarkar, and McDonald 1998)

Figure 2.8 shows a sketch of the dynamic test setup for the wind tunnel experiments. The figure shows a wing attached to the model. Two types of wing were tested as damping devices (flat plate wing and flat plate wing with rounded edges), but experiments were also conducted with no wing. The model had a length scale of 1:4 and was made from wood and aluminum. A wind-tunnel blockage ratio of 6% was estimated.

The experiments were conducted by giving an initial displacement to the model in the lift direction and then suddenly releasing it, allowing the model to vibrate freely in the vertical direction. This procedure was repeated at different wind speeds and the recorded response was used to calculate the non-dimensional number H_1^*, which gives a measure of the aerodynamic damping. H_1^* is calculated as follows:

$$H_1^*(R) = \frac{4m(\zeta_o - \zeta(R))}{\rho B^2} \tag{2-22}$$

where:

$H_1^*(R)$ = a measure of the aerodynamic damping at reduced velocity of R

m = mass of the model per unit length

ζ_o = damping of the system at zero wind speed

$\zeta(R)$ = the overall damping of the system at reduced velocity R

ρ = density of air

B = along-wind dimension of the model (see Figure 2.8)

$R = \dfrac{U}{nB}$ = reduced velocity

U = wind speed

n = frequency of the model suspended from the springs at zero wind speed

TTU researchers plotted H_1^* against the reduced velocity as shown in Figure 2.9. For comparison, calculated values for an airfoil were also plotted in this figure. For the case of the model with no wing, the researchers observed:

> "H_1^* suddenly starts increasing beyond a reduced velocity of 20, which corresponds to a wind speed of 14 mph. At a reduced velocity of 25 (18 mph in field conditions), H_1^* becomes a positive number, which suggests that the signal light configuration has negative aerodynamic damping, and is susceptible to galloping vibrations." (Pulipaka, Sarkar, and McDonald 1998)

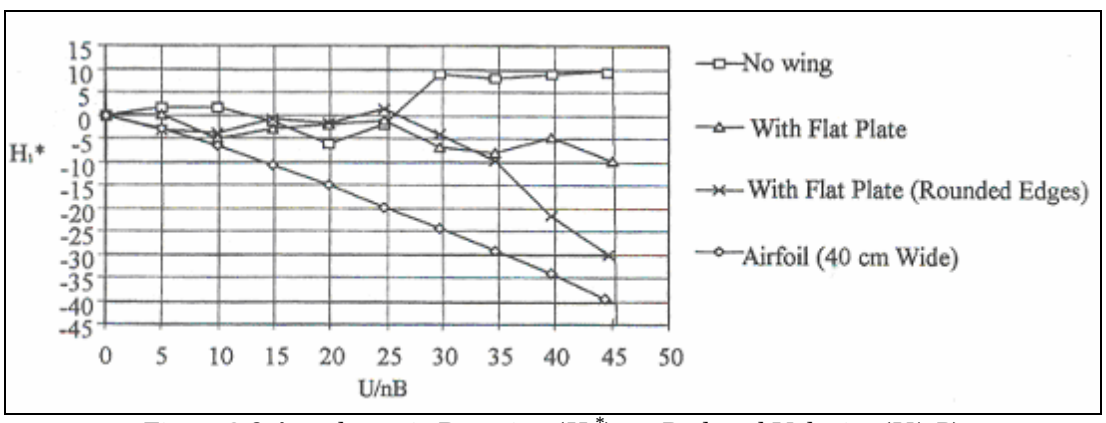

Figure 2.9 Aerodynamic Damping (H_1^*) vs. Reduced Velocity (U/nB)
(Pulipaka, Sarkar, and McDonald 1998)

Field Tests

Pulipaka (1995) tested two cantilever traffic signal structures, each having a bent mast arm. First he tested a structure with a 40-ft long mast arm, then a structure with a 48-ft long arm. When a structure was tested, it was mounted on a rotatable foundation. During testing, an anemometer was used to determine the wind direction and then the structure was rotated so that the mast arm was close to being perpendicular to the direction of the wind.

For the case of the structure with the 40-ft arm, four configurations were tested, but galloping was observed only for the configuration shown in Figure 2.7 (the signal light has a backplate and is suspended below the arm, and the wind is blowing from the back of the signal). When the structure with the 48-ft arm was tested, only the configuration shown in Figure 2.7 was tested. For the experiments with the 48-ft arm, after obtaining the desired arm orientation with respect to the wind direction, the arm was given an initial displacement with a wire and then released to vibrate freely. Pulipaka indicated the following:

> "If the wind speed and direction held steady, vibrations would continue to increase in amplitude until some limiting value was achieved. . . With significant change in wind direction, the vibration amplitudes would decrease and galloping would cease. A change in wind speed resulted in a change in displacement amplitude, if wind direction held steady." (Pulipaka 1995)

Conclusions

Conducting water-table, tow-tank, wind tunnel, and field experiments, the Texas Tech researchers determined that large amplitude vibrations occur when the wind blows from the backside of the signal lights with a backplate attached, as shown in Figure 2.7.

They concluded these large amplitude vibrations are due to the galloping phenomenon. They basically eliminated vortex shedding as a potential cause for the large amplitude vibrations.

TTU researchers explained the mechanism that produces the large amplitude vibrations as follows:

> "At low wind speeds, vortex shedding or gustiness in the wind initiates the vibrations. As the wind picks up beyond the critical speed, the signal structures exhibit the galloping phenomenon. This can be explained either by the Glauert-Den Hartog criterion or by showing that the condition of single-degree-of-freedom (SDOF) flutter in the vertical mode is satisfied." (Pulipaka, Sarkar, and McDonald 1998)

2.3.3 Lehigh University

Kaczinski, Dexter, and Van Dien (1998) conducted research funded by the National Cooperative Highway Research Program (NCHRP). Their study was not limited to cantilevered traffic signal structures; it included cantilevered sign and light supports. Through a literature review, they identified galloping, vortex shedding, natural wind gusts, and truck-induced gusts as the most critical fatigue-loading mechanisms. Their research resulted in the Fatigue Design section of the AASHTO Specifications (2001). They performed a survey of state DOTs as well as wind tunnel tests and finite elements analysis, all of which are discussed here. They also conducted research related to connection details (mast-arm-to-pole, pole-to-base-plate), which is outside the scope of this report.

Survey

The researchers conducted a survey of the state DOTs to learn how the different cantilever support structures (signs, signals, and luminaries) were performing. They reported the following:

> "Among the 36 states which responded, approximately one-half had had problems with wind-induced vibrations of cantilever support structures. Several states reported occurrences of horizontal mast-arm displacement ranges in excess of 48 in under steady-state winds with velocities in the range of *10 to 35 mph*. Generally, the reported vibrations were observed to occur *in the plane* of the structure (i.e., vertical-plane vibrations of the horizontal mast arm) in a direction *normal* to the direction of wind flow. . . . The 36 state departments of transportation, which responded the survey, reported a total of 80 occurrences of fatigue damage in cantilever support structures resulting from wind-loading. Most of the occurrences of fatigue damage were reported at either the mast-arm-to-column connection, column-to-base-plate connection, or anchor bolts. The propagation of these cracks has resulted in the collapse of several cantilevered support structures" (*italics* are current author's emphasis). (Kaczinski, Dexter, and Van Dien 1998)

In the above quote, it is not clear what specifically applies to cantilever traffic signal structures. Also, no indication was given as to when these failures occurred. The details of the survey were apparently kept in an unpublished interim report.

Wind Tunnel Experiments

Kaczinski, Dexter, and Van Dien (1998) noted the research conducted at TTU (see Section 2.3.2) was limited to cantilever traffic signal structures with signal heads mounted horizontally. Therefore for their wind tunnel experiments on signal structures, Lehigh researchers only considered the case of heads mounted vertically, testing two aeroelastic models: Specimens A and B.

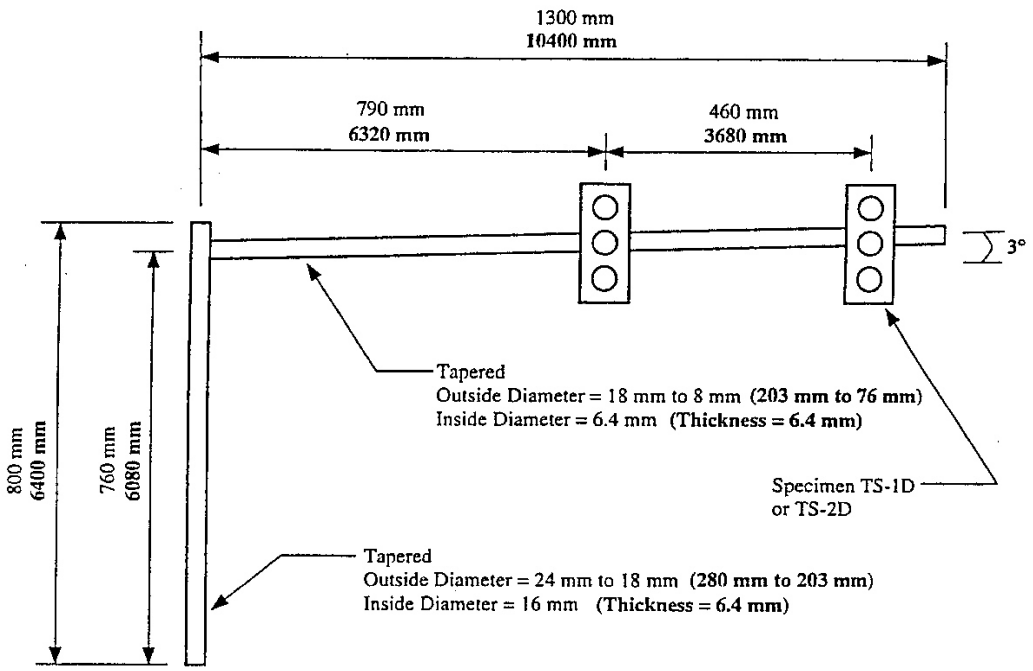

Figure 2.10 Specimen A for Wind Tunnel Testing. Bold Face Indicates the Dimensions of the Prototype (Kaczinski, Dexter, and Van Dien 1998)

Specimen A shown in Figure 2.10 had a length scale of 1:8. Specimen B had the same dimensions as Specimen A, except that it had a prismatic mast arm (i.e., the arm has a constant diameter of 16 mm and a thickness of 0.9 mm). For both specimens, signal heads were tested with and without backplates. Only flow from the front and from the back was considered. During testing, the pole of the model was mounted on a dynamic force balance to measure moments.

Lehigh researchers identified galloping-induced vibrations on only one occasion with Specimen A having signals with backplates and flow from the back. When repeating this same test, they were unable to reproduce the ‘galloping’ behavior nor any other dynamic response involving Specimens A or B. They did not observe any vibrations caused by vortex shedding.

Finite Element Analysis

Kaczinski, Dexter, and Van Dien (1998) performed static and dynamic finite element analysis to estimate the magnitude of galloping, vortex shedding, and natural wind gust equivalent static fatigue limit-state loads for the different types of cantilever support structures (signal, sign, and light). Using results from research conducted on cantilever sign structures (not on supporting structures of traffic signals), they validated a simple static load model for truck-induced gust loads that apply pressure in the vertical direction to a projected area in a horizontal plane of the mast arms and attachments, including mast arms of traffic signals. For the cases of galloping and vortex shedding of cantilever traffic signal structures, they used as a basis the results obtained from their wind tunnel experiments and the findings of the TTU researchers (as discussed in Section 2.3.2). Therefore, no equivalent load for vortex shedding was calculated for cantilever traffic signal structures.

Fatigue Design

Kaczinski, Dexter, and Van Dien (1998) pointed out that Miner's Rule (discussed in TK) is an accepted method for predicting the fatigue life of structures under variable-amplitude loading. Still, they indicated that:

> "Because of the inherent variability in frequency and duration of wind-induced vibrations, designing cantilevered signal, sign, and luminaries structures for a finite fatigue life using Miner's Rule for cumulative damage is impractical. Not only does the possibility exist for a larger number of cycles to be accumulated in a short period of time when resonant vibrations are induced by galloping or vortex shedding, but the long-term cumulative effects of natural wind and truck-induced wind gusts can also result in the development of fatigue damage." (Kaczinski, Dexter, and Van Dien 1998)

As shown in the quote on the previous page, the authors recommended an infinite life approach for fatigue design. This approach uses a constant-amplitude fatigue limit (CAFL) which is the stress range below which the fatigue life appears to be infinite. Basically, the structure is designed so that less than 0.01% of the stress ranges exceed the CAFL. The infinite life approach was developed in another NCHRP project (Fisher et al. 1993) in which full-scale welded details were tested under variable-amplitude tests with varying percentages of the stress ranges exceeding the CAFL. The 0.01% limit was selected because of the following:

> "It was observed that failure could still occur if 0.05 percent or more of the stress ranges exceed the CAFL and that infinite life resulted when 0.01 percent or fewer of the cycles exceed the CAFL." (Kaczinski, Dexter, and Van Dien 1998)

Conclusions

Their research reaffirmed that cantilevered traffic signal structures are not susceptible to vortex shedding and that galloping is the major cause of vibrations that may lead to fatigue failure. Yet they required that natural wind gusts and truck-induced gusts were taken into consideration in the fatigue design of these structures. Therefore, the AASHTO Specifications (2001) require that cantilever traffic signal structures be designed for galloping, natural wind gusts, and truck-induced gusts, but not for vortex shedding.

2.3.4 Missouri Department of Transportation

Over a period of six years, the state of Missouri had over 12 mast arms fail at the arm-post connection (Hartnagel and Barker 1999), leading the Missouri Department of

Transportation (MoDOT) to fund research projects carried out by the University of Missouri – Rolla and the University of Missouri – Columbia. These projects included full-scale tests and forensic investigations which are discussed below.

Full-Scale Tests

Hartnagel and Barker (1999) conducted full-scale experiments to determine the effects that truck-induced gusts have on cantilevered traffic signal structures. They instrumented two mast arms each with an accelerometer at the tip and with strain gages placed both at the arm-to-post connection and at a distance away from said connection. They measured the effects of passing traffic and observed that the back-and-forth (or out-of-plane) bending was more severe than up-and-down (or in-plane) bending of the mast arm, contradicting the model suggested by Lehigh University which only applies truck-induced gust pressures in the vertical direction (as mentioned in Section 2.3.3).

Chen et al. (2001) suspected that the Missouri failures were a result of overstressing, poor welding quality, and low fatigue strength. They conducted full-scale experiments on two structures with the layout shown in Figure 2.11. One structure had a 54-ft long arm and the other had a 42-ft long arm. Notice from Figure 2.11 that the signal heads are vertically mounted. This differs from the experiments conducted at TTU, where the heads were mounted horizontally.

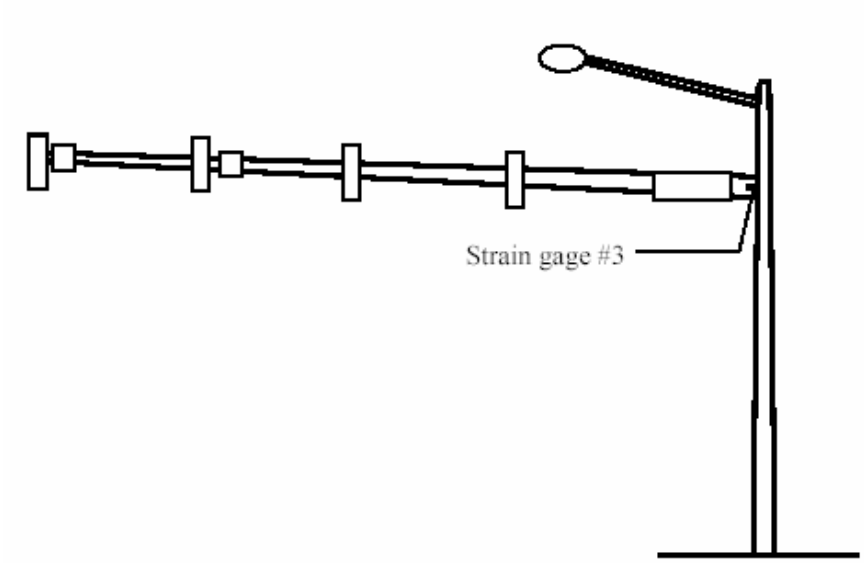

Figure 2.11. Schematic of Structure Studied by MoDOT (Chen et al. 2001)

To monitor truck- and wind-induced vibrations, the two mast arms were instrumented with strain gages at both midspan and near the arm-to-post connection and an anemometer was used to measure the speed of wind gusts. They only took into consideration the wind speed and not the wind direction. They found that the strains caused by truck passage are significantly lower than the ones caused by the natural wind gusts and that the structure with the longest mast arm had a significantly larger average stress. They also concluded that the stress associated with the vertical vibrations caused by natural wind gusts is less than one-third of that with the horizontal vibrations. It appears that these researchers did not consider vibrations induced by galloping or vortex shedding. It is possible that they did not have the appropriate conditions for these to occur.

Chen et al. (2001) also concluded that both the wind speed and the ratio between horizontal stress and the square of the wind speed follow a logarithmic normal

distribution, and that since this ratio was insensitive to wind speed, its distribution could be used for weak and strong wind gusts. To determine the wind speed distribution at Columbia, Missouri, they used data provided by the National Climatic Data Center collected from 1969 through 1978. The original data included monthly and annual statistics on the occurrence of wind events at various hourly mean wind speeds in 16 horizontal directions. Chen et al. (2001) grouped the wind gusts with the same wind speed into one category, regardless of direction. For the ratio distribution they used a total of 969 seconds of accumulated data collected from the two instrumented mast arms.

Chen et al. (2001) suggested the following procedure to estimate the number of stress cycles in the horizontal direction at various levels due to natural wind gusts and to predict the fatigue life of an instrumented signal structure:

1. "Analyze the historical wind gust records (10 years) in the vicinity of the instrumented structures to determine the statistical distribution of the wind speed.
2. Determine the number of cycles at various stress levels (normalized by the square of wind speed) from the field test data on the instrumented mast arms.
3. Extrapolate the stress distribution in Step 2 into the corresponding stress for the rare wind gust at higher speed.
4. Compute the number of cycles corresponding to different stress ranges by multiplying the wind speed distribution by the load spectrum from Steps 2 and 3.
5. Determine the number of cycles that the mast arm can endure before a fatigue failure occurs under different cyclic loads of constant amplitude.

6. Divide the results in Step 4 by those of Step 5 to calculate the minor damages and combine them to predict the fatigue life of the signal structure under a variable stress loading." (Chen et al. 2001)

What Chen et al. suggested in Step 6 is the application of Miner's Rule, which was discussed in Section 2.3.

The procedure suggested by Chen et al. is very similar to the method to predict the fatigue life that was recommended by South (1994) in his report for the Illinois Department of Transportation, as discussed in Section 2.3. Both procedures try to predict the fatigue life by estimating the number of horizontal-vibration cycles instead of the vertical ones, both use wind speed in their calculations without considering wind direction, and both use Miner's Rule (although South also discussed other methods for estimating the fatigue damage under variable-loading conditions) .

Forensic Investigation

Chen et al. (2002 and 2003) performed a forensic investigation of several failed mast arms. They concluded that "the main culprit for the premature fatigue failure of mast arms in Missouri can be attributed to poor weld quality" (Chen et al. 2003). Most of the information of this research is concentrated on the specifics of the arm-post connection (as shown in Figure 2.12), which is out of the scope of this dissertation. Still one interesting observation for this dissertation was the following:

> "The cracks on almost all the failed mast arms are located at the connection of the arm to the base plate. They were observed to initiate on the *top* of the arms and are primarily associated with the bending effect of the mast arms in the *vertical plane*" (*italics* are current author's emphasis). (Chen et al. 2002)

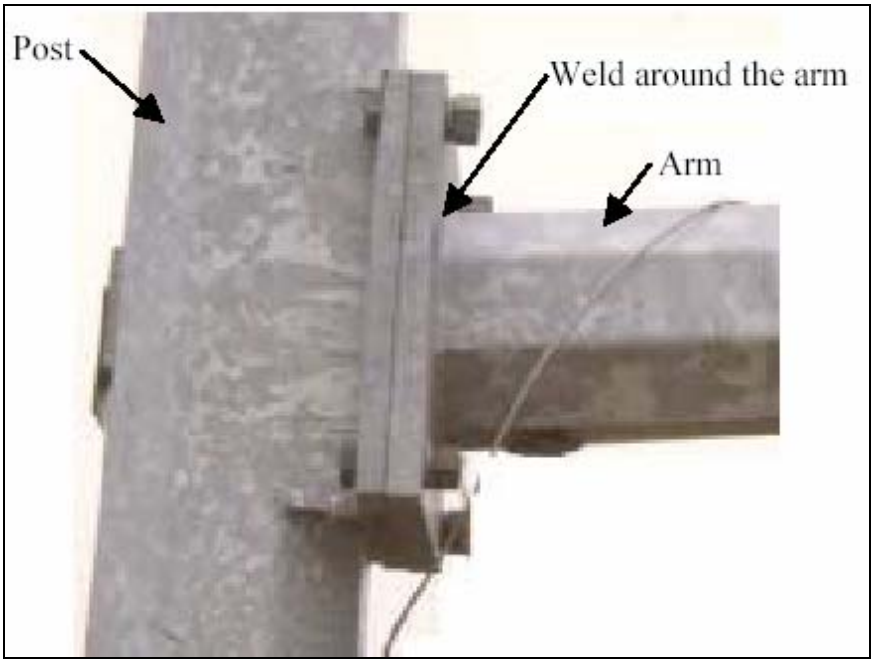

Figure 2.12. Typical Arm-Post Connection used by MoDOT (Chen et al. 2001)

2.3.5 University of Wyoming

Based on the recent failure of two cantilever traffic signal structures in the state of Wyoming (Gray et al. 1999; Hamilton, Riggs, and Puckett 2000), research on this topic commenced at the University of Wyoming. The structure that they studied is shown in Figure 2.13, with a connection as shown in Figure 2.14. Notice in Figure 2.13 that the signal heads are mounted vertically, similar to the structures studied by MoDOT, which differs from the typical TXDOT orientation studied by TTU. Also notice in Figure 2.14 that the base plate of the mast arm is at an angle with respect to the vertical axis of the pole. A typical connection used by TXDOT is the one shown in Figure 1.3, in which the base plate is parallel to the pole's longitudinal axis.

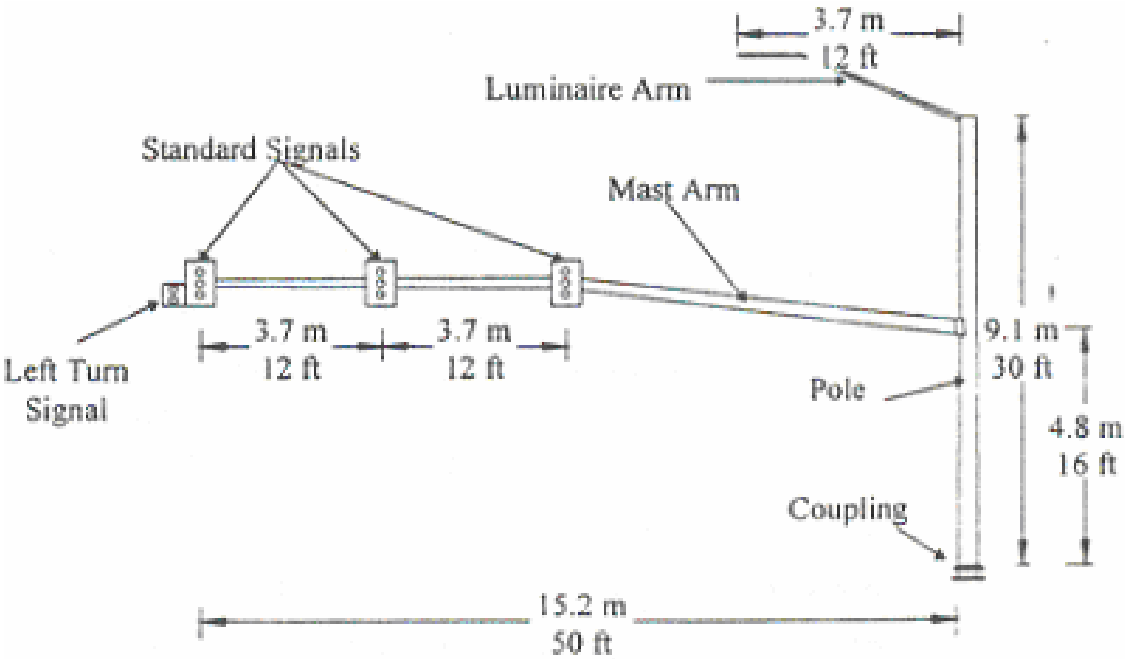

Figure 2.13. Test Cantilevered Traffic Signal Structure in Wyoming
(Hamilton, Riggs, and Puckett 2000)

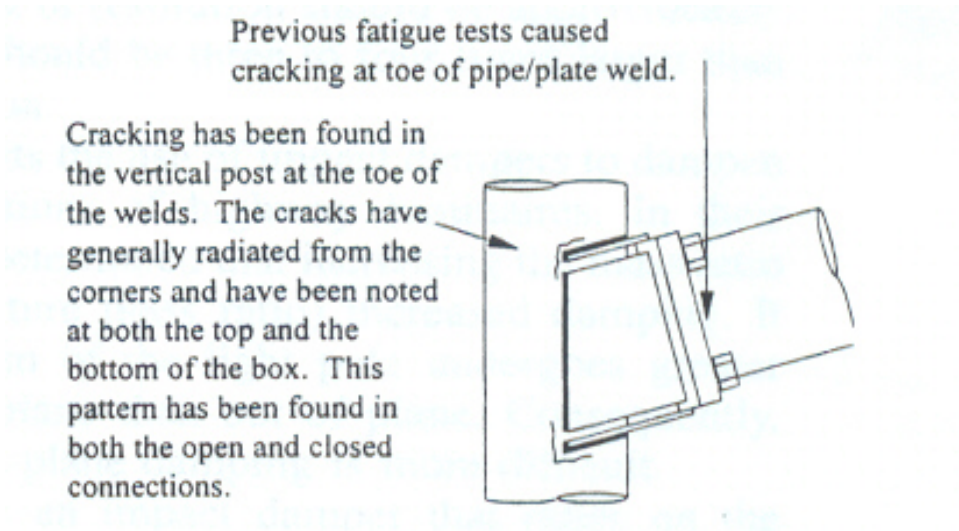

Figure 2.14. Connection Detail used in Wyoming
(Hamilton, Riggs, and Puckett 2000)

Gray et al. (1999) reported that the failures occurred at the connection between the mast and the pole and were due to fatigue cracking on the pole near the base of the weld (see Figure 2.14) resulting from vibrations caused by the wind. Through finite element analysis, the researchers suggested that out-of-plane (or horizontal) bending might be a major consideration in fatigue crack formation on the pole near the connection to the mast arm because they create much higher stresses than the vertical moments.

Hamilton, Riggs, and Puckett (2000) instrumented a signal (like the one shown in Figure 2.13) and observed that the tip of the mast arm displaces in a circular or elliptical pattern. They indicated that the motion created nominal biaxial stresses which occur at the corner of the connection. Figure 2.15 shows the in-plane and out-of-plane moments they plotted incrementally as a function of time. This figure represents a trace of how the tip displacement would appear. These researchers did not indicate under what wind speeds they obtained this sketch, nor the length of time of the data.

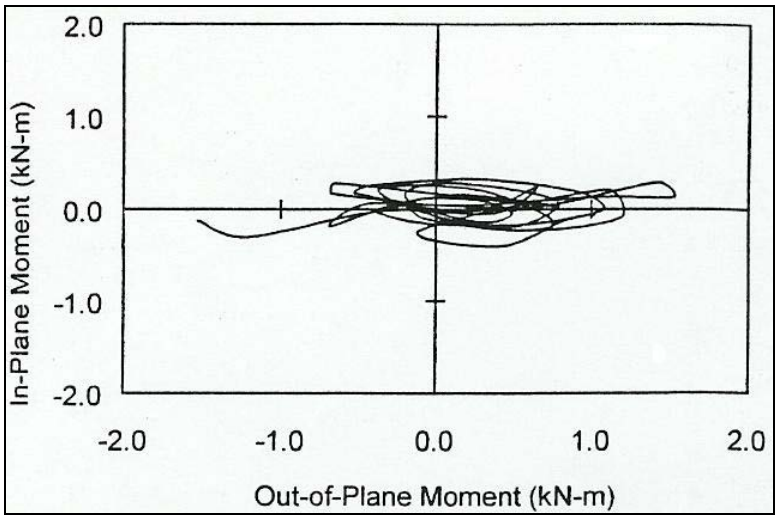

Figure 2.15. Combination of In-Plane and Out-of-Plane Motion (Hamilton, Riggs, Puckett 2000)

Hamilton, Riggs, and Puckett (2000) found from a literature review that galloping was recognized as the primary cause of damaging motion in cantilever traffic signal structures. However, because they observed that the damage that was occurring in Wyoming had been primarily at the pole near the toe of the weld between the box connection and the pole (see Figure 2.14) and because of the circular/elliptical displacement of the tip of the arm they observed (see Figure 2.15), they believed that out-of-plane motions due to natural wind gusts played an important factor in the failures. Therefore they stated that both in-plane (galloping) and out-of-plane (gust) motions are significant contributors to the fatigue damage of the Wyoming structures.

2.3.6 University of Minnesota

Dexter and Ricker (2002) continued at the University of Minnesota the research that was carried out at Lehigh University on cantilever signal, sign, and light supports (see Section 2.3.3). They focused on loads resulting from variable-message signs, methods for mitigating galloping effects, methods for tightening anchor bolts, methods for identifying structures and sign configurations susceptible to galloping, and characterization of importance factors, which are all outside the scope of this study. They also developed a guide on design, installation, inspection, and maintenance of cantilevered supports in which they suggest that traffic signal structures be inspected at least every 4 years.

Another research outside the scope of this study is that conducted by Ocel, Dexter, and Hajar (2006) in which they tested the fatigue resistance of two mast arm-to-

pole connections commonly used in cantilever traffic sign and signal structures in the state of Minnesota. They offered recommendations on how to make the connections stronger.

2.3.7 The University of Texas at Austin

Researchers at the University of Texas at Austin conducted full-scale experiments to study wind-induced vibrations of cantilever traffic signal structures, particularly investigating the loading effects of galloping and truck-induced gusts. For the galloping research, Florea (2005) instrumented three in-service cantilever traffic signal structures each with an anemometer, strain gages, and an accelerometer, as shown in Figure 2.16. The instrumented structures had signals oriented horizontally. Data was recorded for about nine months. Florea (2005) reported "although four large amplitude-displacement events were captured and gave insight into the behaviour of the structures in windy conditions, none of them were determined to be true galloping events."

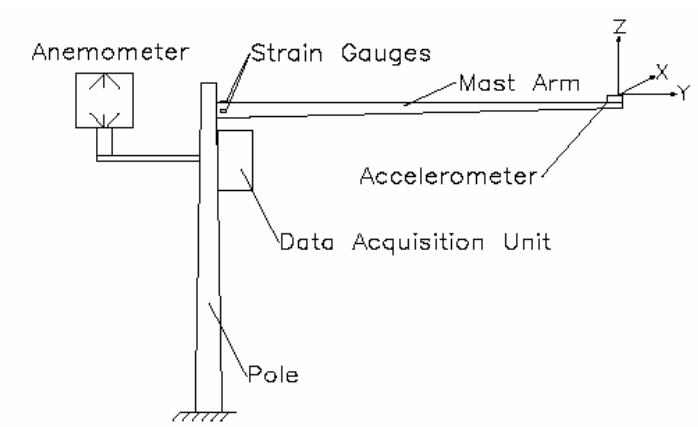

Figure 2.16 Equipment Layout for Galloping Experiment (Florea 2005)

Also of interest are the results they obtained in their research on truck-induced vibrations. Albert (2006) instrumented two in-service structures with anemometers and strain-gages and used a radar gun to measure the effect of truck speed. The following statement summarizes his findings:

> "Interestingly, the truck-induced gusts caused a greater effect in the out-of-plane direction (same direction as traffic flow) instead of the in-plane direction that is included in the AASHTO Specifications. It was determined that overall natural wind gusts produce a larger response in cantilevered traffic signal structures than gusts produced by trucks passing beneath the signals." (Albert 2006)

These results agree with the ones obtained for MoDOT by Hartnagel and Barker (1999) and Chen et al. (2001), as discussed in Section 2.3.4, even though the Missouri signals were oriented vertically, while the Texas signals were oriented horizontally.

2.4 Summary

Vortex shedding, galloping, natural wind gusts, and truck-induced gusts have been identified as potential wind loading phenomena that could lead to excessive vibrations and fatigue of signal, sign, and light cantilever support structures (Kaczinski, Dexter, and Van Dien 1998). In their latest edition, the AASHTO Specifications (2001) take into consideration these phenomena on the section they dedicated to fatigue design.

For the specific case of cantilever traffic signal structures, experimental results have led researchers to believe that galloping is the main cause of large-amplitude vibrations that cause the fatigue failure of mast arms and other components of these structures, that natural wind gusts are contributors to fatigue failure, and vortex shedding does not cause significant vibrations. This is reflected in the AASHTO Specifications

(2001) which do not consider vortex shedding in the fatigue design of cantilever traffic signal structures. Although these specifications give provisions to prevent fatigue against them, the effects of truck-induced gusts appear to be negligible, as suggested by recent research (Hartnagel and Barker 1999; Chen et al. 2001; Albert 2006).

CHAPTER 3

FULL-SCALE EXPERIMENTS

3.1 Introduction

Full-scale experiments were conducted with two out-of-service cantilever traffic signal structures installed at the Reese Technology Center facilities of the Wind Science and Engineering Research Center of Texas Tech University (see Figure 3.1). Each structure is instrumented with a sonic anemometer mounted above the mast together with a video camera monitoring the motion of the tip of the cantilever arm. This chapter summarizes the full-scale experiments and the results obtained.

Figure 3.1 The Two Cantilever Traffic Signal Structures Tested at Reese Technology Center

3.2 Experimental Setup

3.2.1 Geometry and Light Configuration

The two structures tested are known as Traffic Signal 1 (TS1) and Traffic Signal 2 (TS2). Both TS1 and TS2 are fabricated from steel and have straight arms, 60-ft in length for TS1 and 44-ft for TS2. TS1 has one 5-light signal head and three 3-signal heads; while TS2 has one 5-signal head and two 3-signal heads. All signals have removable backplates. The signal heads are mounted horizontally at the height of the mast arm. A street sign is also attached on the arm near the mast. More details of the geometry and light configuration of the structures for the case when the signals have backplates are shown in Figure 3.2 and 3.3. Details of the dimensions of the signal heads are shown in Figure 3.4.

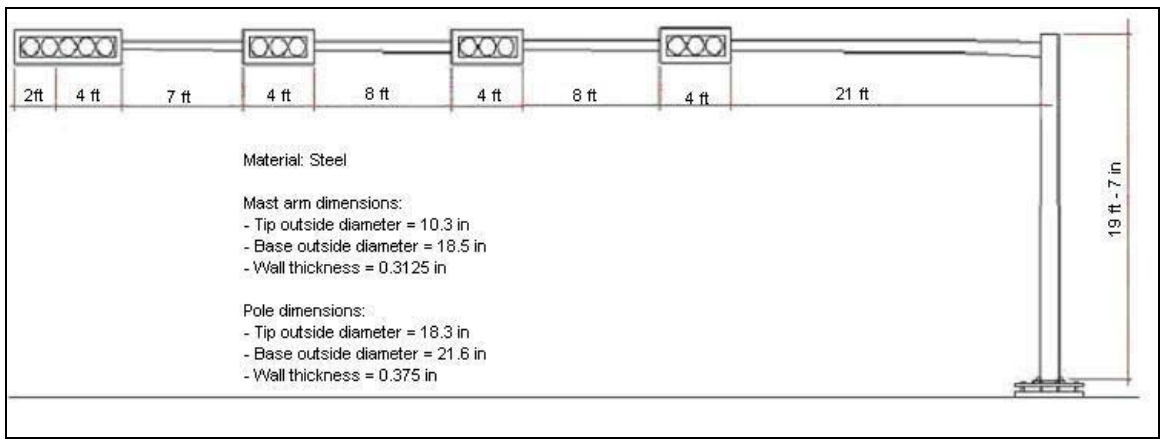

Figure 3.2 Geometry and Light Configuration of TS1 (60’ mast arm)

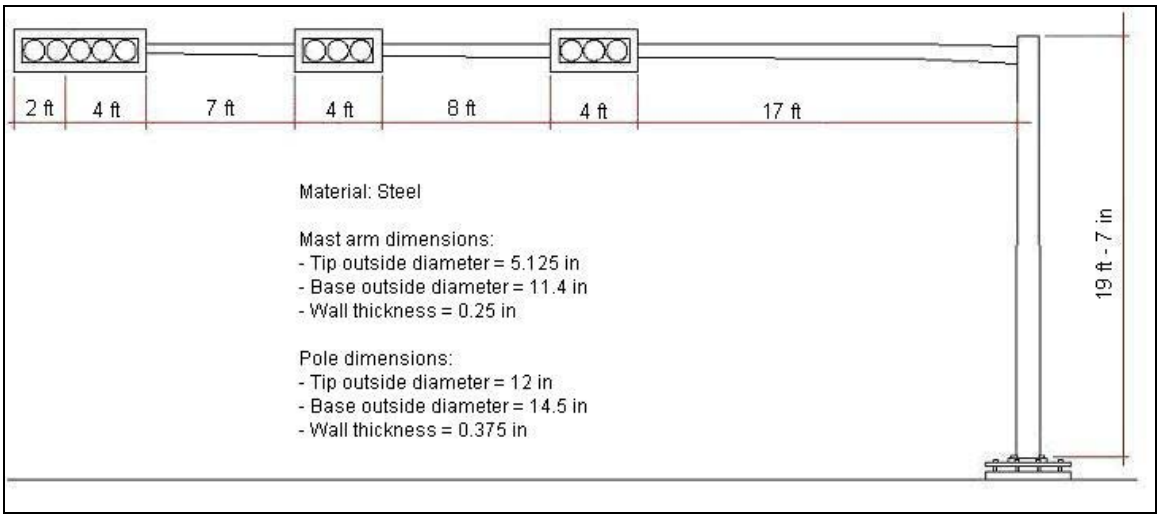

Figure 3.3 Geometry and Light Configuration of TS2 (44' mast arm)

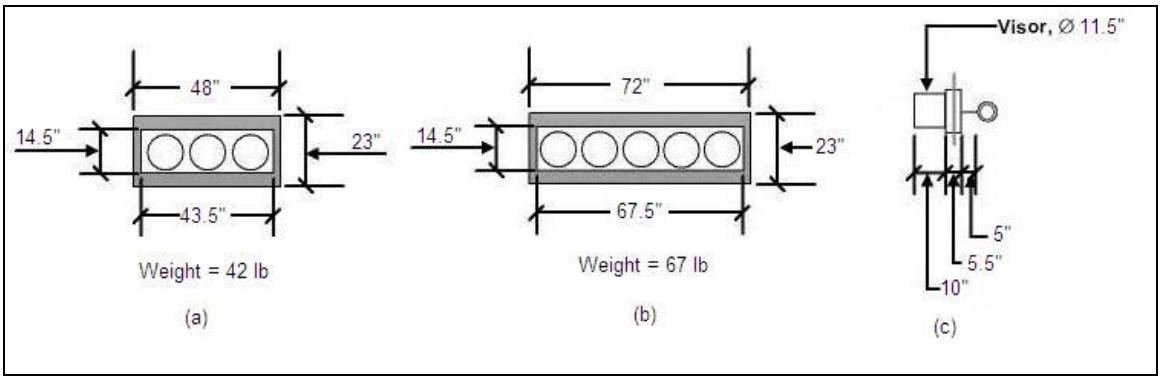

Figure 3.4 Dimensions of Signal Heads Used in Full-Scale Experiments (shown with backplates)

3.2.2 Foundations

Each structure rests on a foundation that allows the whole mast arm assembly to be rotated in 15° increments. Each foundation consists of a circular steel plate on top of a reinforced concrete pile, as shown in Figure 3.5. More details on the base plates and foundations are presented in Figure 3.6 and Figure 3.7.

Figure 3.5 Foundation with Steel Plate

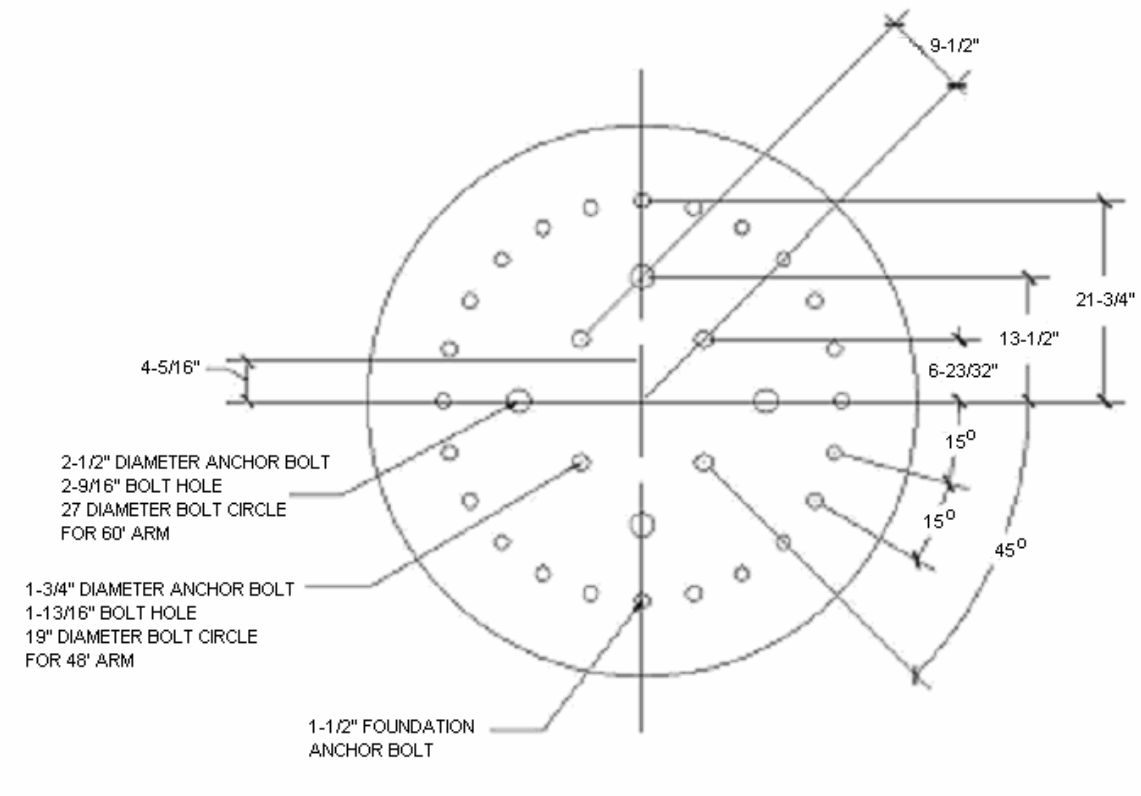

Figure 3.6 Dimensions of Foundation Steel Plate

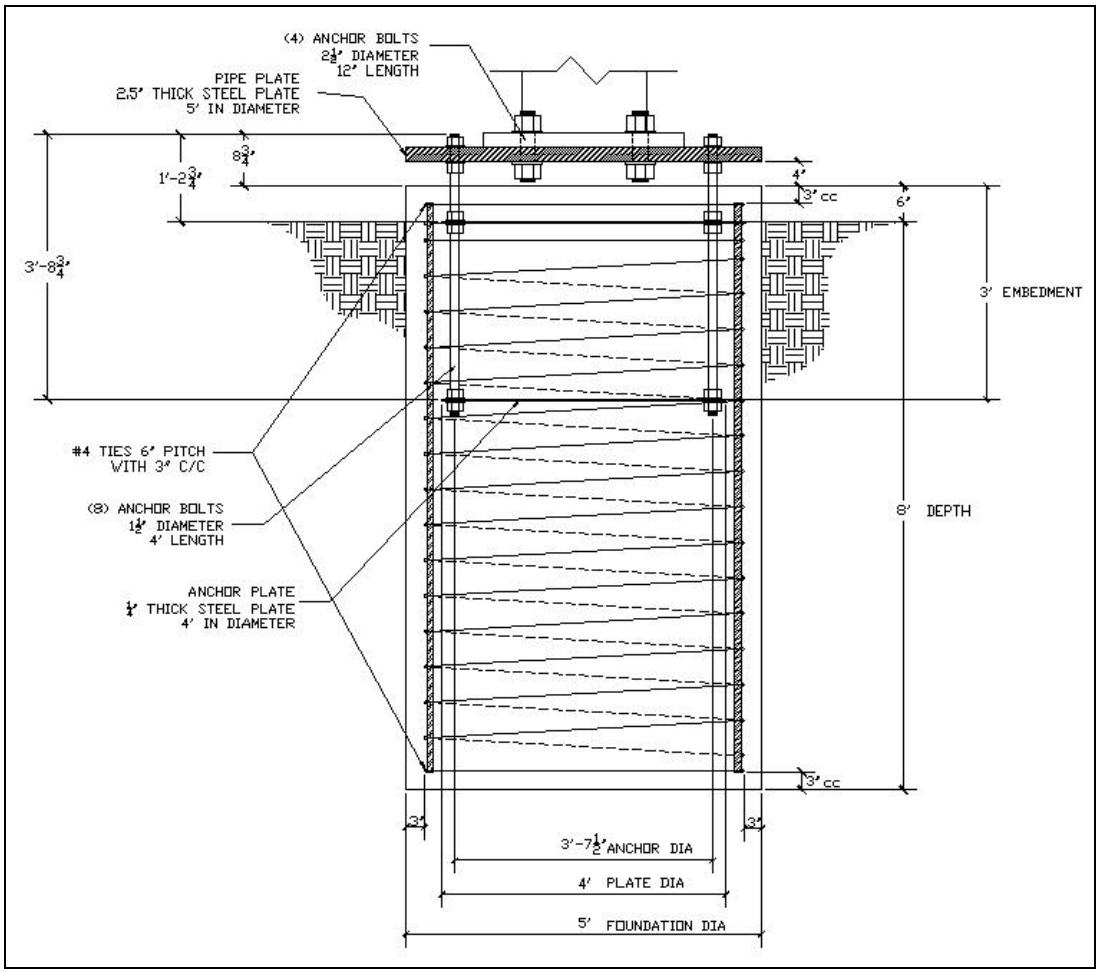

Figure 3.7 Foundation Details

3.2.3 Instrumentation

Figure 3.8 shows a schematic layout of the instrumentation used to collect data for each structure. The instrumentation consists of the following:

- Infrared target made of two Nerlite S-40 infrared lights. The target is rigidly attached near the tip of the arm, as shown in Figure 3.9.
- Basler A601 video camera with National Instrument Compact Vision System (CVS) 1454 to collect displacement data. The camera and the CVS are placed inside a camera enclosure, which is mounted on top of the mast, pointing toward the tip of the arm. The camera has a filter to capture only the two

lights of the infrared target. The camera has a resolution of 0.12 inches at a distance of 60 ft from the target and is set for a sampling rate of 30 Hz. The position of each infrared light is collected and used to calculate the X and Y coordinate in pixels of the midpoint between the two lights. These instruments are calibrated by using the physical separation of the centers of the infrared lights (G Systems 2005). The instruments, along with the coordinates, also record calibration factors for each X and Y coordinates to change the values from pixels to inches. Other data collected by these instruments that was not used in this research is: radius in pixels and circularity factors for each of the infrared lights, angle in degrees for the segment between the infrared lights, calculated metric threshold value used in the image analysis, and cumulative image buffer number.

- R. M. Young Model 81000 ultrasonic anemometer mounted about 4 ft above the top of the pole. The anemometer measures three-dimensional wind velocity and is also sampled at 30 Hz. It collects u, v, and w wind components as voltages. The anemometer is oriented so that positive u and v are measured as shown on Figure 3.10, with w being the vertical component, which is positive going upwards. Also shown on Figure 3.10 is the angle of attack sign convention. The anemometers were calibrated by the manufacturer in a wind tunnel before data collection began and the calibration is usually good for two years. Table 3.1 lists the wind speed and direction resolutions and accuracies of the anemometer for wind speeds in the range of 0 to 67 mph. This instrument also records relative humidity and temperature, but this data was not used in this research.

- National Instruments FP-2000 Intelligent Ethernet Controller Interface for FieldPoint which gathers the data from the anemometer and the camera/CVS and sends it to a computer at the field site.

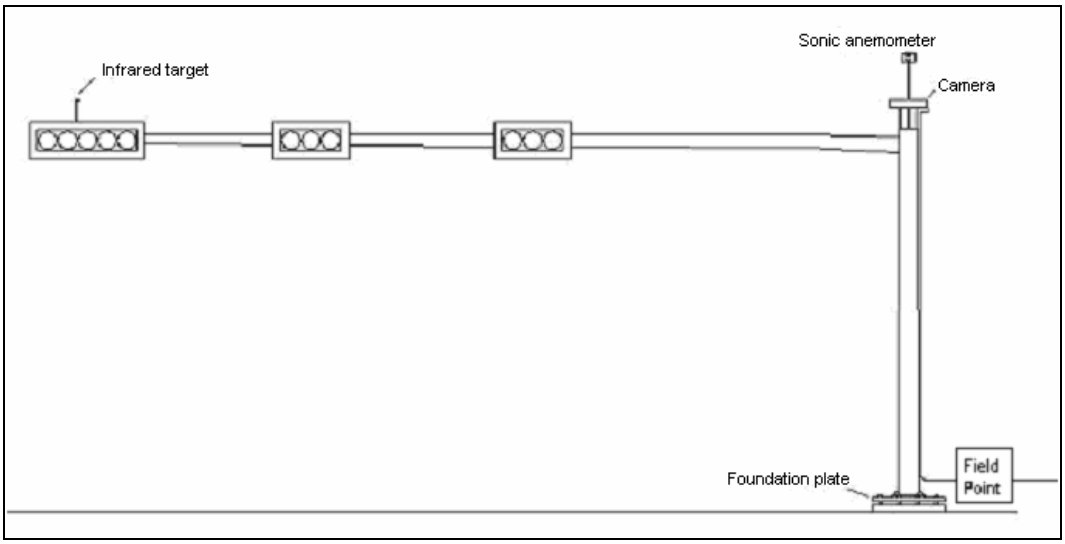

Figure 3.8 Instrumentation

Figure 3.9 Infrared Target as Viewed from Top of Pole

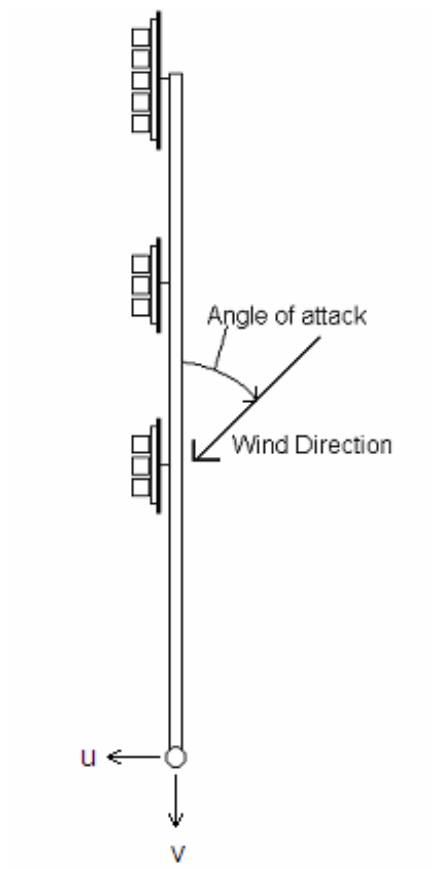

Figure 3.10 Anemometer Orientation and Angle of Attack Sign Convention

Table 3.1 Resolution and Accuracy of Anemometer for Wind Speeds in the 0-67 mph Range

Measurement	Resolution	Accuracy
Wind speed	0.22 mph	± 1% rms ± 0.11 mph
Wind direction	0.1^{o}	$\pm 2^{o}$

This instrumentation only measures the relative displacement of the tip of the arm with respect to the mast/pole top. It does not account for any displacement of the pole itself. This research is mostly interested in this relative displacement because most fatigue failures occur in the arm, close to where it connects to the pole (Pulipaka 1995;

Gray et al. 1999; Hartnagel and Barker 1999; Hamilton, Riggs and Puckett 2000; Chen et al. 2001; Cook et al. 2001).

The field site computer has software developed by G Systems (2005) and designed to save the data collected by four instruments:

1. Anemometer of TS1,
2. Camera/CVS of TS1,
3. Anemometer of TS2, and
4. Camera/CVS of TS2.

The software starts recording data from all four instruments at the same time. One hour later, the software stops recording, saving a time history file for each of the four instruments, and one minute later begins data collection again. The file name convention is as follows:

M####_R####_DTmmddyy_TMhhmmss_TR_D##_HW_Platform.csv

- M#### is MODE number. The number can be changed to describe different experiments.
- R#### is RUN number. The number automatically increases by one for each new run. One hour of data is a run.
- DT is the DATE of the run.
- TM is the TIME that the run file was created.
- TR is the indication that this is a run data file rather than another type of file such as calibration data.
- D## is the device number.

  - D01 = anemometer on TS1
  - D02 = CVS on TS1
  - D03 = anemometer on TS2
  - D04 = CVS on TS1

- HW is the hardware type: FP for anemometer data or CV for camera data.
- Platform is the platform type, in this case SIGNALLIGHT. (This software is used on other experiments, so those would have different platforms.)

It is noted here that the four data files recorded at the same time have almost the same name, but they can be differentiated by the device number and the hardware type.

Approximately once a week, the recorded data was taken from the field computer and saved on a server at the Wind Science and Engineering Research Center. There the data was processed with software developed at Texas Tech. This software groups the four hour-long files recorded at the same time into one file, converting both the voltages collected by the anemometers and the displacements collected by the cameras to engineering units (mph and inches, respectively). For the processed data, the file name convention is as follows:

M####_R####_DTmmddyy_TMhhmmss

where:

- M#### is MODE number. The same mode number that it had when the data was collected.
- R#### is RUN number. The same run number that it had when the data was collected.
- DT is the DATE when the data was processed.
- TM is the TIME when the data was processed.

Each processed file has approximately 108,000 lines (1 hour collection at a 30 Hz sampling rate), but it has exactly 24 columns.

Table 3.2 lists the content of each of the columns of processed files.

Table 3.2 Content of Each Column of the Processed Files

Column No.	Content
1	Temperature of TS1 (Fahrenheit)
2	U velocity component for TS1 (mph)
3	V velocity component for TS1 (mph)
4	W velocity component for TS1 (mph)
5	X coordinate of the midpoint between infrared lights for TS1 (inches)
6	Y coordinate of the midpoint between infrared lights for TS1 (inches)
7	Calibration factor for X coordinate of TS1 (inches/pixels)
8	Calibration factor for Y coordinate of TS1 (inches/pixels)
9	Temperature of TS2 (Fahrenheit)
10	U velocity component for TS2 (mph)
11	V velocity component for TS2 (mph)
12	W velocity component for TS2 (mph)
13	X coordinate of the midpoint between infrared lights for TS2 (inches)
14	Y coordinate of the midpoint between infrared lights for TS2 (inches)
15	Calibration factor for X coordinate of TS2 (inches/pixels)
16	Calibration factor for Y coordinate of TS2 (inches/pixels)
17	Wind velocity for TS1 (mph)
18	Wind direction for TS1 (mph)
19	Along-wind velocity component for TS1 (mph)
20	Cross-wind velocity component for TS1 (mph)
21	Wind velocity for TS2 (mph)
22	Wind direction for TS2 (mph)
23	Along-wind velocity component for TS2 (mph)
24	Cross-wind velocity component for TS2 (mph)

3.2.4 Quality Assurance Measures

Data from the West Texas Mesonet station located at Reese Technology Center was sporadically used for comparison to assure that the data collected by the anemometers on the traffic signals was of good quality. This station is located less than 1,500 ft away from each of the signals. (Details about the station are given in Section 5.2.1.) Figure 3.11 is an example of such a comparison in which a random hour of data collected by the anemometers of TS1 and TS2 was used to calculate 5-minute mean time histories of wind speed and direction and these were compared to data collected by the Mesonet station. A moderate difference is expected between the wind speeds collected by the Mesonet and the traffic signals because the Mesonet collects data at a height of 33 ft, while TS1 and TS2 record wind velocities at 27 and 24 ft, respectively. Still, similar time histories are expected for wind directions because normally only small changes of wind direction occur between a few hundred feet above the ground (Liu 1991).

To monitor the quality of data collected by the camera/CVS, the time history of the X and Y coordinates of the two infrared lights was used to calculate a time history of the distance between the two infrared lights of each hour-long file. This calculated distance should remain close to constant, since the actual distance of the lights never varies. Figure 3.12 shows an example of a comparison being made. Notice that the calculated values show little variability and they remain fairly close to the actual value. Using the time history of the calculated distance, an average value was computed. If a run had an average value with an error of more than 1.5 %, then the run was not considered of good quality and it was not used for analysis of results.

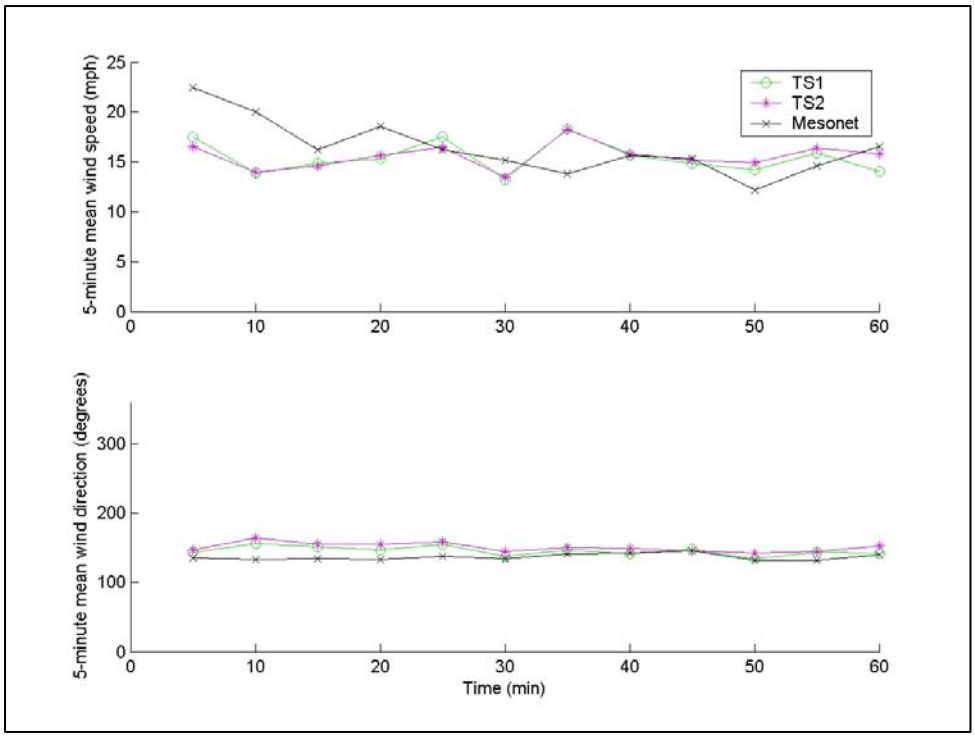

Figure 3.11 Comparison Between Traffic Signals' Anemometers and Mesonet Wind Data

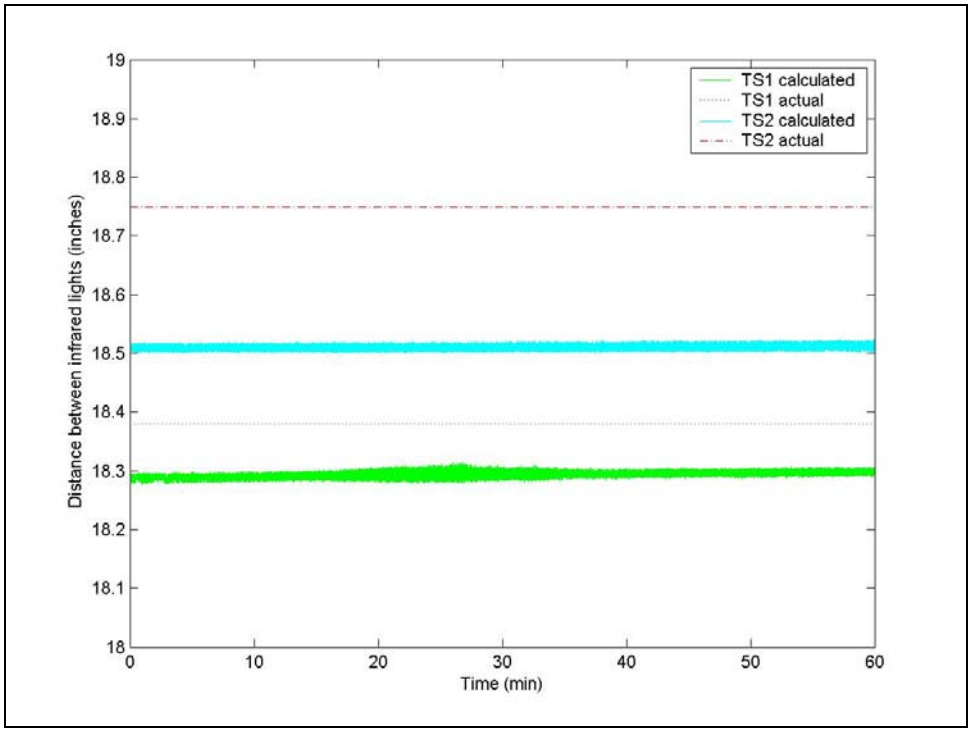

Figure 3.12 Comparison Between Actual and Calculated Distances Between Infrared Lights

3.2.5 Pluck Test

A pluck test was conducted to determine the fundamental frequencies and the damping ratios of the arms of the structures at the Reese site. The tests were conducted by pulling and pushing the tip of the arm in either the horizontal or the vertical direction and then letting the arm vibrate freely until it stopped. There were a total of four cases tested:

1. Horizontal vibrations of 60-ft arm,
2. Vertical vibrations of 60-ft arm,
3. Horizontal vibrations of 44-ft arm, and
4. Vertical vibrations of 44-ft arm.

For each of the four cases, three runs were conducted. While conducting the runs, the instrumentation would record a time history of the displacement. Figure 3.13 is an example of a plotted time history of one run for the case of the 44-ft arm with horizontal vibrations. This history has a length of 56.13 seconds, and it can be seen from the figure that 50 cycles of motion were completed, so the fundamental frequency was calculated as:

$$f_o = \frac{50}{56.13} = 0.89 \text{ Hz} \tag{3-1}$$

The damping ratio is determined by using the Logarithmic Decrement method (Paz 2002), which in Figure 3.13 is represented by the red curve. The curve should be given by:

$$X = A\exp(-\zeta\omega_o t) \tag{3-2}$$

where:

ζ = damping ratio

ω_o = fundamental circular frequency = $2\pi f_o$

t = time

A = initial amplitude or X at t = 0

Therefore, for the case of Figure 3.13, the damping ratio is calculated as:

$$\zeta = \frac{0.028}{2\pi\ f_o} = \frac{0.028}{2\pi(0.89)} = 0.50\ \% \tag{3-3}$$

The results obtained for the three runs were used to calculate average values for each case. The resulting average values are presented in Table 3.3.

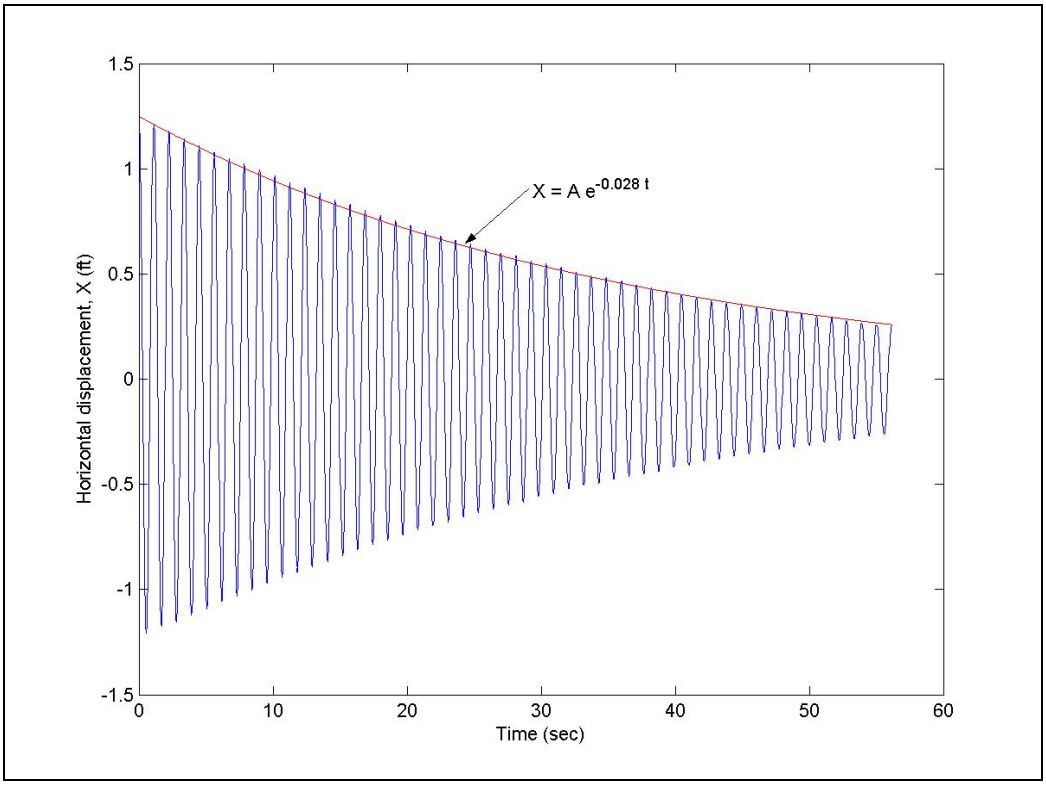

Figure 3.13 Pluck Test Run for Case of 44-ft Arm Under Horizontal Vibrations

Table 3.3 Fundamental Frequency (f_o) and Damping Ratio (ζ) of Mast Arms

		Mast Arm Length	
		60 ft	44 ft
f_o			
	Horizontal	0.92 Hz	0.89 Hz
	Vertical	0.98 Hz	0.98 Hz
ζ			
	Horizontal	0.25 %	0.55 %
	Vertical	0.23 %	0.28 %

3.2.6 Experimental Program

The experimental program is summarized in Table 3.4 with each experiment given a mode number. Only Modes 1100 and 1101 are discussed in this report. Initially, the traffic signals were set up at the Reese site with the arm pointing east (meaning that the camera also pointed east) to take advantage of the predominant north-south winds in the area. Although some interesting and significant data was collected under these conditions, the camera had problems collecting data during the morning, when the sun was rising. So a decision was made to change the orientation of the structures to have the arm pointing north. Later, modifications were made to the software that allows data collection with the structure pointing to the southeast.

Table 3.4 Experimental Program

Mode	Experiment description	Direction to which mast arm points	Dates
1100	Signals with backplates	north	April 2005 – March 2006
1101	Signals without backplates	north	March 2006 – Feb. 2007
1102	Used for equipment adjustment	north	March 2007
1103	Signals with vented backplates	southeast	March – June 2007
1104	Used for equipment adjustment	southeast	June 2007
1105	Signals with backplates and mast arm with damping device	southeast	July – Sept. 2007

3.3 Results

In this section three sets of results are discussed:

1. the preliminary data obtained on March 29, 2005, for TS2 with the arm pointing east and the signals with backplates,
2. the data obtained under Mode 1100, and
3. the data obtained under Mode 1101.

3.3.1 March 29, 2005

On March 29, 2005, data was recorded only for TS2 (the structure with a 44-ft arm) when it was recently operational and had its arm pointing east and signals with backplates. The instrumentation recorded vertical vibrations of the arm tip with peak-to-peak oscillations as large as 11 inches. Presented in Figure 3.14 are 10 hours of the recorded data. The orientation of the u- and v-components is shown in Figure 3.10. The vertical component (w) is positive when upwards.

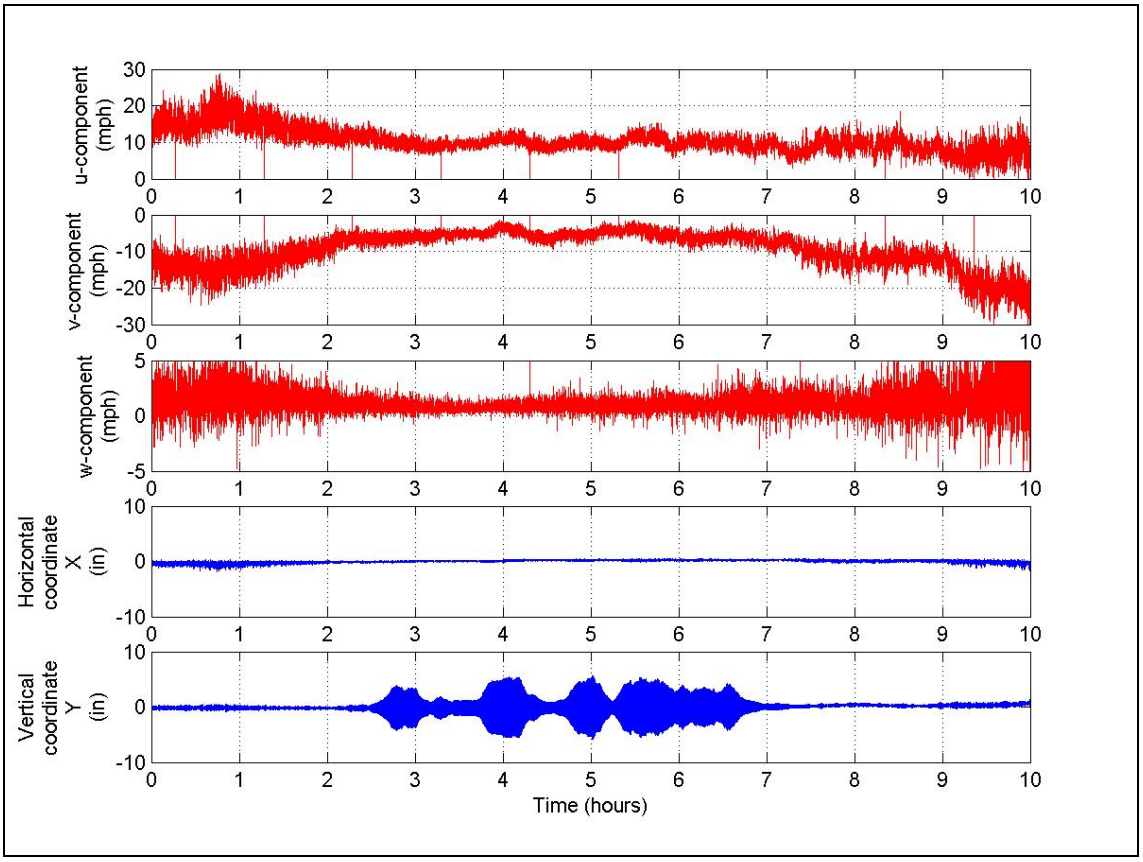

Figure 3.14 Wind and Displacement Data Collected on March 29, 2005

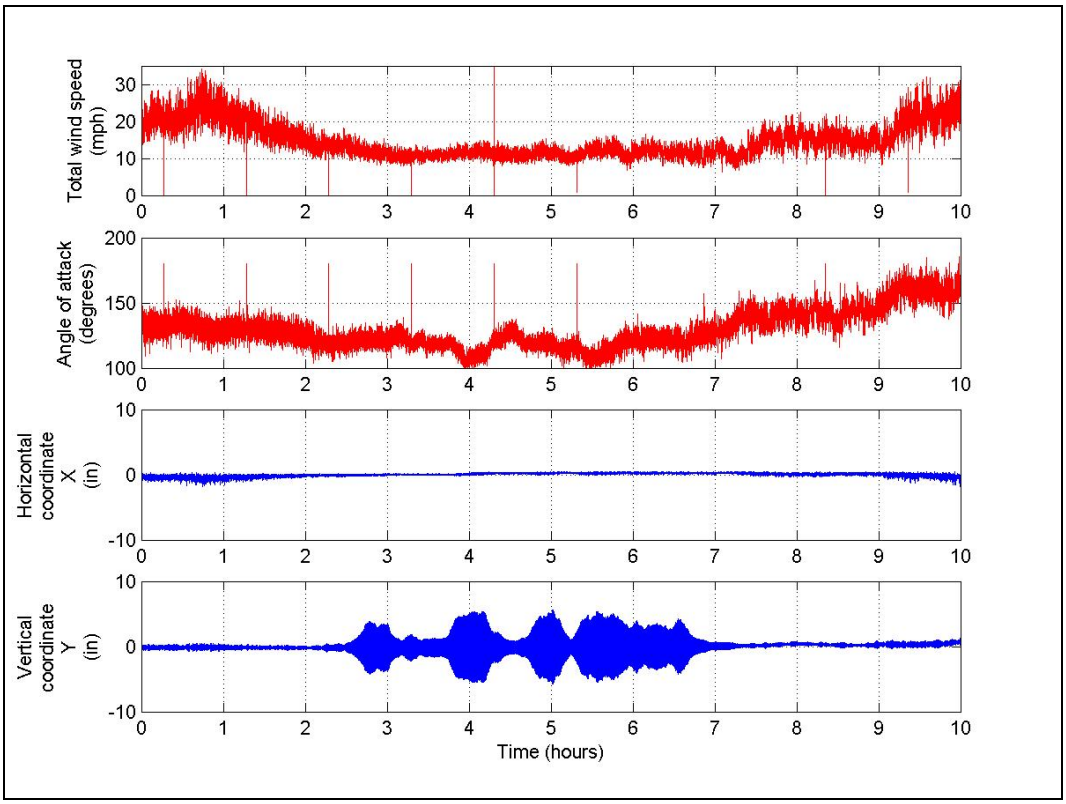

Figure 3.15 Time Histories of Total Wind Speed, Angle of Attack, and Tip Displacement

The u-, v-, and w-components were vectorially added to obtain a time history of the wind speed and the u- and v-components were used to calculate the angle of attack (with sign convention shown in Figure 3.10). The results are shown with the recorded coordinates in Figure 3.15.

The following observations are made:

1. Horizontal vibrations had larger amplitudes when the wind is more turbulent.
2. Vertical vibrations had larger amplitudes when the total wind speed averaged about 10 mph.
3. Vertical vibrations reached much higher amplitudes than horizontal vibrations.

4. When the vertical vibrations are larger, the horizontal vibrations are smaller, and vice versa.

After evaluating sample lengths of between 30 and 300 seconds, 100 cycles of vibrations were selected for subsequent analyses. Knowing that the fundamental frequency of the structure is close to 1 Hz, the data presented in Figure 3.15 was divided into smaller segments of 100 seconds. For each segment the mean and the standard deviation of the total wind speed and the angle of attack were calculated, along with the standard deviation of the horizontal and the vertical coordinates. These values were used to produce the plots presented in Figure 3.16 to Figure 3.23. In lieu of peak amplitudes of vibration, standard deviations directly proportional to the amplitudes of vibration are plotted in Figures 3.16 through 3.23, and throughout the remainder of this report.

Figure 3.16 shows that low-amplitude horizontal vibrations occurred when the mean wind speed was about 10 mph and that vibrations increased as the total wind speed increased. In Figure 3.17 it can be seen that high-amplitude vertical vibrations were observed when the total wind speed was between 10 and 12 mph. From Figure 3.18 no clear relationship can be established between the horizontal vibrations and the turbulence intensity. Likewise, no relationship can be established clearly between the vertical vibrations and the turbulence intensity by observing Figure 3.19.

Figure 3.20 demonstrates there was more scatter in the horizontal vibrations when the angle of attack was over 130°. Figure 3.21 shows larger vibrations occurred when the angle of attack was below 130°. In Figure 3.22 it can be seen that larger horizontal

vibrations occurred when there was higher variability in the angle of attack. To the contrary, Figure 3.23 shows that higher vertical vibrations occurred when the angle of attack was less variable.

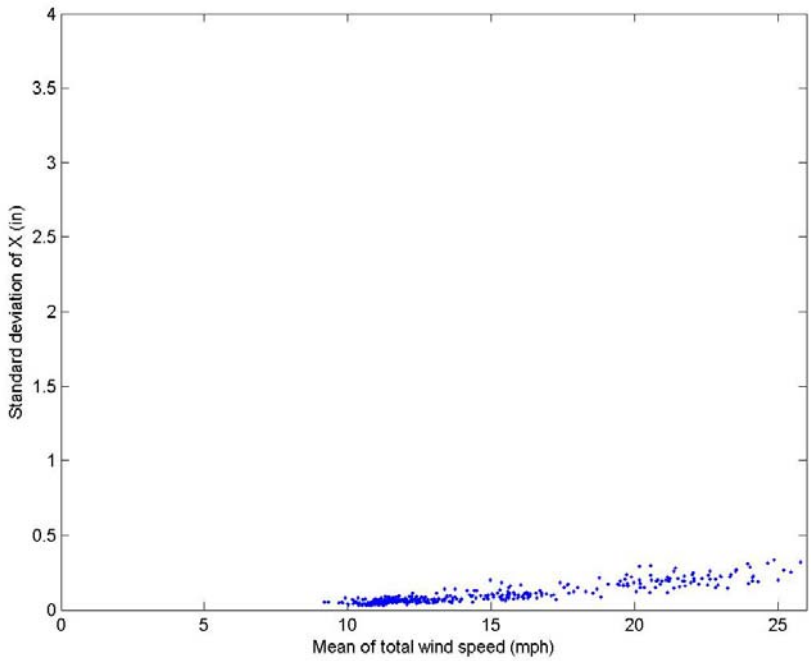

.

Figure 3.16 Effect of Wind Speed on Horizontal Vibrations of the Arm

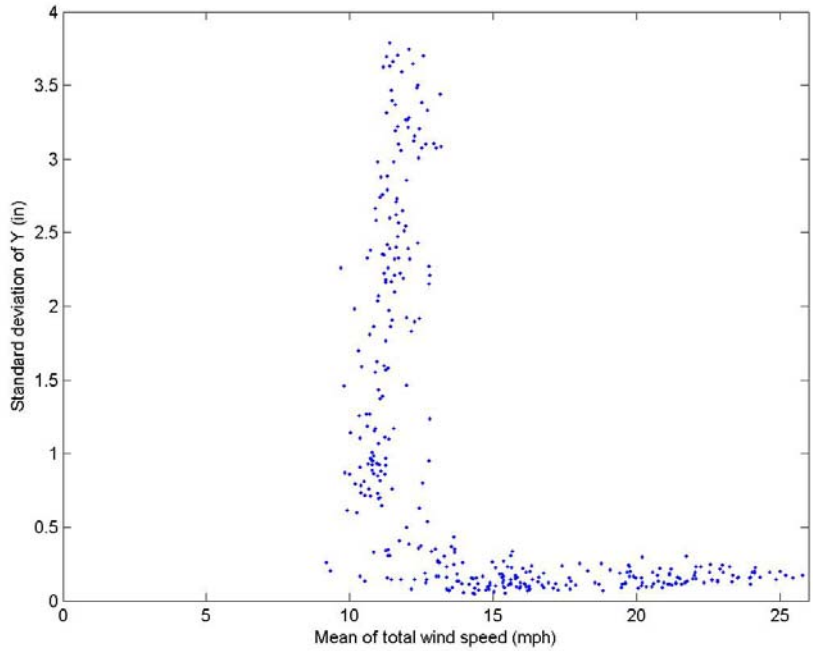

Figure 3.17 Effect of Total Wind Speed on Vertical Vibrations of the Arm

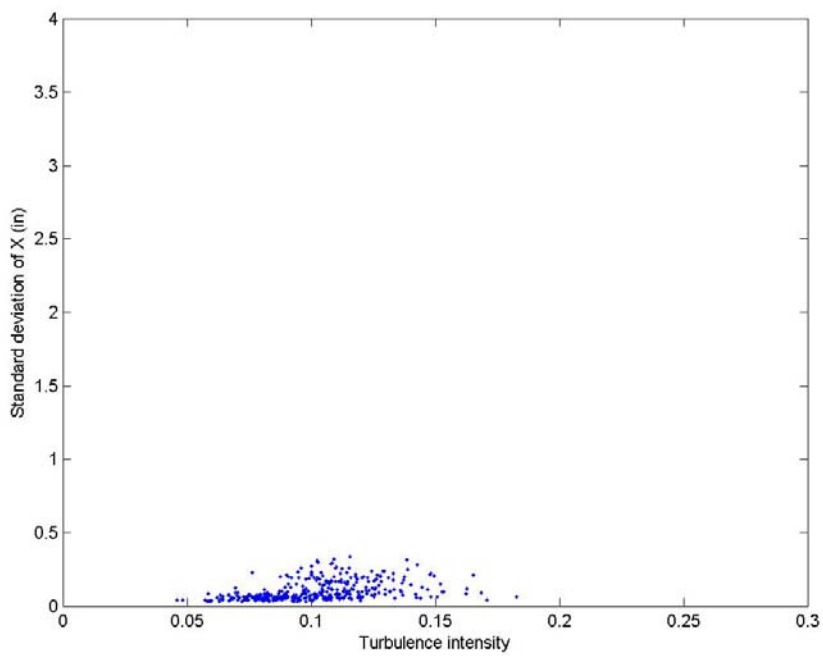

Figure 3.18 Effect of Turbulence on Horizontal Vibrations of the Arm

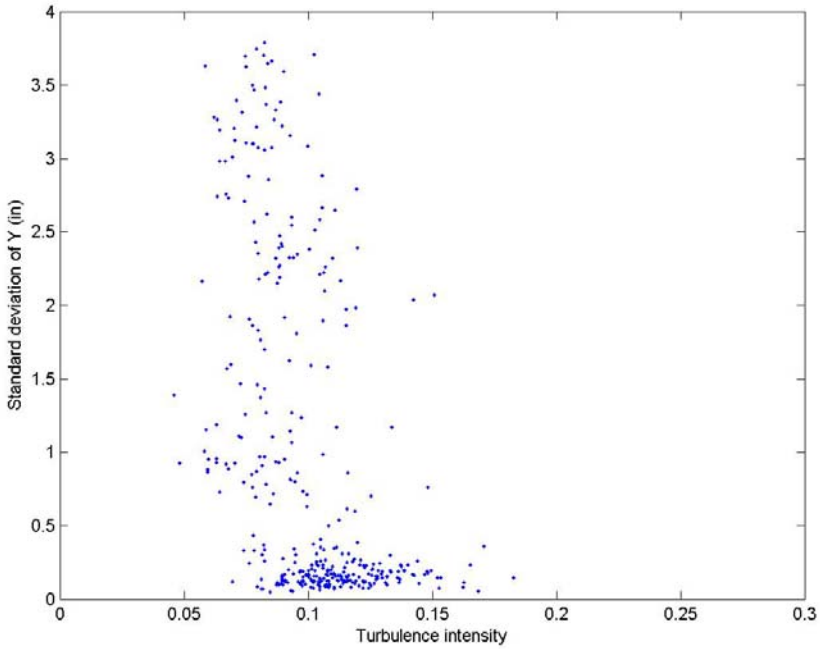

Figure 3.19 Effect of Turbulence on Vertical Vibrations of the Arm

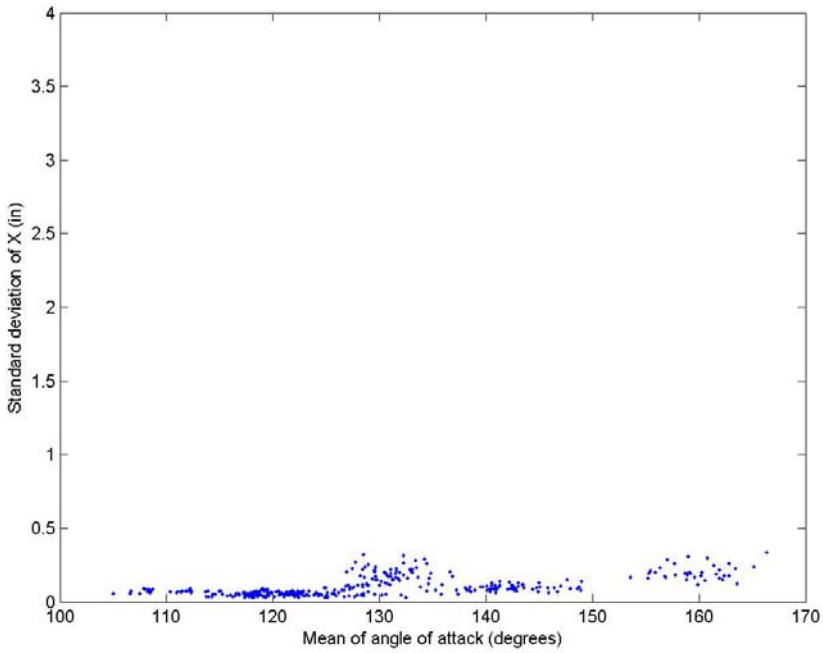

Figure 3.20 Effect of Wind Angle of Attack on Horizontal Vibrations

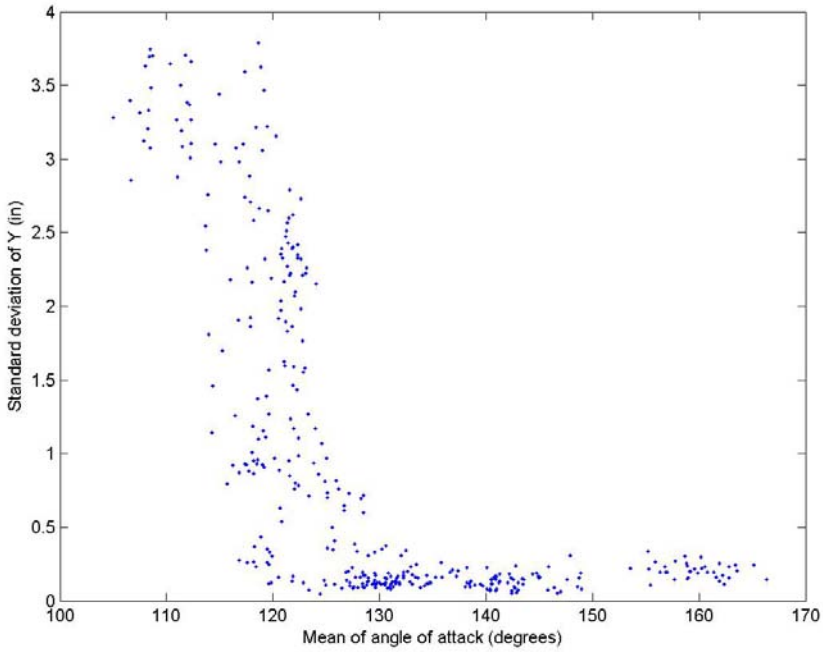

Figure 3.21 Effect of Wind Angle of Attack on Vertical Vibrations

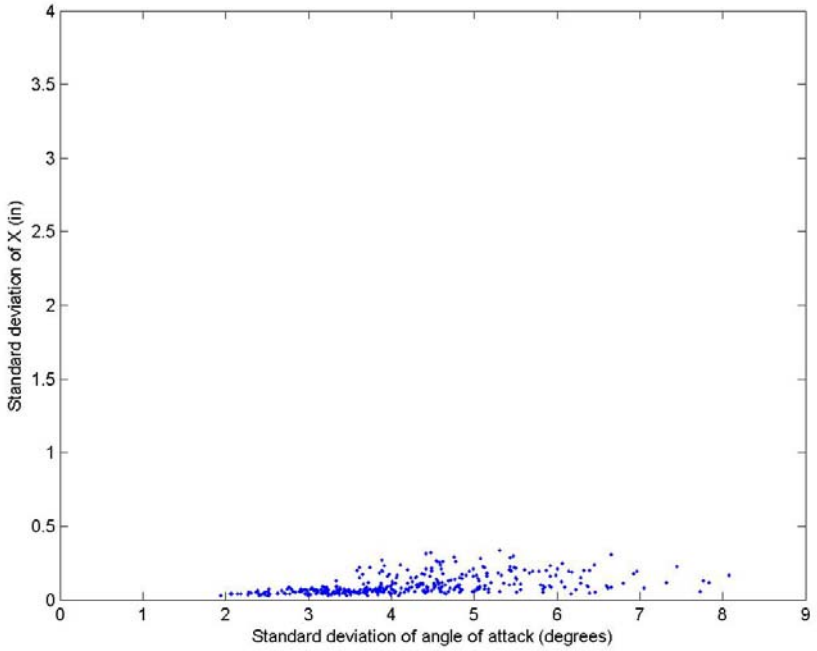

Figure 3.22 Effect of Variations in Angle of Attack on Horizontal Vibrations

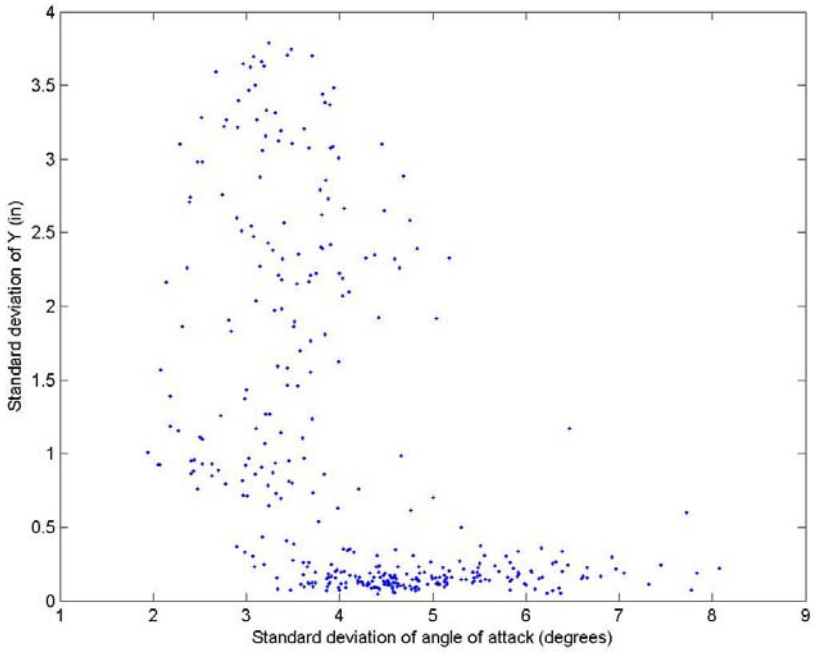

Figure 3.23 Effect of Variations in Angle of Attack on Vertical Vibrations

As explained before, Figure 3.16 to Figure 3.23 were plotted using data segments of 100 seconds. It should be pointed out that data was also analyzed using longer and shorter segments and the same trends were observed. An example of this is shown in Figure 3.24 in which the effect of the total wind speed on vertical vibrations is plotted using both 100- and 300-second segments. In both cases it can be seen that high-amplitude vertical vibrations are observed when the total wind speed is between 10 and 12 mph.

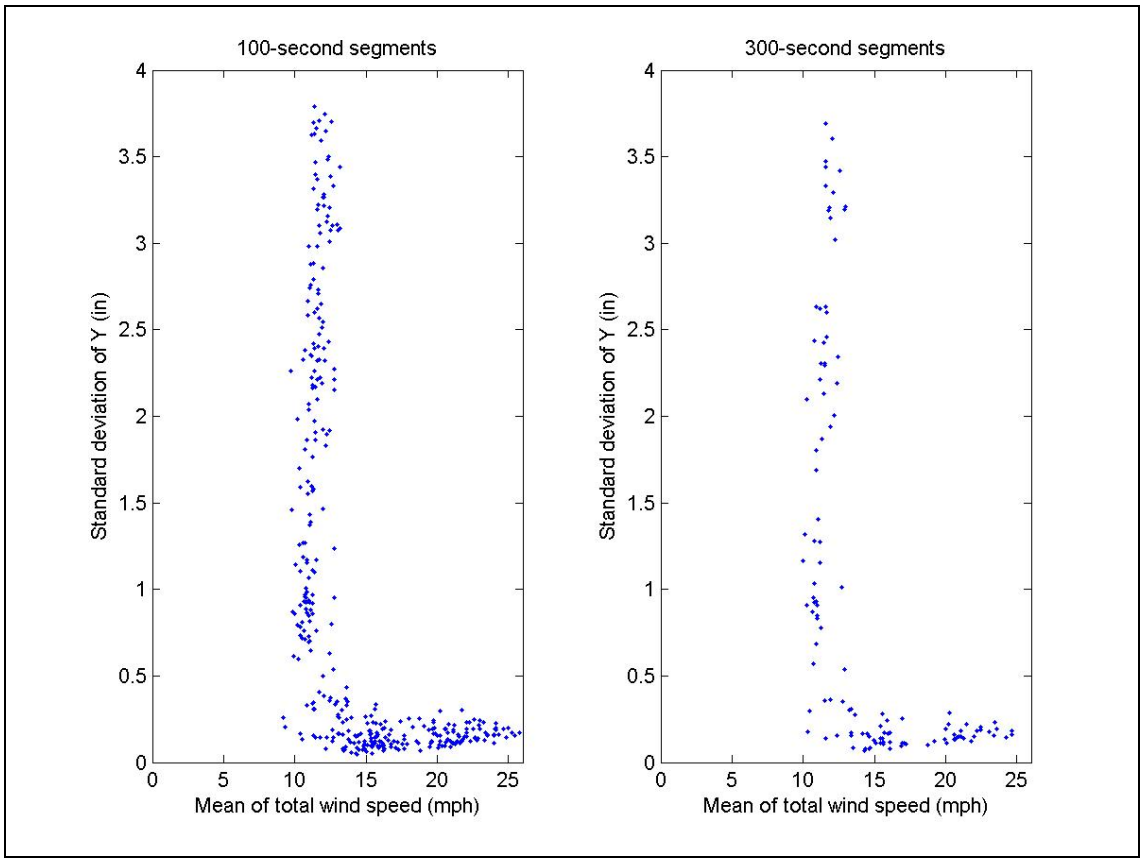

Figure 3.24 Comparison of Data Analysis Using Segments of 100 and 300 Seconds

The Strouhal number when the wind was approximately perpendicular to the backplate vibrating at 0.98 Hz and using a cross-wind body width (*B*) of a traffic signal head with backplate is:

$$St = \frac{f\,B}{U} = \frac{(0.98\,\text{Hz})\,(23\,\text{in})}{11\,\text{mph}} = \frac{(0.98\,\text{Hz})\,(1.92\,\text{ft})}{16\,\text{ft/sec}} = 0.12 \qquad (3\text{-}4)$$

This Strouhal number is close to the published value of 0.15 for a flat plate perpendicular to the flow (Blevins 1977; Hirsch and Bachmann 1995) and the response exhibits the classic lock-in phenomena for vortex shedding.

3.3.2 Mode 1100

From April 2005 to March 2006, data was collected under Mode 1100 with the arm pointing north and the signals having backplates. During this period, 4858 hours of data were collected for both TS1 and TS2. All the data was analyzed by dividing the long time histories into 2-minute segments, calculating summary statistics for different measured parameters, and plotting graphs. Some of the graphs are presented and discussed here. To see all the plotted graphs, refer to Appendix A. Outline data points have been retained for completeness and have not been individually validated.

Figure 3.25 and Figure 3.26 show the effect of the wind speed component perpendicular to the arm (the u-component) on the vertical vibrations of TS1 and TS2, respectively. A positive u means that it approaches the mast arm from behind the signals (as shown in Figure 3.10). In the case of TS1, there seems to be higher vibrations when u is about -10 and +7 mph, but unlike the data of May 29, 2005, only very occasionally did the standard deviation of Y exceed 2 inches. The few times it did, it was mostly in the speed range of 0 to +10 mph. For TS2, there were more cases of the standard deviation of Y exceeding 2 inches, and most of these were also in the 0 to +10 mph range, with only three cases in the -5 to 0 mph range.

Figure 3.27 and Figure 3.28 show the effect of the mean wind speed (the vector sum of u, v, and w) on the vertical vibrations of the mast arm of TS1 and TS2, respectively. Notice that in both cases, the standard deviation of Y never exceeds 2 inches when the mean wind speed is over 25 mph.

Figure 3.29 and Figure 3.30 show the effect of wind direction on the vertical vibrations of the arms of TS1 and TS2, respectively. (The sign convention of the angle of attack is given in Figure 3.10.) For the case of TS1, there is a concentration of cases at around 60 and 300 degrees, but again very few cases exceeded a standard deviation of Y of 2 inches. For both TS1 and TS2, most of the higher vibrations (standard deviation of Y over 2 inches) occur between 0 and 180 degrees, which corresponds to when there is a wind component blowing from the back of the signals. The exceptions are one and three data points for TS1 and TS2, respectively.

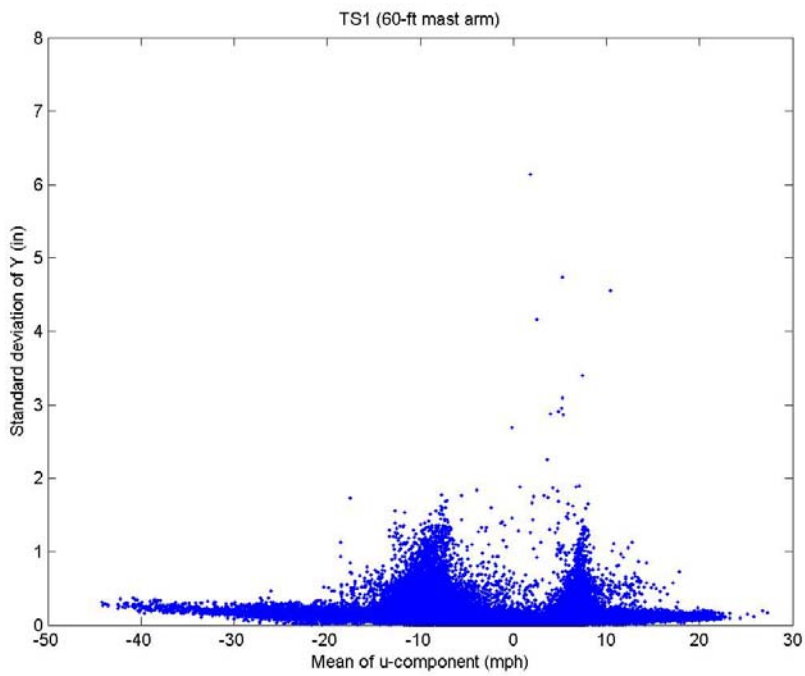

Figure 3.25 Effect of u-Component on Vertical Vibrations of TS1 with Backplates

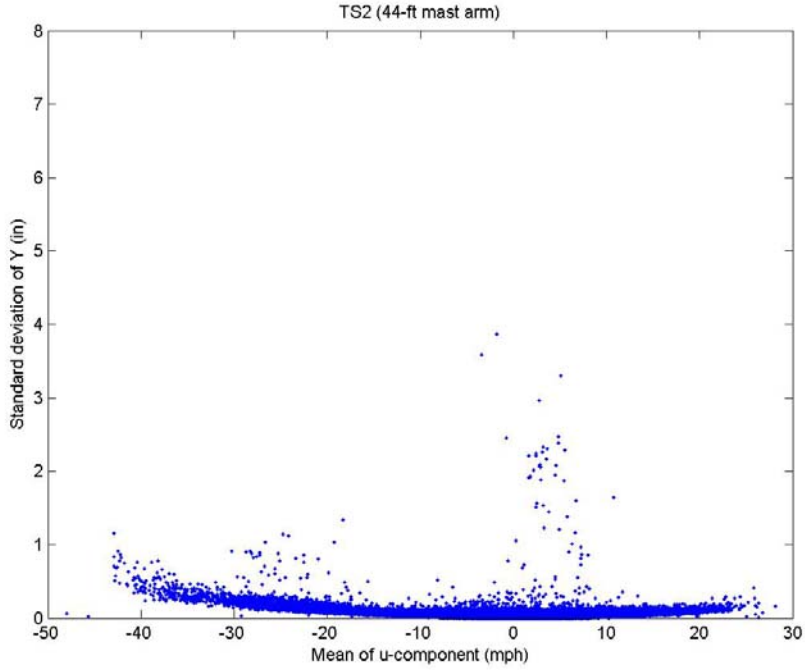

Figure 3.26 Effect of u-Component on Vertical Vibrations of TS2 with Backplates

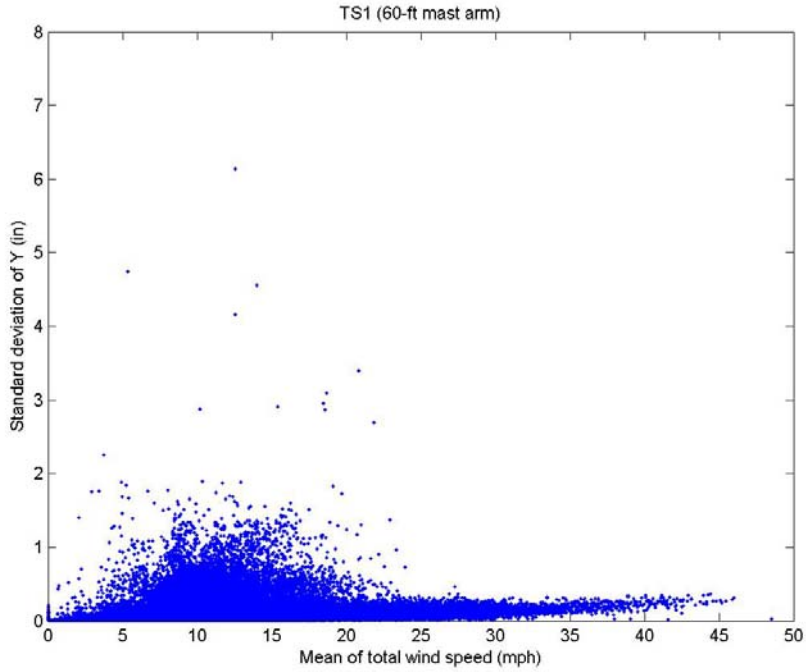

Figure 3.27 Effect of Mean Wind Speed on Vertical Vibrations of TS1 with Backplates

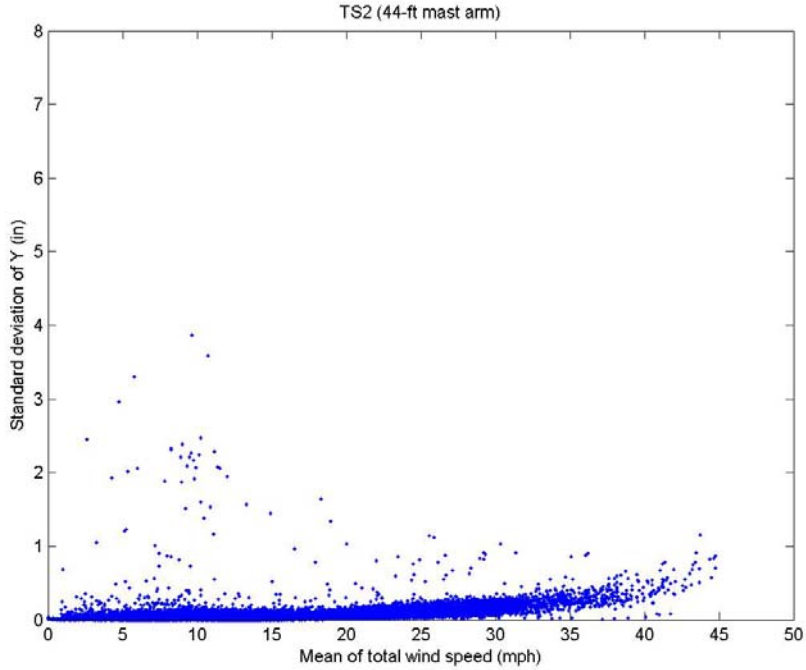

Figure 3.28 Effect of Mean Wind Speed on Vertical Vibrations of TS2 with Backplates

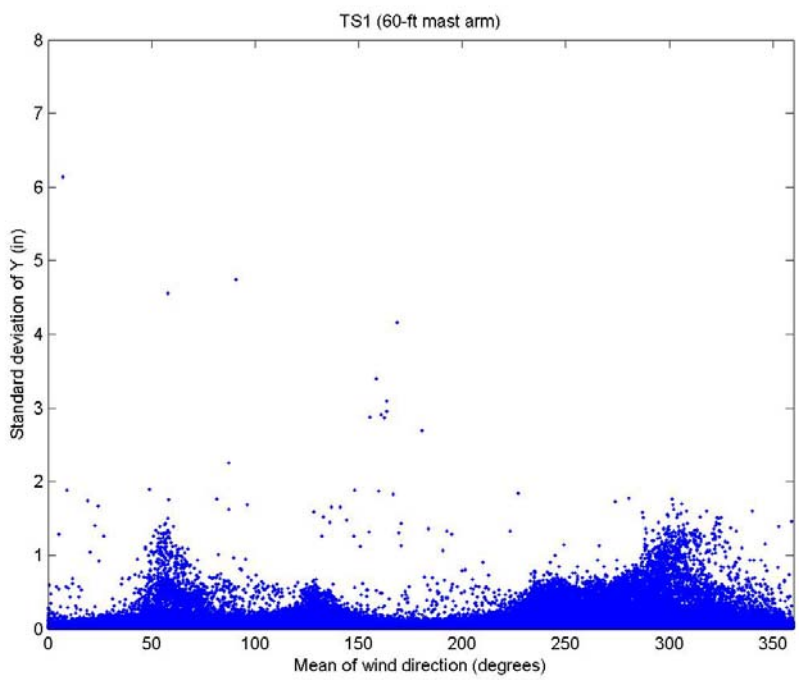

Figure 3.29 Effect of Angle of Attack on Vertical Vibrations of TS1 with Backplates

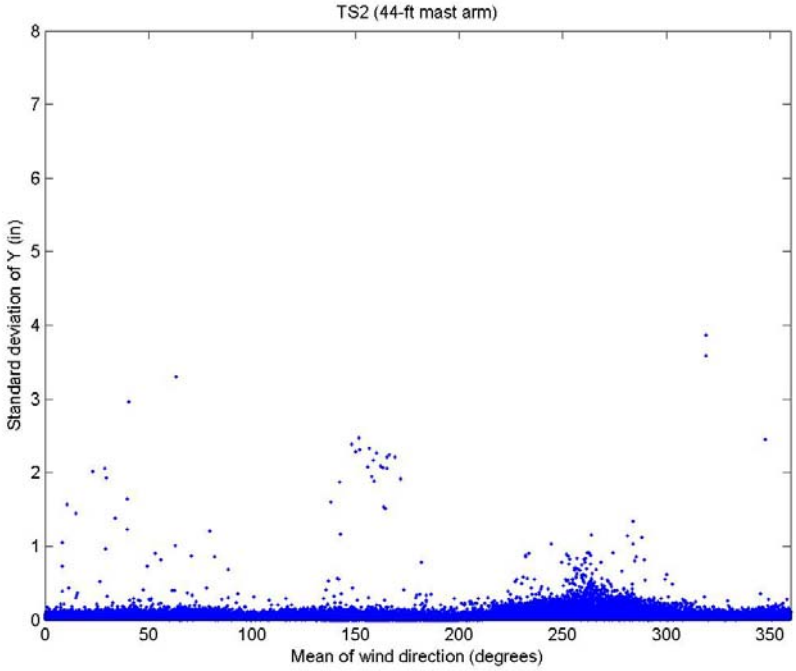

Figure 3.30 Effect of Angle of Attack on Vibrations of TS2 with Backplates

Very few cases of large vibrations were observed under Mode 1100, possibly because wind conditions were less than ideal given that most of the time the angle of attack was between 180 and 360 degrees (the u-component approaches the signals from the front), as shown in Figure 3.31. In this figure each range is of 20 degrees and the x-axis labels indicate the midpoint of the range.

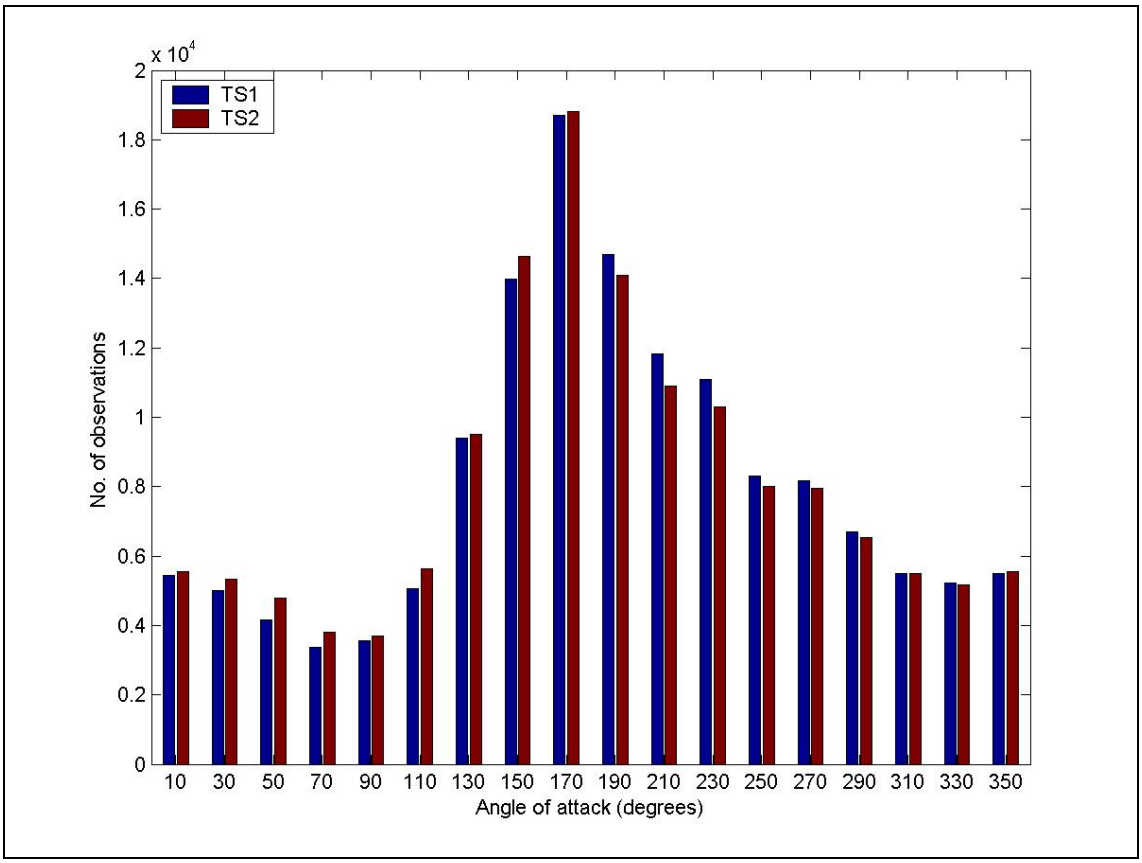

Figure 3.31 Number of Observations per Range of Angle of Attack for Mode 1100

3.3.3 Mode 1101

From March 2006 to February 2007, data was collected under Mode 1101 with the arm pointing north and the signals having no backplates. During this period, 2862 hours of data were collected for TS1 and 2037 hours of data were collected for TS2. The reason for not having the same number of hours of data for TS1 and TS2 and for not having as many hours as for Mode 1100 is that there were problems with the infrared lights of the target. At different times, moisture got into the lights, causing them to malfunction. So at times the TS1 instrumentation was working correctly, while the TS2 instrumentation was being repaired, and vice versa. As before, all data was analyzed by

dividing the long time histories into 2-minute segments, calculating summary statistics for different measured parameters, and plotting graphs. All the plotted graphs are presented in Appendix B. Some of those graphs are discussed here.

Figure 3.32 and Figure 3.33 show the effect of the mean wind speed on the vertical vibrations of the mast arm of TS1 and TS2, respectively. Notice that the few times the standard deviation of Y was higher than 2 inches (all of them for TS1), the mean wind speed was below 25 mph. For TS2, the standard deviation of Y was never higher than 2 inches.

Figure 3.34 and Figure 3.35 show the effect of wind direction on the vertical vibrations of the arms of TS1 and TS2, respectively. (The sign convention of the angle of attack is given in Figure 3.10.) For the case of TS1, there are a concentration of cases at around 90 and 310 degrees, but again very few cases exceeded a standard deviation of Y of 2 inches.

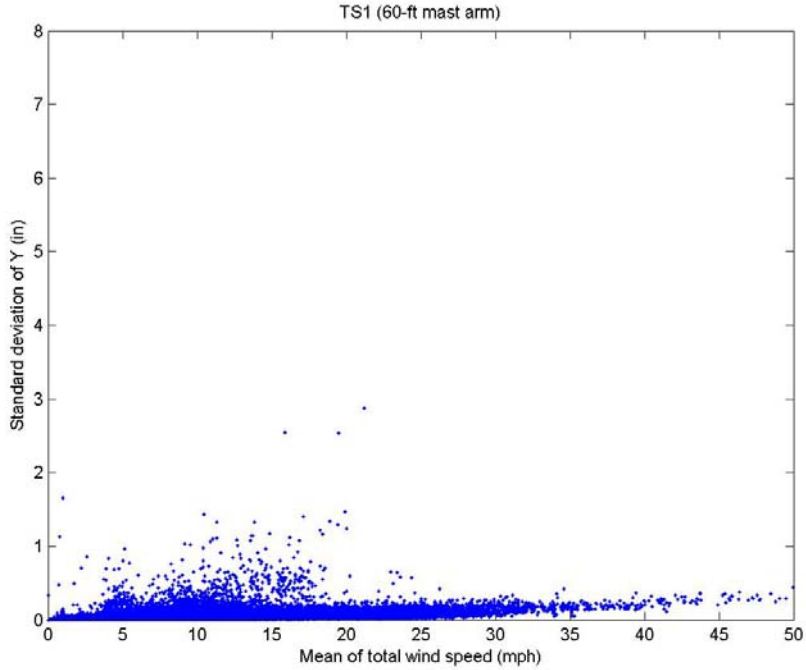

Figure 3.32 Effect of Mean Wind Speed on Vertical Vibrations of TS1 without Backplates

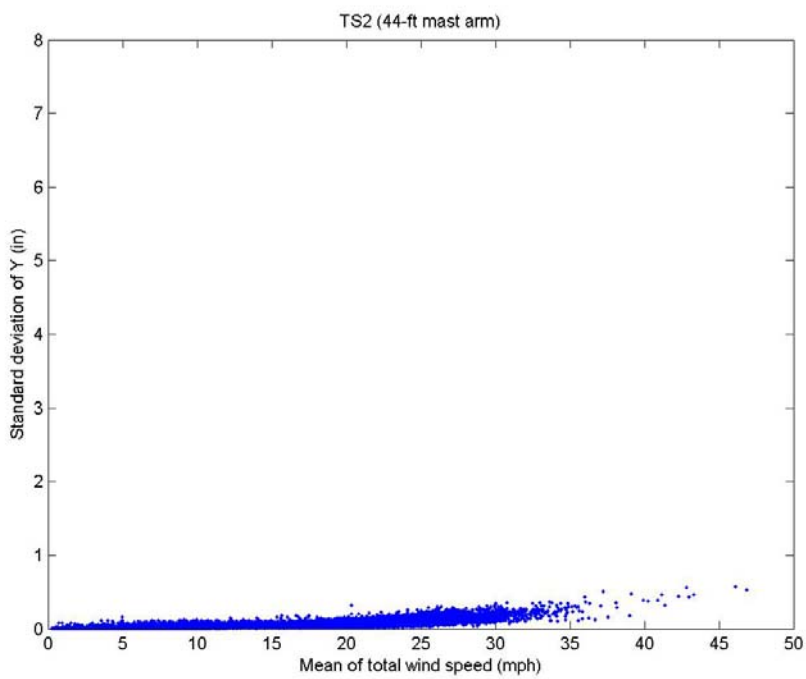

Figure 3.33 Effect of Mean Wind Speed on Vertical Vibrations of TS2 without Backplates

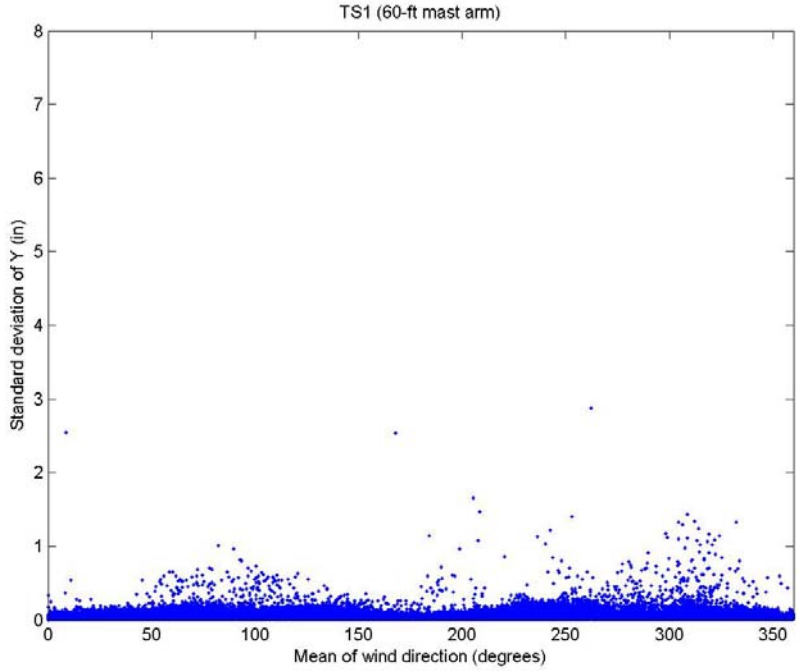

Figure 3.34 Effect of Angle of Attack on Vertical Vibrations of TS1 without Backplates

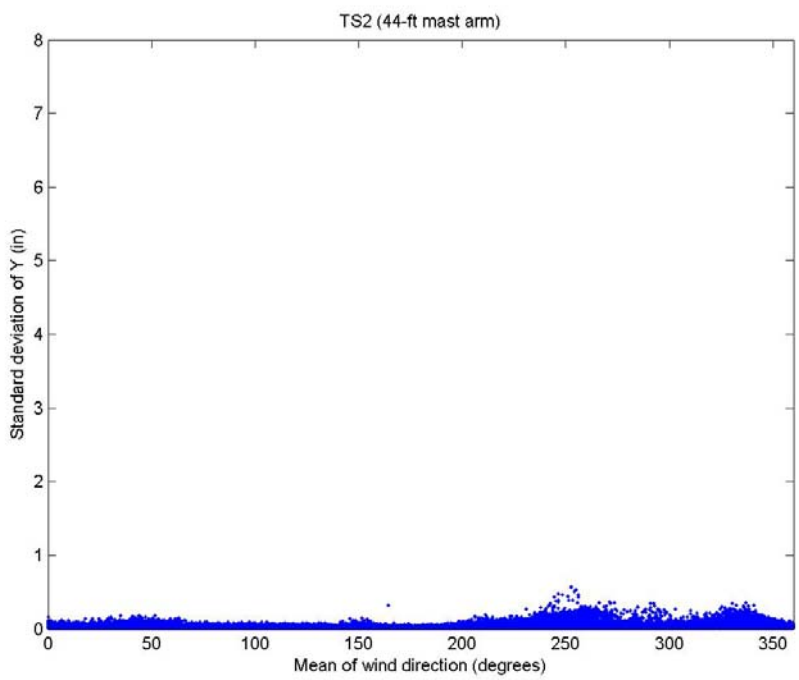

Figure 3.35 Effect of Angle of Attack on Vertical Vibrations of TS2 without Backplates

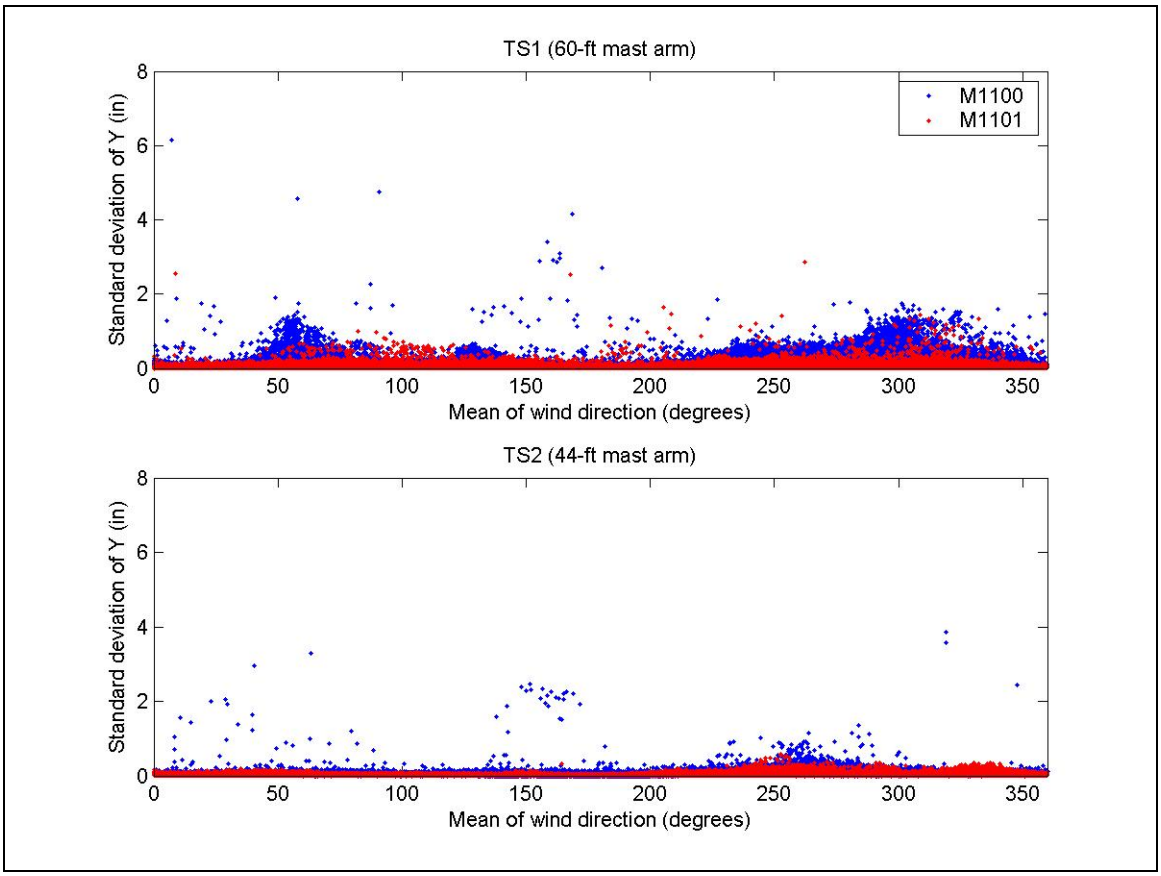

Figure 3.36 Comparison between Modes 1100 and 1101

Figure 3.36 compares the vertical vibrations results of Modes 1100 and 1101. For this figure, the data of Mode 1101 was plotted on top of the Mode 1100 data. Even though more hours of data were recorded for Mode 1100 than for Mode 1101, it is apparent from the figure that the structures with backplates (Mode 1100) vibrate more than the structures without backplates (Mode 1101).

Assuming that cross-wind vibrations are more prone to occur when the wind approaches the signals from behind (between 0 and 180°), then TS1 had a better chance of recording significant vibrations during Mode 1101 than it did during Mode 1100 and than TS2 under any mode. This becomes apparent in Figure 3.37, where it can be seen

that for most of the time the angle of attack was between 0 and 180 degrees (the u-component approaches the signals from the behind). In this figure, each range is of 20 degrees and the x-axis labels indicate the midpoint of the range. Even with these favorable conditions, TS1 did not vibrate much during Mode 1101, most probably due to the removal of backplates.

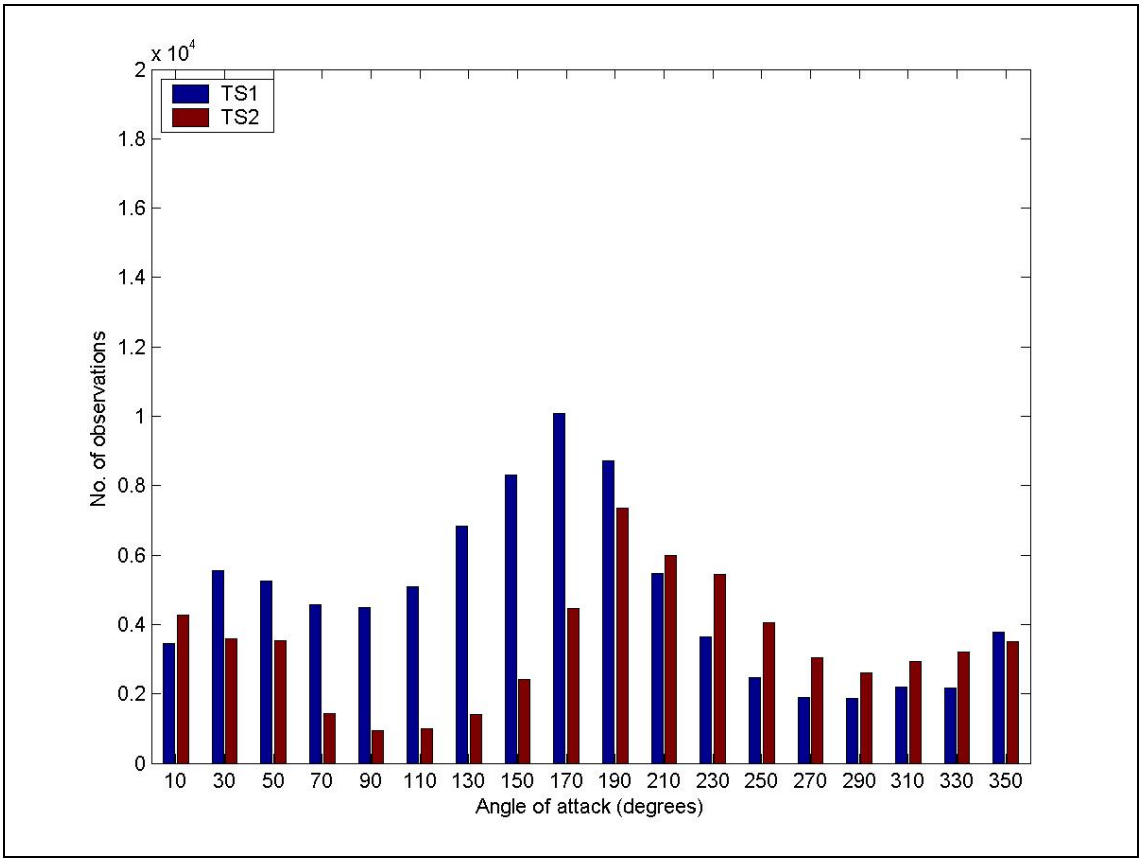

Figure 3.37 Number of Observations Per Range of Angle of Attack for Mode 1101

3.4 Conclusions

It has been observed throughout this experiment that large amplitude vertical vibrations of mast arms with signals with backplates occur for the most part at low wind

speed ranges, and as the wind speed increases the amplitude of the vertical vibrations decreases. Having large vibrations at a certain wind speed and direction ranges reflect the typical behavior of vibrations induced by vortex shedding. This contradicts the generally accepted belief that vortex shedding does not cause significant vibrations of mast arms that could lead to fatigue failure. This is generally attributed to galloping (Pulipaka, Sarkar, and McDonald 1998; Kaczinski, Dexter, and Van Dien 1998; AASHTO 2001; Cook et al. 2001; Dexter and Ricker 2002), where larger vibrations occur at increasingly higher wind speeds. This phenomenon was not captured in this experiment.

It seems that the higher amplitude vertical oscillations have a greater probability of occurring when the wind speed is between 5 to 15 mph. It also appears that they are more likely to occur when the wind approaches the mast arm from the back of the signal (i.e., an angle of attack between 0 and 180°) and when the signals have backplates.

Very few large-amplitude vibration cases were observed under Mode 1100 (signals with backplates), possibly because wind conditions were less than ideal. This is a typical difficulty of conducting full-scale experiments. Still, the large amplitude vibrations that were collected during March 29, 2005, appear to indicate that cantilever traffic signal structures are susceptible to vibrations due to vortex shedding.

CHAPTER 4

WIND TUNNEL STUDIES

4.1 Introduction

From August 15 to December 15, 2005, the research was conducted at the Boundary Layer Wind Tunnel Laboratory (BLWTL) at the University of Western Ontario (UWO) located in London, Ontario, Canada. With its state-of-the-art facilities and 40 years of operation conducting wind tunnel tests for countless research and commercial projects, the BLWTL is the premiere facility of its kind in the world.

An aeroelastic model of a cantilever traffic signal structure was designed and tested in one of the wind tunnels of the BLWTL. Once back at TTU, the researcher used the same design to construct another aeroelastic model of a cantilever structure and tested it in the TTU Boundary Layer Wind Tunnel.

This chapter summarizes the wind tunnel experiments conducted at both UWO and TTU.

4.2 Dimensional Analysis

Table 4.1 shows the six scales that were taken into consideration for the design of the wind tunnel model. The length, density, and velocity scales are straightforward.

Following is an explanation of how the mass, elastic stiffness, and time scales were obtained. Also included in this section is a brief explanation of *Froude's model law*, which was also considered during the design of the wind tunnel model.

Table 4.1 Scale Parameters Considered in Wind Tunnel Modeling

Parameter	Scale
Length (L)	$\lambda_L = L_m / L_p$
Density (ρ)	$\lambda_\rho = \rho_m / \rho_p$
Velocity (U)	$\lambda_U = U_m / U_p$
Mass (M)	$\lambda_M = \lambda_\rho \lambda_L^3$
Elastic stiffness (EI)	$\lambda_{EI} = \lambda_U^2 \lambda_L^4$
Time (T)	$\lambda_T = \lambda_L / \lambda_U$

Note: Subscripts m and p denote model and prototype, respectively.

4.2.1 Mass Scale

The mass scale can be expressed as:

$$\lambda_M = M_m / M_p \tag{4-1}$$

where M_m and M_p are the model mass and the prototype mass, respectively. It is commonly known that mass of an object can be calculated as:

$$M = \rho V \tag{4-2}$$

where ρ is the density and V is the volume. Therefore Equation (4-1) can be written as:

$$\lambda_M = (\rho_m V_m) / (\rho_p V_p) = (\rho_m / \rho_p) (V_m / V_p) \quad (4\text{-}3)$$

The term (ρ_m / ρ_p) is the density scale λ_ρ. It is known that the units for volume are the units of length to the third power. Therefore the term (V_m / V_p) is the same as (L_m^3 / L_p^3), which is the cube of the length scale (i.e., $L_m^3 / L_p^3 = \lambda_L^3$). Thus Equation (4-3) can be expressed as follows:

$$\lambda_M = (\rho_m / \rho_p) (V_m / V_p) = \lambda_\rho \lambda_L^3 \quad (4\text{-}4)$$

Equation (4-4) is the mass scale presented in Table 4.1.

4.2.2 Elastic Stiffness Scale

The elastic stiffness scale can be expressed as:

$$\lambda_{EI} = (E_m I_m) / (E_p I_p) = (E_m / E_p) (I_m / I_p) \quad (4\text{-}5)$$

where E_m and E_p are the modulus of elasticity of the model and the prototype, respectively, and I_m and I_p are the moment of inertia of the cross-section of the model and the prototype, respectively.

The non-dimensional Cauchy number is the ratio of internal forces in a structure to inertial forces in the air (Holmes 2001). It can be written as:

$$Ca = E / (\rho_a U^2) \quad (4\text{-}6)$$

where ρ_a is the density of air. Assuming that the density of air in the wind tunnel is equal to the one around the prototype and requiring that the Cauchy number of the model is equal to the Cauchy number of the prototype, then:

$$[E_m / (\rho_a U_m^2)] = [E_p / (\rho_a U_p^2)] \quad (4\text{-}7)$$

$$(E_m / E_p) = (U_m^2 / U_p^2) \quad (4\text{-}8)$$

$$(E_m / E_p) = \lambda_U^2 \quad (4\text{-}9)$$

It is known that the units for moment of inertia are the units of length to the fourth power. Therefore the term (I_m / I_p) is the same as (L_m^4 / L_p^4), which is the length scale to the fourth power (i.e., $L_m^4 / L_p^4 = \lambda_L^4$). Therefore Equation (4-5) can be changed as follows:

$$\lambda_{EI} = (E_m / E_p)\,(I_m / I_p) = \lambda_U^2\,\lambda_L^4 \quad (4\text{-}10)$$

Equation (4-10) is the elastic stiffness scale presented in Table 4.1.

4.2.3 Time Scale

The non-dimensional Strouhal number can be written as:

$$St = f_o\,L / U \quad (4\text{-}11)$$

where f_o is the fundamental frequency of the structure. Requiring that the Strouhal number of the model is equal to the Strouhal number of the prototype, then:

$$f_m\,L_m / U_m = f_p\,L_p / U_p \quad (4\text{-}12)$$

$$f_m / f_p = (U_m / U_p)\,(L_p / L_m) \quad (4\text{-}13)$$

$$f_m / f_p = (U_m / U_p) / (L_m / L_p) \quad (4\text{-}14)$$

$$\lambda_f = \lambda_U / \lambda_L \quad (4\text{-}15)$$

where λ_f is the frequency scale. Recognizing that the units of frequency are the inverse of the units of time, then:

$$\lambda_T = 1 / \lambda_f = \lambda_L / \lambda_U \quad (4\text{-}16)$$

Equation (4-16) is the time scale presented in Table 4.1.

4.2.4 Froude's Model Law

In wind tunnel modeling, one law that is often used is Froude's model law, which accounts for inertial and gravitational forces, but disregards viscous forces (Dyrbye and Hansen 1997). This law requires that the Froude number of the model be equal to the Froude number of the prototype.

Froude number is defined as the ratio of inertia forces to gravity forces. Froude number is usually expressed as follows:

$$Fr = U^2 / (g\ L) \tag{4-17}$$

where g is the acceleration of gravity. Applying Froude's model law, then:

$$[U_m^2 / (g\ L_m)] = [U_p^2 / (g\ L_p)] \tag{4-18}$$

$$(U_m^2 / U_p^2) = (L_m / L_p) \tag{4-19}$$

$$(\lambda_U)^2 = \lambda_L \tag{4-20}$$

$$\lambda_U = (\lambda_L)^{½} \tag{4-21}$$

Thus, in order to fulfill Froude's model law, once a length scale is selected, the velocity scale is automatically selected (i.e., the velocity scale is dependent on the length scale).

4.3 University of Western Ontario Experiments

4.3.1 Model Design and Construction

The researchers decided the model used in the UWO testing should specifically replicate the cantilever traffic signal structure with a 44-ft mast arm used in full-scale measurements by TTU because this structure had been seen vibrating significantly on the field experiments (as discussed in Section 3.3.1).

The model was tested in the Open Circuit Small Wind Tunnel (OCSWT) at UWO, which has an 18”x18” section, because other tunnels of the BLWTL with larger sections had busy schedules making them difficult to reserve. This decision affected the model design in two ways:

1. Because of the limitations on specimen size, only the mast arm of the cantilever traffic signal structure could be modeled. Otherwise the length scale of the model would have to be too small for the OCSWT. The elimination of the pole was justified by the fact that the stiffness of the mast arm is significantly lower than the stiffness of the pole (as shown in Appendix C). In addition, most failures have been documented at the pole-mast junction (Pulipaka 1995; Gray et al. 1999; Hartnagel and Barker 1999; Hamilton, Riggs and Puckett 2000; Chen et al. 2001; Cook et al. 2001).

2. A length scale (λ_L) of 1/50 was selected. Therefore the mast arm model would have a length of a little over 11”, which would be a good size for the OCSWT.

With the pole eliminated, the mast arm model was to be placed vertically and tested under uniform flow, which seems a good approximation because under full-scale conditions, the mast arm cantilevers horizontally, so it is believed that an atmospheric boundary layer would not have significant effects (i.e., it is assumed that, in full scale, only the portion of the wind speed at the height of the mast arm is going to have an effect on it). Also, by placing the mast arm vertically, the effects of gravitational loads were neglected. It seemed reasonable to assume that, in full-scale, gravity loads would give an initial displacement to the mast arm soon after installed, but afterward gravity loads would be relatively small and have little to no effect in wind-induced oscillations.

As mentioned before, the length scale λ_L was selected as 1/50. Initially, Froude scaling (explained in Section 4.2.4) was attempted. Therefore, the initial calculation of the velocity scale was:

$$\lambda_U = (\lambda_L)^{1/2} = (1/50)^{1/2} \approx 1/7 \tag{4-22}$$

This velocity scale was problematic because the full-scale data indicated that vibrations of these structures occur at low wind speeds, translating to wind speeds of less than 2 mph in the wind tunnel at this scale. The OCSWT becomes unstable at speeds of less than 9 mph. Since gravity loads had already been neglected by placing the mast arm model vertically, Froude scaling was ignored and a velocity scale of $\lambda_U = 1/1$ was selected. Therefore the elastic stiffness scale (λ_{EI}) was obtained as follows:

$$\lambda_{EI} = \lambda_U^2\, \lambda_L^4 = (1/1)^2\, (1/50)^4 = 1.6 \times 10^7 \tag{4-23}$$

By not maintaining Froude's Model Law, no proper scale was kept between the weight of the prototype and the model, therefore the effect of gravity loads was neglected. As explained before, it seemed reasonable to neglect them because in full-scale, gravity loads would give an initial displacement to the mast arm soon after installed, but afterward gravity loads would be relatively small and have little to no effect in wind-induced oscillations.

To avoid the high cost of fabrication, researchers used available sizes of aluminum or steel tubing to make the mast arm model. Since these are not available in tapered sections like the full-scale mast arm, three different sizes of tubing were attached to form a single, tapered arm. Researchers decided to use the middle segment to carry the

two 3-signal heads. The mass, stiffness, and diameter that each segment required was determined using the corresponding scales (as shown in Table 4.1).

Researchers designed a mast arm made of aluminum with no cladding. The difficulty of this was finding available pieces of aluminum tubing that would have the required diameter, mass, and stiffness.

Table 4.2 on the following page shows the best fit found. In the table, Segment 1 is connected to the fixed end, Segment 2 is the middle one supporting the two 3-signal heads, and Segment 3 has the free end supporting the 5-signal head. The table shows how the physical properties of the tubing (under the "Actual" columns) match the required properties (as determined by the scales). Some difficulty was found matching the elastic stiffness (*EI*). The scaled design is shown in Figure 4.1 . Also shown in Figure 4.1 is the design of the signal heads, which were made of foam and attached to aluminum backplates.

Table 4.2 Comparison Between Actual and Required Properties of Mast Arm Model

Segment	Diameter (in)			Mass (g)			EI (kips-in^2)		
	Required	Actual	% Diff.	Required	Actual	% Diff.	Required	Actual	% Diff.
1	0.205	7/32	-6.7	1.55	1.57	-1.3	0.457	0.503	-9.9
2	0.157	5/32	0.5	1.32	1.23	6.8	0.199	0.169	14.9
3	0.117	1/8	-6.8	0.54	0.53	1.9	0.080	0.081	-1.5

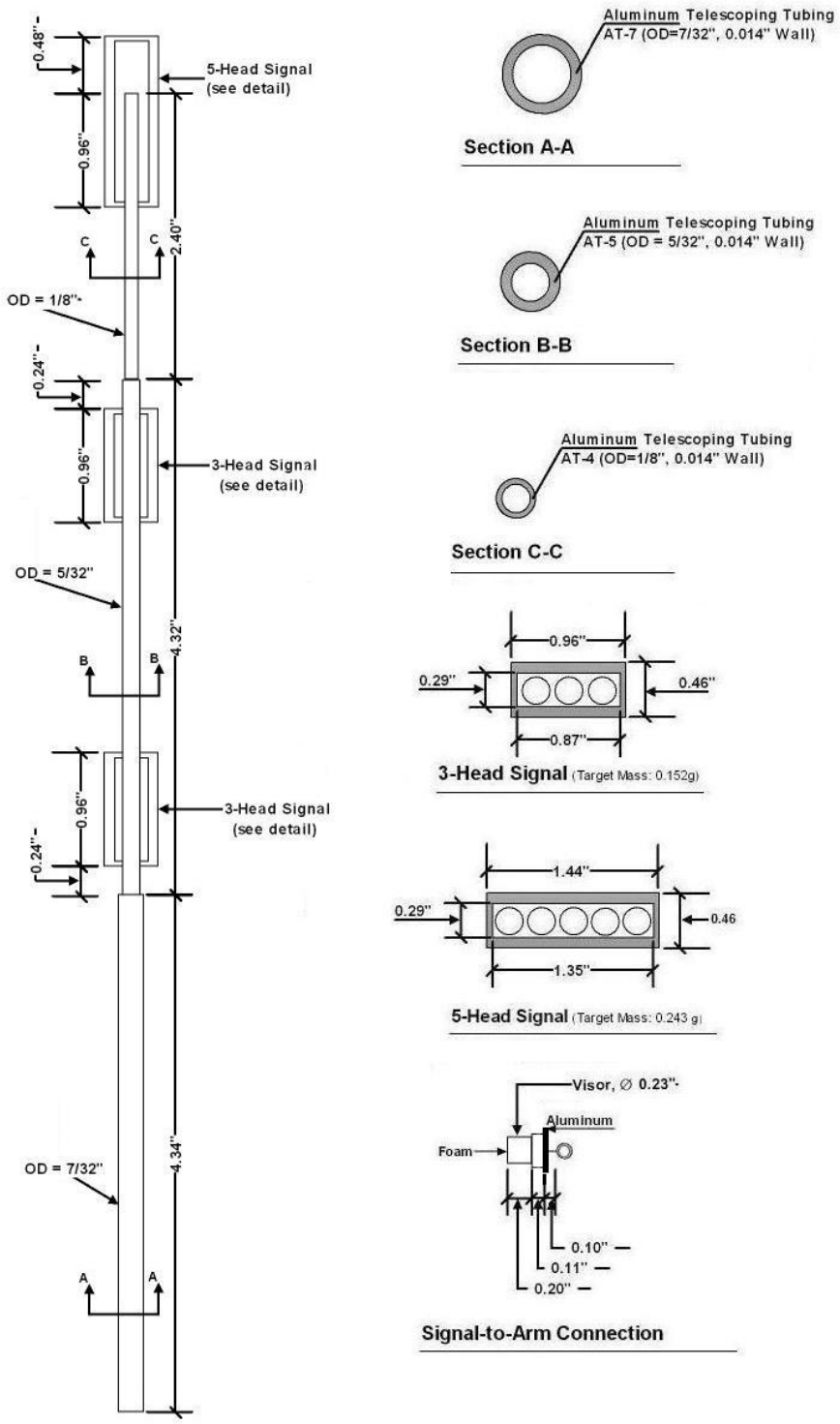

Figure 4.1 Design Drawing for Wind Tunnel Model

As explained in Section 4.2.3, it is known that:

$$\lambda_f = \lambda_U / \lambda_L \tag{4-24}$$

$$f_m / f_p = \lambda_U / \lambda_L \tag{4-25}$$

$$f_m = f_p \, \lambda_U / \lambda_L \tag{4-26}$$

Since it is known that the in-plane fundamental frequency of the full-scale prototype is f_p = 0.98 Hz ≈ 1 Hz and that the model was designed with a length scale of λ_L = 1/50 and a velocity scale of λ_U = 1/1, then, substituting in Equation (4-26), the expected fundamental frequency of the model was obtained:

$$f_m = (1 \text{ Hz}) \, (1/1) \, / \, (1/50) = 50 \text{ Hz} \tag{4-27}$$

Once constructed, the model was attached to a JR3 load cell, which was connected to a computer. Tapping the tip of the model, the computer measured the fundamental frequency of the model from a Fast Fourier Transform (FFT) analysis of the load cell data. The model's fundamental frequency was measured as f_m = 62 Hz, which is 24% over the expected value. The researchers believe this large discrepancy is mostly due to the difference between the target and the actual stiffness of the three segments. Therefore, the velocity scale had to be revised. Solving Equation (4-24) for the velocity ratio and substituting the actual values:

$$\lambda_U = \lambda_f \, \lambda_L = (62/1) \, (1/50) = 1.24 \tag{4-28}$$

Therefore, the velocity scale was taken as λ_U = 1.24/1.

4.3.2 Experimental Setup and Procedure

The model was tested on the Open Circuit Small Wind Tunnel (OCSWT), which is shown in Figure 4.2. The OCSWT can generate a maximum wind speed of 45 mph. A Pitot tube was used to measure wind speed and a Keyence LB-60 laser sensor was mounted next to the model (as shown in Figure 4.3) to measure the cross-wind displacements at the tip of the model. All the data was collected at a sampling rate of 200 Hz (this translates to 3.2 Hz in the full scale).

To generate some turbulence, a fine grid and a coarse grid were available. These grids are shown in Figure 4.4 and their dimensions are presented in Table 4.3. The grids were placed about 2.5 ft in front of the model. When one of the grids is installed, the maximum wind speed of the OCSWT is reduced. Table 4.4 summarizes how the performance of the wind tunnel is affected by the grids.

Figure 4.2 Open Circuit Small Wind Tunnel (OCSWT)

Figure 4.3 Model and Laser Mounted in the OCSWT

Figure 4.4 Fine and Coarse Grids

Table 4.3 Dimensions of Grids

Grids	Bar thickness (inches)	Clear spacing between bars (inches)	Material
Fine	0.5	1.375	Wood
Coarse	1.25	4.75	Steel

Table 4.4. Wind Tunnel Performance

Case	Max wind speed (mph)	TI (%)
No grid	45	2
Fine grid	20	7
Coarse grid	15	30

Six types of tests were conducted:

1. Signals facing the wind with no grid,
2. Signals facing the wind with the fine grid,
3. Signals facing the wind with the coarse grid,
4. Signals' back to the wind with no grid,
5. Signals' back to the wind with the fine grid, and
6. Signals' back to the wind with the coarse grid.

For each of the tests, data was collected at several wind speeds. For each data collection, a target wind speed was sought in the wind tunnel and, once obtained, data was recorded for two minutes. At no point was the tip of the model restricted. Therefore, the tip of the model was free to vibrate when the target wind speed was being sought and data was not being recorded.

4.3.3 Results

When the model was tested with the wind blowing into the front of the signals, only small along-wind vibrations were observed and these only occurred when either of the grids was installed. Significant cross-wind vibrations were observed when the model was tested with the wind blowing into the back of the signals. These vibrations had a maximum peak-to-peak magnitude of about 0.8 inches in the model scale, and only occurred in a narrow wind speed range. This appears to indicate that the observed vibrations were due to vortex shedding. To the contrary, a typical galloping behavior would be to increase the magnitude of vibrations with an increase of wind speed; galloping vibrations wouldn't occur just in a narrow wind speed range.

Figure 4.5 shows the time histories of the wind speed and of the cross-wind displacement of the tip when the model was tested with the wind blowing into the back of the signals and with no grid installed in the tunnel. It should be pointed out that these plots are not true time histories because the data was not recorded continuously. Instead, as explained previously, a target wind speed was sought in the wind tunnel and, once obtained, data was recorded. The values of this figure were adjusted to full-scale using the length scale of 1/50, the velocity scale of 1.24/1, and the time scale of 1/62. It can be seen in the figure that large amplitude vibrations, sometimes having peak-to-peak amplitudes of 40 inches, were measured when the wind speed was close to 10 mph. Peak-to-peak amplitudes of 40 inches appear to be too high when compared to the values reported by Pulipaka (1995) of peak-to-peak amplitudes of 20 to 24 inches. The likely

reason the amplitudes in the case with no grid were so high is that the flow was too smooth when compared to real-life conditions.

Figure 4.6 shows the time histories for the case with fine grid and Figure 4.7 shows them for the case with the coarse grid, both with the wind coming from behind the signals. Again, these figures are not true time histories because the data was not recorded continuously. For each of these two figures, the plot of the wind speed was obtained by calculating 1-second mean in the model scale. This was done because, with the turbulence caused by the grids, the Pitot tube measures a negative wind speed about every 10 measurements that, when plotted, makes difficult to distinguish the average velocity. Both figures were adjusted to full-scale values. In both cases, the maximum peak-to-peak amplitudes are close to 20 inches. The peak-to-peak amplitudes obtained with the grids are within the range reported by Pulipaka (1995) of peak-to-peak amplitudes of 20 to 24 inches.

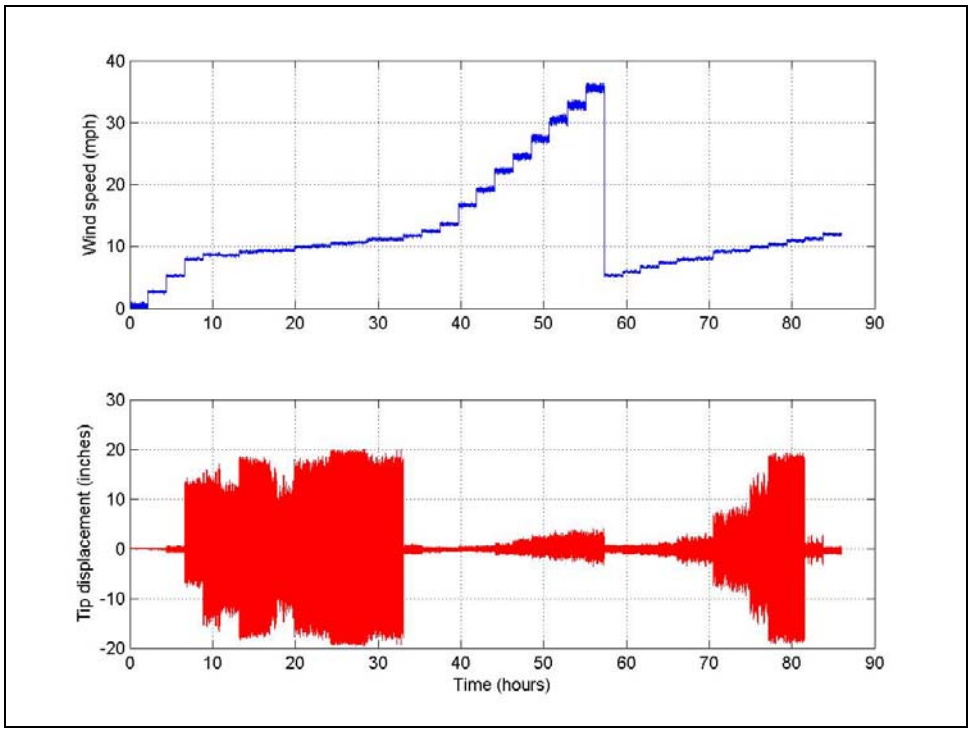

Figure 4.5 Time Histories for Wind Tunnel Tests with No Grid

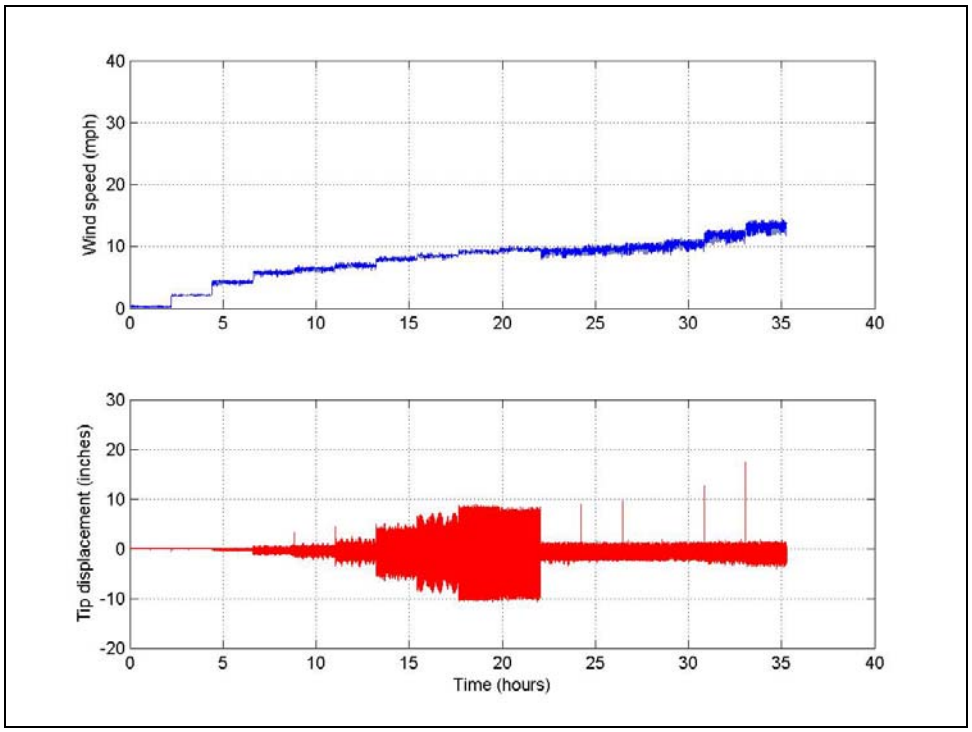

Figure 4.6 Time Histories for Wind Tunnel Tests with Fine Grid

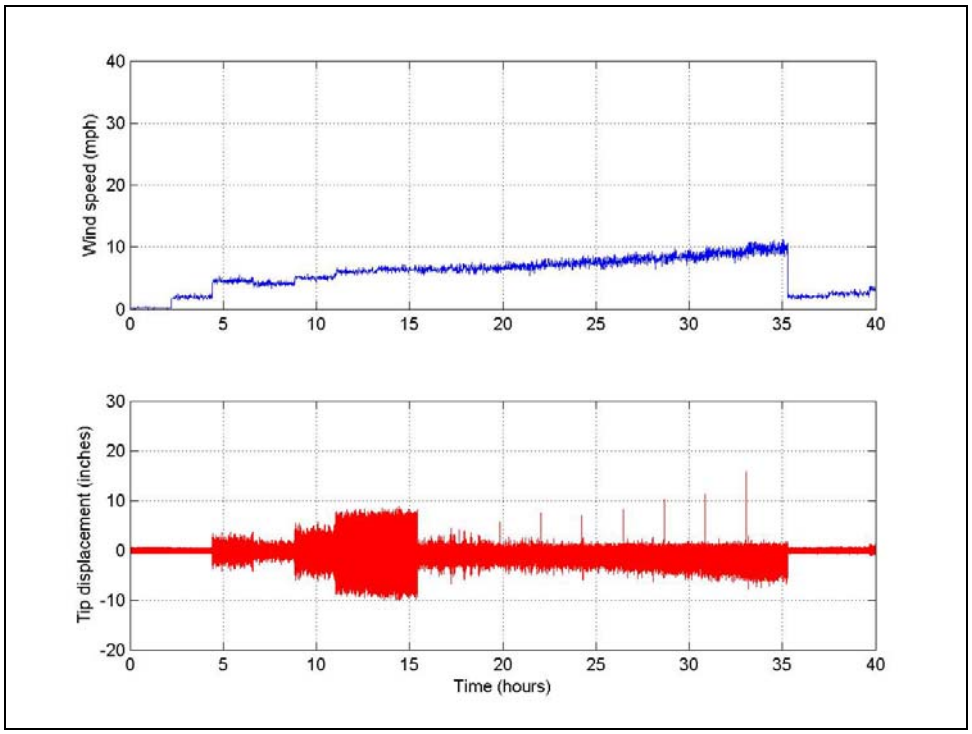

Figure 4.7 Time Histories for Wind Tunnel Tests with Coarse Grid

Figure 4.8 was generated using the data presented in

Figure 4.5. This data was divided into 30-second segments. For each segment, an average wind speed and the standard deviation of the cross-wind displacement were calculated and then plotted as shown. Figure 4.8 clearly shows that the maximum vibrations occur when the wind speed is in the range 8 to 11 mph. It should be pointed out that it was checked that the general shape of the graph on Figure 4.8 remained unchanged for different observation periods (for example, 120 seconds instead of 30 seconds).

Figure 4.9 and Figure 4.10 show how the tip displacement was affected when the different grids were installed, increasing the turbulence intensity. These figures were developed using the same procedure that was followed to generate Figure 4.8. They both show that an increase in turbulence intensity reduces the magnitude of the maximum vibrations as well as the velocity at which they occur. The results of the experiments are summarized on Table 4.5.

Obtaining a target wind speed in the wind tunnel was difficult. Given the experimental procedure (in which a target wind speed was sought in the wind tunnel and data was recorded after the sought speed was obtained), the plots of Figure 4.8, Figure 4.9, and Figure 4.10 were not checked for hysteresis.

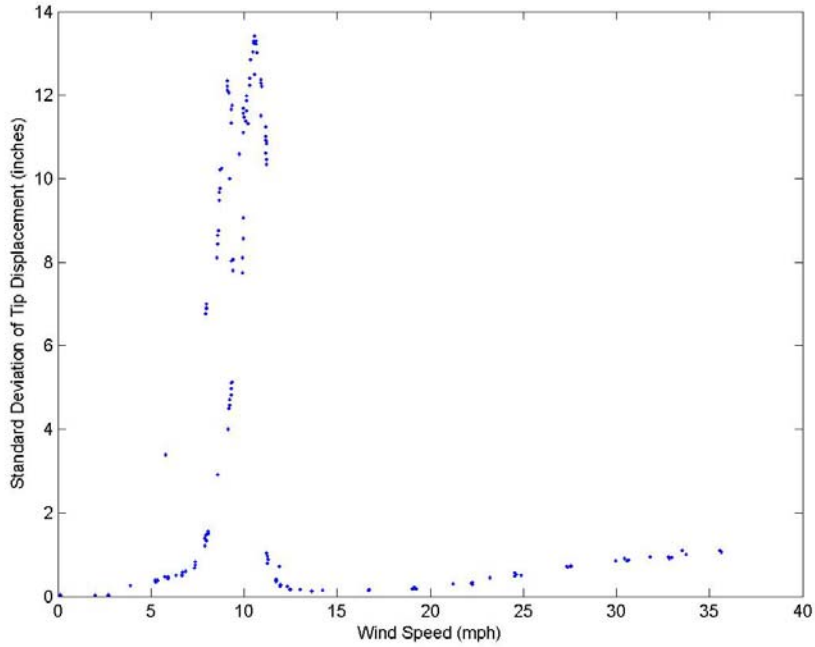

Figure 4.8 Effect of Wind Speed on Cross-Wind Displacement of Tip with No Grid

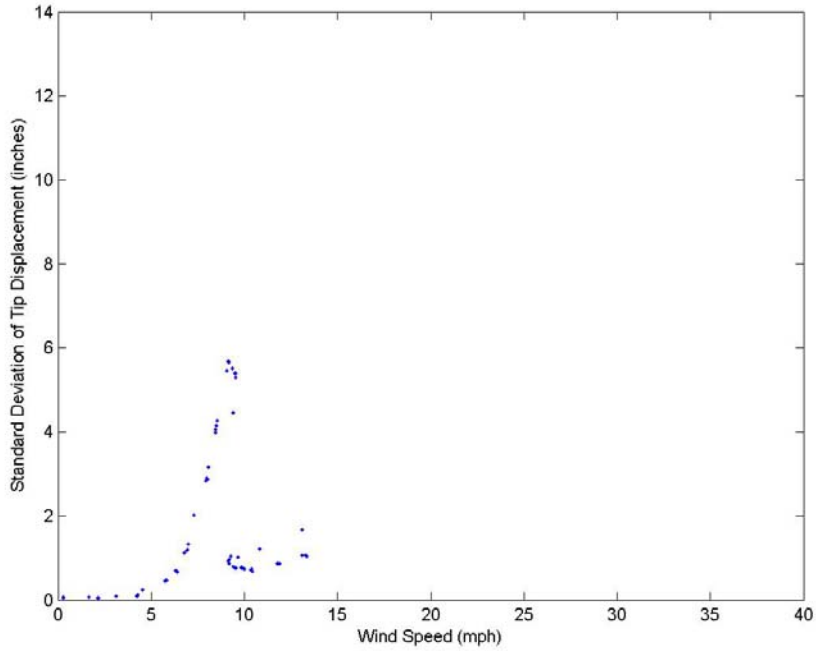

Figure 4.9 Effect of Wind Speed on Cross-Wind Displacement of Tip with Fine Grid

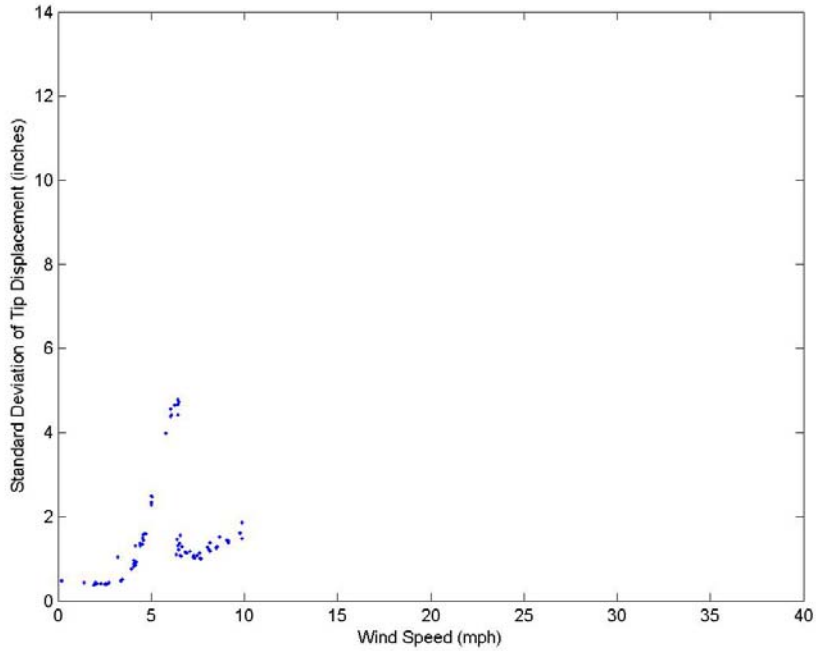

Figure 4.10 Effect of Wind Speed on Cross-Wind Displacement of Tip with Coarse Grid

Table 4.5 Results of UWO Wind Tunnel Experiments

Case	TI (%)	Max standard deviation of displacement (in)	Speed at which it occurred (mph)
No grid	2	13.4	10.5
Fine grid	7	5.7	9.1
Coarse grid	30	4.8	6.4

4.4 Texas Tech University Experiments

4.4.1 Model Design and Construction

The same design of the aeroelastic model of a mast arm having signals with backplates used at the UWO experiments was again used to make a model for the TTU experiments. In addition, a similar model was built, except that the signals did not have backplates (i.e., the aluminum plate to which a signal is attached did not extend further that the foam simulating the signals).

4.4.2 Experimental Setup and Procedure

The mast arm model was attached to a rigid pole (solid steel bar with ¾-in diameter), which itself is attached to the turntable in the wind tunnel, as shown in Figure 4.11. The pole was not modeled aeroelastically because, as explained in Section 4.3.1, this research is concerned with arm-pole relative displacements.

Tests were conducted in TTU's Boundary Layer Wind Tunnel which has a 5.9-ft by 3.9-ft working section. Because the same model of the mast arm used at UWO was again used at TTU, the velocity scale was again 1.24:1. By doing this, Froude Model Law was disregarded and the effect of gravitational forces were neglected again. As mentioned before, this seemed reasonable because, in full-scale, gravity loads would give an initial displacement to the mast arm soon after installed, but afterward gravity loads would be relatively small and have little to no effect in wind-induced oscillations. Each model was tested under different angles of attack for two different turbulence intensities:

(1) nominally Exposure D, as specified by the ASCE (2005), and (2) low turbulence smooth flow. At the mast arm height, the first simulation had a turbulence intensity (TI) of about 16%, while the second had a TI of about 6%. The angle of attack convention is the same as that used for the full-scale experiments (see Figure 3.10). Table 4.6 indicates the conditions of TI and angle of attack for which each model (with or without backplates) was tested.

For each of the different cases tested, data was collected at several wind speeds. For each data collection, a target wind speed was sought in the wind tunnel and, once obtained, data was recorded for one minute. At no point was the tip of the model restricted. Therefore, the tip of the model was free to vibrate when the target wind speed was being sought and data was not being recorded.

A Micro-Epsilon ILD-1401 laser displacement sensor with a resolution of 20 μm was used to measure cross-wind displacements of the tip of the model. To measure wind speed in the wind tunnel at the height of the model's mast arm, a Turbulent Flow Series 100 Cobra Probe was placed at a distance of 45 cm in front of the model's pole. Both probes were sampled at 1,000 Hz.

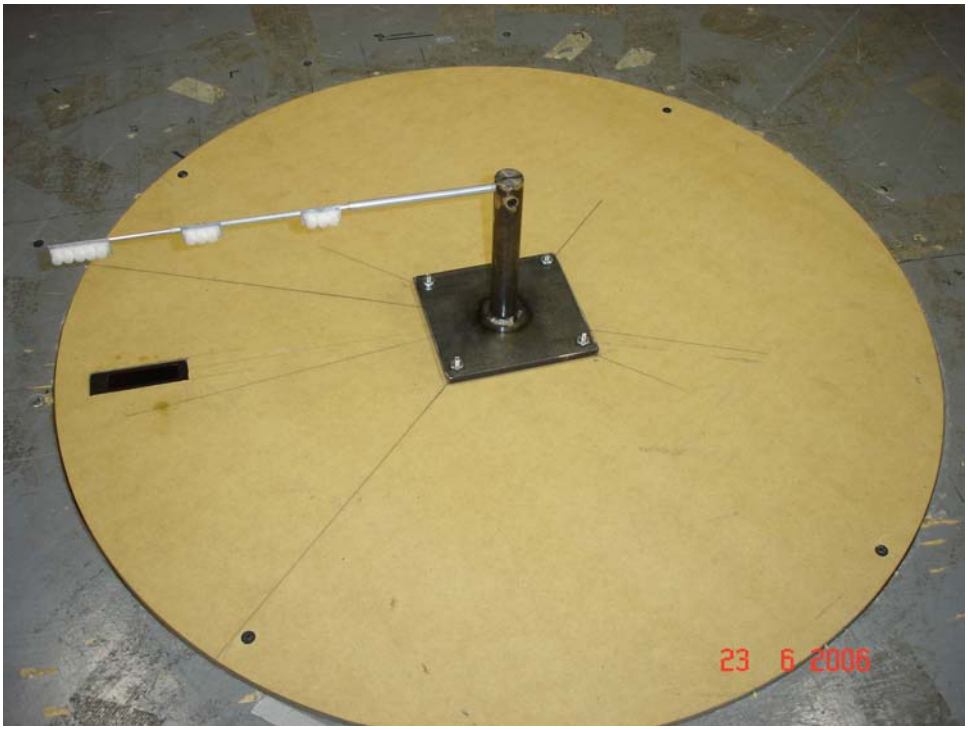

Figure 4.11 Model with Backplates Mounted in TTU Wind Tunnel

Table 4.6 Cases for Which Experiments Were Conducted

Angle of attack (degrees)	Exposure D (TI = 16%)		Smooth flow (TI = 6%)	
	With backplates	Without backplates	With backplates	Without backplates
0	X	X	X	
15			X	
25			X	
35	X		X	
45	X	X	X	
55	X		X	
65	X		X	
75	X		X	
85	X		X	
90	X	X	X	X
95	X		X	
105	X		X	
115	X		X	

125	X		X
135	X	X	X
145	X		X
180	X	X	X
225	X	X	X
270	X	X	X
315	X	X	X

X = Experiment conducted for this case

A pluck test was conducted to determine the fundamental frequency in the vertical direction and the damping ratio of the models. Using the same procedure used for the full-scale structures (see Section 3.2.5), the results presented in Table 4.7 were obtained.

Table 4.7 Vertical Fundamental Frequency (f_o) and Damping Ratio (ζ) of Models

Model	f_o (Hz)	ζ (%)
With backplates	62	0.33
Without backplates	62	0.51

4.4.3 Results

For each angle of attack tested in the wind tunnel, data was recorded at different wind speeds at a rate of 1-minute per wind speed. For each of these speeds, the average wind speed and the standard deviation of the vertical displacement were calculated. Both sets of values were adjusted to the full-scale and used to generate the plots presented in

Appendix D. Some of the plots are discussed here. In these figures, BP stands for backplates.

Figure 4.12 shows the results obtained for the case of the models tested with an angle of attack of 90°. The figure shows that for all four test cases there is a spike in the vibration amplitude when the reduced wind speed is between 5 and 20 mph. In the case of models without backplates, the spike is much lower than for the cases with backplates, but is still noticeable. These low-speed spikes are typical of a vortex shedding phenomenon causing the vibrations. This behavior was observed when the model with backplates was tested at angles of attack between 55° and 125° with vibrations achieving peak amplitude when the wind speed is between 10 and 15 mph. Clearly, this is a very wide range of velocities for large response and represents phenomena beyond classical Kármán vortex shedding.

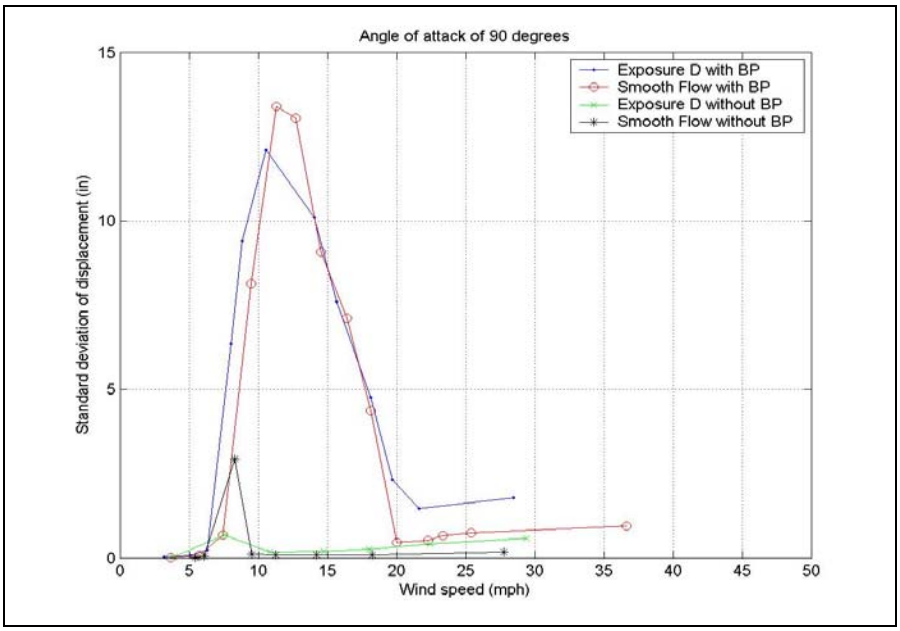

Figure 4.12 Wind Tunnel Results for Angle of Attack of 90 Degrees

Table 4.8. TTU Results for 90° Angle of Attack

Flow	TI (%)	Max. standard deviation of displacement (inches)	
		With backplates	Without backplates
Exposure D	16	12.10	0.68
Smooth	6	13.04	2.93

Table 4.8 provides the maximum displacement values for the experiments conducted with 90° angle of attack. These results are compared in Figure 4.13 with those obtained at UWO (as originally presented in Table 4.5). In this figure there are unexpected discrepancies. It was expected that the signals with backplates under smooth flow experiment at TTU (TI = 6%) would yield a similar result to the case of the fine grid at UWO (TI = 7%), yet the maximum standard deviation of displacements were 13.0” and 5.7”, respectively. Similarly, the signal with backplates under Exposure D case at

TTU (TI = 16%) was expected to yield smaller standard deviation of displacement values than the fine grid case at UWO (TI = 7%), but the opposite was true. Since the models all had the same fundamental frequency, the reason for the discrepancy in results is unclear. The discrepancy could be due to the fact that in the UWO experiments the model was oriented vertically through a shallow boundary layer, while at TTU the experiments were conducted with the model oriented horizontally, completely immersed within the boundary layer. It is anticipated that the TTU results should be more realistic. Yet in the vibration values obtained in full-scale experiments are much closer to the UWO results. Even with the discrepancies in peak-to-peak amplitudes obtained at UWO and TTU, there were a lot of agreements between the two sets of experiments, mainly that large amplitude vibrations of mast arms occur at a narrow wind speed range when the wind approaches the signals from behind.

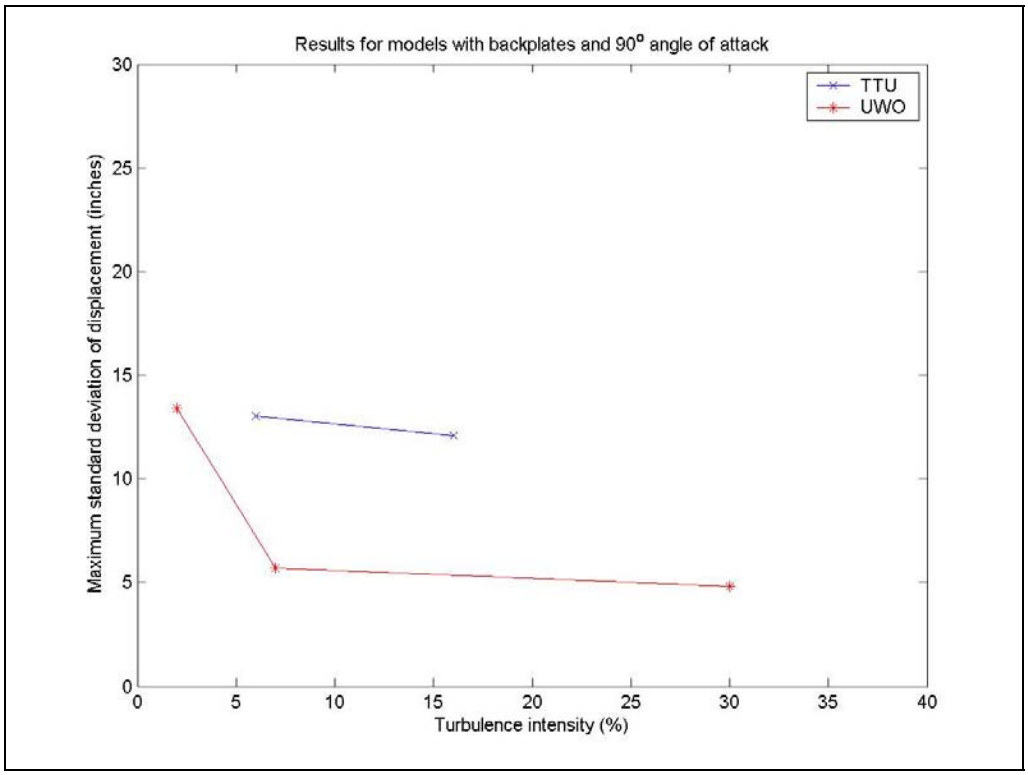

Figure 4.13 Comparison of TTU and UWO Wind Tunnel Results

For the case of the model with backplates with an angle of attack of 55°, the maximum amplitude of vibration commences somewhere between 5 and 10 mph, but extends over a broader range of reduced wind speeds as shown in Figure 4.14.

For the case of the model with backplates under smooth flow, when the angle of attack was either 45° (Figure 4.15) or 125° (Figure 4.16) there were two spikes on the data instead of the typical single spike. In both cases, the first peak occurs at about 10 mph, while the second one occurs at approximately 35 mph.

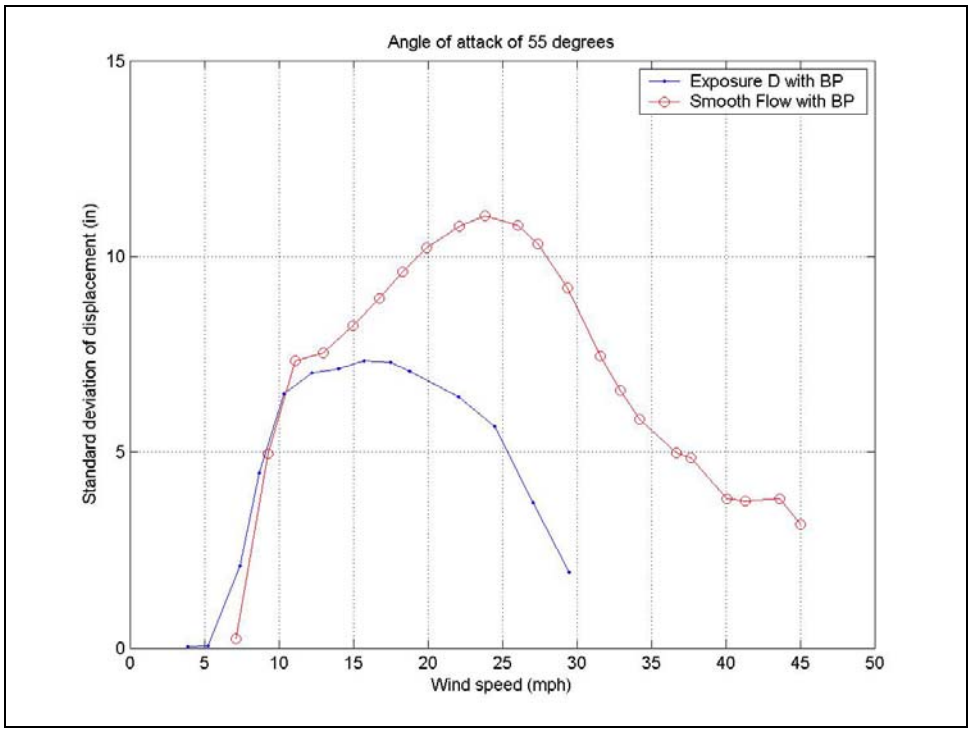

Figure 4.14 Wind Tunnel Results for Angle of Attack of 55 Degrees

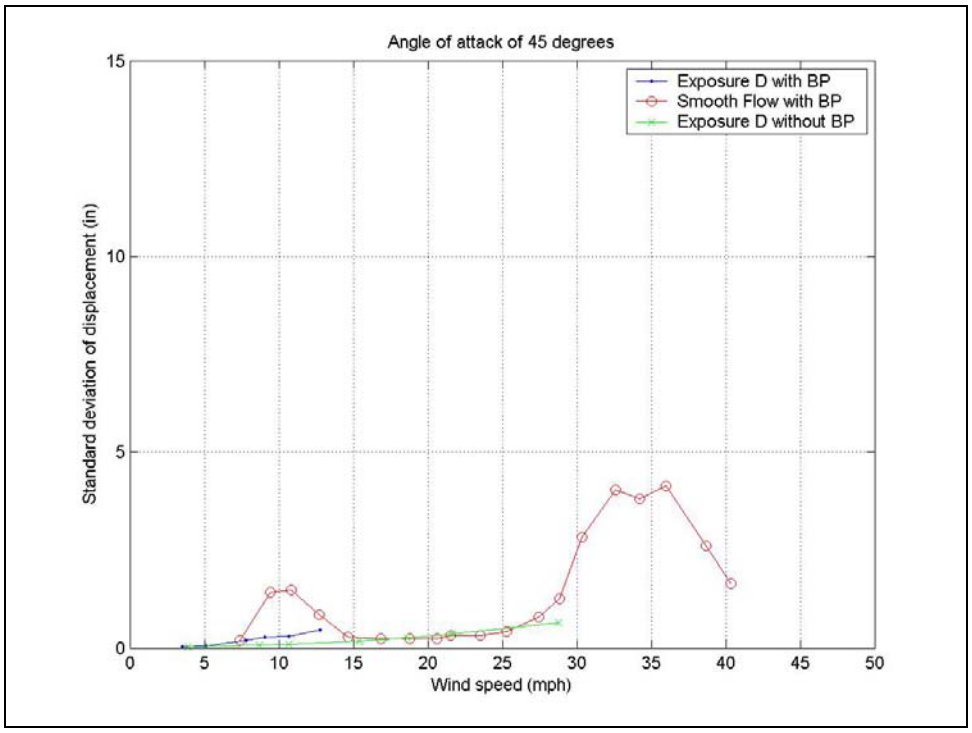

Figure 4.15 Wind Tunnel Results for Angle of Attack of 45 Degrees

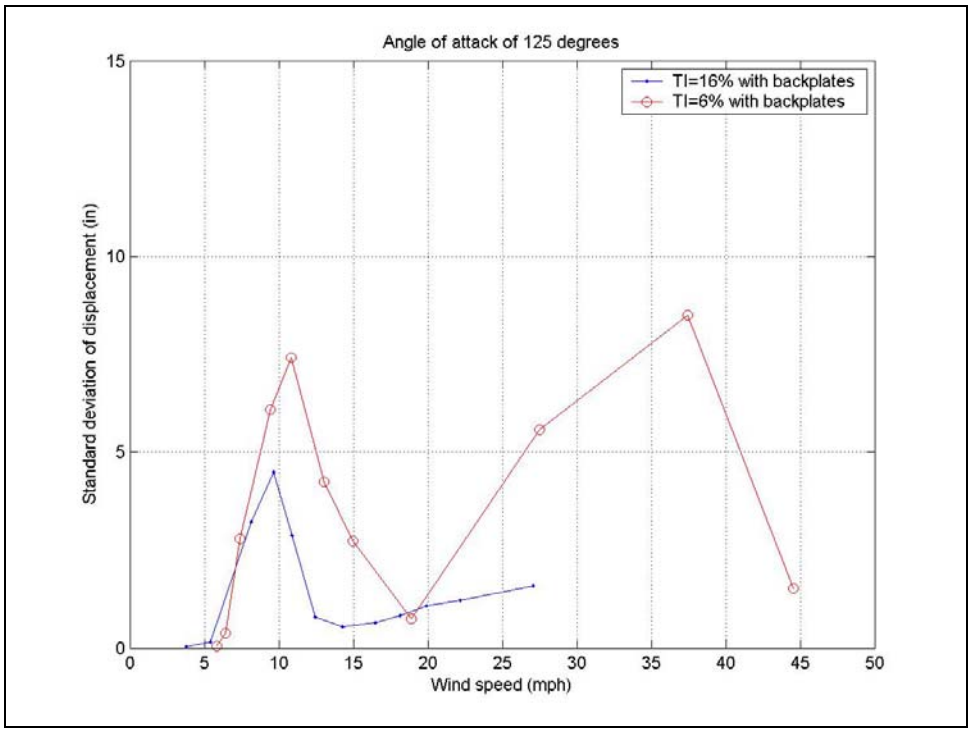

Figure 4.16 Wind Tunnel Results for Angle of Attack of 125 Degrees

For the case of the model with backplates under smooth flow, when the angle of attack was 135° there was a spike in the data followed by an increase in the amplitude of the vibration with an increase in wind speed, as shown in Figure 4.17. The increase in amplitude with the increase of speed suggests a galloping response.

Cases when the angle of attack was outside the range of 45° to 135° did not exhibit large amplitude vibrations (an example of this is shown in Figure 4.18). In many of these cases, data at wind speeds higher than those presented in the plots was not collected because horizontal (along-wind) vibrations became too large, preventing the laser displacement sensor from recording accurate measurements. Still, the models were

visually inspected under higher wind speeds and no significant vertical vibrations were observed.

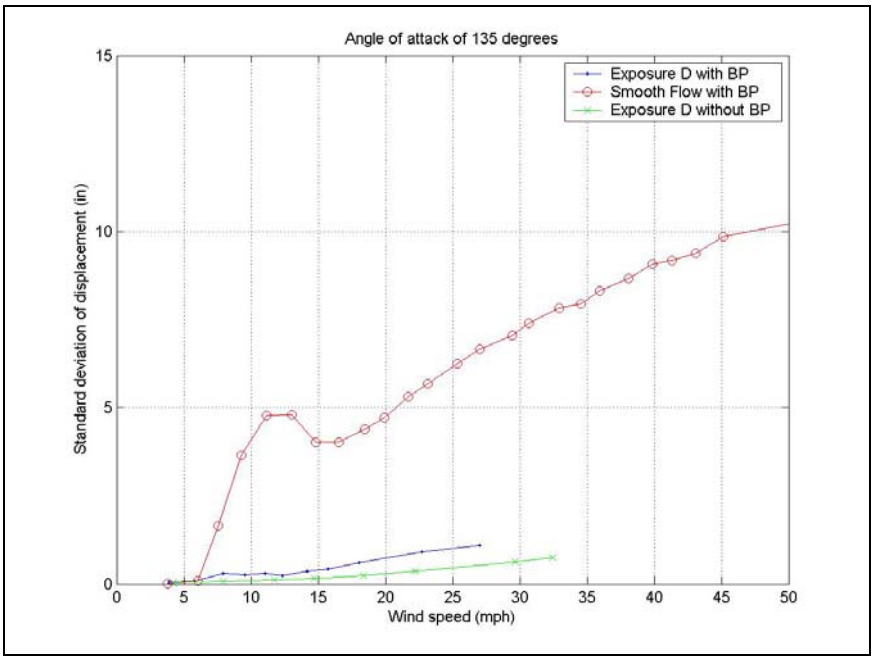

Figure 4.17 Wind Tunnel Results for Angle of Attack of 135 Degrees

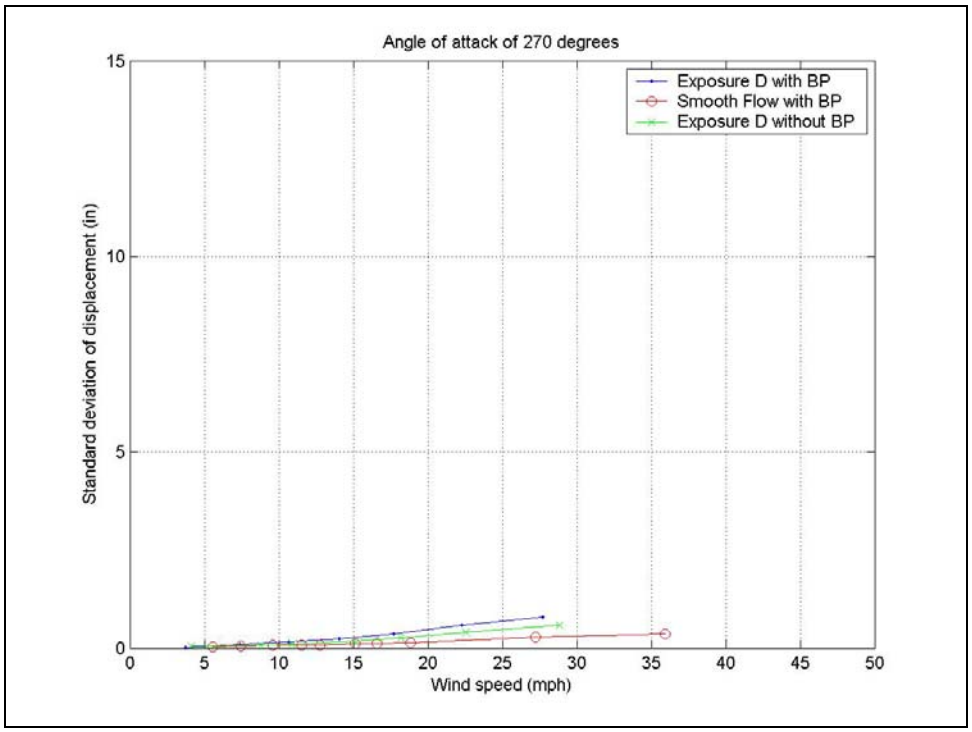

Figure 4.18 Wind Tunnel Results for Angle of Attack of 270 Degrees

Figure 4.19 was obtained by plotting the maximum value of the standard deviation of the displacement observed when the full-scale wind speed was in the range of 0-15 mph for each angle of attack. The case of smooth flow without backplates is not included in the figure because, as indicated in Table 4.6, data was only collected for this case at an angle of attack of 90°. Three observations can be made from Figure 4.19 are:

1. Structures with backplates have larger vibrations than those without them.
2. Vibrations with large amplitude occur when the angle of attack is between 45° and 135°.
3. In the critical range of angle of attack of 45° to 135°, the magnitude of vibrations decreases as turbulence intensity increases.

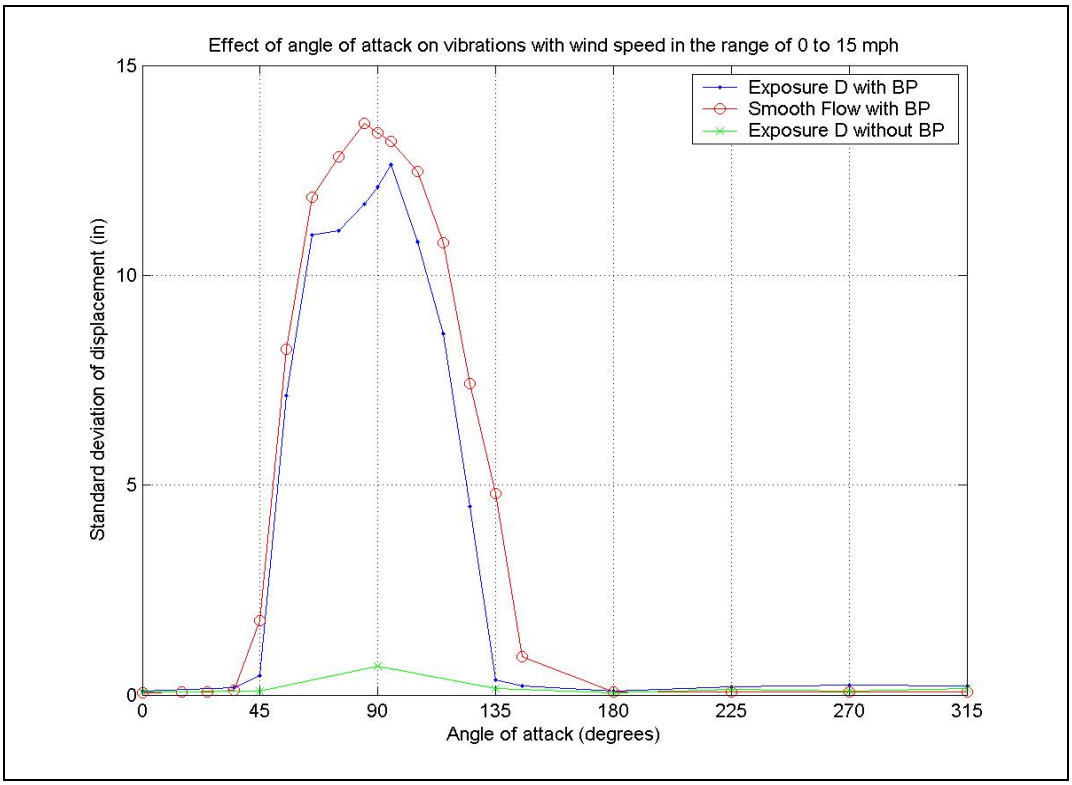

Figure 4.19 Maximum Amplitude of Vibration Observed for Full-Scale Wind Speed in the 0-15 MPH Range

Using the vertical fundamental frequency f_o and the cross-wind width B (23" and 14.5" in full-scale for the cases of with and without backplates, respectively), a reduced wind velocity of $U / f_o B$ can be calculated. In Figure 4.20, the reduced velocity is plotted against the standard deviation of the vertical displacement for the case of 90° angle of attack. Again, it can be seen in the figure that there is a very wide range of velocities for large response and this represents phenomena beyond classical Kármán vortex shedding.

The values plotted in Figure 4.20 were used to calculate the Strouhal number (St) for the different test cases. The number is computed as the inverse of the reduced velocity at which the maximum standard deviation of displacement occurs. The results are

presented in Table 4.9. The values obtained for *St* are close to the one of 0.12 computed for the full-scale data of March 29, 2005 (see Section 3.3.1).

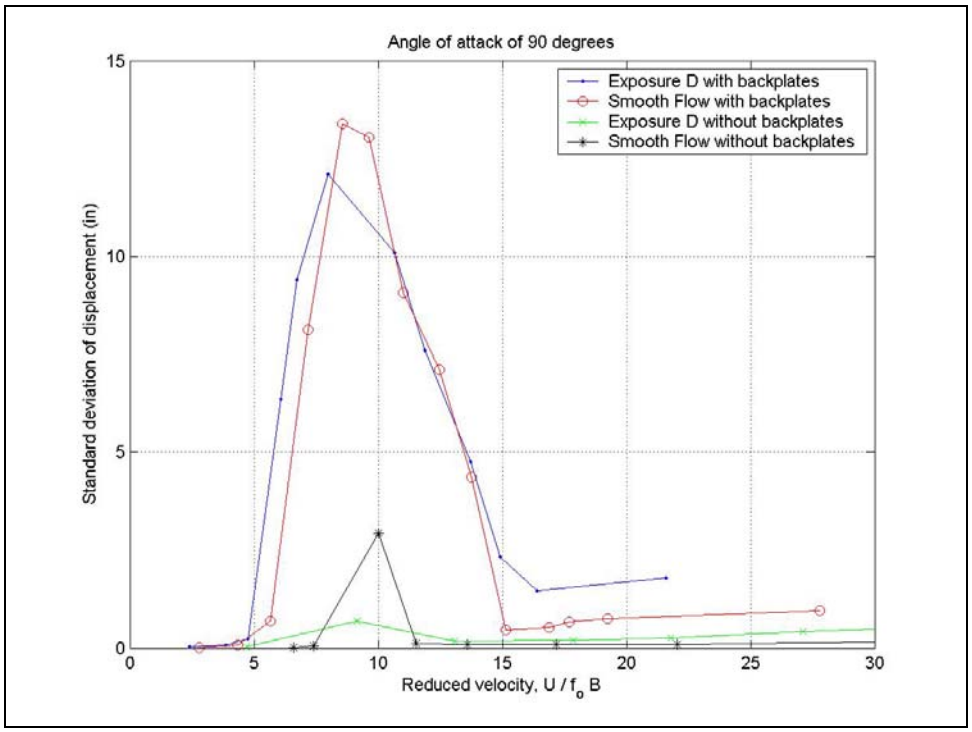

Figure 4.20 Effect of Reduced Velocity on Amplitudes of Vibrations

Table 4.9 Calculation of Strouhal Number (*St*)

Case	Maximum standard deviation of displacement (inches)	Reduced velocity at which maximum response occurs	*St*
Exposure D with backplates	12.10	8.00	0.125
Smooth flow with backplates	13.04	9.62	0.104
Exposure D without backplates	0.68	9.15	0.109
Smooth flow without backplates	2.93	10.03	0.100

4.5 Conclusions

Even though the UWO and TTU models have almost the same fundamental frequency, there were some unexpected differences in the results, mainly that the vibrations obtained for TTU at a 90° angle of attack were significantly larger than the ones obtained at UWO for similar turbulence intensity. Still, there was much agreement between the two sets of experiments. The results of testing an aeroelastic model in two different wind tunnels indicate that vortex shedding can induce large amplitude vibrations of mast arms. Most of the time, vortex shedding was identified as the cause of these vibrations because they occurred at certain speed ranges, a typical characteristic of the vortex-shedding-induced vibrations. That the speed ranges at which the high amplitude vibrations occurred were not very narrow (especially in the TTU experiments) suggests that the vibrations are vortex-induced by a more complex phenomenon that goes beyond classic Kármán vortex shedding.

Structures that have signals with backplates can undergo much larger vibrations than structures that have signals without backplates. Also, the amplitude of vibrations increases as the turbulence intensity decreases. For these vibrations to occur, the wind must be blowing towards the back of the signals, with an angle of attack in the range 45° to 135° and at wind speeds in the range of 5 to 15 mph.

The findings of these wind tunnel experiments agree with some of the findings initially reported by TTU researchers, mainly that large-amplitude vibrations of mast arms are more prone to occur when the signals have backplates and when the wind blows from the back of the signals. On the other hand, galloping, which is generally considered

to be the main cause of fatigue failures, was rarely found to occur in this study. A typical galloping behavior would be to increase the magnitude of vibrations with an increase of wind speed, yet this was only observed for an angle of attack of 135° under very smooth flow. This contradicts the notion that galloping is the main cause of fatigue failures of cantilever traffic signal structures. The experiments did reveal that there are complex interactions between angle of attack and response which is likely to be the case with vortices being shed from upwind backplates and interacting with downwind structures (visors) for particular oblique wind directions.

CHAPTER 5

ESTIMATION OF FATIGUE LIFE

5.1 Methodology for Predicting Fatigue Life

The following methodology is proposed to estimate the fatigue life of mast arm of cantilever traffic signal structures:

1. Using wind records for the location, establish a matrix that provides the probabilities that the wind will blow at certain speeds and directions. This matrix will be called the W-matrix and will have the following form:

$$[\mathrm{W}] = \begin{bmatrix} W_{1,1} & W_{1,2} & \cdots & W_{1,r} \\ W_{2,1} & W_{2,2} & \cdots & W_{2,r} \\ \vdots & \vdots & \ddots & \vdots \\ W_{p,1} & W_{p,2} & \cdots & W_{p,r} \end{bmatrix} \tag{5-1}$$

   where $W_{i,j}$ is the probability of the wind blowing in the ith direction range and in the jth speed range, and p and r are the number of discrete categories for direction and speed, respectively.

2. Calculate a matrix (called the n-matrix) that provides the number of vibrations that the arm will experience in an specific time period for the different wind speeds and directions as follows:

$$[\mathrm{n}] = f_o t\,[\mathrm{W}] = \begin{bmatrix} n_{1,1} & n_{1,2} & \cdots & n_{1,r} \\ n_{2,1} & n_{2,2} & \cdots & n_{2,r} \\ \vdots & \vdots & \ddots & \vdots \\ n_{p,1} & n_{p,2} & \cdots & n_{p,r} \end{bmatrix} \tag{5-2}$$

where $n_{i,j}$ is the number of vibrations at i^{th} wind direction range and j^{th} wind speed range, f_o is the vertical fundamental frequency of the mast arm, and t is the length of the time period.

3. Use results of wind tunnel experiments to produce a matrix that provides the standard deviation of the vertical vibrations for different wind speeds and direction. This matrix will be called the Y-matrix and it will have the following form:

$$[\mathrm{Y}] = \begin{bmatrix} Y_{1,1} & Y_{1,2} & \cdots & Y_{1,r} \\ Y_{2,1} & Y_{2,2} & \cdots & Y_{2,r} \\ \vdots & \vdots & \ddots & \vdots \\ Y_{p,1} & Y_{p,2} & \cdots & Y_{p,r} \end{bmatrix} \tag{5-3}$$

where $Y_{i,j}$ is the standard deviation of the vertical vibration for the wind blowing in the ith wind direction range and in the jth wind speed range as estimated for wind tunnel experiments.

4. Transform the Y-matrix to provide average peak-to-peak amplitudes of vertical vibrations for different wind speeds and directions. This matrix will be called the $\hat{\mathrm{Y}}$-matrix (not to be confused with the Y-matrix) and is calculated as follows:

$$[\hat{\mathrm{Y}}] = C\,R\,[\mathrm{Y}] = \begin{bmatrix} \hat{Y}_{1,1} & \hat{Y}_{1,2} & \cdots & \hat{Y}_{1,r} \\ \hat{Y}_{2,1} & \hat{Y}_{2,2} & \cdots & \hat{Y}_{2,r} \\ \vdots & \vdots & \ddots & \vdots \\ \hat{Y}_{p,1} & \hat{Y}_{p,2} & \cdots & \hat{Y}_{p,r} \end{bmatrix} \tag{5-4}$$

where $\hat{Y}_{i,j}$ is the peak-to-peak amplitude of the vertical vibration for the wind blowing in the ith wind direction range and in the jth wind speed range, R is a factor to change the standard deviation values to peak-to-peak values, and C is a calibration factor that can be used to adjust for errors in the wind tunnel data or to adjust the same data for the turbulence of the location.

5. Using structural dynamics principles, calculate the S-matrix which provides

the stress ranges experienced by the mast arm for different wind speeds and directions as follows:

$$[\mathrm{S}] = d\,[\hat{\mathrm{Y}}] = \begin{bmatrix} S_{1,1} & S_{1,2} & \cdots & S_{1,r} \\ S_{2,1} & S_{2,2} & \cdots & S_{2,r} \\ \vdots & \vdots & \ddots & \vdots \\ S_{p,1} & S_{p,2} & \cdots & S_{p,r} \end{bmatrix} \tag{5-5}$$

where $S_{i,j}$ is the stress range for the wind blowing in the ith wind direction range and in the jth wind speed range and d is a dynamic factor that changes peak-to-peak amplitudes to stress ranges.

6. Using an S-N curve, change the S-matrix to give the number of cycles to failure at constant stress range for the mast-to-pole connection for different wind speeds and directions. This matrix will be called the N-matrix (not to be confused with the n-matrix) and will have the following form:

$$[\mathrm{N}] = \begin{bmatrix} N_{1,1} & N_{1,2} & \cdots & N_{1,r} \\ N_{2,1} & N_{2,2} & \cdots & N_{2,r} \\ \vdots & \vdots & \ddots & \vdots \\ N_{p,1} & N_{p,2} & \cdots & N_{p,r} \end{bmatrix} \tag{5-6}$$

where $N_{i,j}$ is number of cycles at constant amplitude stress range $S_{i,j}$ that it would take for the arm to fail.

7. Using the n-matrix (calculated in step 2) and the N-matrix (calculated in step 5), apply Miner's Rule (discussed in Section 2.3) to estimate the fatigue damage sustained by the mast arm for time period t as follows:

$$D = \sum \frac{n_{i,j}}{N_{i,j}} \tag{5-7}$$

From this, the fatigue life of the mast arm can be estimated.

From hereon, these steps are referred to as the methodology. In the next section, an example demonstrates the application of this methodology. The reader may notice that

the methodology has certain similarities to the procedures proposed by South (1994) and Chen et al. (2001), as presented in Sections 2.3 and 2.3.4, respectively. Unlike South's and Chen's procedures, this new methodology takes into consideration the effects of wind direction and estimates damage due to vertical vibrations, not horizontal ones.

5.2 Example of Application of Methodology

In this section, the methodology is applied to a cantilever traffic signal structure located in the city of Lubbock with a 44-ft mast arm and with the geometry shown in Figure 3.3. The dimensions of the signal lights of this structure are shown in Figure 3.4. It will be considered that the signal light is pointing north, although results for other mast arm directions will be presented at the end of the section.

5.2.1 Step 1: The W-Matrix

The information presented in this section is based on research performed by Vega and Letchford (2006). They extended the two-parameter Weibull probability distribution function (pdf), which is often used to fit parent wind speed data, to account also for wind directionality. They described the pdf as follows:

$$f_U(U_j, \theta_i) = P(U > 0, \theta_i) \frac{k(\theta_i)}{c(\theta_i)} \left(\frac{U_j}{c(\theta_i)} \right)^{k(\theta_i)-1} \exp\left\{ -\left(\frac{U_j}{c(\theta_i)} \right)^{k(\theta_i)} \right\} \quad (5\text{-}8)$$

where:

U = wind speed

θ = wind direction

$P(U > 0, \theta_i)$ = probability that the wind is blowing from direction θ_i

$k(\theta_i)$ = Weibull shape parameter specialized as a function of wind direction θ_i

$c(\theta_i)$ = Weibull scale parameter specialized as a function of wind direction θ_i

The Weibull cumulative distribution function (cdf) is then given by:

$$F_U(U_j, \theta_i) = P(U > 0, \theta_i)\left[1 - \exp\left\{-\left(\frac{U_j}{c(\theta_i)}\right)^{k(\theta_i)}\right\}\right] \tag{5-9}$$

The researchers used six years of continuous 5-minute mean wind data collected by a meteorological station located at the Reese Technology Center in Lubbock, Texas. The 33-ft tower is located in flat open terrain and is part of the West Texas Mesonet, a network of 48 stations spread throughout West Texas. To measure wind speed and direction, the station uses an R. M. Young 05103 propeller-type anemometer at a sampling interval of 3 seconds. This anemometer has a starting threshold of 2.24 mph.

For the directional analysis, researchers classified the wind speed into intervals of 1 m/sec, while the wind direction was classified by dividing the wind rose into 16 sectors, each with an interval of 22.5^o, with 0° being the midpoint of the first sector, as shown in Figure 5.1. The sector “0,” also shown in the figure, was used to classify calms, which corresponds to wind speeds of less than 2.24 mph due to the anemometer’s threshold.

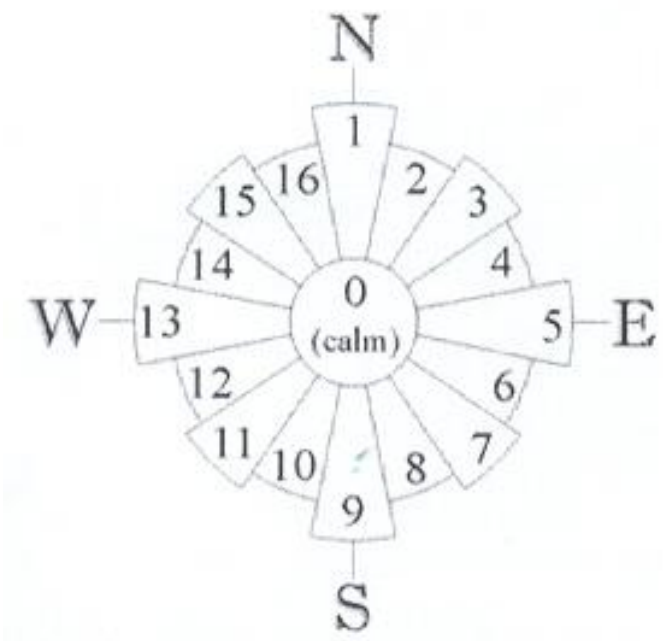

Figure 5.1 Wind Direction Classification (Vega and Letchford 2006)

The number of occurrences in each wind speed and direction classification was determined and stored in a matrix. The total number of calms was distributed proportionally to the number of occurrences in each direction using the first wind speed class (1-2 m/sec). Using this matrix, the three-dimensional histogram shown in Figure 5.2(a) was developed. The midpoint of wind speed and direction classification will be used for subsequent histograms and tables. In Figure 5.2(b) the Weibull distribution fitted to the data is presented. The probability that the wind is blowing from a certain direction and the Weibull parameters for that direction are shown in Table 5.1. Using the values of this table in the calculation of [W] determined that the value of *p* in Equation (5-1) would be taken as 16.

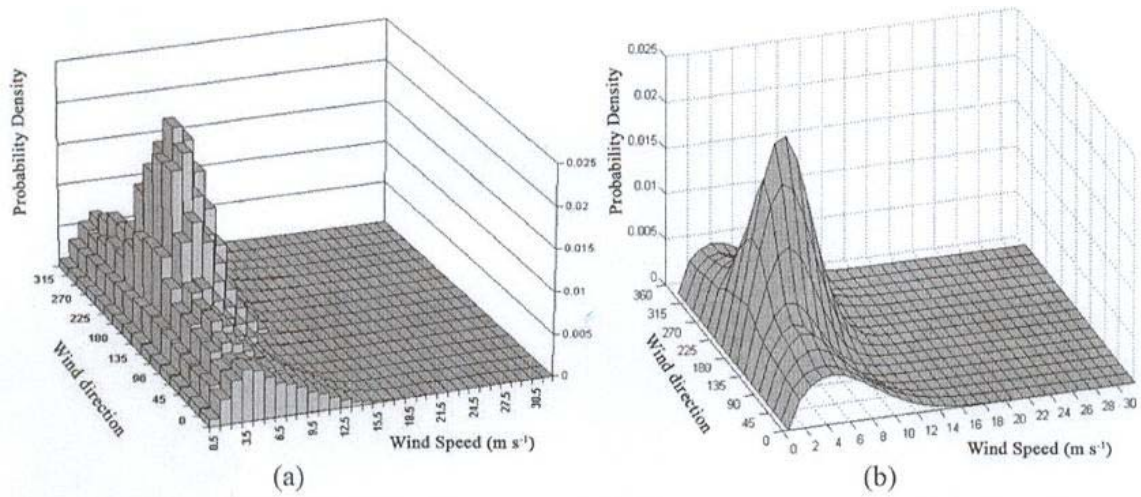

Figure 5.2 (a) Three-Dimensional Histogram and (B) Directional Analysis Using Weibull Distribution of Wind Data at Reese Station, Lubbock, Texas (Vega and Letchford 2006)

Table 5.1 Probability of Wind Blowing and Parameters for Weibull Distribution for Given Wind Direction (Vega and Letchford 2006)

Wind direction classification (degrees)	$P(U > 0, \theta_i)$	$k(\theta_i)$	$c(\theta_i)$ (mph)
0	0.043	1.875	14.784
22.5	0.042	1.843	14.411
45	0.043	1.992	13.134
67.5	0.043	2.076	12.046
90	0.039	2.099	11.105
112.5	0.047	2.179	11.468
135	0.076	2.369	12.309
157.5	0.113	2.453	13.093
180	0.141	2.579	13.939
202.5	0.111	2.519	13.338
225	0.078	2.311	12.823
247.5	0.057	2.007	13.794
270	0.048	1.839	13.876
292.5	0.038	1.835	12.548
315	0.029	1.907	11.209
337.5	0.035	1.827	12.824

Note: The probability of the wind not blowing can be calculated as: $P(U = 0) = 1 - \sum_i P(U > 0, \theta_i)$

The elements of the W-matrix can then be calculated with the following formula:

$$W_{i,j} = F_U(U_j, \theta_i) - F_U(U_{j-1}, \theta_i) \tag{5-10}$$

Table 5.2 shows part of the results obtained using Equation (5-10). Wind speed ranges of 2 mph were chosen because Vega and Letchford (2006) used ranges of 1 m/sec = 2.24 mph ≈ 2 mph. Columns of wind speed classifications higher than 19 mph are not included in the table due to space restrictions, and the probability values are shown rounded. All columns with unrounded probability values will be taken into consideration for all subsequent calculations. The highest wind speed range taken into calculations has a midpoint of 63 mph (i.e., r = 32). A complete version of Table 5.2 constitutes the W-matrix of wind probabilities.

Table 5.2 Portion of the W-Matrix

Wind direction classification (degrees)	Wind speed classification (mph)									
	1	3	5	7	9	11	13	15	17	19
0	0.10%	0.25%	0.37%	0.44%	0.47%	0.47%	0.44%	0.39%	0.33%	0.27%
22.5	0.11%	0.27%	0.38%	0.45%	0.48%	0.47%	0.43%	0.38%	0.32%	0.26%
45	0.10%	0.28%	0.43%	0.52%	0.55%	0.54%	0.48%	0.40%	0.31%	0.23%
67.5	0.10%	0.31%	0.48%	0.59%	0.62%	0.58%	0.49%	0.39%	0.28%	0.18%
90	0.11%	0.33%	0.51%	0.61%	0.62%	0.55%	0.44%	0.32%	0.21%	0.12%
112.5	0.10%	0.35%	0.57%	0.71%	0.75%	0.69%	0.56%	0.41%	0.27%	0.16%
135	0.10%	0.41%	0.75%	1.03%	1.17%	1.16%	1.00%	0.77%	0.53%	0.33%
157.5	0.11%	0.49%	0.95%	1.37%	1.64%	1.71%	1.57%	1.28%	0.93%	0.61%
180	0.09%	0.46%	0.96%	1.48%	1.89%	2.08%	2.02%	1.75%	1.35%	0.93%
202.5	0.09%	0.43%	0.87%	1.29%	1.58%	1.68%	1.57%	1.30%	0.96%	0.63%
225	0.11%	0.41%	0.73%	0.99%	1.14%	1.14%	1.02%	0.82%	0.60%	0.40%
247.5	0.12%	0.34%	0.52%	0.65%	0.71%	0.70%	0.64%	0.55%	0.45%	0.34%
270	0.13%	0.33%	0.46%	0.54%	0.56%	0.54%	0.49%	0.43%	0.35%	0.28%
292.5	0.13%	0.31%	0.43%	0.48%	0.49%	0.45%	0.39%	0.32%	0.25%	0.19%
315	0.11%	0.28%	0.38%	0.43%	0.42%	0.37%	0.30%	0.23%	0.16%	0.10%
337.5	0.11%	0.27%	0.38%	0.43%	0.43%	0.41%	0.36%	0.30%	0.23%	0.18%

5.2.2 Step 2: The N-Matrix

To estimate the number of vibrations that a mast arm would sustain under each wind speed and direction, it is assumed that the arm is constantly vibrating at its

fundamental frequency. It might appear excessive to estimate so many vertical vibrations occurring for a time period, but it will become evident later that many of these vibrations will have no effect in determining the damage to the structure. For the structure with the 44-ft mast arm, the fundamental frequency in the vertical direction is f_o = 0.98 Hz (as shown in Table 3.3). The time length will be taken as 1 day (i.e., t = 86,400 sec), therefore the calculation will be the number of vibrations per wind speed and direction in an average day. Applying Equation (5-2), the n-matrix of number of vibrations is obtained. A portion of the matrix of number of vibrations is presented in Table 5.3.

Table 5.3 Portion of the N-Matrix

Wind direction classification (degrees)	Wind speed classification (mph)									
	1	3	5	7	9	11	13	15	17	19
0	84	215	311	372	400	399	374	333	283	231
22.5	93	229	323	380	402	395	366	322	270	218
45	84	239	361	439	468	454	406	339	266	197
67.5	86	263	409	500	525	492	418	326	234	156
90	90	279	432	516	523	466	372	268	176	105
112.5	88	297	484	603	632	581	475	348	231	138
135	86	346	637	873	994	980	851	655	450	275
157.5	95	414	807	1162	1393	1447	1327	1083	789	514
180	80	389	817	1255	1597	1760	1711	1480	1141	784
202.5	78	363	733	1089	1339	1423	1330	1103	813	533
225	90	345	619	840	961	965	864	697	509	337
247.5	99	288	443	548	597	593	545	469	380	291
270	114	278	390	454	475	460	419	362	299	236
292.5	109	264	362	410	414	385	334	273	212	157
315	91	233	325	365	357	316	256	193	135	89
337.5	97	232	319	362	368	345	302	251	198	149

5.2.3 Step 3: The Y-Matrix

The Y-matrix was assembled using the results of the TTU wind tunnel experiments with the smooth flow case (as discussed in Section 4.4). The values of

smooth flow were used because they give higher values of standard deviation of vertical vibration (i.e., is more conservative to use these values). It can be noted that for the case of the traffic signal structure pointing north being analyzed here, the angle of attack definition used for full-scale and wind tunnel experiments (as shown in Figure 3.10) has the same orientation used for wind direction in the matrix of wind probability (i.e., angle of attack = wind direction).For the most part, linear interpolation and extrapolation were used to calculate values at the midpoint of the wind speed and direction classifications as needed. For example, for the wind classification with a midpoint of 90o, the wind tunnel data for an angle of attack of 90o was used, as shown in Figure 5.3

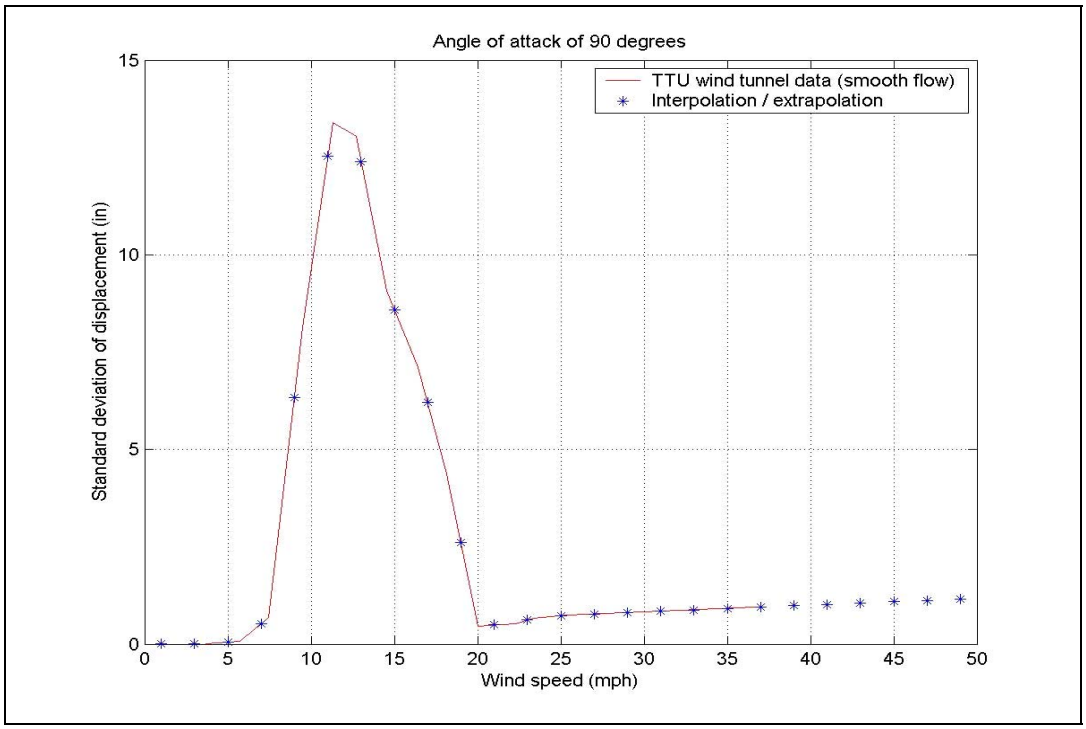

Figure 5.3 Interpolation and Extrapolation for Angle of Attack of 90°

For certain cases, two conservative measures were taken. The first measure was that the amplitude value recorded at the lowest wind speed in the wind tunnel was used for wind speed ranges lower than the wind speeds collected in the wind tunnel. For example, if an amplitude of 0.5 inches was recorded at 5.3 mph in the wind tunnel and this was the lowest wind speed recorded for the angle of attack, then an amplitude of 0.5 was used in the matrix for wind speed classes 1, 3, and 5 mph. The second measure was that the amplitude value recorded at the highest wind speed in the wind tunnel was used for wind speed ranges higher than the wind speeds collected in the wind tunnel only if the wind tunnel data ended at negative slope, otherwise linear extrapolation was used (as shown in Figure 5.4).

Notice how these pseudo extrapolations obtained with the two measures form horizontal lines before and after the wind tunnel data.

In cases where the midpoint of the wind direction classification did not match any of the data collected in the wind tunnel, linear interpolation was performed using data from adjacent angles. For example, the amplitude of vibration values for the wind direction classification of 22.5^{o} were obtained by interpolating the data collected in the wind tunnel for angles of attack of 15° and 25°.

A portion of the resulting Y-matrix is presented as Table 5.4.

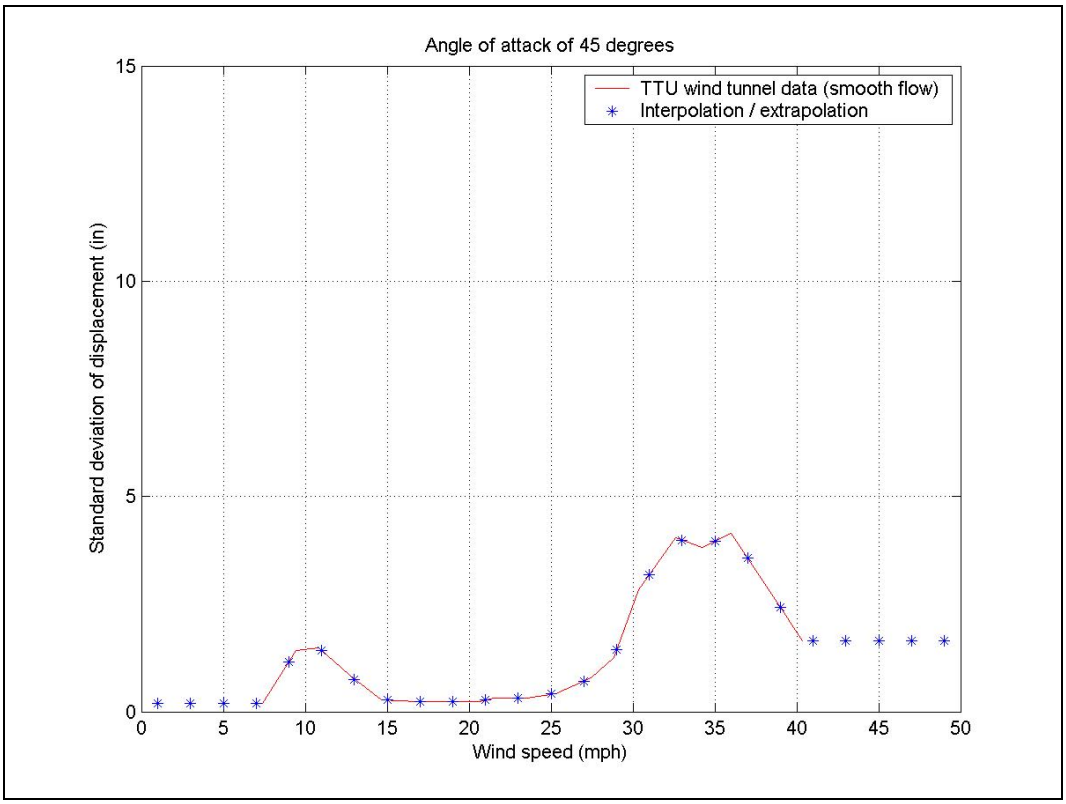

Figure 5.4 Interpolation and Extrapolation for Angle of Attack of 45°

Table 5.4. Portion of the Y-Matrix (values in inches)

Wind direction classification (degrees)	Wind speed classification (mph)									
	1	3	5	7	9	11	13	15	17	19
0	0.04	0.04	0.04	0.04	0.04	0.05	0.05	0.05	0.06	0.07
22.5	0.04	0.04	0.04	0.05	0.05	0.06	0.07	0.07	0.10	0.12
45	0.20	0.20	0.20	0.20	1.16	1.43	0.76	0.27	0.23	0.23
67.5	0.04	0.04	0.04	1.80	7.84	11.37	11.60	9.93	7.76	4.83
90	0.02	0.02	0.06	0.53	6.33	12.53	12.39	8.59	6.22	2.60
112.5	0.03	0.03	0.31	2.07	6.91	10.60	8.79	4.03	1.24	0.40
135	0.01	0.01	0.06	1.09	3.35	4.70	4.81	4.02	4.12	4.51
157.5	0.05	0.05	0.04	0.04	0.12	0.46	0.35	0.14	0.12	0.12
180	0.04	0.04	0.03	0.02	0.04	0.06	0.07	0.06	0.06	0.06
202.5	0.04	0.04	0.04	0.03	0.04	0.06	0.07	0.07	0.08	0.09
225	0.04	0.04	0.04	0.05	0.05	0.06	0.07	0.07	0.10	0.12
247.5	0.04	0.04	0.04	0.05	0.05	0.06	0.07	0.09	0.11	0.13
270	0.03	0.03	0.03	0.05	0.06	0.07	0.08	0.11	0.12	0.14
292.5	0.04	0.04	0.04	0.06	0.06	0.07	0.08	0.10	0.12	0.13
315	0.05	0.05	0.05	0.08	0.06	0.06	0.07	0.09	0.11	0.12
337.5	0.04	0.04	0.04	0.06	0.05	0.06	0.06	0.07	0.08	0.10

5.2.4 Step 4: The Ŷ-matrix

To obtain the Ŷ-matrix, the values of *C* and *R* need to be determined. As explained before, *C* is a calibration factor to adjust for errors in the wind tunnel data or to adjust for the turbulence intensity of the location. For this example it will be assumed that the TTU wind tunnel results for smooth flow are acceptable to be applied to the City of Lubbock, therefore *C* = 1. (The *C* factor is further discussed in Section 5.2.7.) *R* is a factor to change the standard deviation values of the Y-matrix to peak-to-peak amplitudes. Following is an explanation of how the value of *R* was determined.

For sinusoidal motion, the amplitude A can be calculated as:

$$A = \sqrt{2}\sigma_{\text{rms}} \tag{5-11}$$

where σ_{rms} is the root-mean-square. For a function where the mean is zero, the root-mean-square is equal to the standard deviation. Therefore:

$$A = \sqrt{2}\sigma_{\text{n}} \tag{5-12}$$

where σ_{n} is the standard deviation. It has been observed that the vibration of mast arm resembles a sinusoidal function, so the peak-to-peak amplitude of vibration Ŷ can be estimated as:

$$\hat{Y} = 2A = 2\sqrt{2}\sigma_{\text{n}} \tag{5-13}$$

Figure 5.5 shows one case of vibration data collected in the TTU wind tunnel with the laser transducer (values are in model scale). Also shown are the amplitudes for a sinusoidal function, namely $\sqrt{2}$ times the standard deviation of the laser data. These two amplitudes enveloped the data well. In not all cases of wind speed and angle of attack did the sinusoidal amplitude match as closely as the case shown in Figure 5.5, but it appears

that $2\sqrt{2}$ times the standard deviation was a reasonable estimate of the peak-to-peak amplitude since by and large the wind tunnel responses are due to vortex shedding locking-in to the fundamental frequency of the structure. Therefore, it will be assumed that $R = 2\sqrt{2}$.

With C =1 and R = $2\sqrt{2}$, Equation (5-4) is used to calculate the $\hat{Y}$-matrix of peak-to-peak amplitudes. A portion of the $\hat{Y}$-matrix is shown in Table 5.5.

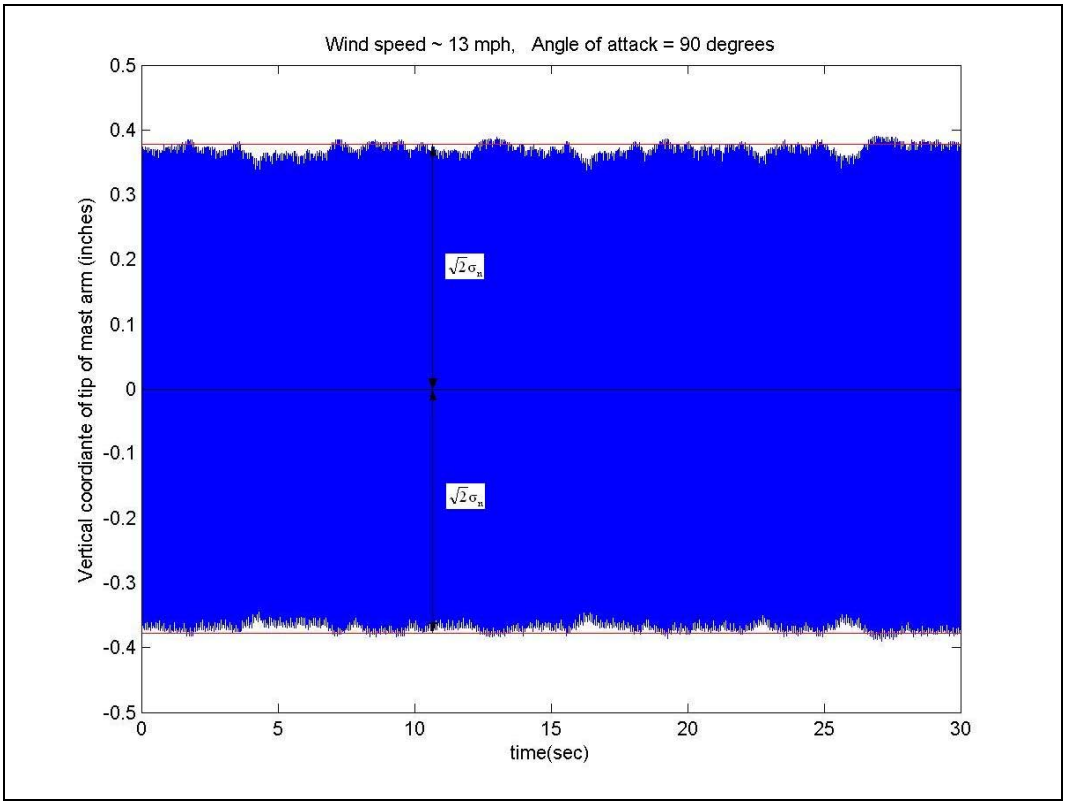

Figure 5.5 Sample Data Collected in TTU Wind Tunnel for Smooth Flow

Table 5.5 Portion of the Ŷ-matrix (values in inches)

Wind direction classification (degrees)	Wind speed classification (mph)									
	1	3	5	7	9	11	13	15	17	19
0	0.11	0.11	0.11	0.11	0.11	0.15	0.15	0.15	0.17	0.20
22.5	0.12	0.12	0.12	0.13	0.14	0.17	0.19	0.21	0.27	0.34
45	0.57	0.57	0.57	0.57	3.28	4.05	2.14	0.76	0.64	0.65
67.5	0.11	0.11	0.11	5.09	22.18	32.16	32.82	28.08	21.93	13.65
90	0.04	0.04	0.16	1.49	17.91	35.45	35.04	24.29	17.58	7.35
112.5	0.09	0.09	0.89	5.85	19.54	29.99	24.87	11.39	3.50	1.13
135	0.04	0.04	0.16	3.09	9.48	13.29	13.59	11.37	11.64	12.77
157.5	0.13	0.13	0.11	0.12	0.33	1.30	0.98	0.39	0.34	0.35
180	0.12	0.12	0.08	0.06	0.10	0.17	0.19	0.17	0.17	0.18
202.5	0.12	0.12	0.10	0.10	0.12	0.17	0.19	0.19	0.22	0.26
225	0.12	0.12	0.12	0.13	0.14	0.17	0.19	0.21	0.27	0.34
247.5	0.10	0.10	0.10	0.13	0.15	0.18	0.21	0.26	0.31	0.38
270	0.09	0.09	0.09	0.13	0.17	0.19	0.24	0.32	0.35	0.41
292.5	0.11	0.11	0.11	0.17	0.17	0.18	0.22	0.28	0.33	0.38
315	0.13	0.13	0.13	0.21	0.18	0.18	0.21	0.24	0.30	0.35
337.5	0.12	0.12	0.12	0.16	0.14	0.16	0.18	0.20	0.24	0.27

5.2.5 Step 5: The S-Matrix

It should be noted that the S-matrix is a matrix of stress ranges, not of total stresses. Since what is desired are the peak-to-peak amplitudes of stresses, the gravitational loads do not need to be considered since they are constant. To determine the

S-matrix, the dynamic factor *d* that changes peak-to-peak amplitudes to stress ranges needs to be calculated.

A method to determine the stresses caused by displacements in a beam is to estimate an equivalent load that would produce the same displacements. Having an equivalent load allows for the calculation of reactions and stresses. To determine the equivalent load, the cantilever beam shown in Figure 5.6 was taken into consideration. If it is assumed that only the first mode shape of the beam is significant, the load p(x, t) can be calculated as follows (Chen 2006):

$$p(x, t) = m(x)\, \omega_1^2\, \phi_1(x)\, q(t) \tag{5-14}$$

where:

x = distance from fixed end

t = time

m(x) = mass per unit length

ω_1 = first natural frequency in radians per second

$\phi_1(x)$ = 1st mode shape

q(t) = tip displacement

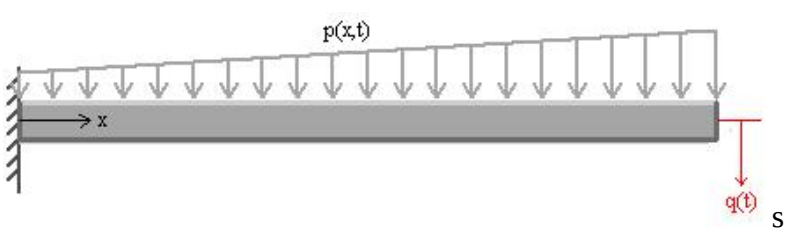

s

Figure 5.6 Cantilever Beam Subjected to Load p(x,t) and Having Tip Displacement q(t).

Therefore, to determine the equivalent load, the mass per unit length, the first natural frequency, and the first mode shape need to be determined. For the 44-ft mast arm being analyzed here, the vertical fundamental frequency has already been determined on the full-scale prototype as f_o = 0.98 Hz (see Section 3.2.5), thus $\omega_1 = 2\,\pi\, f_o$ = 6.157 rad/sec.

Making the following definition:

$$p_o(x) = m(x)\,\omega_1^2\,\phi_1(x) \tag{5-15}$$

then Equation (5-14) becomes:

$$p(x, t) = p_o(x)\,q(t) \tag{5-16}$$

To determine the mode shape, a finite element model of the 44-ft mast arm was made using a demo version of the commercial software RISA-3D version 6 by RISA Technologies. Initially, the mast arm was modeled as a cantilever beam made of 44 elements, each member having a length of 1 ft and the same thickness as the prototype (0.25 inches). The diameter of each member was determined by calculating the average diameter (d_{avg}) of the segment it represents in the prototype, as shown in the example of Figure 5.7. Using RISA-3D it was determined that the first natural frequency was 1.425 Hz, which has an error of 45% with respect to the value measured directly from the prototype. Probably the large difference is due to not including the pole in the finite element model.

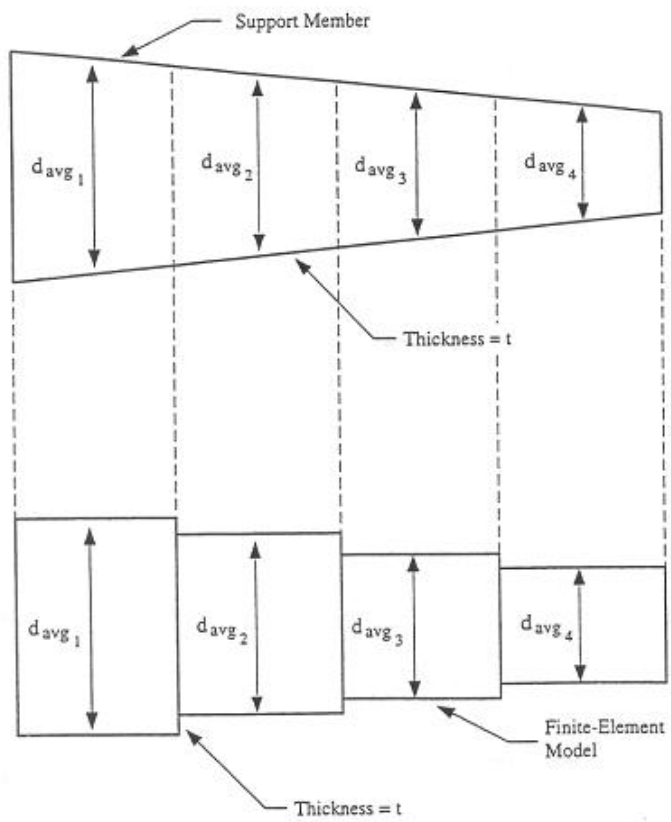

Figure 5.7 Finite-Element Modeling of Tapered Element
(Kaczinski, Dexter, and Van Dien 1998)

The model was recalculated with a pole, as shown in Figure 5.8. The pole was modeled with one member having the average diameter of the prototype (13.25 in) and the length from the top of the foundation to the midpoint of the base of the mast arm (18.108 ft). A mass of 0.001 kips-sec^2/ft was placed on each node 20 and node 32 to represent each of the 3-signal heads, while a mass of 0.002 kips-sec^2/ft was placed at node 45 to represent the 5-signal head. (The weights used to calculate these masses are shown in Figure 3.4.) This time, the first natural frequency determined using RISA-3D

came out as 1.174 Hz, which is closer to that measured directly from the prototype, although still with an error of about 20%.

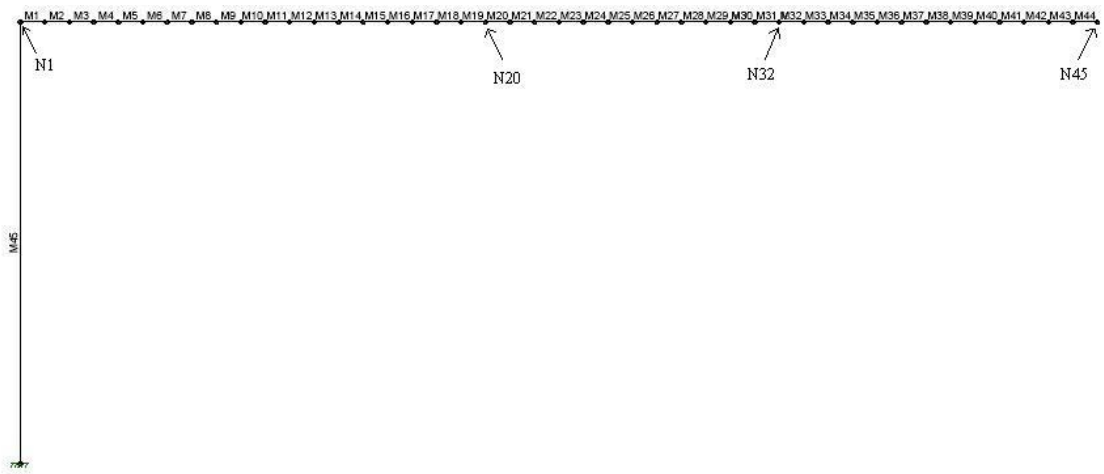

Figure 5.8 Finite Element Model (M = Member, N = Node)

The first mode shape was determined using RISA-3D and is shown in Table 5.6. Also shown in Table 5.6 is the mass per unit length determined by the following formula:

$$m(x) = (\pi \gamma / 4g) \{[OD(x)]^2 - [OD(x) - 2t]^2\} \qquad (5\text{-}17)$$

where:

x = longitudinal coordinate of the node, zero at the arm-to-post connection

γ = unit weight of steel = 0.283 lb/in^3

g = acceleration due to gravity = 386.4 in/sec^2

OD(x) = outside diameter of mast arm = 11.4 - 0.01188x (for OD and x in inches)

t = wall thickness of the mast arm = 0.25 in

Also shown in Table 5.6 is the product $p_o(x)$, calculated using Equation (5-15). In this calculation, the fundamental frequency obtained directly from the prototype (0.98 Hz) was used, not the one obtained using RISA-3D.

Table 5.6 Results of Dynamic Analysis

Node	x (in)	m(x) [(lb-sec^2/in)/in]	$\phi_1(x)$	$p_o(x)$ [(lb/in)/in]
1	0	0.0064	0.00	0.0000
2	12	0.0063	0.01	0.0017
3	24	0.0062	0.01	0.0035
4	36	0.0062	0.02	0.0054
5	48	0.0061	0.03	0.0075
6	60	0.0060	0.04	0.0097
7	72	0.0059	0.05	0.0120
8	84	0.0058	0.07	0.0144
9	96	0.0058	0.08	0.0169
10	108	0.0057	0.09	0.0196
11	120	0.0056	0.11	0.0223
12	132	0.0055	0.12	0.0251
13	144	0.0054	0.14	0.0280
14	156	0.0053	0.15	0.0309
15	168	0.0053	0.17	0.0339
16	180	0.0052	0.19	0.0369
17	192	0.0051	0.21	0.0400
18	204	0.0050	0.23	0.0431
19	216	0.0049	0.25	0.0463
20	228	0.0049	0.27	0.0495
21	240	0.0048	0.29	0.0526
22	252	0.0047	0.31	0.0558
23	264	0.0046	0.34	0.0589
24	276	0.0045	0.36	0.0621
25	288	0.0044	0.39	0.0652
26	300	0.0044	0.41	0.0682
27	312	0.0043	0.44	0.0712
28	324	0.0042	0.47	0.0742
29	336	0.0041	0.49	0.0771
30	348	0.0040	0.52	0.0799
31	360	0.0040	0.55	0.0826
32	372	0.0039	0.58	0.0852
33	384	0.0038	0.61	0.0877
34	396	0.0037	0.64	0.0901
35	408	0.0036	0.67	0.0924
36	420	0.0035	0.70	0.0946
37	432	0.0035	0.74	0.0966
38	444	0.0034	0.77	0.0984
39	456	0.0033	0.80	0.1001
40	468	0.0032	0.83	0.1016
41	480	0.0031	0.87	0.1029
42	492	0.0031	0.90	0.1041
43	504	0.0030	0.93	0.1050
44	516	0.0029	0.97	0.1058
45	528	0.0028	1.00	0.1064

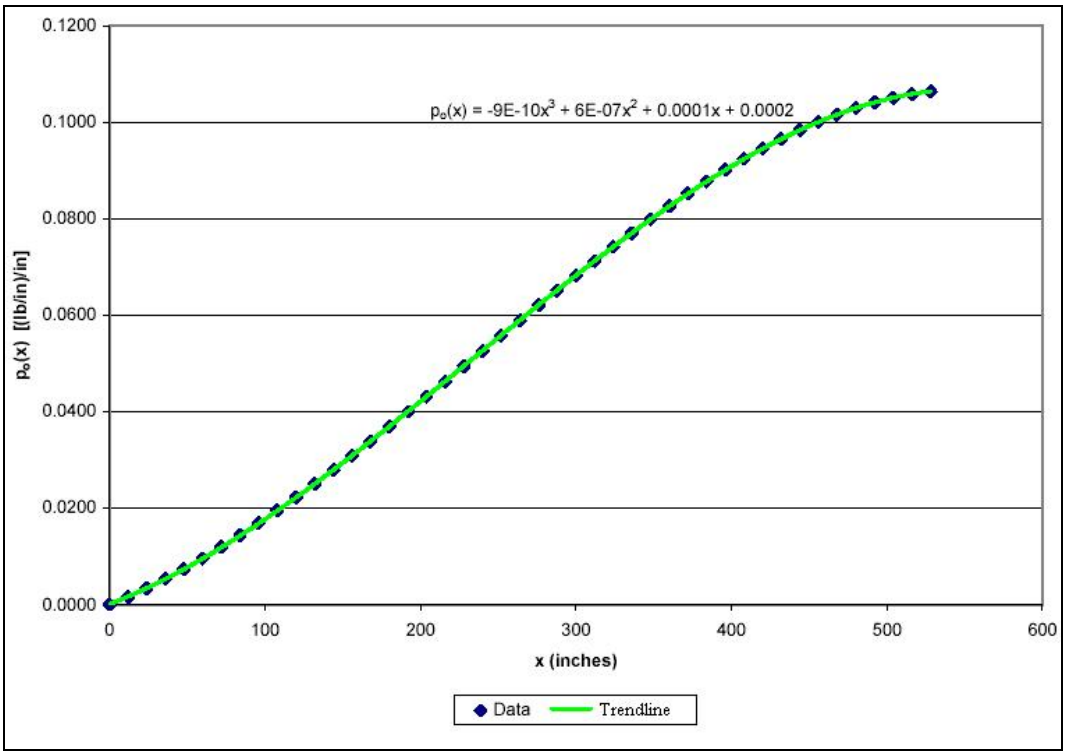

Figure 5.9. x vs. $p_o(x)$

Using Microsoft Excel, a plot of x vs. $p_o(x)$ was obtained, as well as a cubic equation of a trendline that adjusted very well to the data, as shown in Figure 5.9. This equation will be used in further calculations.

Figure 5.10 shows the loads acting on the mast arm. In this figure, $P_1(t)$, $P_2(t)$, and $P_3(t)$ represent the dynamic loads caused on the arm by the 3 signals while V and M are the shear and moment reactions, respectively, at the base of the arm. To calculate the loads due to the signals, the following formula is used:

$$P_i(t) = m_i\, \omega_1^2\, \phi_1(x_i)\, q(t) \qquad (5\text{-}18)$$

where m_i is the mass of the signal light and is $\phi_1(x_i)$ is the value of the mode shape at the x_i location.

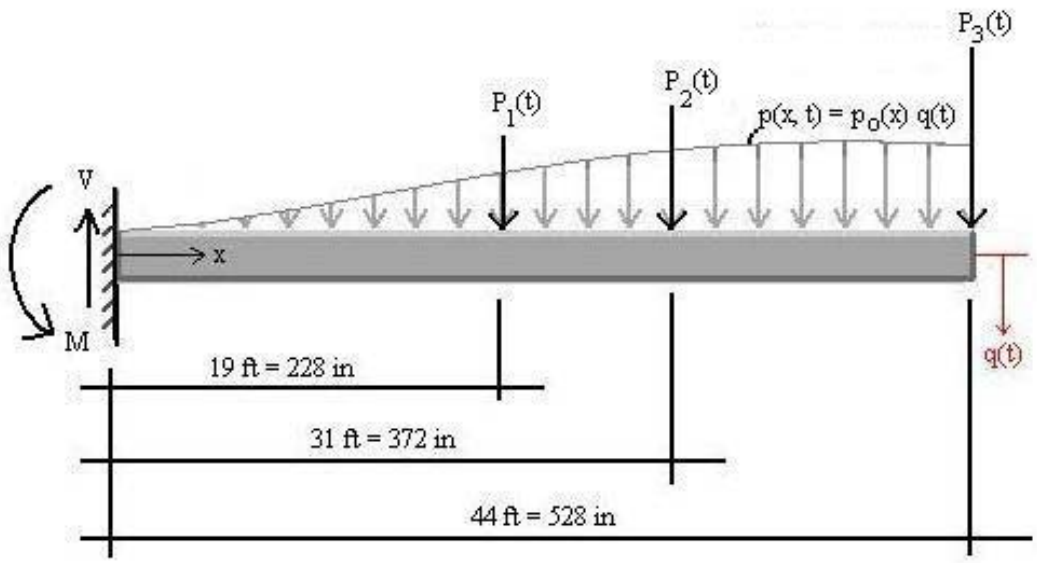

Figure 5.10 Loads Acting on Mast Arm

Adding moments about the fixed support:

$$M = 228 \cdot P_1(t) + 372 \cdot P_2(t) + 528 \cdot P_3(t) + \int_0^{528} x\, p(x,t)dx \tag{5-19}$$

Substituting Equation (5-16), Equation (5-18) and the $p_o(x)$ equation presented in Figure 5.9:

$$M = 13{,}820\ q(t) \tag{5-20}$$

where q(t) must be entered in inches and M will be given in pounds-inches.

To determine the maximum bending stress σ_{max} of the mast arm at the arm-to-post connection, the following well-known formula is used:

$$\sigma_{max} = \frac{Mc}{I} \tag{5-21}$$

where I is the moment of inertia of the cross-section and c is the perpendicular distance from the neutral axis of the cross-section to the farthest point away from the axis. Using

the dimensions of the mast arm at the arm-to-post connection as given by and substituting Equation (5-20):

$$\sigma_{max} = 578.55\ q(t) \tag{5-22}$$

where q(t) must be entered in inches and σ_{max} will be given in pounds per square inch.

Substituting values of displacement in Equation (5-22) will not give the total stress on the structure, but it will give the change of stress in the structure. By substituting values of peak-to-peak vibration amplitudes $\hat{Y}$, the equation will give the stress ranges S:

$$S = 578.55\ \hat{Y} \tag{5-23}$$

where $\hat{Y}$ must be entered in inches and S will be given in pounds per square inch.

The stress range S is the magnitude of the stress peak-to-peak amplitude. Therefore, d = 578.55 psi/in. Using Equation (5-5) the S-matrix is calculated. A portion of the S-matrix is presented as Table 5.7.

Table 5.7 Portion of the S-Matrix (values in psi)

Wind direction classification (degrees)	Wind speed classification (mph)									
	1	3	5	7	9	11	13	15	17	19
0	62	62	62	62	62	85	89	90	100	116
22.5	67	67	67	77	79	100	108	122	157	197
45	332	332	332	332	1899	2343	1236	439	373	374
67.5	61	61	61	2944	12830	18609	18989	16248	12690	7899
90	26	26	93	865	10365	20509	20275	14053	10171	4255
112.5	51	51	514	3387	11307	17351	14390	6591	2024	653
135	21	21	94	1785	5487	7688	7863	6576	6734	7386
157.5	74	74	66	71	194	751	566	226	197	202
180	72	72	48	34	60	99	110	100	100	106
202.5	69	69	57	55	70	100	109	111	128	152
225	67	67	67	77	79	100	108	122	157	197
247.5	59	59	59	77	89	105	122	153	181	217
270	50	50	50	77	99	110	137	183	205	237
292.5	63	63	63	100	100	106	129	162	190	219
315	76	76	76	123	102	103	121	141	176	201
337.5	69	69	69	93	82	94	105	115	138	159

5.2.6 Step 6: The N-Matrix

The fatigue life of materials is often represented by plots of stress ranges (*S*) versus numbers of cycles to failure (*N*). These plots are typically known as S-N curves, and they are obtained by testing several material specimens. In a particular test, a

specimen “is subjected to alternating stresses that vary between fixed limits of maximum and minimum stress” (Brockenbrough and Jonhston 1981), counting the number of cycles to failure. Each specimen is tested under a different stress range. Figure 5.11 shows the typical shape of an S-N curve (usually the axes are presented in logarithmic scale). The horizontal part of the curve represents the constant amplitude fatigue level (CAFL), as discussed in Section 2.3.3.XX

The AASHTO Specifications (2001) classify different steel details into stress categories. In Figure 5.12, which shows a typical mast-arm-to-column connection used in cantilever traffic signal structures, the fillet weld identified as “Detail 16” is classified as stress category E'. The connection shown in the figure is very similar to the one used in the structure being analyzed in this chapter.

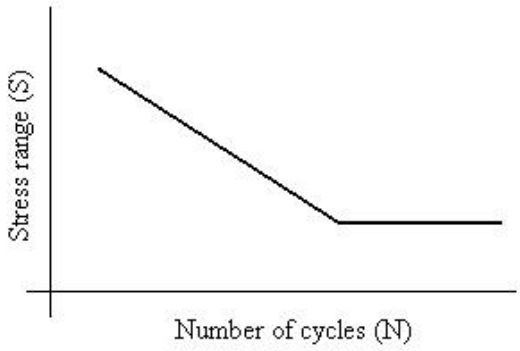

Figure 5.11 Typical S-N Curve

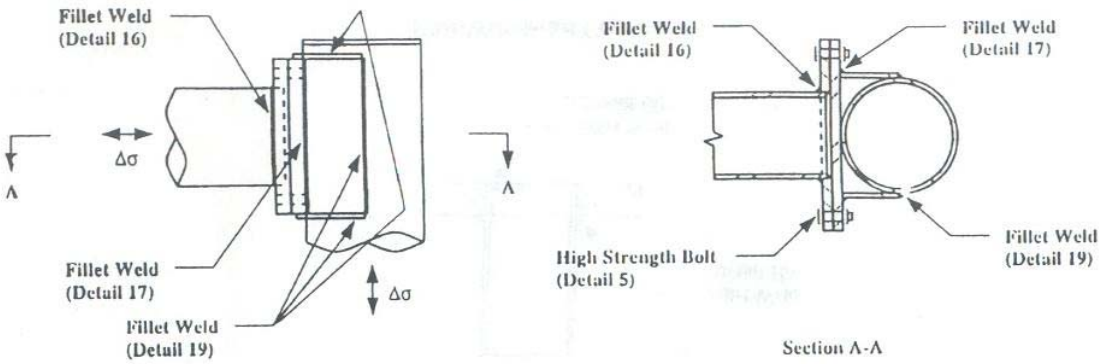

Figure 5.12 Fillet-Welded Mast-Arm-To-Column Connection (AASHTO 2001)

Figure 5.13 shows the S-N curves for the seven primary stress categories used by AASHTO, as well as the American Welding Society (AWS), the American Institute of Steel Construction (AISC), and the American Railway Engineers Association (AREA). In the figure the dotted lines represent the CAFL. To obtain the equation of the S-N curve for stress category E', the “redundant load path structures” values for the category presented in Table 5.8 are used. This table was copied from the AASHTO *Standard specifications for highway bridges* (1996). Even though cantilevers certainly do not have redundant load paths, the “redundant” values were selected because the CAFL (or threshold) value indicated by the AASHTO Specifications (2001) matches the allowable stress range value for over 2 million cycles presented in the table, presumably because Kaczinski, Dexter, and Van Dien (1998) felt that the “nonredundant” values were too conservative for cantilever supporting structures of signs, signals, and lighting.

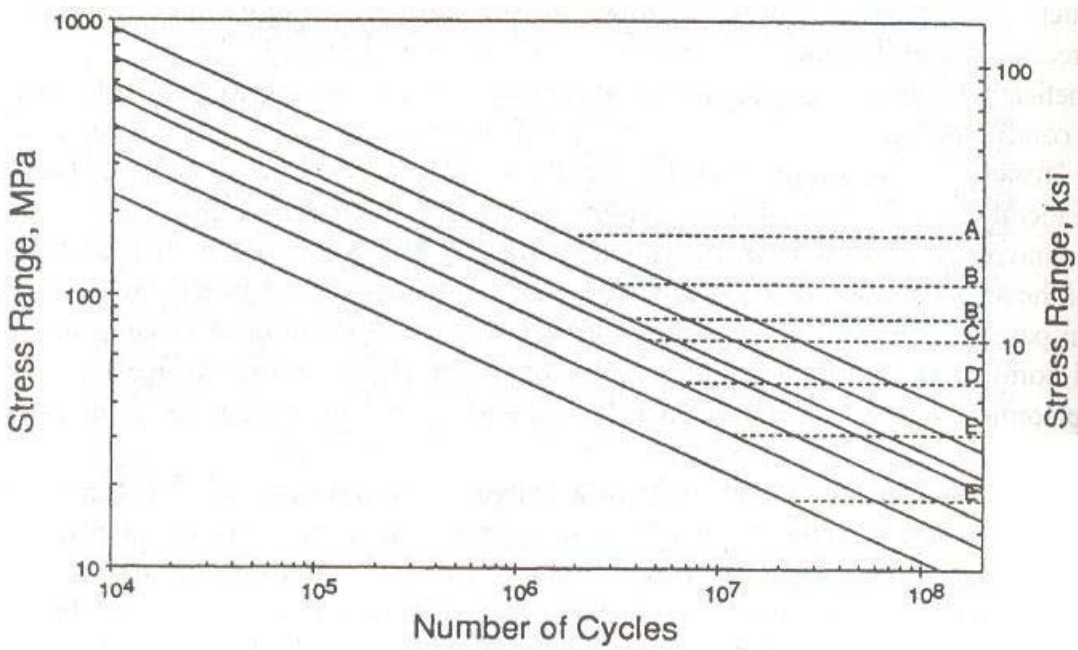

Figure 5.13. Lower-Bound S-N curves for AASHTO's seven primary fatigue categories (Chen and Duan 2000)

The equation of the S-N curve for category stress E' is:

$$\begin{aligned} S &= \exp\left[-0.3389\ln(N) + 6.6713\right] \quad &for\ \ N < 21{,}162{,}641 \\ S &= 2.6\ ksi \quad &for\ \ N \geq 21{,}162{,}641 \end{aligned} \tag{5-24}$$

where S will be given in kips per square inch (ksi). Solving for N and adding subscripts to apply to the methodology:

$$\begin{aligned} N_{i,j} &= \exp\left(\frac{\ln(S_{i,j}) - 6.6713}{-0.3389}\right) \quad &for\ S_{i,j} > 2.6\ ksi \\ N_{i,j} &= \infty \quad &for\ S_{i,j} \leq 2.6 ksi \end{aligned} \tag{5-25}$$

where S must be entered in ksi. Applying Equation (5-25) to each of the elements of the S-matrix, the N-matrix is obtained. A portion of the N-matrix is presented as Table 5.9.

Table 5.8. Allowable Fatigue Stress Range (AASHTO 1996)

Redundant Load Path Structures*				
	Allowable Range of Stress, F_{sr} (ksi)[a]			
Category (See Table 10.3.1B)	For 100,000 Cycles	For 500,000 Cycles	For 2,000,000 Cycles	For over 2,000,000 Cycles
A	63 (49)[d]	37 (29)[d]	24 (18)[d]	24 (16)[d]
B	49	29	18	16
B′	39	23	14.5	12
C	35.5	21	13	10
				12[b]
D	28	16	10	7
E	22	13	8	4.5
E′	16	9.2	5.8	2.6
F	15	12	9	8

Nonredundant Load Path Structures				
	Allowable Range of Stress, F_{sr} (ksi)[a]			
Category (See Table 10.3.1B)	For 100,000 Cycles	For 500,000 Cycles	For 2,000,000 Cycles	For over 2,000,000 Cycles
A	50 (39)[d]	29 (23)[d]	24 (16)[d]	24 (16)[d]
B	39	23	16	16
B′	31	18	11	11
C	28	16	10	9
			12[b]	11[b]
D	22	13	8	5
E[c]	17	10	6	2.3
E′	12	7	4	1.3
F	12	9	7	6

*Structure types with multi-load paths where a single fracture in a member cannot lead to the collapse. For example, a simply supported single span multi-beam bridge or a multi-element eye bar truss member has redundant load paths.

[a]The range of stress is defined as the algebraic difference between the maximum stress and the minimum stress. Tension stress is considered to have the opposite algebraic sign from compression stress.

[b]For transverse stiffener welds on girder webs or flanges.

[c]Partial length welded cover plates shall not be used on flanges more than 0.8 inches thick for nonredundant load path structures.

[d]For unpainted weathering steel, A 709, all grades, when used in conformance with the FHWA *Technical Advisory on Uncoated Weathering Steel in Structures*, dated October 3, 1989.

Table 5.9. Portion of the N-Matrix

Wind direction classification (degrees)	Wind speed classification (mph)									
	1	3	5	7	9	11	13	15	17	19
0	∞	∞	∞	∞	∞	∞	∞	∞	∞	∞
22.5	∞	∞	∞	∞	∞	∞	∞	∞	∞	∞
45	∞	∞	∞	∞	∞	∞	∞	∞	∞	∞
67.5	∞	∞	∞	1.E+7	2.E+5	6.E+4	6.E+4	9.E+4	2.E+5	8.E+5
90	∞	∞	∞	∞	4.E+5	5.E+4	5.E+4	1.E+5	4.E+5	5.E+6
112.5	∞	∞	∞	1.E+7	3.E+5	8.E+4	1.E+5	1.E+6	∞	∞
135	∞	∞	∞	∞	2.E+6	9.E+5	8.E+5	1.E+6	1.E+6	1.E+6
157.5	∞	∞	∞	∞	∞	∞	∞	∞	∞	∞
180	∞	∞	∞	∞	∞	∞	∞	∞	∞	∞
202.5	∞	∞	∞	∞	∞	∞	∞	∞	∞	∞
225	∞	∞	∞	∞	∞	∞	∞	∞	∞	∞
247.5	∞	∞	∞	∞	∞	∞	∞	∞	∞	∞
270	∞	∞	∞	∞	∞	∞	∞	∞	∞	∞
292.5	∞	∞	∞	∞	∞	∞	∞	∞	∞	∞
315	∞	∞	∞	∞	∞	∞	∞	∞	∞	∞
337.5	∞	∞	∞	∞	∞	∞	∞	∞	∞	∞

5.2.7 Step 7: Miner's Rule

In this step, Equation (5-7) is applied, (i.e., each of the elements of the n-matrix is divided by their corresponding element of the N-matrix, and all the results are added together to determine the damage *D*). Table 5.10 shows not only the results for the

structure being used as an example in this section (mast arm pointing north with signals with backplates and under smooth flow), but also for other cases. The results obtained are not realistic. For the cases of the structures with backplates, the estimated daily damage is too high. These structures would fail before completing a month of service. Meanwhile, for the cases of the structures without backplates, the estimated damage is too low, predicting that the structures would fail after millions of years in service.

Table 5.10. Damage (*D*) Prediction after One Day with *C* = 1

Direction to which mast arm points	Signals with backplates Smooth flow	Signals with backplates Exposure D	Signals without backplates Smooth flow
N	0.061	0.048	4.68E-10
W	0.049	0.039	7.37E-11
S	0.062	0.052	2.43E-12
E	0.196	0.162	1.96E-10

Probably the unrealistic results were obtained because the standard deviation of the vertical vibration values obtained in the TTU wind tunnel were too high when compared to the values obtained in the full-scale experiments. The discrepancy between both set of results was probably caused by the following two reasons:

1. The wind tunnel values were obtained for a turbulence intensity that is too low to represent the city of Lubbock. A more appropriate value would be TI = 22%, which would correspond to Exposure C in the ASCE Standard (2005).

The wind tunnel model is not a perfect representation of the full-scale structure. The tapering of the mast arm was modeled with three segments of different size. Either a tapered model or a model with more segments would be expected to yield closer results to the full-scale values. The three-segment model itself was off from the required values of elastic stiffness and mass per unit length (as shown in

2. Table 4.2). Also, the visors of the signals were modeled as solid circular cylinders when in reality they are hollow.

The value of *C* should be used to account for the differences between the full-scale and wind tunnel results. Therefore, it was a mistake to assume a value of $C = 1$ in step 4 for the example discussed here.

Different values of *C* were used to calculate the fatigue life of the mast arms with backplates. The TTU wind tunnel results for Exposure D were used in the calculations. The results are presented in Table 5.11 and plotted in Figure 5.14. It can be seen that more realistic values of fatigue life can be obtained when $C < 0.2$, but then at $C = 0.13$ the methodology predicts an infinite fatigue life. To determine an appropriate value of *C*, research must be performed to determine the typical fatigue life of mast arms.

Table 5.11. Fatigue Life (in years) for Different Values of *C* for Structures with Backplates

C	Direction mast arm points to			
	N	W	S	E
1.00	0.06	0.07	0.05	0.02
0.9	0.08	0.10	0.07	0.02
0.8	0.11	0.14	0.10	0.03
0.7	0.16	0.20	0.15	0.05
0.6	0.26	0.32	0.24	0.08
0.5	0.44	0.55	0.41	0.13
0.4	0.86	1.07	0.79	0.26
0.3	2.01	2.50	1.86	0.60
0.2	8.12	9.98	7.42	2.33
0.19	9.44	11.62	8.64	2.71
0.18	13.11	16.29	11.57	3.76
0.17	15.52	19.28	13.70	4.45
0.16	24.69	30.20	21.66	6.85
0.15	39.12	45.82	34.95	10.28
0.14	109.58	128.16	110.99	29.03
0.13	∞	∞	∞	∞

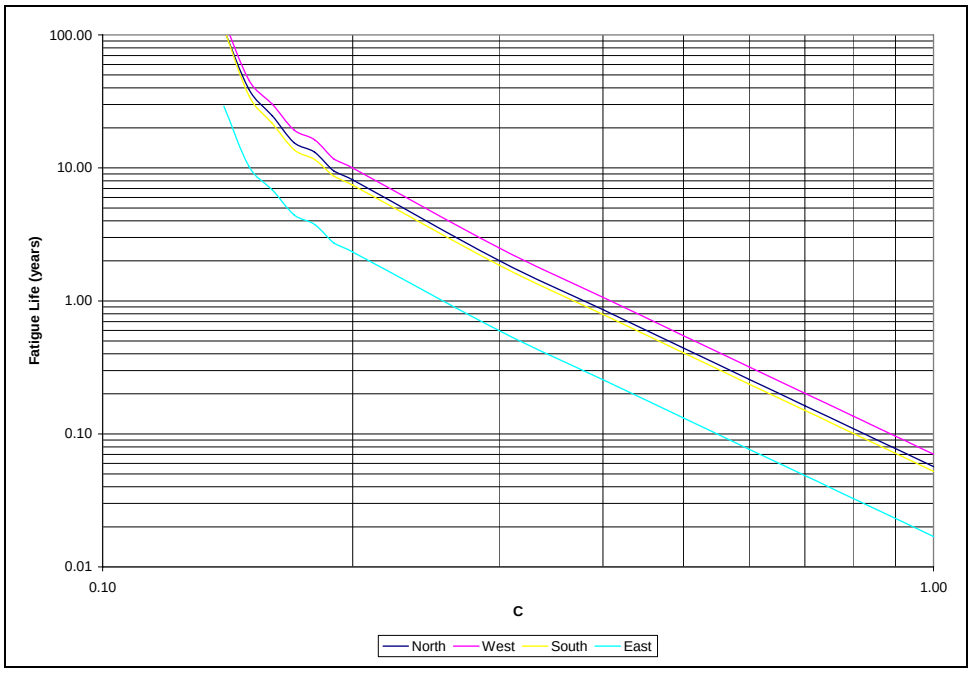

Figure 5.14. Effect of Factor *C* on the Prediction of the Fatigue Life of Mast Arms with Backplates

The results obtained for the structure without backplates using *C* =1 indicate that it is very unlikely that these structures will fail due to fatigue, assuming that they are properly assembled (i.e., assuming that the arm-to-base-plate weld has the required strength and that there are no fabrication defects). Therefore it is very important that backplates be used only when necessary.

5.3 Conclusions

A methodology for estimating the fatigue life of cantilever traffic signal structures was presented in this chapter. The methodology only takes into consideration cross-wind vibrations. Out-of-plane vibrations were not considered because it is believed that most fatigue cracks initiate at the top of the mast arm (Chen et al. 2002), which suggest they

are caused by vertical oscillations. Also not considered were the vibrations caused by truck-induced gusts because recent research suggest they are negligible (Chen et al. 2001; Albert 2006).

The methodology was applied as a risk assessment model to the structure with the 44-ft mast arm that was studied in both full-scale experiments (Chapter 3) and wind tunnel studies (Chapter 4). The climatology of the city of Lubbock was used along with the wind tunnel results. To apply this methodology to another structure, the appropriate climatology of its location must be used. If the structure is different from the 44-ft mast arm either in length, shape, or the way the signal heads are connected, the appropriate wind tunnel experiments should be conducted.

Knowing that CAFL = 2.6 ksi, the minimum peak-to-peak vertical vibration amplitude that causes fatigue damage can be calculated from Equation (5-23) as follows:

$$2600 = 578.55\ \hat{Y} \tag{5-26}$$

$$\hat{Y} = 4.5 \text{ inches} \tag{5-27}$$

Then, using Equation (5-13), the minimum standard deviation of the vertical vibration at which fatigue damage occurs can be estimated:

$$4.5 = 2\sqrt{2}\sigma_n \tag{5-28}$$

$$\sigma_n = 1.6 \text{ inches} \tag{5-29}$$

Therefore, for the 44-ft mast arm analyzed in this research, it is estimated that fatigue damage occurs when the standard deviation of the vertical displacement (Y) is equal to or larger than 1.6 inches. Knowing these, the results of the full-scale experiment of the 44-ft mast arm (discussed in Chapter 3) can be rechecked. These results are re-plotted in

Figure 5.15 for both cases of with and without backplates (M1100 and M1101, respectively). It is seen in the figure that the structure did not suffer fatigue damage when it did not have backplates (i.e., for M1101, the standard deviation of Y was always below 1.6 inches). Fatigue damage did occur when the structure had backplates. This is consistent with the fatigue-life predictions presented in this chapter.

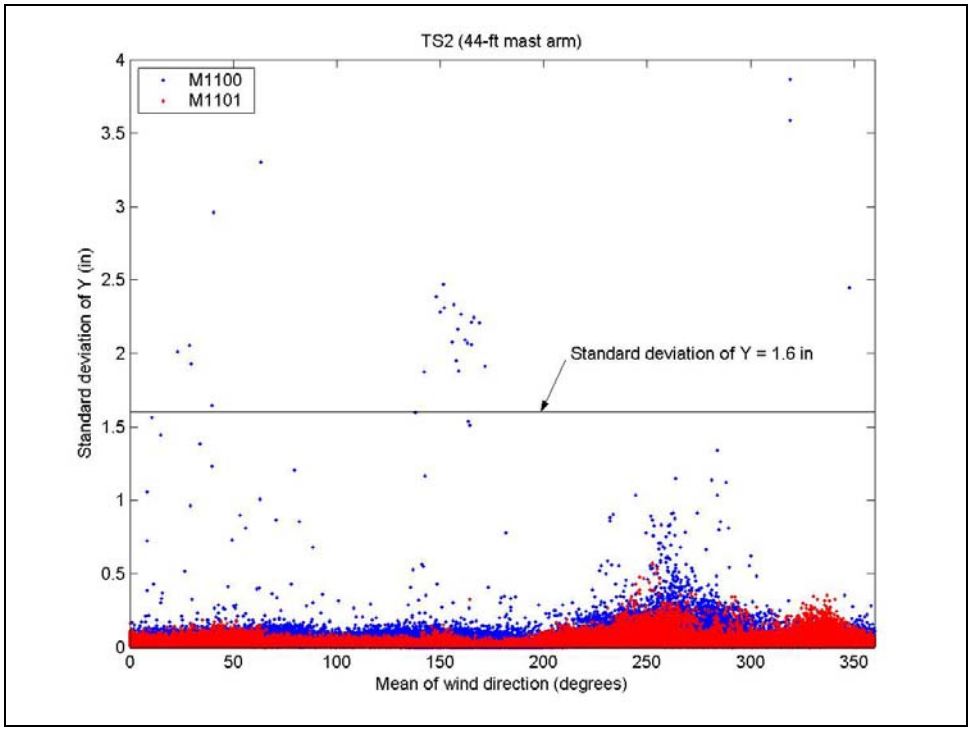

Figure 5.15. Occurrences of Fatigue Damage

CHAPTER 6

LIFE-CYCLE COST ANALYSIS

6.1 Introduction

> "In 1990, two cantilevered signal structures collapsed in close succession in Michigan, resulting in property damage, injuries, and one fatality. Both collapses were attributed to loss of strength from fatigue cracks in the anchor bolts. As a result of this accident, the Michigan Department of Transportation had to pay out a large settlement that in turn disrupted their maintenance schedule for a three-year period." (Ocel, Dexter, and Hajjar 2006)

Certainly, state and government officials in charge of traffic signal structures would like to avoid a situation like the one that occurred in Michigan. Even in the cases where no deaths occur or even when there is no collision, the collapse of a traffic signal structure could disrupt traffic, which in turn could have a negative impact on the local economy. How negative of an impact depends on the location of the structure and on the time of the collapse, factors which determine if there is a high or low volume of traffic at the time of the collapse.

One of the best ways to avoid a collapse is to regularly inspect the structures for fatigue damage, but inspections also cost money. So officials in charge of the structures may not want to spend too much of their budgets inspecting for failures that most of the time are caught before collapse anyway (Dexter and Ricker 2002).

Life-cycle cost analysis is an economics' tool that could be used by officials to select what type of mast arm and signal light head configuration to use, while taking into consideration costs of inspection and maintenance of the structure. This is assuming that they have used the methodology presented in Chapter 5 to predict the fatigue life of said arm and signal configuration.

In this chapter, a brief explanation of life-cycle cost analysis is presented. This is followed by an example in which the method is applied to cantilever traffic signal structures. Finally, some recommendations are given to officials in charge of cantilever traffic signal structures.

6.2 Life-Cycle Cost Analysis Defined

Life-cycle cost analysis (LCCA) is the economic evaluation of expected costs over the entire life of a proposed project (Riggs 1977). It is used to calculate all the cost and revenues over the life of the project, including initial costs, operating costs, residual salvage values, revenues, and profits of the project (Bowman 2003). It can be used to evaluate different alternatives of the proposed project, competing on the basis of cost (Humphreys and Wellman 1996). For example, when deciding which type of cantilever traffic signal structure to put at a certain location, LCCA can be used to select between a very expensive structure that requires very little maintenance and a low-priced structure that requires a lot of maintenance. This is done by calculating the total cost over the life of each of the structures and selecting the one with the lowest cost.

When performing LCCA, it is common practice to estimate all future costs and benefits as present values. Therefore, to calculate the life-cycle cost (LCC) of an alternative, the following formula can be used:

$$\text{LCC} = \sum_{t=0}^{N} \frac{1}{(1+r)^t} A_t \tag{6-1}$$

where:

t = time (in years)

N = number of years in the analysis period

r = discount rate for adjusting cash flows to present value

A_t = amount of benefit or cost on year t

There are cases when not all costs need to be quantified in LCCA. This is because of the following:

> "…alternatives that accomplish identical objectives often have many costs in common. Costs that are identical (in terms of both their amount and when they occur) among all alternatives need not be quantified, as they will 'wash out' in a cost comparison. In short, the analyst should focus only on those costs that vary among alternatives." (USDOT 2003)

Different alternatives can be legitimately compared using LCCA only when all of them satisfy the same performance requirements (Humphreys and Wellman 1996). For example, it does not make sense to use LCCA to consider a cantilever traffic structure design which has a mast arm that is not long enough for the location where the structure is needed.

The U. S. Department of Transportation (USDOT 2003) states that, as a rule of best practice, LCCA should be done using dollars and discount rates that do not include the effects of inflation. This is explained as follows:

> "Inflation is very hard to predict, particularly more than a few years into the future. More importantly, if inflation is added to benefits and costs projected for future years, it will only have to be removed again before these benefits and costs can be compared in the form of dollars of any given base year." (USDOT 2003)

6.3 Example of Life-Cycle Cost Analysis

In this section, a simple example showing the application of life-cycle cost analysis is shown. Consider the situation where a cantilever traffic signal structure is needed. There are two design alternatives which are being considered. Alternative No. 1 (A1) has an initial cost of $3000 and needs to be serviced every 5 years. Alternative No. 2 (A2) has an initial cost of $4000 and needs to be serviced every 10 years. The cost of servicing any structure is $500 (this includes welding the mast arm of structure due to accumulated fatigue damage). It is estimated that the structure selected will be used for a period of 30 years. A discount rate of 5 percent will be assumed.

A1 will need to be serviced in years 5, 10, 15, 20, and 25. On year 30 it will be taken down, so no servicing is needed. Applying Equation (6-1), the life-cycle cost of A1 is determined as follows:

$$\begin{aligned} \mathrm{LCCA}_{\mathrm{A1}} &= \frac{\$3000}{1.05^{0}} + \frac{\$500}{1.05^{5}} + \frac{\$500}{1.05^{10}} + \frac{\$500}{1.05^{15}} + \frac{\$500}{1.05^{20}} + \frac{\$500}{1.05^{25}} \\ &= \$4{,}275.32 \end{aligned} \tag{6-2}$$

Meanwhile, A2 will need to be serviced in years 10 and 20. Applying Equation (6-1), the life-cycle cost of A2 is determined as follows:

$$LCC_{A2} = \frac{\$4000}{1.05^0} + \frac{\$500}{1.05^{10}} + \frac{\$500}{1.05^{20}} = \$4{,}495.40 \qquad (6\text{-}3)$$

Alternative No. 1 should be selected because it has the lowest life-cycle cost.

6.4 Recommendations

As mentioned before, there are many different kinds of mast arms and traffic signal configurations in use. It is still not known if these other cases behave similarly to the ones studied in Chapters 3 to 5. So until the behavior under wind-loading of these other types of structures is understood, it is recommended that each structure be inspected at least every 4 years, as suggested by Dexter and Ricker (2002).

For cases where the behavior of the cantilever traffic signal structures are well understood, the methodology presented in Chapter 5 could be used to predict the fatigue life. Then inspections and maintenances could be scheduled according to their expected fatigue life. For example, it might be desired to inspect each arm when they have suffered 75% of the damage necessary to collapse.

It has been seen in previous chapters that arms that have signals without backplates have lower amplitude of vibration than those with backplates, so it can be reasoned that arms without backplates can be inspected less frequently, therefore reducing further the inspection expenditure if the predicted fatigue life is used. The 4-year criterion recommended by Dexter and Ricker (2002) does not consider if the structure has backplates.

If a city wants to predict the fatigue life to determine when the structures need to be inspected and maintained, it will require a good database with all the necessary information. These include the date when the structure was installed, when was the last time it was inspected and repaired, the direction of the mast arm, and an indication of if the signals have backplates (the last two affect how much the mast arm vibrates, as explained in Chapter 5). Other information that should be kept in the database is the length and shape of the mast arm and the signal light head configuration because they could affect the occurrence of wind-induced vibrations that could lead to fatigue damage.

CHAPTER 7

CONCLUSIONS AND RECOMMENDATIONS

Through both full-scale and wind tunnel experiments, evidence was found that at least one traffic signal configuration is susceptible to experiencing vortex shedding vibrations. The configuration in question has the signal heads supported at the same height of the mast arm, as shown in Figure 7.1. The experiments also indicated that vortex shedding vibrations are more likely to occur when the signals have backplates, when the wind speed is steady between 5 to 15 mph, and when the wind approaches the mast arm from the back of the signal. It was also found that the vibrations caused stress ranges larger than the constant amplitude fatigue limit (CAFL), therefore these vibrations can lead to fatigue failure of mast arms. The results also indicated that galloping is very unlikely to occur for this configuration.

Since this configuration was initially reported as not being susceptible to vortex shedding vibrations nor to galloping by Pulipaka (1995), it is possible that other configurations studied by him are also vulnerable to vortex shedding vibrations. In any case, the experimental results indicate that the AASHTO Specifications (2001) need to be re-written to consider oscillations induced by vortex shedding in the fatigue design of cantilever traffic signal structures.

Figure 7.1. Traffic Signal Configuration Susceptible to Vortex Shedding

Since fatigue failures can lead to collapses that may cause deaths, it is important for managers responsible for traffic signal structures to establish inspection schedules for these structures. These schedules should take into consideration the orientation of the mast arm and the wind climatology of the location to determine which structures are at most risk of suffering fatigue failure and therefore need to be inspected more frequently. To aid in the establishing of the inspection schedule, it is recommended that these managers keep a database with all the necessary information to calculate the remaining fatigue life of each of their structures.

As explained before, the mast arm undergoes larger amplitudes of vibration when the signals have backplates. Therefore managers should also make sure that signal heads have backplates only when necessary. In the city of Lubbock there are several arms pointing east or west that have signals with backplates, even though they are not needed given that drivers will be facing north or south when in front of these structures.

Given the experimental results and limitations of this research, the following research is suggested:

- The many different traffic signal configurations with the different types of mast arms should be tested to determine how susceptible they are to galloping, vortex shedding, and natural wind gusts.

- An equivalent static load for vortex shedding needs to be determined to be included in the AASHTO Specifications (2001) or measures to suppress vortex shedding altogether should be investigated.

- Research should be conducted to improve the methodology to predict fatigue life that was presented in Chapter 5. Some of the things that could be researched are the following:

    - The determination of accurate values of the *C* factor which establishes the relationship between wind tunnel results to full-scale values of peak-to-peak amplitude of vertical vibrations.
    - The estimation of a more accurate dynamic factor *d*. This could include taking into consideration the effect that other mode shapes (besides the first) have on the stresses of the mast arm.
    - Determine a better way to estimate the cumulative fatigue damage other than the application of Miner's Rule. There are many cumulative fatigue damage theories for metals and their alloys other than Miner's Rule. For a comprehensive review of these, Fatemi and Yang (1998) can be consulted. Applying a different theory may produce more accurate results.

REFERENCES

AASHTO. 1996. *Standard specifications for highway bridges*. 16th ed. Washington, DC: American Association of State Highway and Transportation Officials.

AASHTO. 2001. *Standard specifications for structural supports for highway signs, luminaires, and traffic signals*. 4th ed. Washington, DC: American Association of State Highway and Transportation Officials.

Albert, Matthew Nielsen. 2006. Field testing of cantilevered traffic signal structures under truck-induced gust loads. Masters thesis, The University of Texas at Austin.

ASCE. 2005. *Minimum design loads for buildings and other structures*. ASCE Standard 7-05. Reston, VA: American Society of Civil Engineers.

Billah, K. Yusuf, and Robert H. Scanlan. 1991. Resonance, Tacoma Narrows bridge failure, and undergraduate physics textbooks. *American Journal of Physics* 59(2), 118-24.

Blevins, Robert D. 1977. *Flow-induced vibration*. New York: Van Nostrand Reinhold Company.

Bowman, Michael S. 2003. *Applied economic analysis for technologists, engineers and* manages. 2nd ed. Columbus, OH: Prentice Hall.

Brockenbrough, R. L., and B. G. Johnston. 1981. *USS steel design manual*. Pittsburgh: United States Steel Corporation.

Chen, Genda, Jingning Wu, Jiaqing Yu, Lokeswarappa R. Dharani, and Michael Barker. 2001. Fatigue assessment of traffic signal mast arms based on field test data under natural wind gusts. *Transportation Research Record*, n. 1770: 188-94.

Chen, Genda, Michael Baker, D. Scott MacKenzie, Christopher Ramsay, Joe Alderson, Lokeswarappa Dharani, and Jiaqing Yu. 2002. Forensic investigation of failed mast arms of traffic signal supported structures. *Transportation Research Record*, n. 1814: 9-16.

Chen, Genda, M. Barker, L. R. Dharani, and C. Ramsay. 2003. *Signal mast arm failure investigation*. Missouri Department of Transportation – Research, Development and Technology 03-010. Jefferson City, MO: Missouri Department of Transportation.

Chen, Wai-Fah, and Lian Duan, editors. 2000. *Bridge engineering handbook*. Boca Raton: CRC Press.

Chen, Xinzhong, Assistant Professor, Department of Civil and Environmental Engineering, Texas Tech University. 2006. Personal communication.

Cook, R. A., D. Bloomquist, D. S. Richard, and M. A. Kalajian. 2001. Damping of cantilevered traffic signal structures. *Journal of Structural Engineering* 127, n. 12: 1476-83.

Den Hartog, J. P. 1985. *Mechanical vibrations*. New York: Dover Publications.

Dexter, R. J., and M. J. Ricker. 2002. *National Cooperative Highway Research Program Report 469: Fatigue-resistant design of cantilevered signal, sign, and light supports.* Washington, DC: National Cooperative Highway Research Program.

Dyrbye, Claës, and Svend O. Hansen. 1997. *Wind loads on structures*. New York: John Wiley & Sons.

Fatemi, A., and L. Yang. 1998. Cumulative fatigue damage and life prediction theories: a survey of the state of the art for homogenous material. *International Journal of Fatigue* 20, n. 1: 9-34.

Fisher, J. W., A. Nussbaumer, P. B. Keating, and B. T. Yen. 1993. *National Cooperative Highway Research Program Report 354: Resistance of welded details under variable amplitude long-life fatigue loading.* Washington, DC: National Cooperative Highway Research Program.

Florea, Micah J. 2005. Field tests and analytical studies of the dynamic behavior and the onset of galloping in traffic signal structures. Masters thesis, The University of Texas at Austin.

G Systems. 2005. *Structural performance DAQ user manual*. Texas Tech University Wind Science and Engineering Version 2.0. Plano, TX: G Systems.

Gray, B., P. Wang, H. R. Hamilton, and J. A. Puckett. 1999. Traffic signal structure research – Univ. of Wyoming. In *Structural Engineering in the 21st Century: Proceedings of the 1999 Structures Congress held in New Orleans, Louisiana, April 18-19, 1999*, edited by R. Avent and M. Alawady, 1107-10. Reston, VA: American Society of Civil Engineers.

Hamilton III, H. R., G. S. Riggs, and J. A. Puckett. 2000. Increased damping in cantilevered traffic signal structures. *Journal of Structural Engineering* 126, n. 4: 530-7.

Hart, Jeryl (Jere) D., City Traffic Engineer of Lubbock, Texas. 2005. Personal communication.

Hartnagel, Bryan A., and Michael G. Barker. 1999. Strain measurements of traffic signal mast arms. In *Structural Engineering in the 21st Century: Proceedings of the 1999 Structures Congress held in New Orleans, Louisiana, April 18-19, 1999*, edited by R. Avent and M. Alawady, 1111-4. Reston, VA: American Society of Civil Engineers.

Hirsch, Gerhard H., and Hugo Bachmann. 1995. Dynamic effects from wind. Appendix H of *Vibration problems in structures: Practical guidelines*, by Hugo Bachman et al. Basel, Switzerland: Birkhäuser.

Holmes, John D. 2001. *Wind loading of structures.* London: Spon Press.

Humphreys, Kenneth K., and Paul Wellman. 1996. *Basic cost engineering*. 3rd ed. New York: Marcel Dekker.

Kaczinski, M. R., R. J. Dexter, and J. P. Van Dien. 1998. *National Cooperative Highway Research Program Report 412: Fatigue-resistant design of cantilevered signal, sign, and light supports.* Washington, DC: National Academy Press.

Lee, Yung-Li. 2005. Fatigue damage theories. Chapter 2 of *Fatigue testing and analysis (Theory and practice)*, by Yung-Li Lee, Jwo Pan, Richard B. Hathaway, and Mark E. Barkey. Amsterdam: Elsevier.

Letchford, Chris. 2003. Notes of the Wind Engineering course, spring semester, Texas Tech University.

Liu, Henry. 1991. *Wind engineering: A handbook for structural engineers*. Englewood Cliffs, NJ: Prentice Hall.

McDonald, J. R., K. C. Mehta, W. Oler, and N. Pulipaka. 1995. *Wind load effects on signs, luminaires, and traffic signal structures.* Report No. 1303-F. Austin, TX: Texas Department of Transportation.

Ocel, Justin M., Robert J. Dexter, and Jerome F. Hajjar. 2006. *Fatigue-resistant design for overhead signs, mast-arm signal poles, and lighting standards.* St. Paul, MN: Minnesota Department of Transportation.

Paz, Mario. 2002. *Structural dynamics: Theory and computation.* 4th ed. Boston: Kluwer Academic Publishers.

Pulipaka, Narendra. 1995. Wind-induced vibrations of cantilevered traffic signal structures. PhD dissertation, Texas Tech University.

Pulipaka, N., J. R. McDonald, and K. C. Mehta. 1995. Wind effects on cantilevered traffic signal structures. In *Wind Engineering retrospect and prospect: Papers for the Ninth International Conference 1995 Volume IV, January 9-14, 1995*, by International Association for Wind Engineering, 2043-50. New Delhi, India: Wiley Eastern Limited.

Pulipaka, Narendra, Partha P. Sarkar, and James R. McDonald. 1998. On galloping vibration of traffic signal structures. *Journal of Wind Engineering and Industrial Aerodynamics* 77 & 78 (Sep-Dec): 327-36.

Riggs, James L. 1977. *Engineering economics*. New York: McGraw-Hill.

Simiu, Emil, and Toshio Miyata. 2006. *Design of buildings and bridges for wind: A practical guide to ASCE-7 Standard users and designers of special structures*. Hoboken, NJ: John Wiley & Sons.

South, Jeffrey M. 1994. *Fatigue analysis of overhead sign and signal structures*. Physical Research Report No. 115. Springfield, IL: Illinois Department of Transportation.

Texas Department of Transportation, Traffic Operations Division. 1995. Traffic signal pole standards. In *Traffic standards (Metric & English)*, http://www.dot.state.tx.us/insdtdot/orgchart/cmd/cserve/standard/toc.htm.

USDOT, Federal Highway Administration, Office of Asset Management. 2003. *Economic analysis primer*. Washington, DC: U.S. Department of Transportation.

Vega, Rolando, and Chris W. Letchford. 2006. Wind directionality and uncertainties in the parameters of the Weibull parent distribution. TMs (photocopy). Texas Tech University. Submitted for publication to the *Journal of Wind Engineering and Industrial Aerodynamics*.

APPENDIX A

MODE 1100 RESULTS

In this section, all the figures obtained by analyzing the data collected under Mode 1100 (arms pointing north, signals with backplates) are shown, as discussed in Section 3.3.2. A dot on a given plot represents two minutes of data. The sign convention of the angle of attack and of the wind speed components u and v is shown in Figure 3.10. The w-component is positive in the upward direction. X and Y refer to out-of-plane (or horizontal) and in-plane (or vertical) displacements of the tip of the arm, respectively.

TS1 (60-ft mast arm)

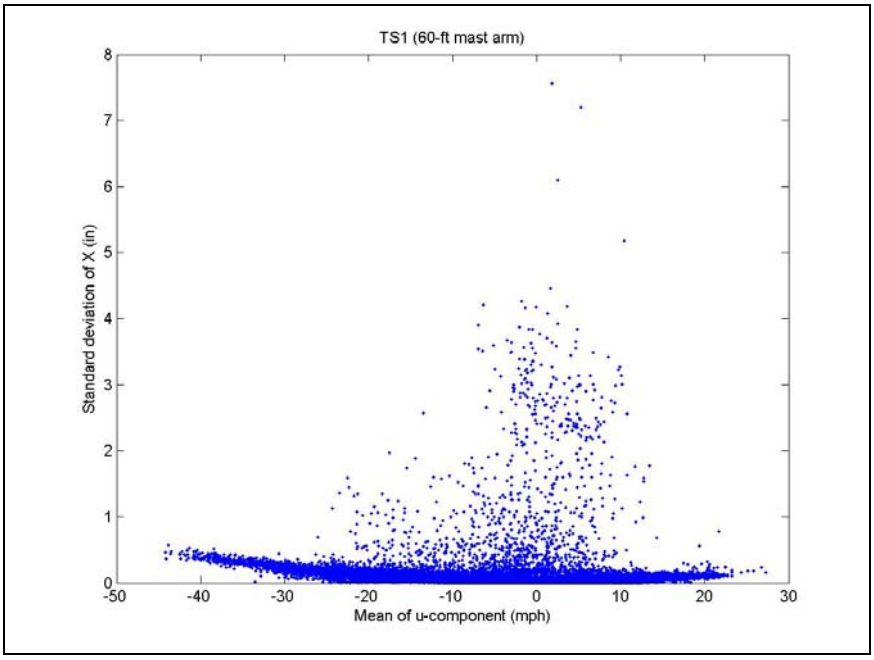

Figure A.1. Effect of u-component on horizontal vibrations of TS1 with backplates

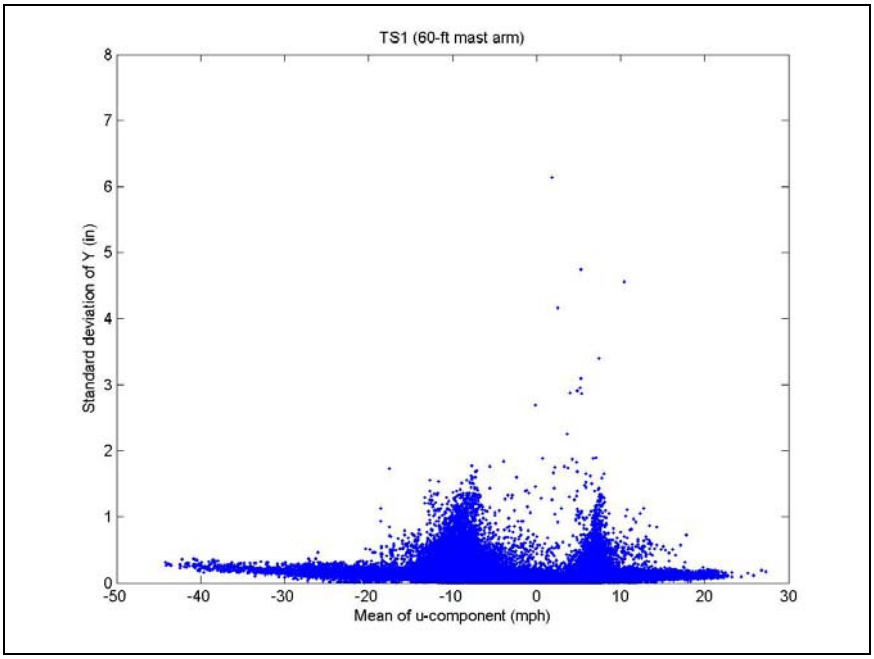

Figure A.2. Effect of u-component on vertical vibrations of TS1 with backplates

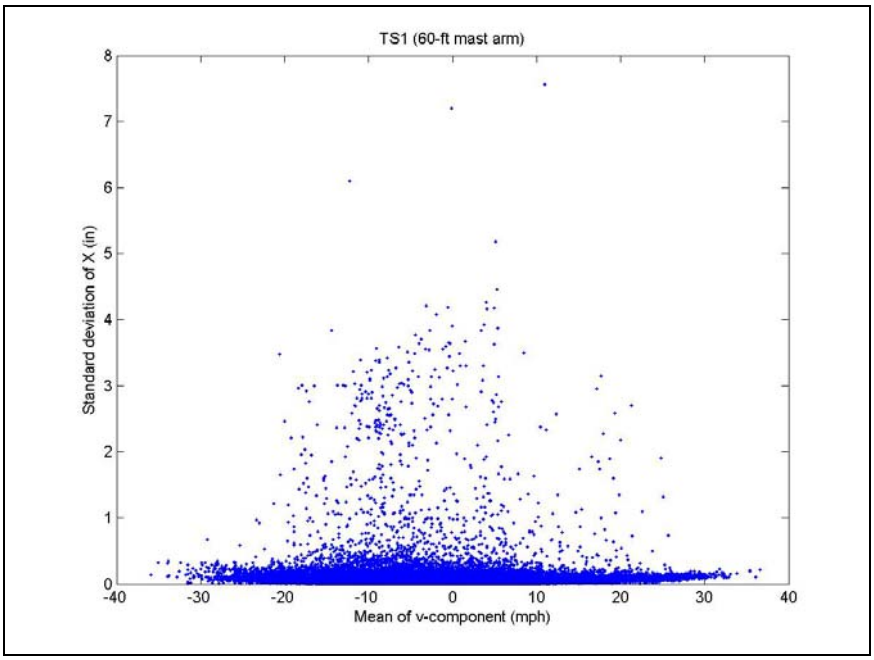

Figure A.3. Effect of v-component on horizontal vibrations of TS1 with backplates

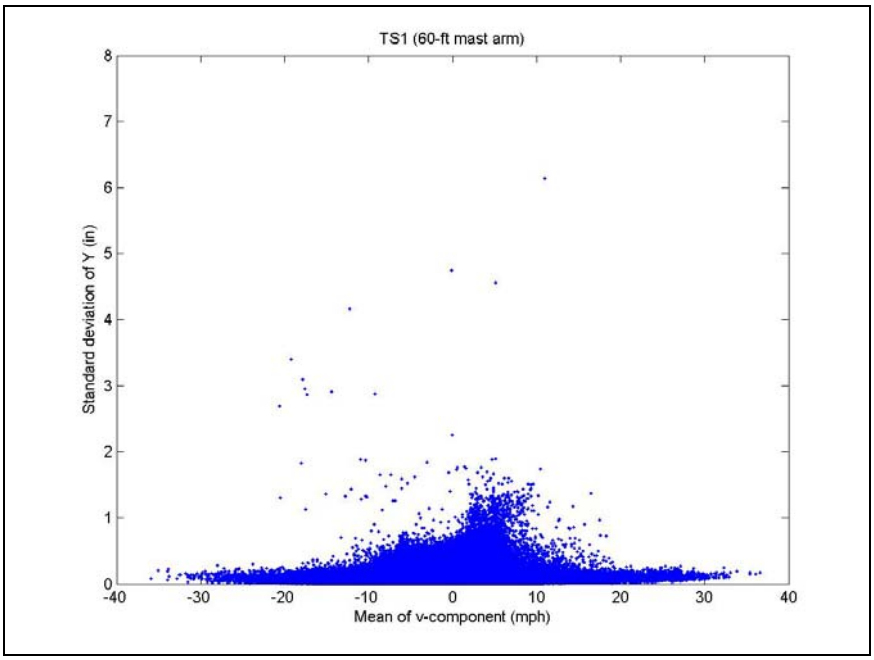

Figure A.4. Effect of v-component on vertical vibrations of TS2 with backplates

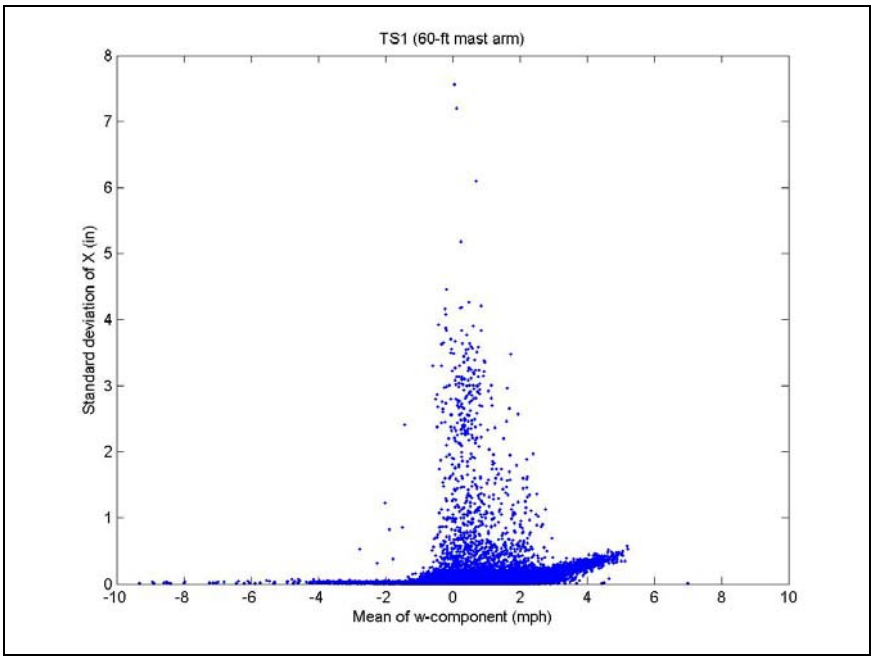

Figure A.5. Effect of w-component on horizontal vibrations of TS1 with backplates

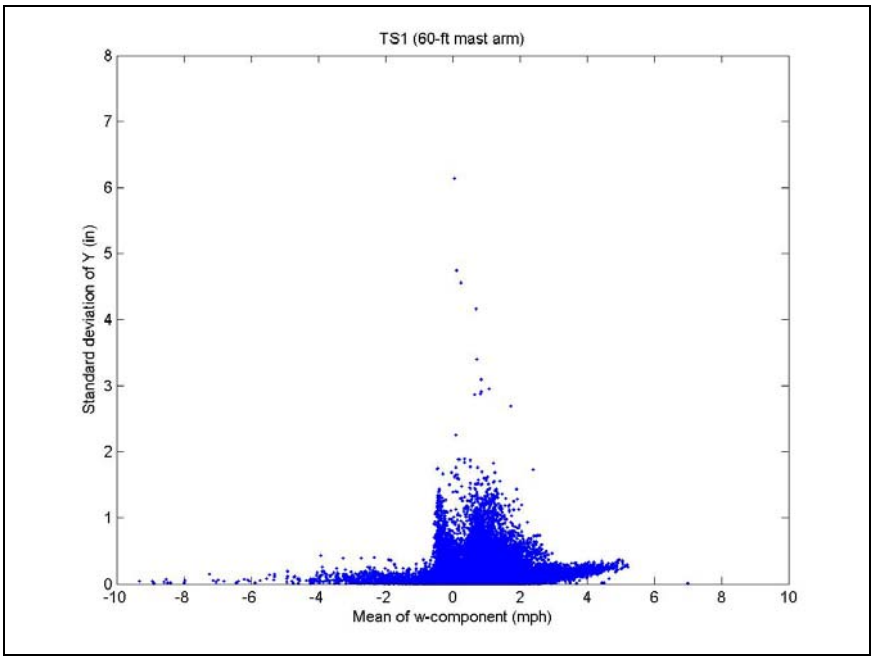

Figure A.6. Effect of w-component on vertical vibrations of TS1 with backplates

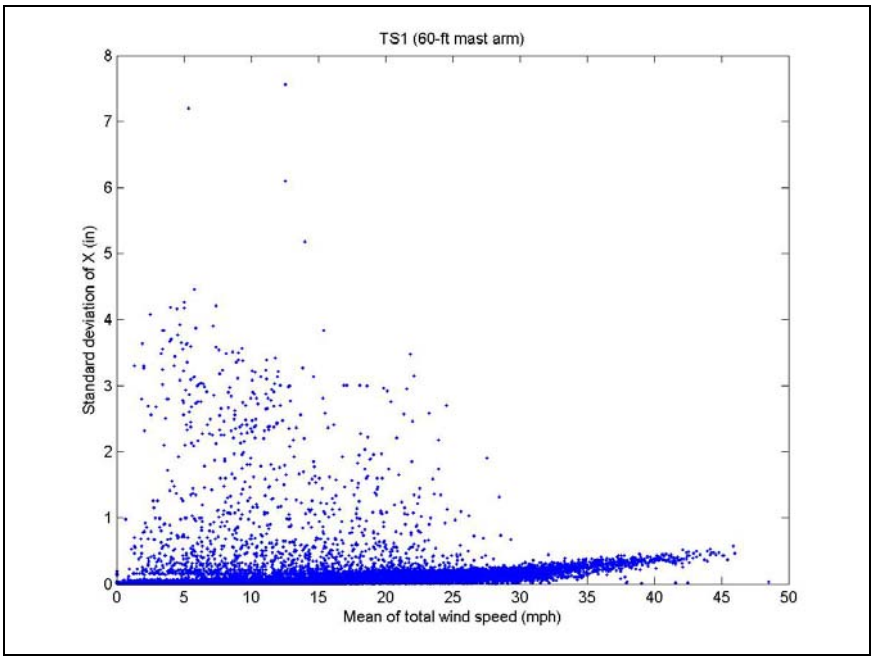

Figure A.7. Effect of total wind speed on horizontal vibrations of TS1 with backplates

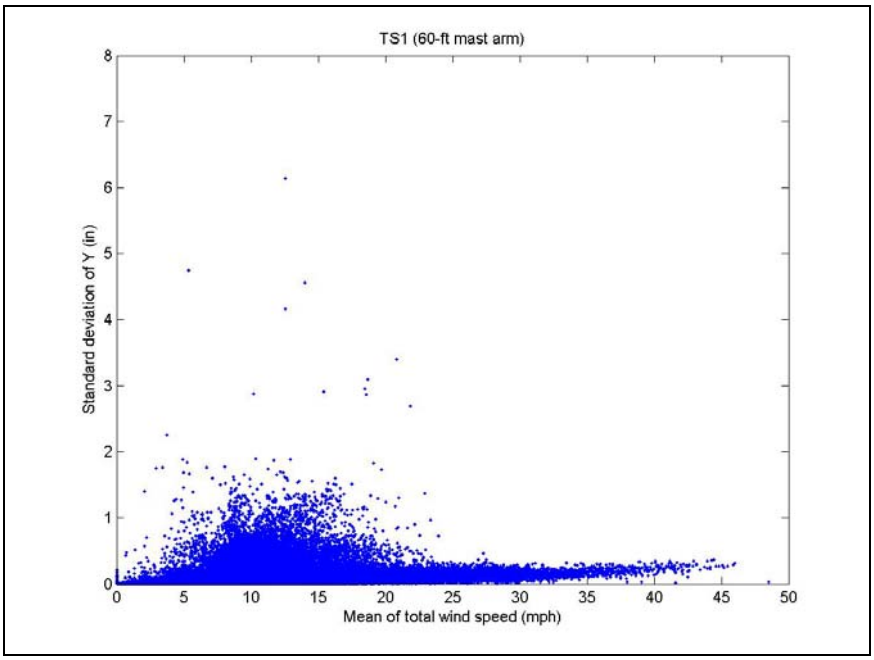

Figure A.8. Effect of total wind speed on vertical vibrations of TS1 with backplates

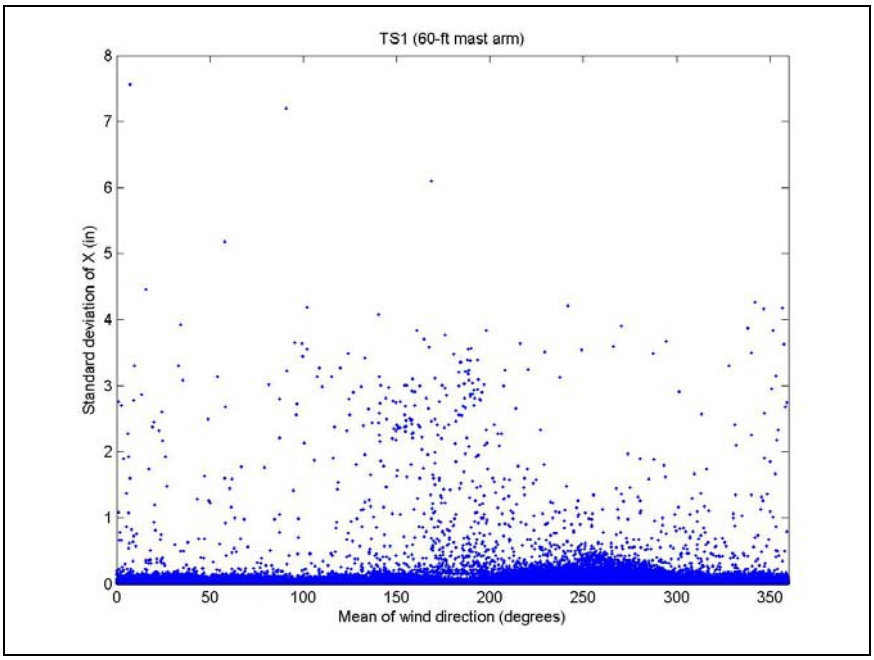

Figure A.9. Effect of wind direction on horizontal vibrations of TS1 with backplates

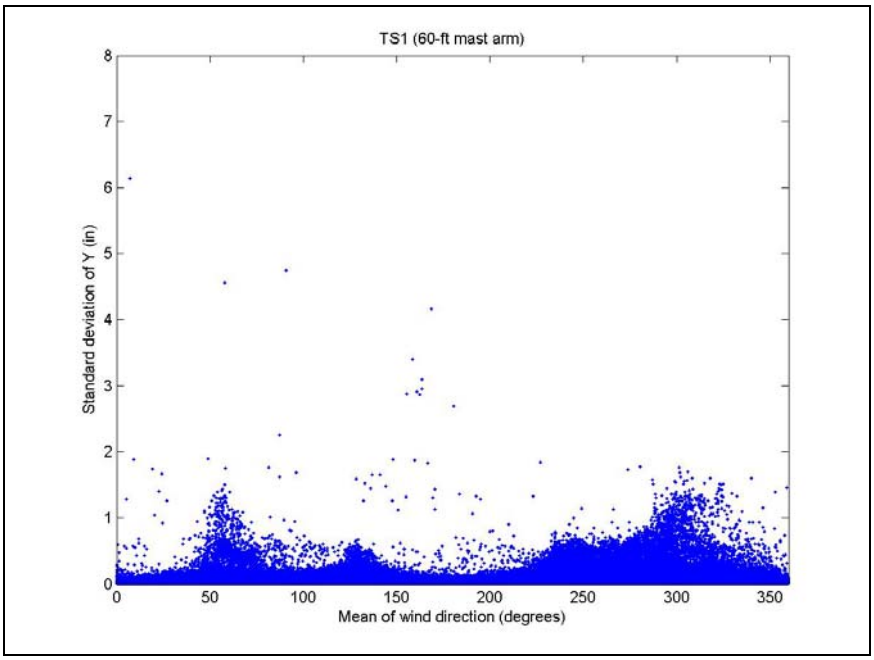

Figure A.10. Effect of wind direction on vertical vibrations of TS1 with backplates

TS2 (44-ft mast arm)

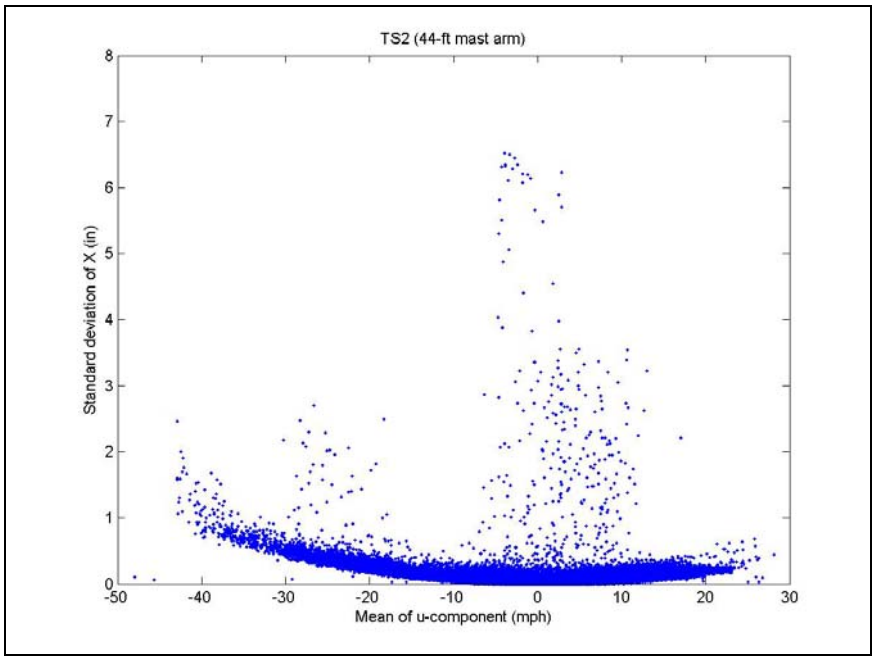

Figure A.11. Effect of u-component on horizontal vibrations of TS2 with backplates

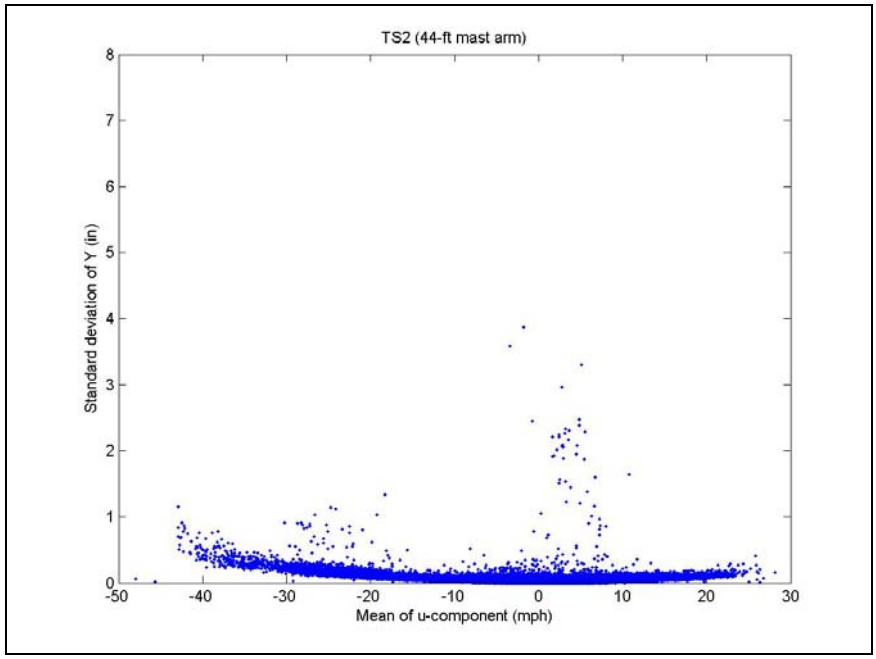

Figure A.12. Effect of u-component on vertical vibrations of TS2 with backplates

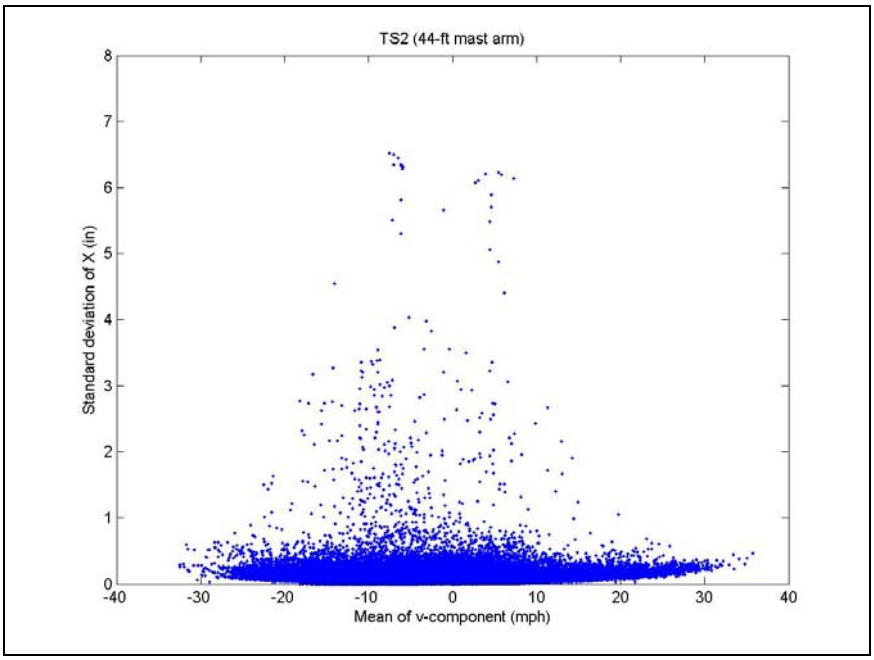

Figure A.13. Effect of v-component on horizontal vibrations of TS2 with backplates

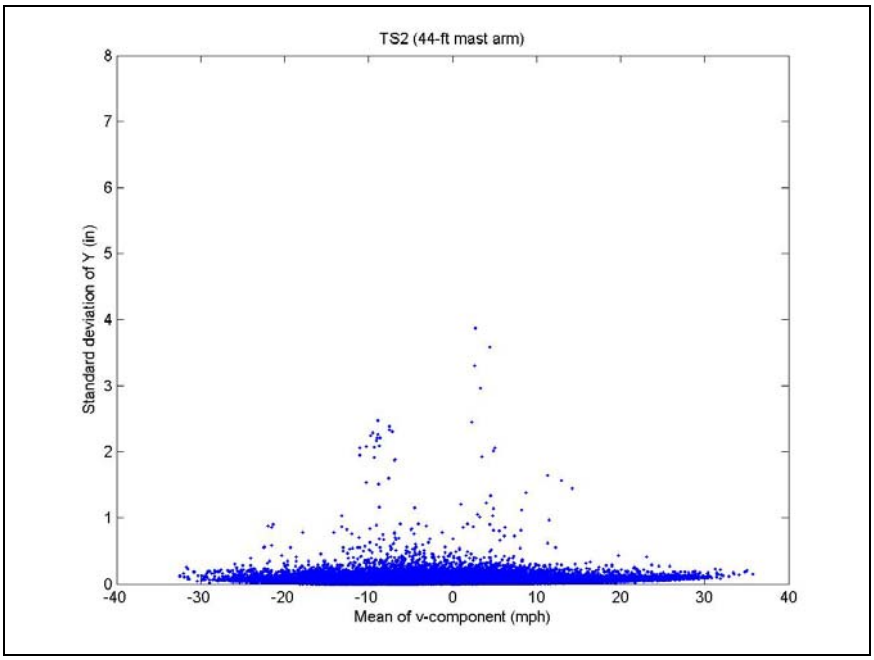

Figure A.14. Effect of v-component on vertical vibrations of TS2 with backplates

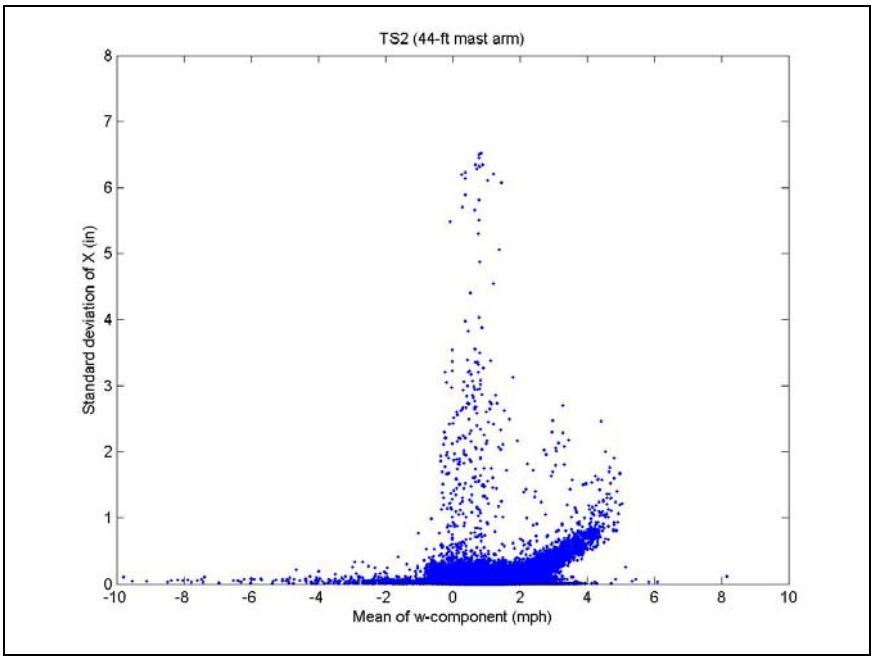

Figure A.15. Effect of w-component on horizontal vibrations of TS2 with backplates

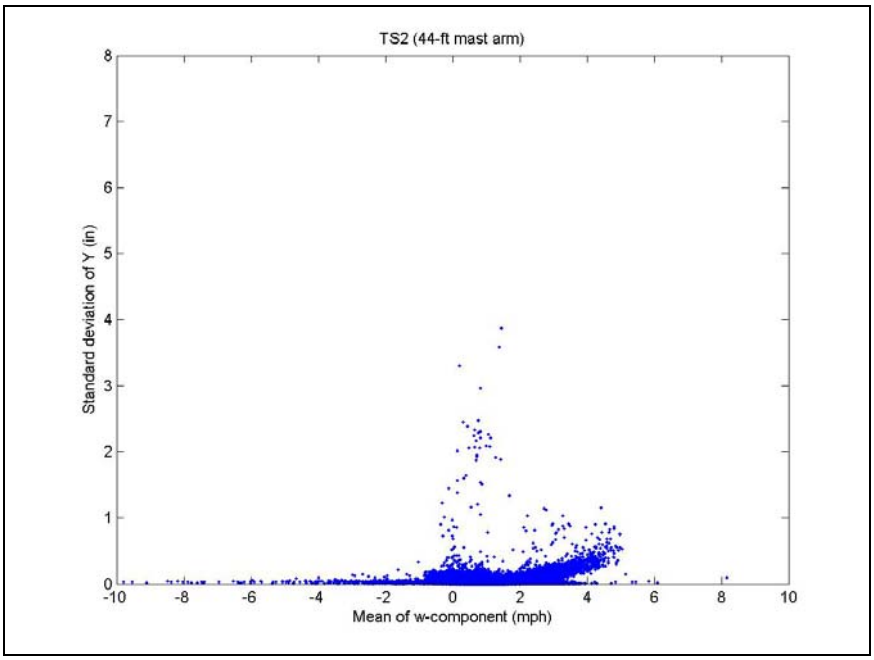

Figure A.16. Effect of w-component on vertical vibrations of TS2 with backplates

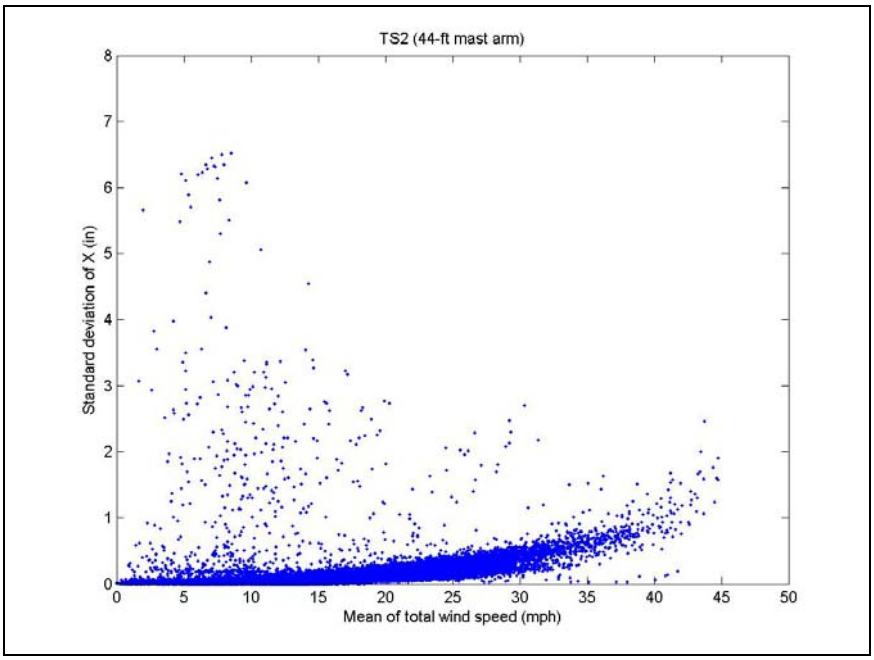

Figure A.17. Effect of total wind speed on horizontal vibrations of TS2 with backplates

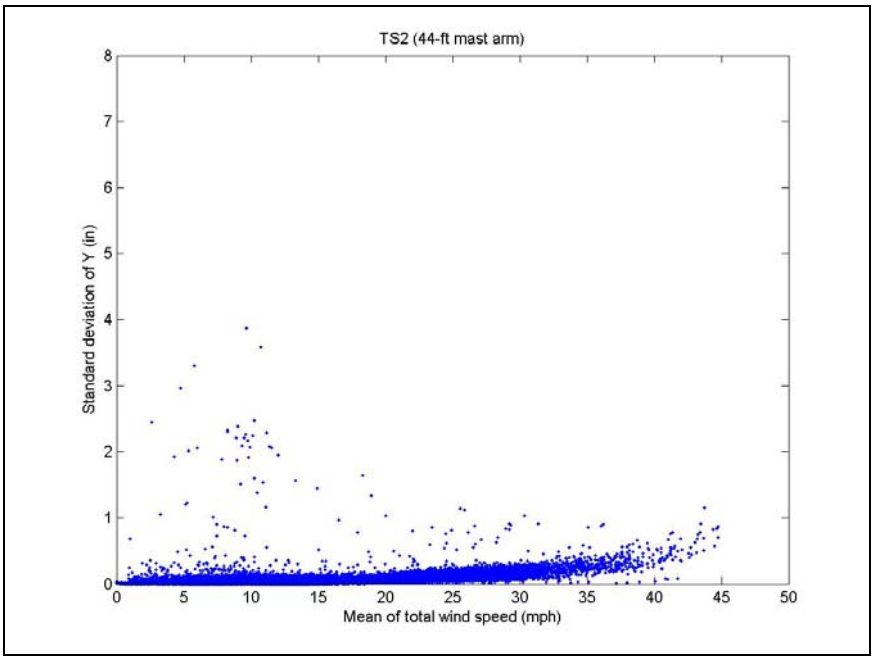

Figure A.18. Effect of total wind speed on vertical vibrations of TS2 with backplates

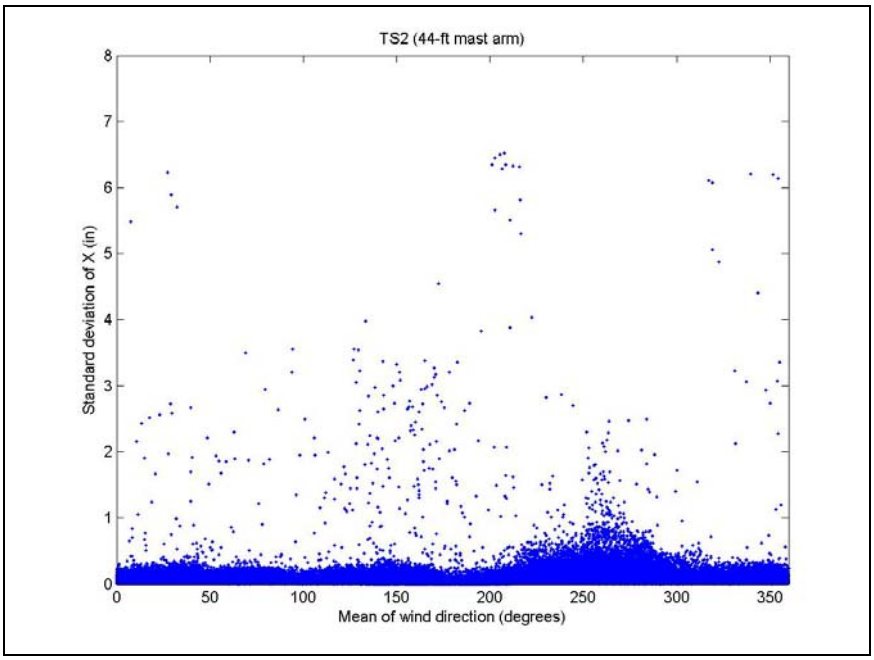

Figure A.19. Effect of wind direction on horizontal vibrations of TS2 with backplates

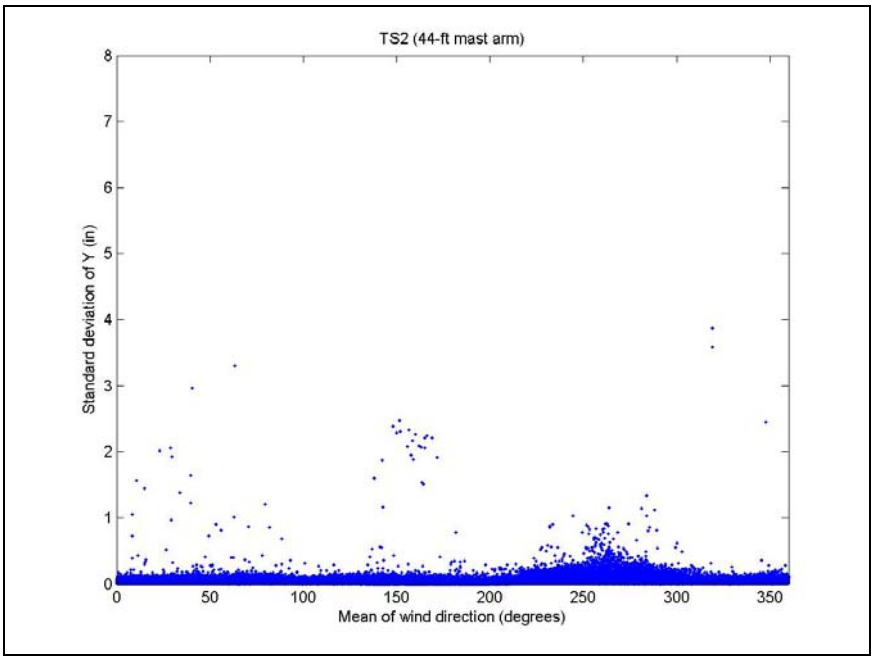

Figure A.20. Effect of wind direction on vertical vibrations of TS2 with backplates

APPENDIX B

MODE 1101 RESULTS

In this section, all the figures obtained by analyzing the data collected under Mode 1101 (arms pointing north, signals without backplates) are shown, as discussed in Section 3.3.3. A dot on a given plot represents two minutes of data. The sign convention of the angle of attack and of the wind speed components u and v is shown in Figure 3.10. The w-component is positive in the upward direction. X and Y refer to out-of-plane (or horizontal) and in-plane (or vertical) displacements of the tip of the arm, respectively.

TS1 (60-ft mast arm)

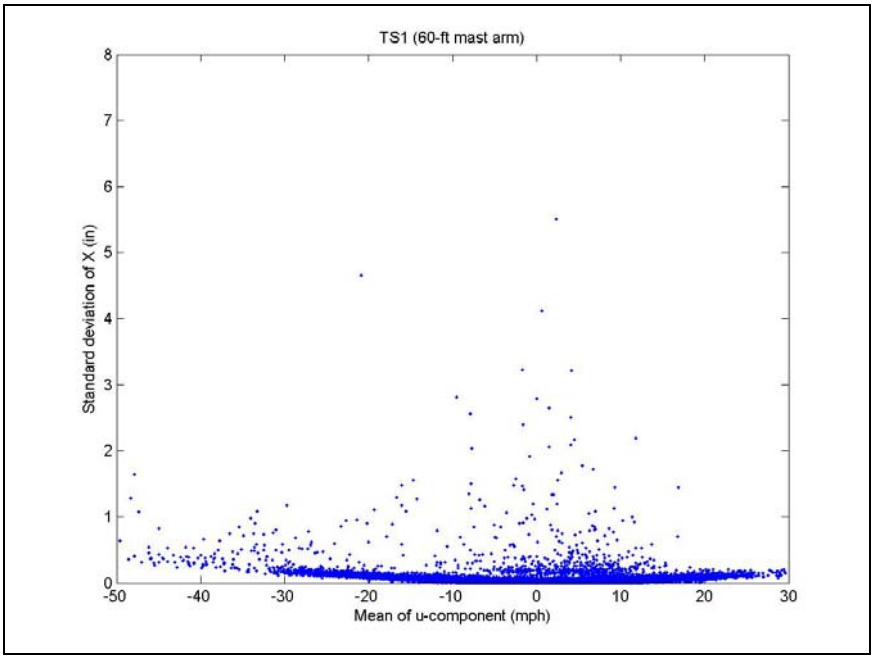

Figure B.1. Effect of u-component on horizontal vibrations of TS1 without backplates

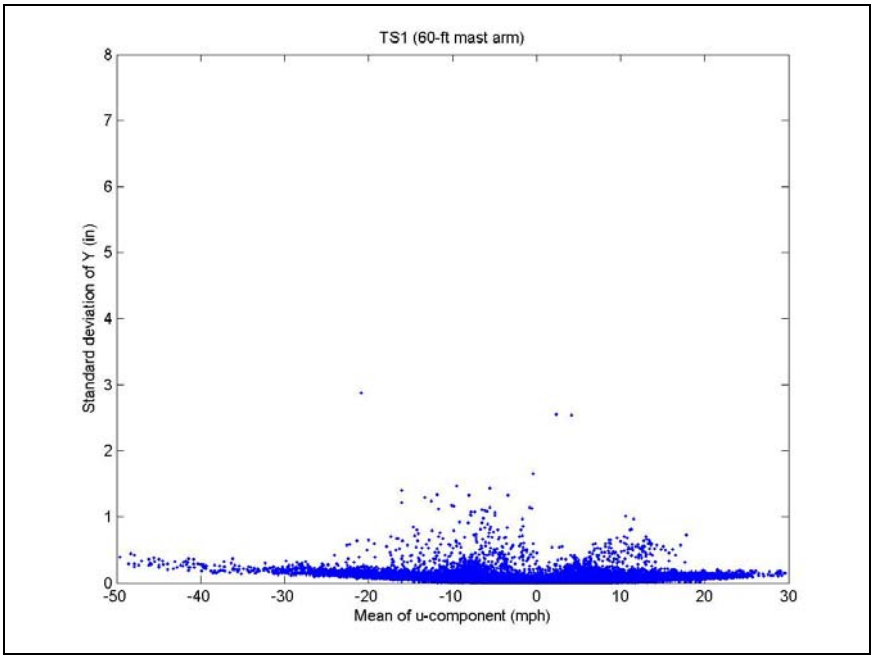

Figure B.2. Effect of u-component on vertical vibrations of TS1 without backplates

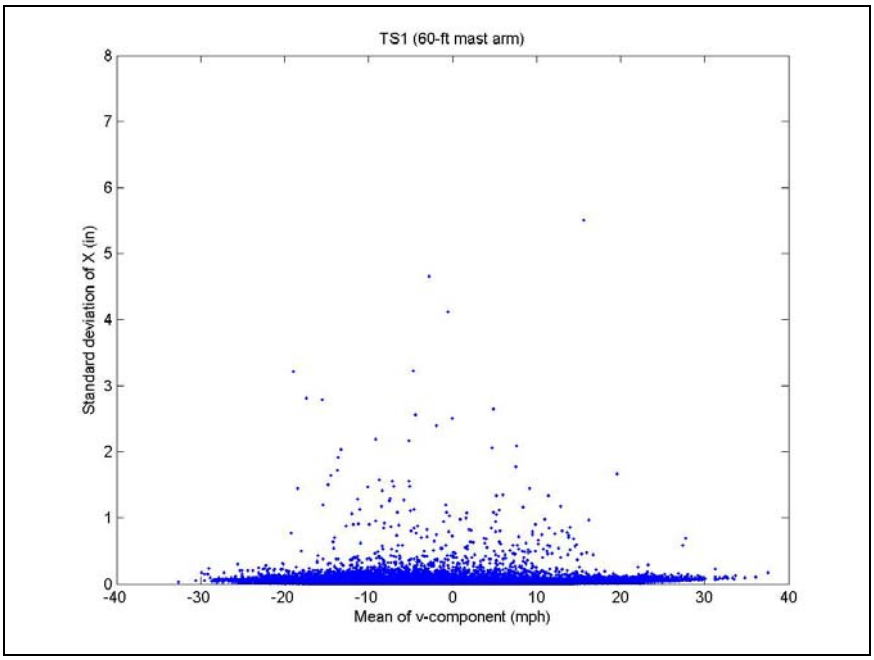

Figure B.3. Effect of v-component on horizontal vibrations of TS1 without backplates

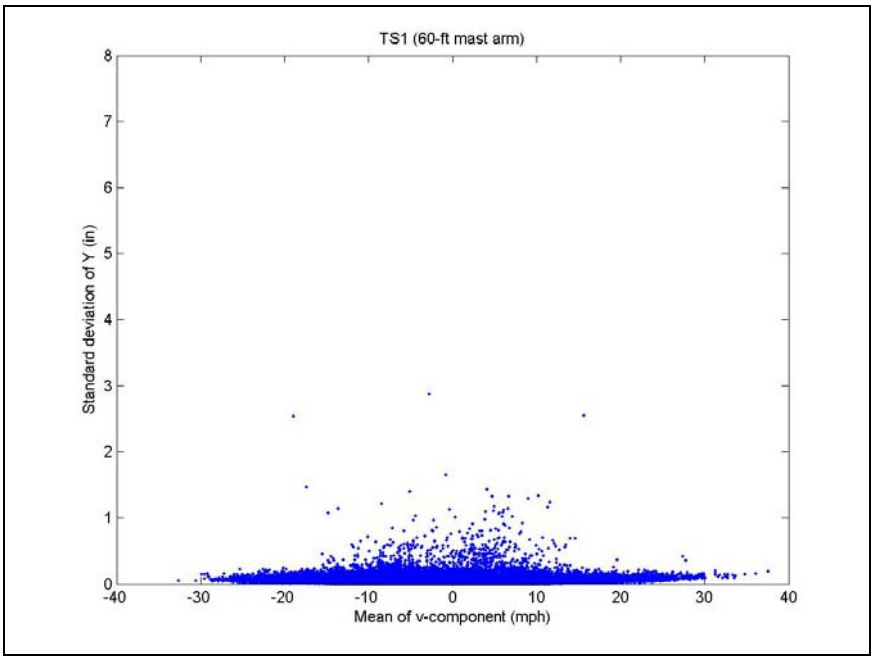

Figure B.4. Effect of v-component on vertical vibrations of TS2 without backplates

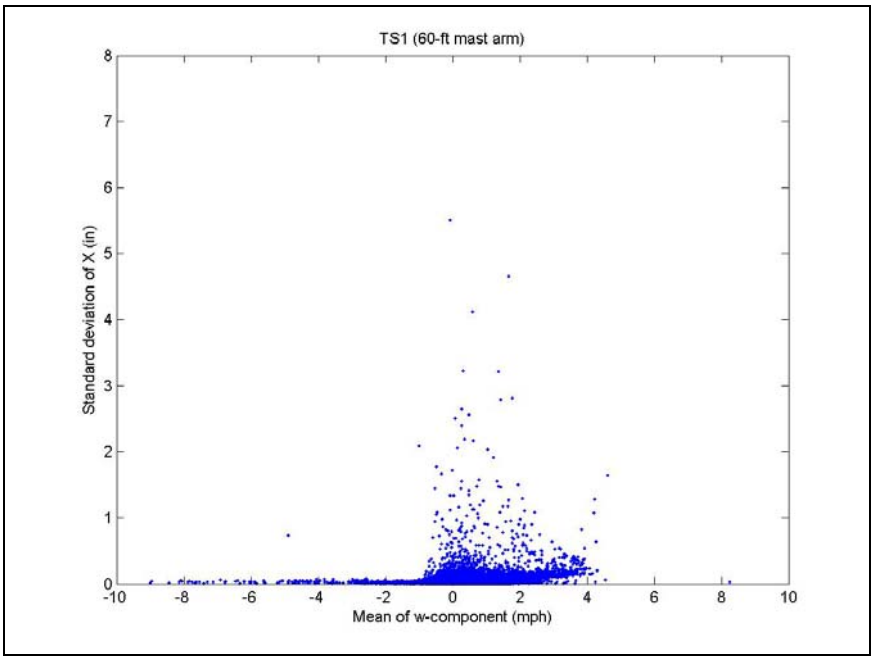

Figure B.5. Effect of w-component on horizontal vibrations of TS1 without backplates

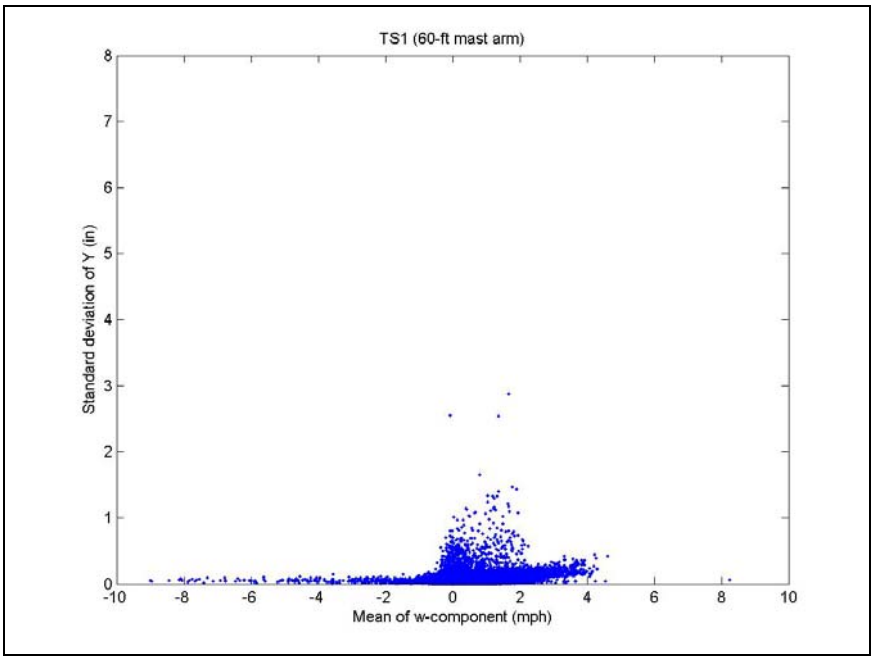

Figure B.6. Effect of w-component on vertical vibrations of TS1 without backplates

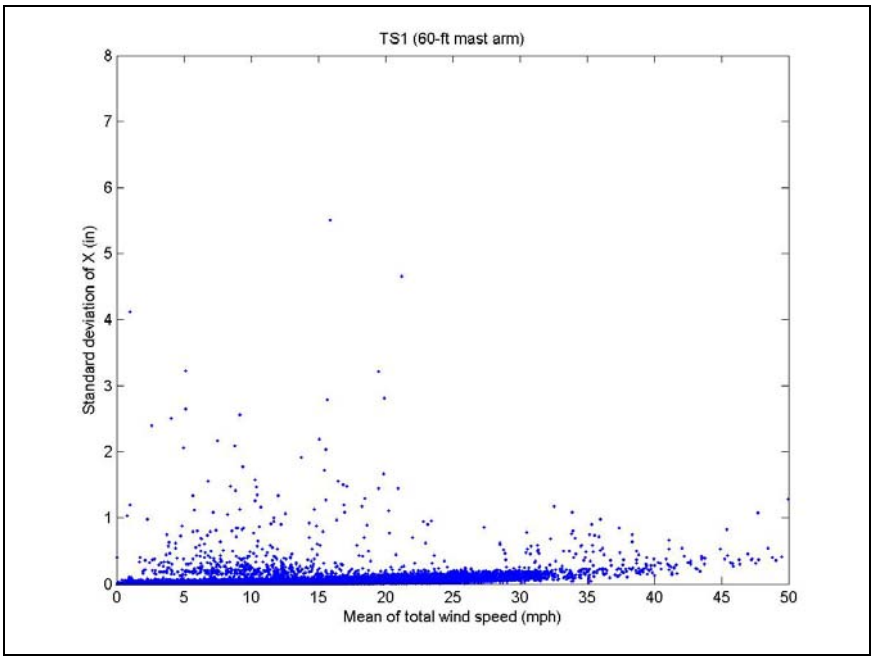

Figure B.7. Effect of total wind speed on horizontal vibrations of TS1 without backplates

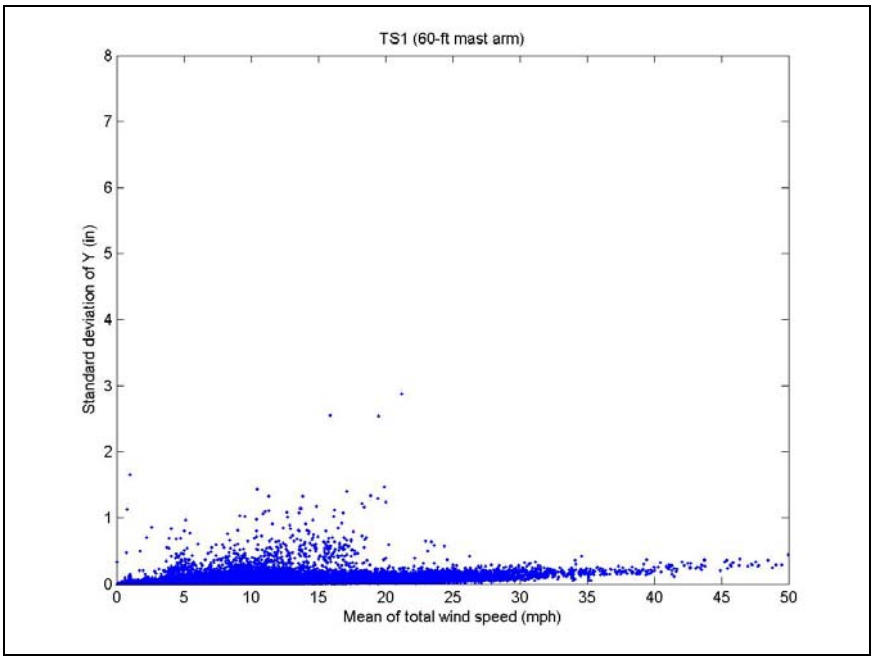

Figure B.8. Effect of total wind speed on vertical vibrations of TS1 without backplates

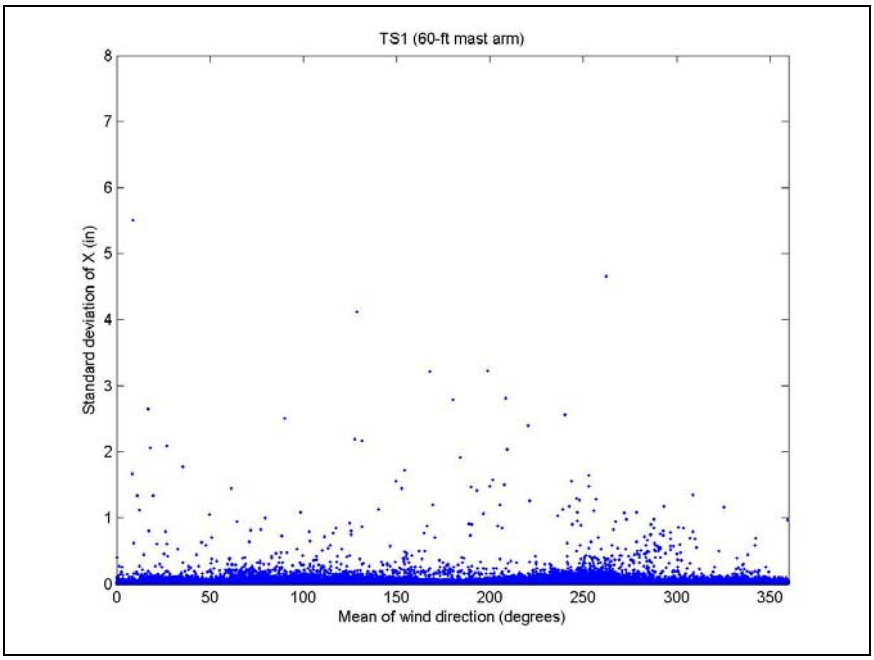

Figure B.9. Effect of wind direction on horizontal vibrations of TS1 without backplates

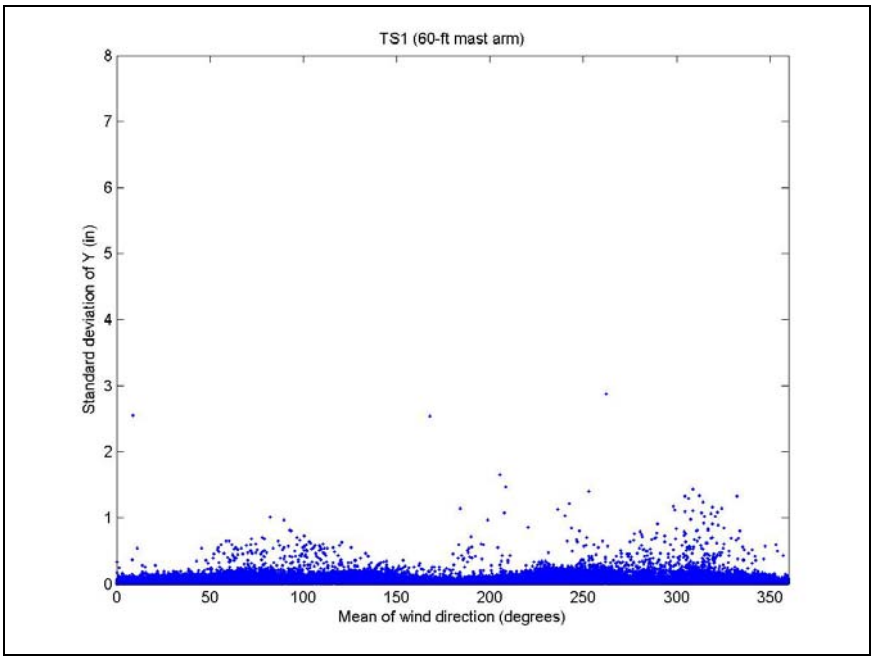

Figure B.10. Effect of wind direction on vertical vibrations of TS1 without backplates

TS2 (44-ft mast arm)

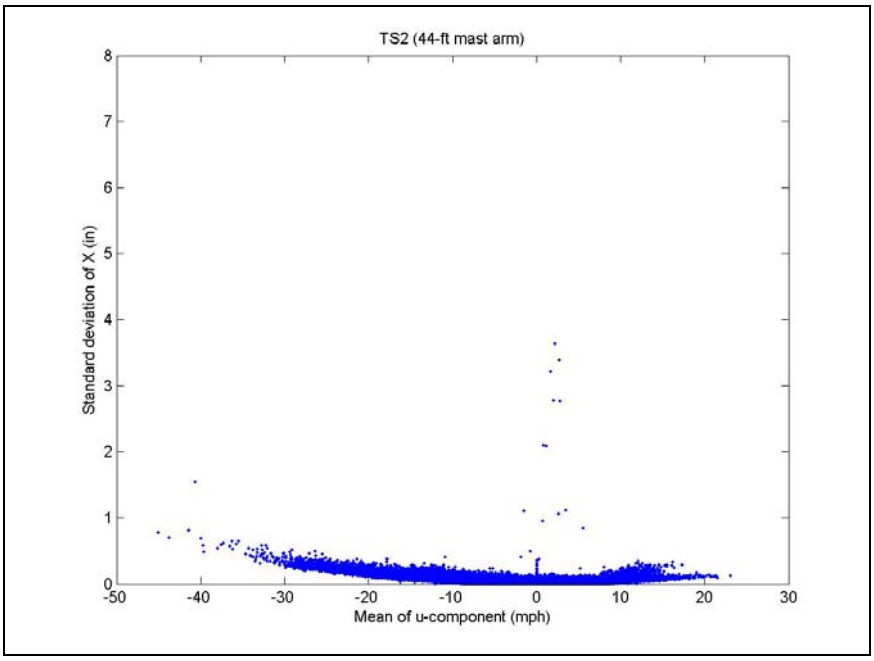

Figure B.11. Effect of u-component on horizontal vibrations of TS2 without backplates

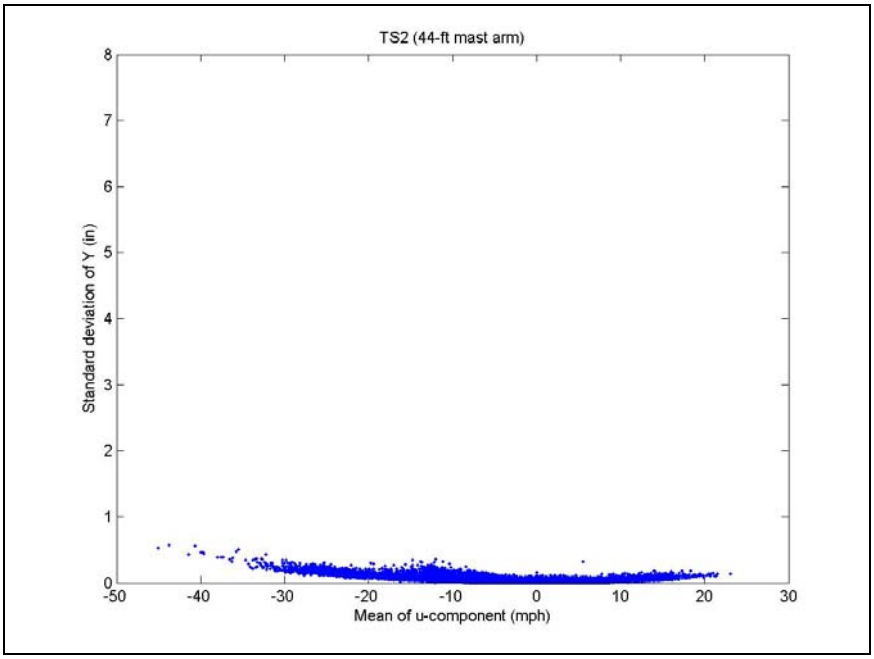

Figure B.12. Effect of u-component on vertical vibrations of TS2 without backplates

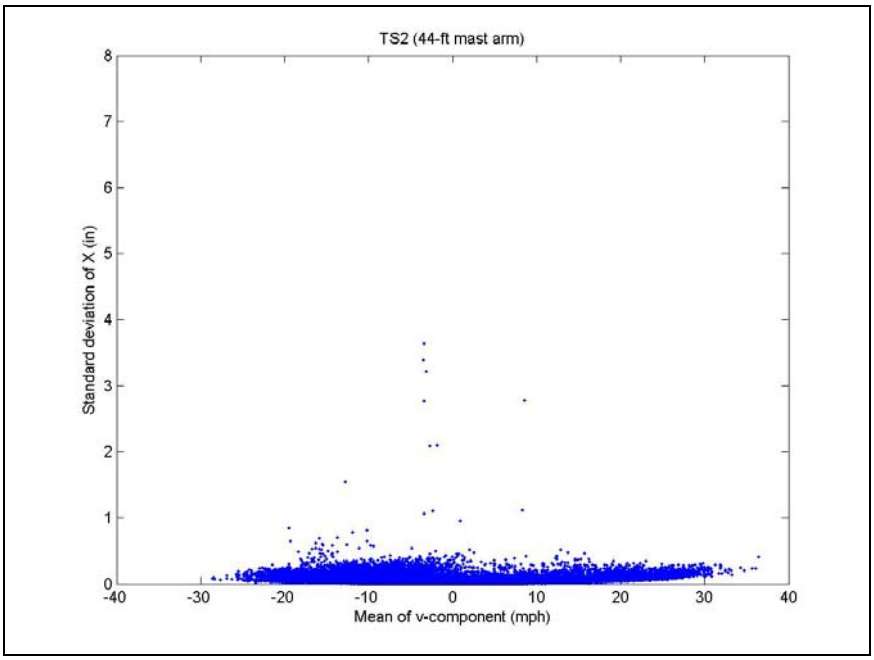

Figure B.13. Effect of v-component on horizontal vibrations of TS2 without backplates

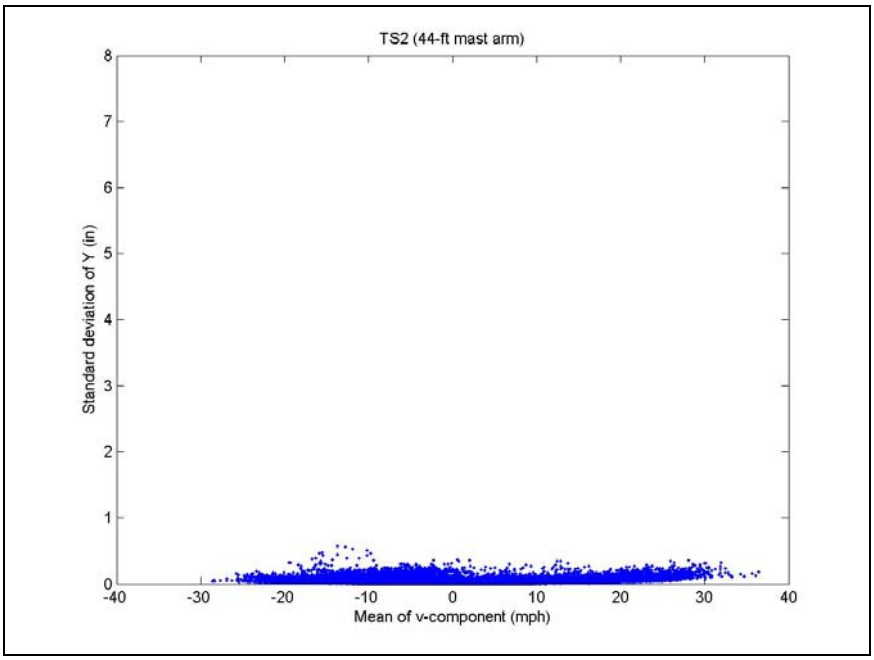

Figure B.14. Effect of v-component on vertical vibrations of TS2 without backplates

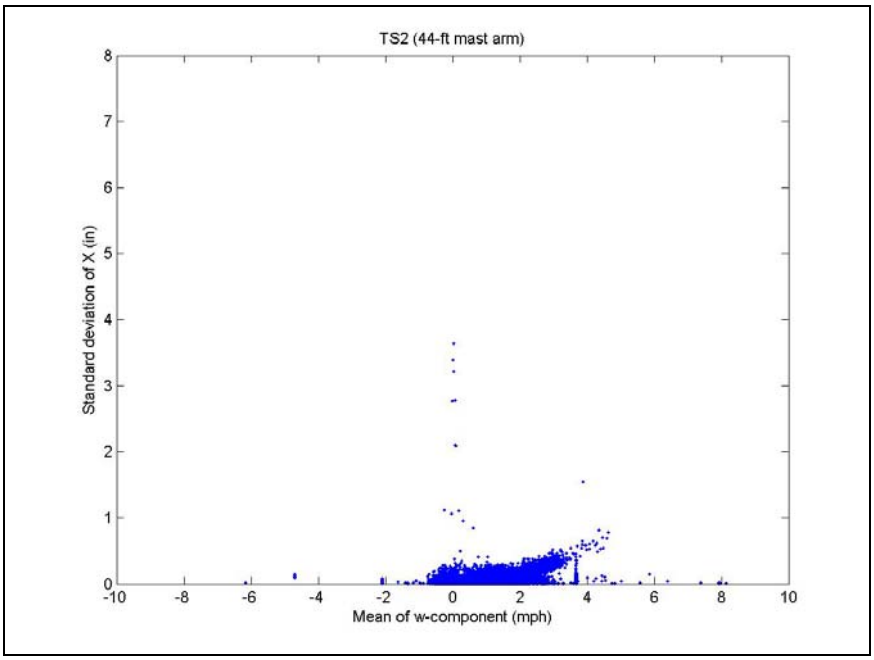

Figure B.15. Effect of w-component on horizontal vibrations of TS2 without backplates

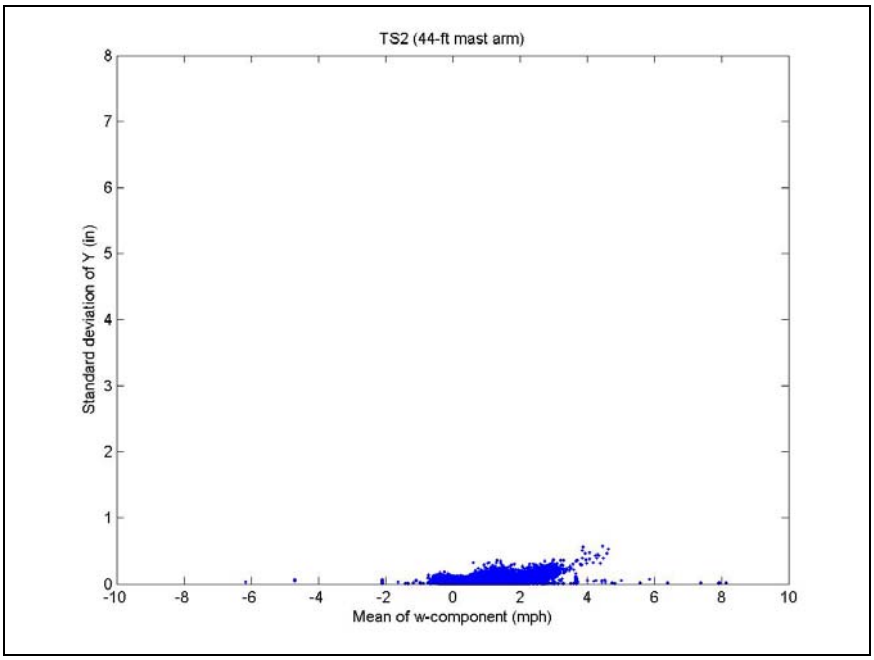

Figure B.16. Effect of w-component on vertical vibrations of TS2 without backplates

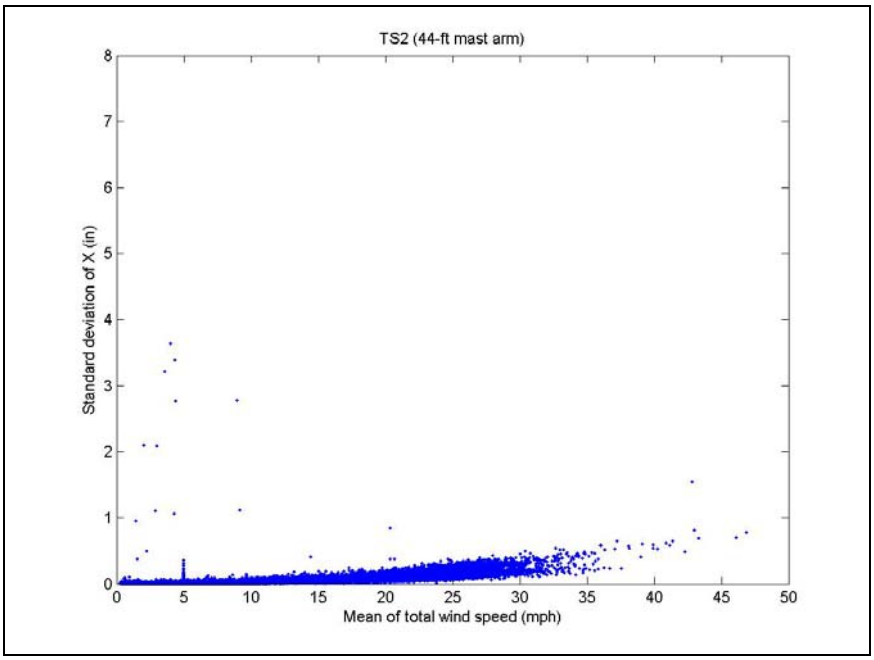

Figure B.17. Effect of total wind speed on horizontal vibrations of TS2 without backplates

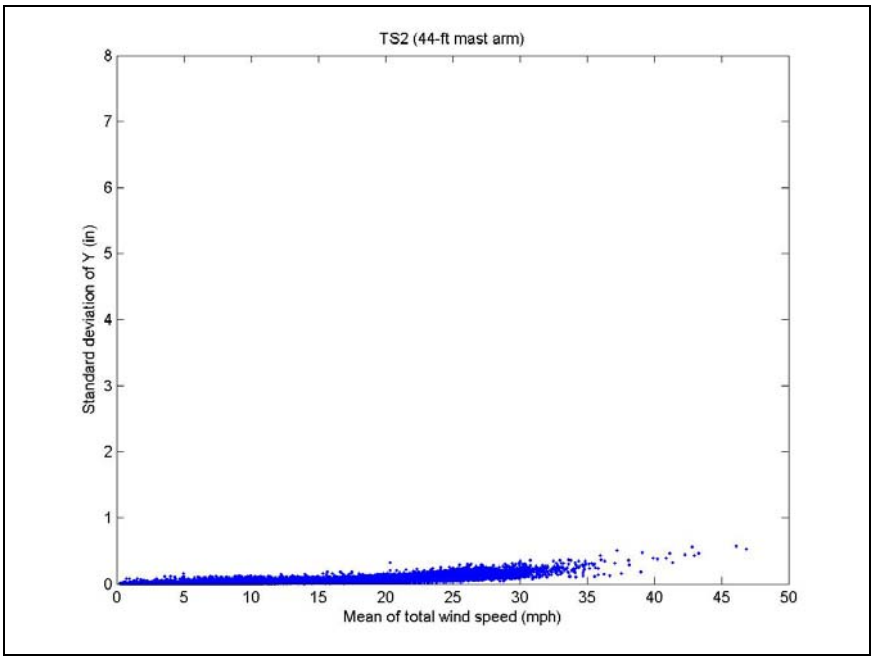

Figure B.18. Effect of total wind speed on vertical vibrations of TS2 without backplates

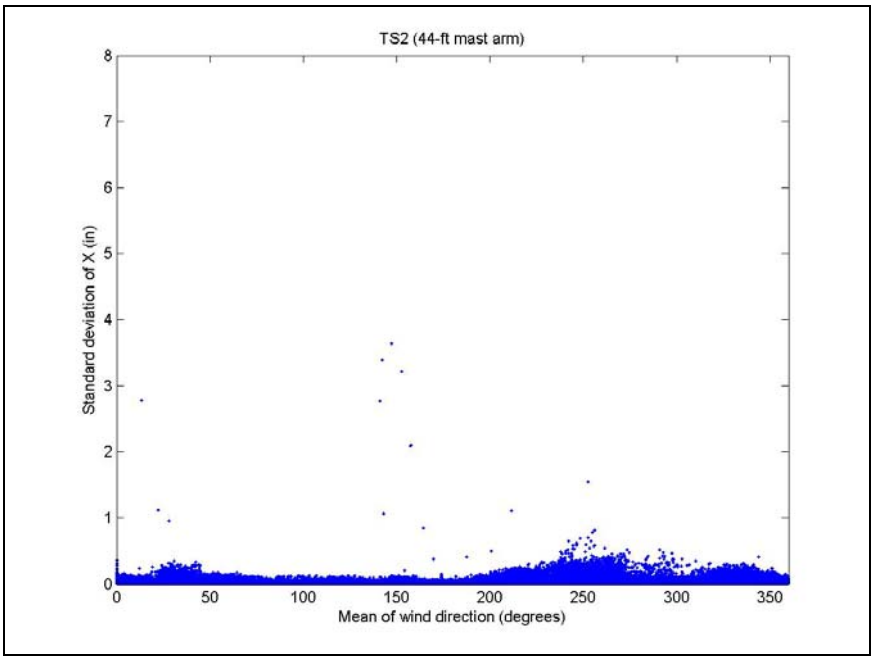

Figure B.19. Effect of wind direction on horizontal vibrations of TS2 without backplates

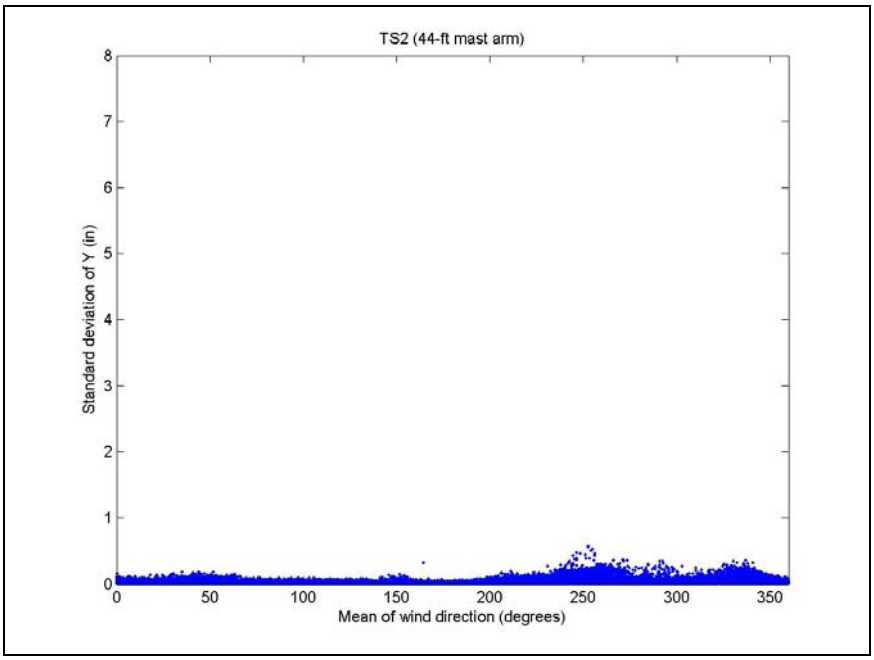

Figure B.20. Effect of wind direction on vertical vibrations of TS2 without backplates

APPENDIX C

JUSTIFICATION FOR ELIMINATION OF THE POLE FROM THE WIND TUNNEL MODEL

As discussed on Section 4.3.1, only the mast arm of a cantilever traffic signal structure was aeroelastically modeled for the wind tunnel experiments conducted for this research. The aeroelastic properties of the pole were not included into any of the models. To justify this, it was confirmed that the stiffness of the pole is much larger than the stiffness of the mast arm as shown in the following calculations.

To simplify calculations, an average outside diameter (*OD*) was computed for each the mast and the pole using the dimensions shown on Figure 3.3.

$$OD_{mast} = \frac{5.125'' + 11.4''}{2} = 8.2625'' \tag{C-1}$$

$$OD_{pole} = \frac{12'' + 14.5''}{2} = 13.25'' \tag{C-2}$$

With the average outside diameter, and knowing the thickness (*t*) of each of the elements (also shown in Figure 3.3), a moment of inertia (*I*) was calculated for each the mast and the pole.

$$I = \frac{\pi}{64}[(OD)^4 - (OD - 2t)^4] \tag{C-3}$$

$$I_{mast} = \frac{\pi}{64}[(8.2625)^4 - (8.2625 - 2 \times 0.25)^4] = 50.55\,\text{in}^4 \tag{C-4}$$

$$I_{pole} = \frac{\pi}{64}[(13.25)^4 - (13.25 - 2 \times 0.375)^4] = 314.56\,\text{in}^4 \tag{C-5}$$

The mast and the pole of a cantilever traffic signal structure are each essentially a cantilever beam. Columns 1 and 2 of Table C-1 show common loading cases for cantilever beams as well as the equations to calculate the stiffness (k) for each case. Columns 3 and 4 show the stiffness values calculated for each the mast and the pole using the appropriate equations. For the calculations, the lengths (L) were also taken from Figure 3.3 and the modulus of elasticity (E) for steel was taken as 29,000 ksi. Column 5 shows the ratio of the pole stiffness to the mast stiffness, which clearly demonstrate that the pole is much stiffer than the mast arm.

Table C.1. Stiffness calculations

Loading Case (1)	k (2)	k_{mast} (3)	k_{pole} (4)	k_{pole} / k_{mast} (5)
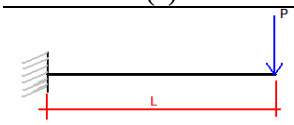	$\frac{3EI}{L^3}$	0.299 kips/in	2.109 kips/in	70.6
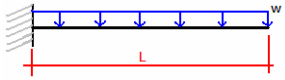	$\frac{8EI}{L^4}$	.000151 kips/in^2	.0239 kips/in^2	158.6
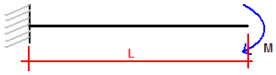	$\frac{2EI}{L^2}$	10.51 kips-in/in	330.4 kips-in/in	31.4

APPENDIX D

TEXAS TECH WIND TUNNEL RESULTS

In this section all the figures obtained by analyzing the data collected in the wind tunnel experiments conducted at Texas Tech University are shown, as discussed in Section 4.4. The sign convention of the angle of attack is the same one used for the full-scale experiments and is shown in Figure 3.10. In these figures, BP stands for backplates.

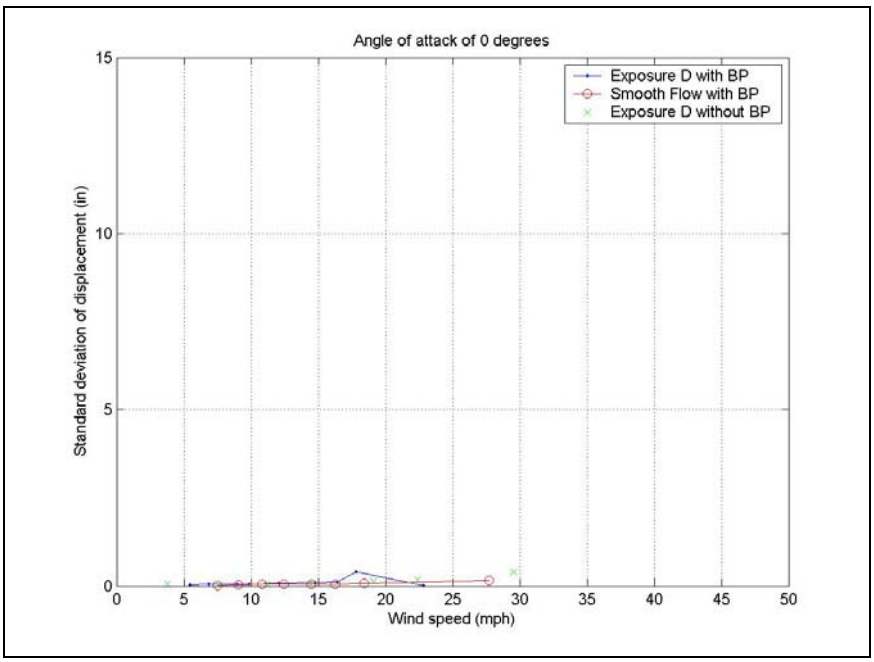

Figure D.1. Wind tunnel results for angle of attack of 0 degrees

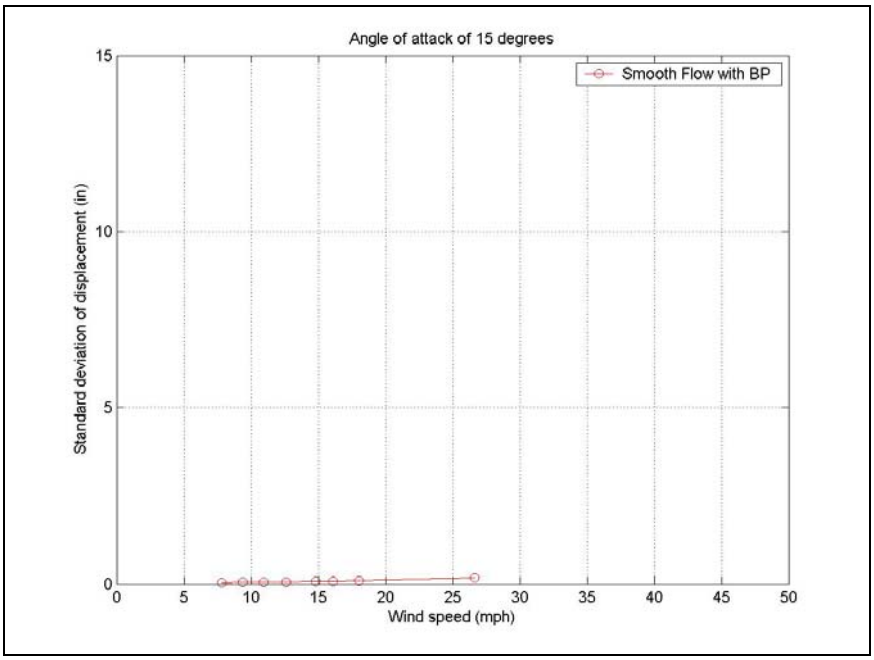

Figure D.2. Wind tunnel results for angle of attack of 15 degrees

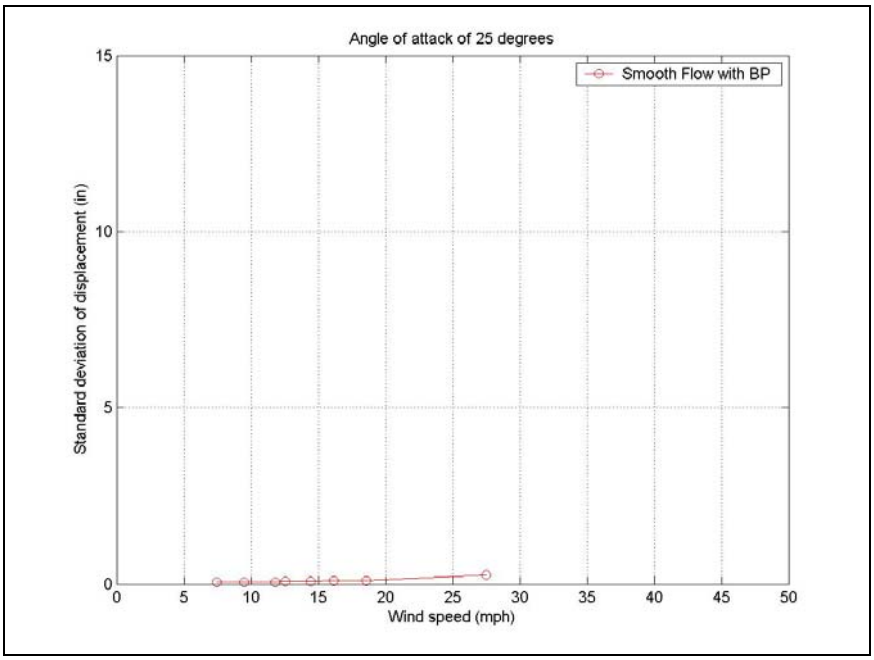

Figure D.3. Wind tunnel results for angle of attack of 25 degrees

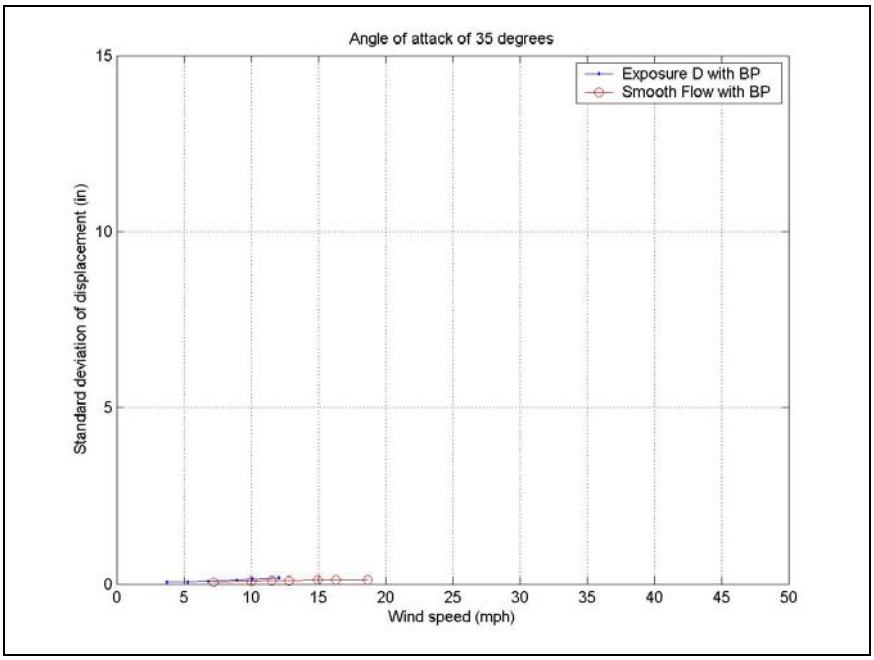

Figure D.4. Wind tunnel results for angle of attack of 35 degrees

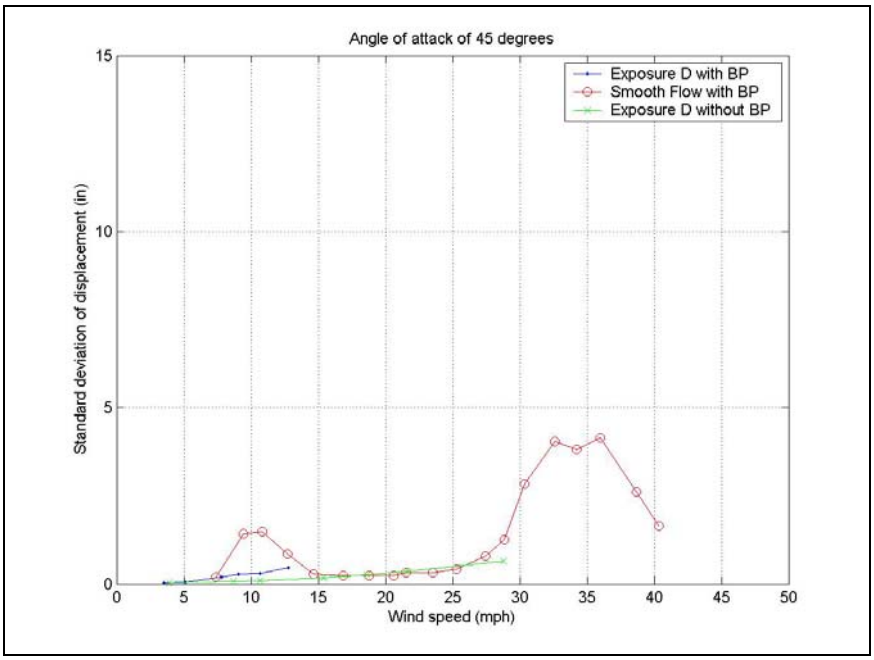

Figure D.5. Wind tunnel results for angle of attack of 45 degrees

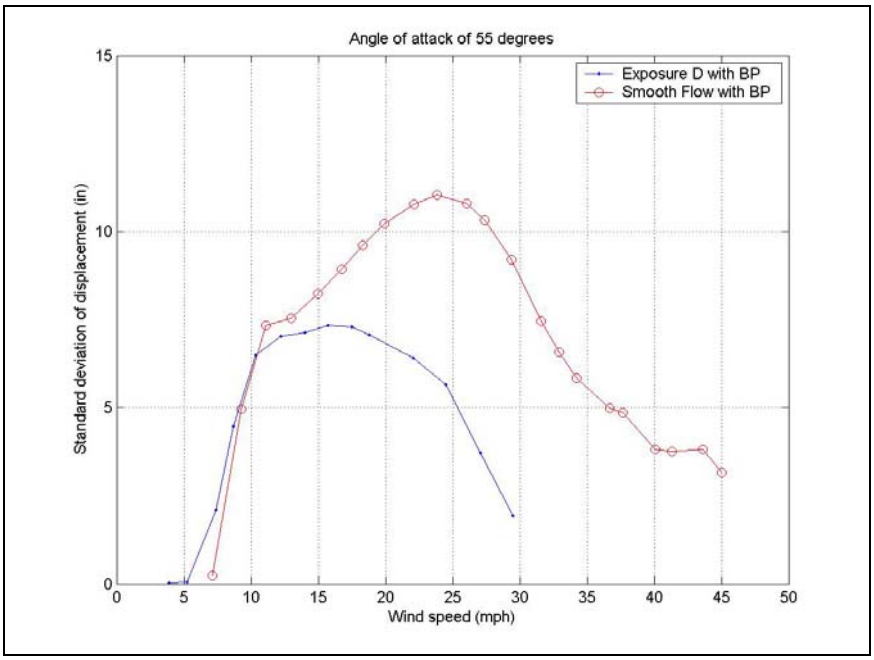

Figure D.6. Wind tunnel results for angle of attack of 55 degrees

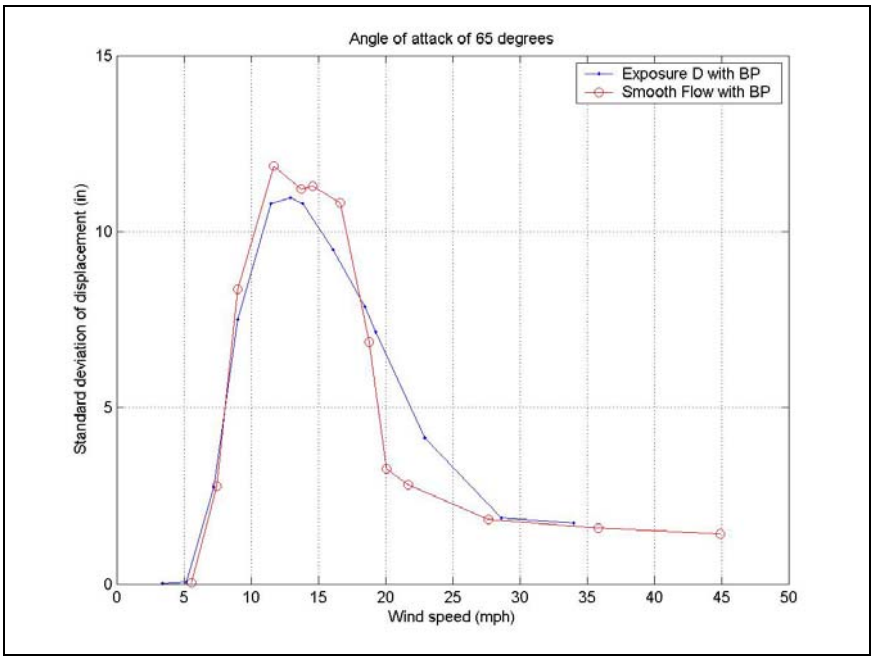

Figure D.7. Wind tunnel results for angle of attack of 65 degrees

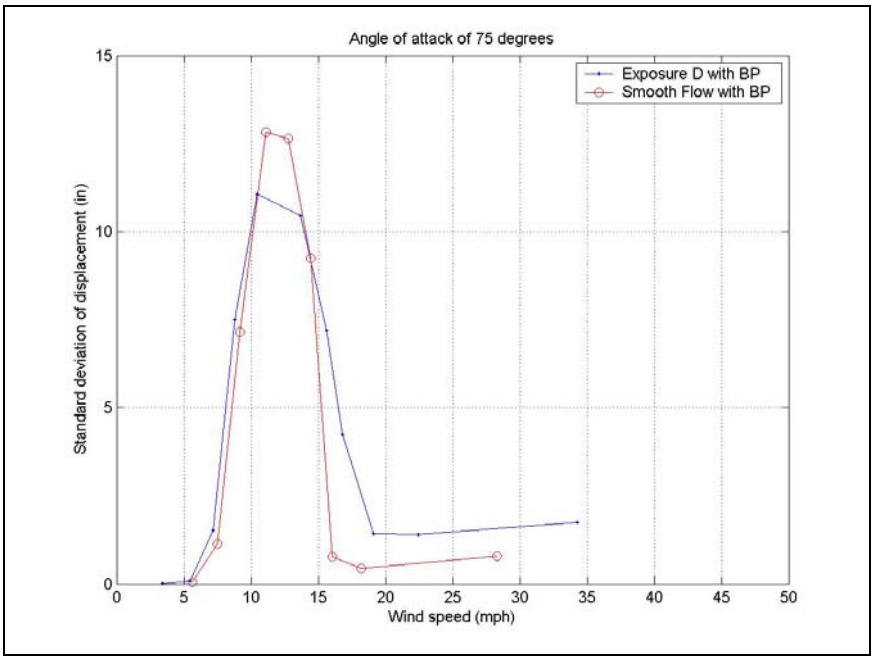

Figure D.8. Wind tunnel results for angle of attack of 75 degrees

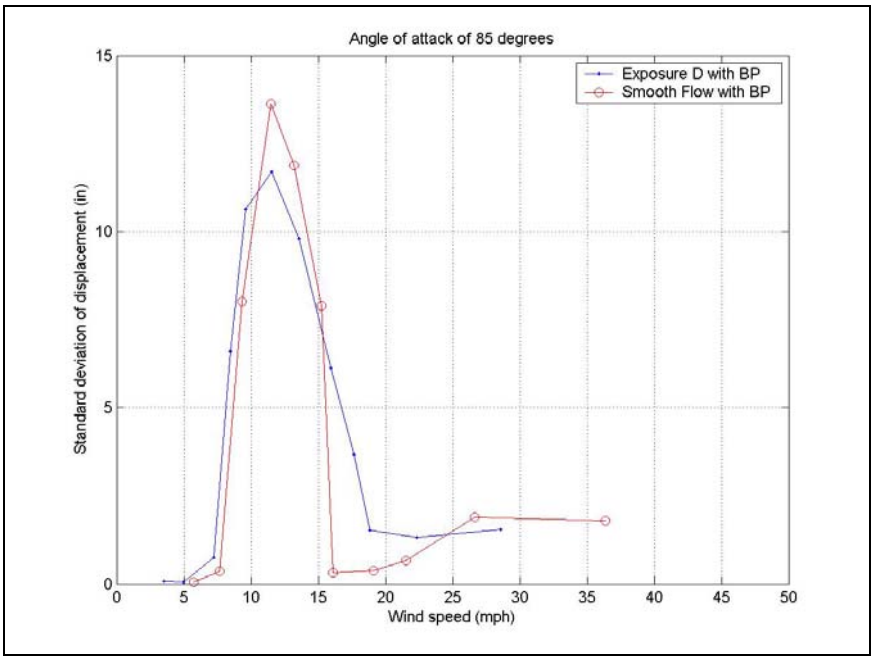

Figure D.9. Wind tunnel results for angle of attack of 85 degrees

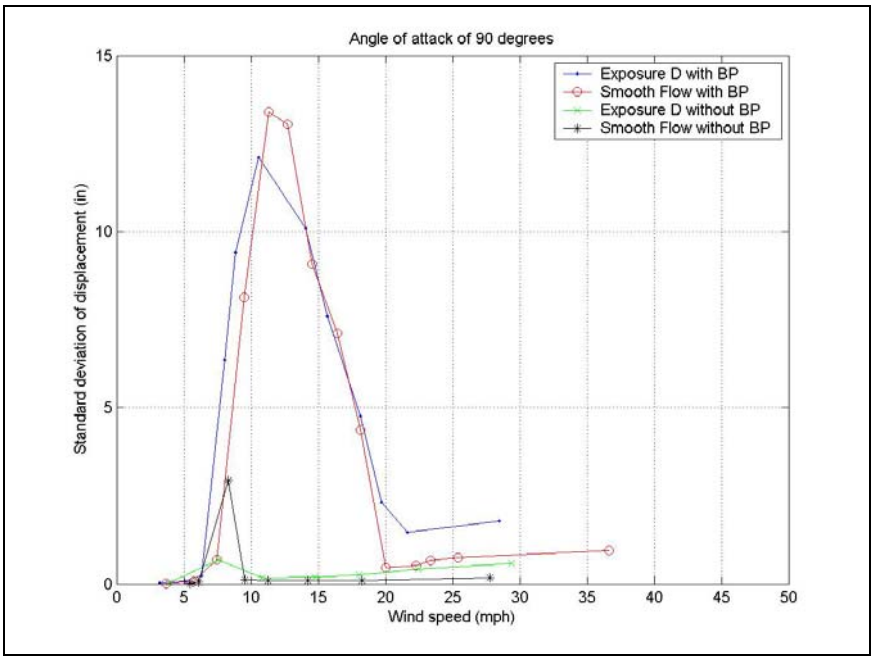

Figure D.10. Wind tunnel results for angle of attack of 90 degrees

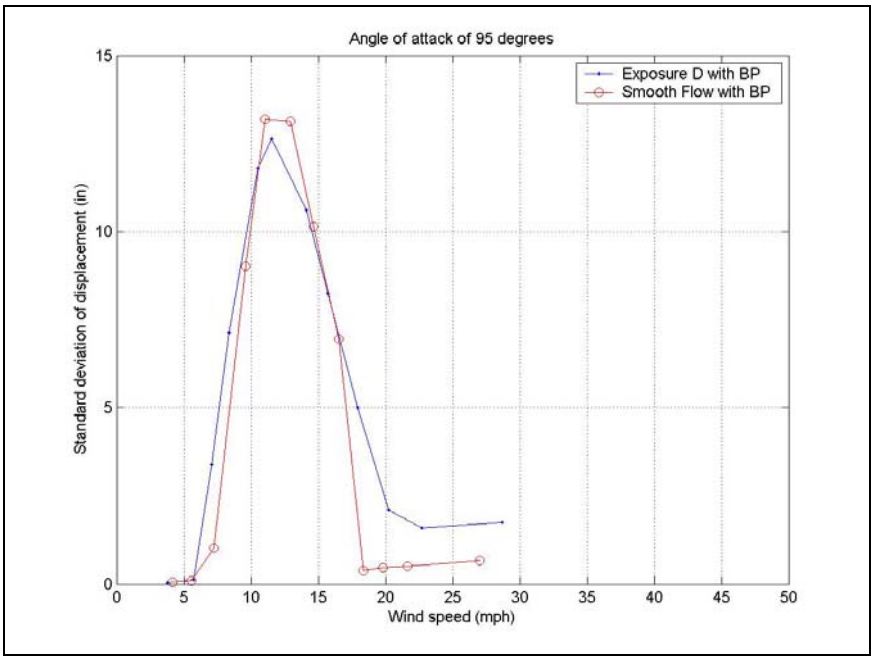

Figure D.11. Wind tunnel results for angle of attack of 95 degrees

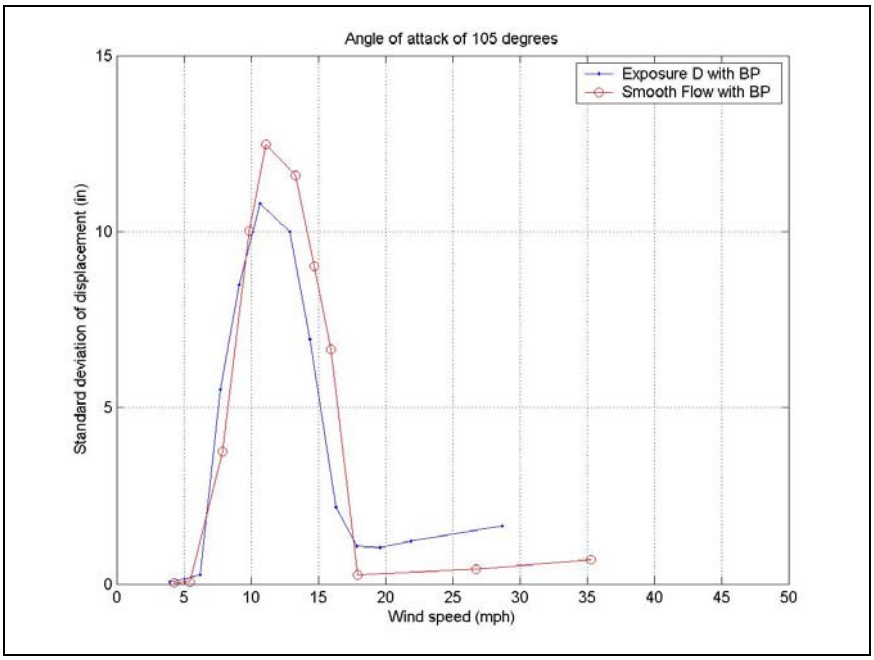

Figure D.12. Wind tunnel results for angle of attack of 105 degrees

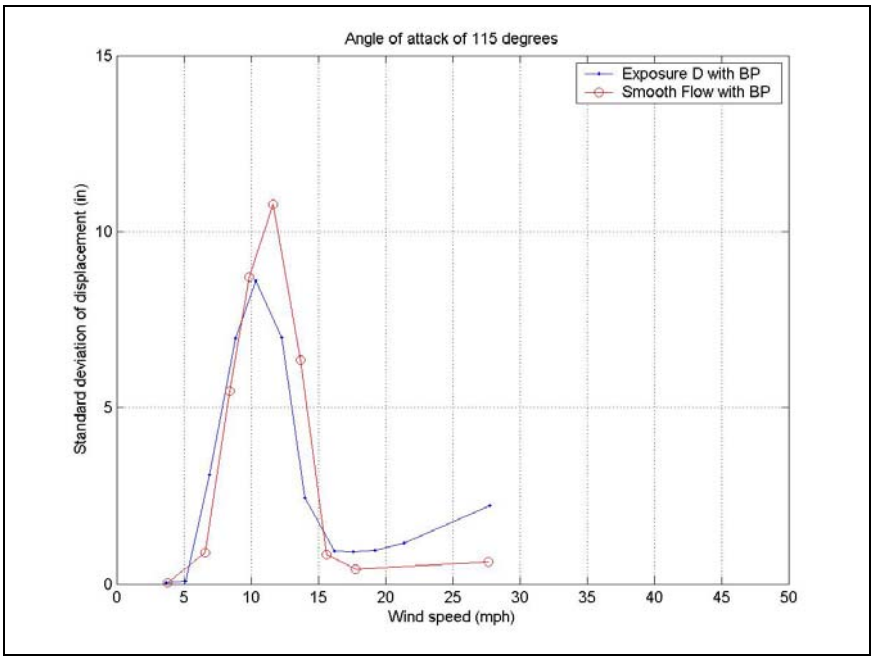

Figure D.13. Wind tunnel results for angle of attack of 115 degrees

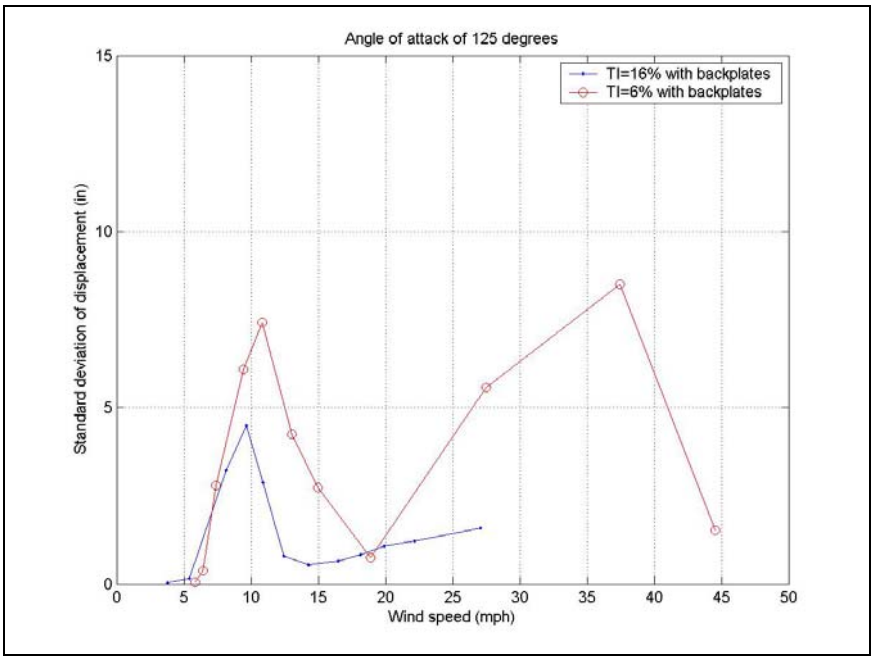

Figure D.14. Wind tunnel results for angle of attack of 125 degrees

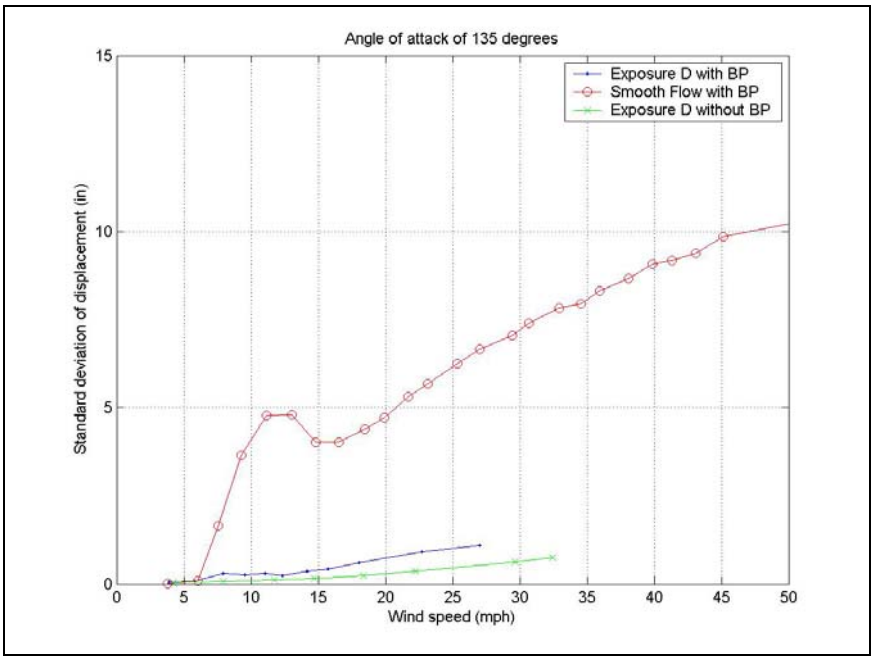

Figure D.15. Wind tunnel results for angle of attack of 135 degrees

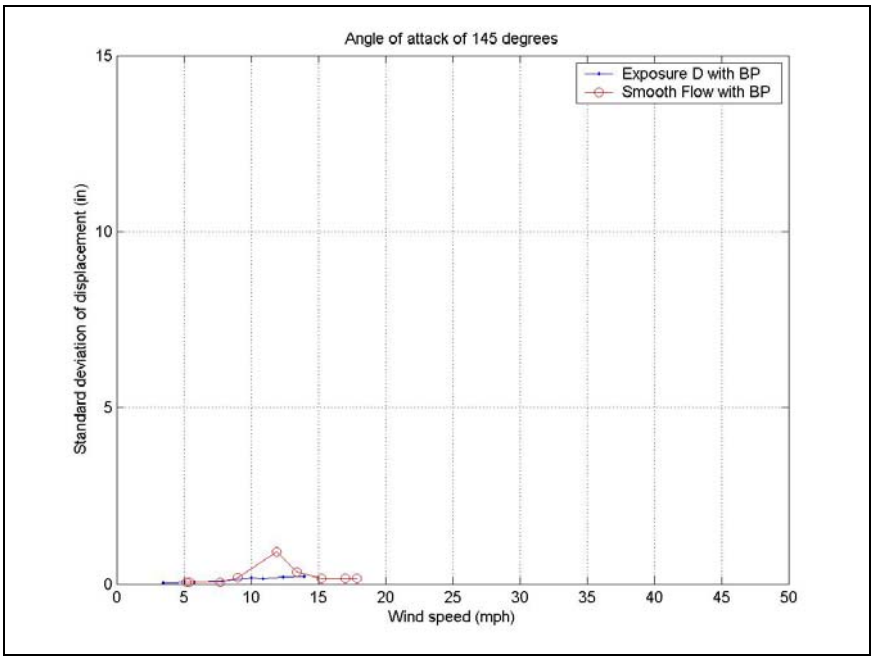

Figure D.16. Wind tunnel results for angle of attack of 145 degrees

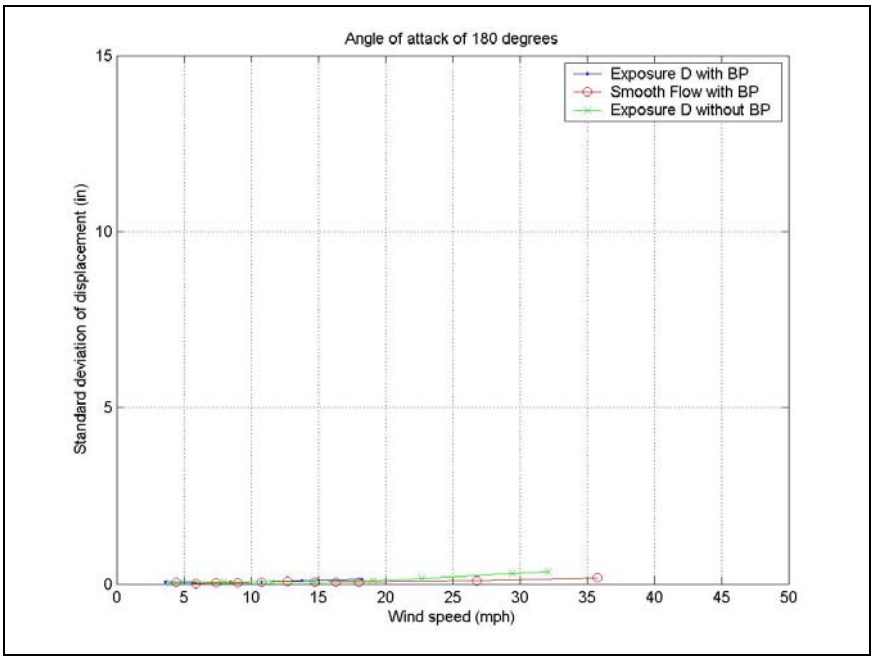

Figure D.17. Wind tunnel results for angle of attack of 180 degrees

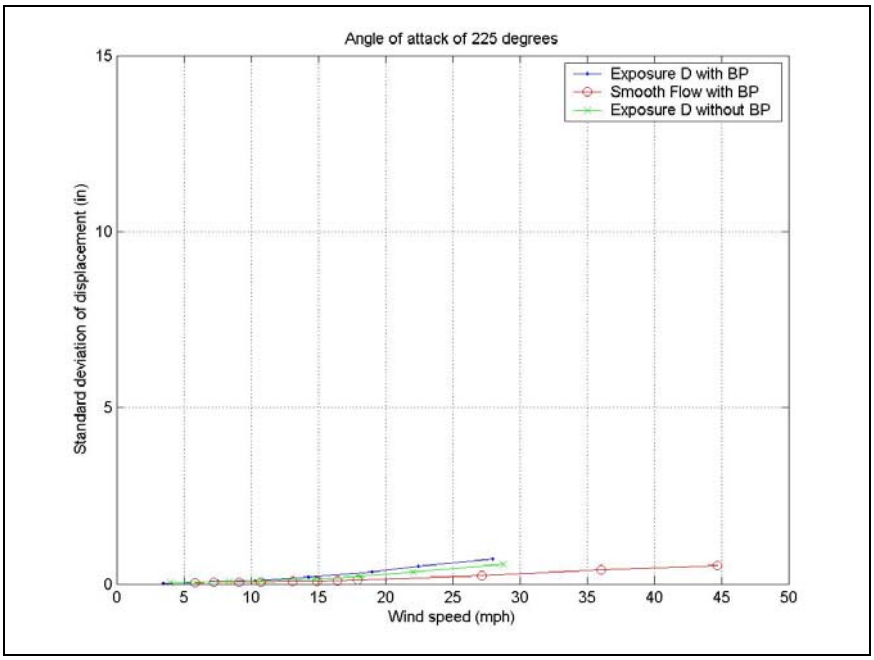

Figure D.18. Wind tunnel results for angle of attack of 225 degrees

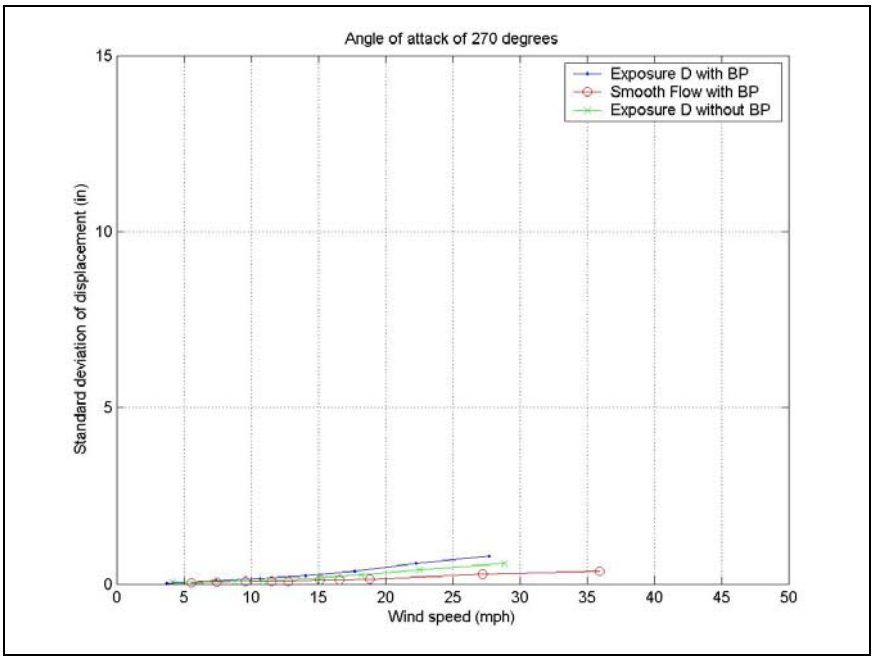

Figure D.19. Wind tunnel results for angle of attack of 270 degrees

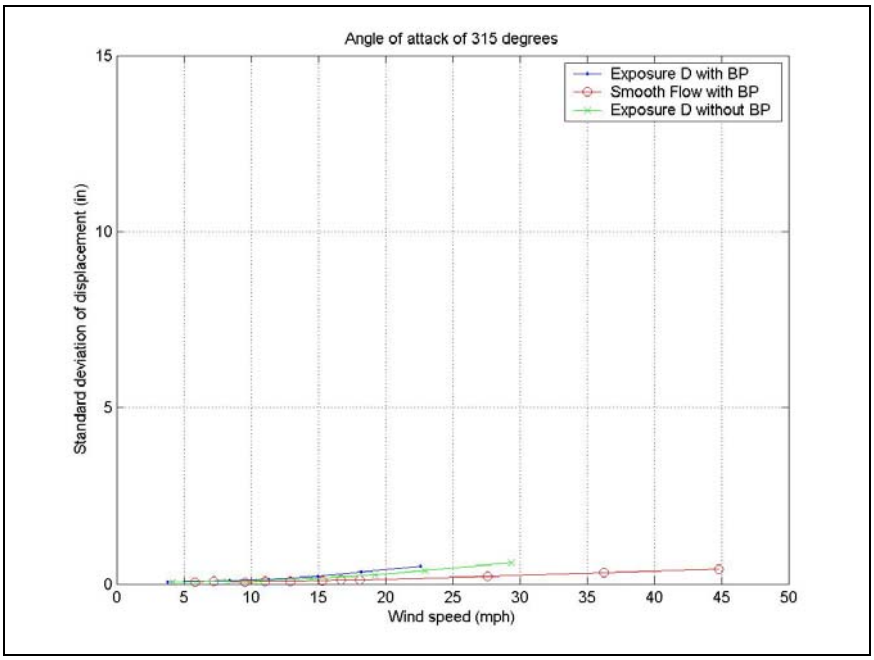

Figure D.20. Wind tunnel results for angle of attack of 315 degrees

APPENDIX E

FULL-SCALE EXPERIMENTS WITH VENTED BACKPLATES AND DAMPING PLATES

E. 1 Introduction

This appendix is an addendum to the report titled *Risk assessment model for wind-induced fatigue failure of cantilever traffic signal structures*. The addendum discusses the full-scale experiments that were not covered in the original report. These are the experiments performed under Modes 1103 and 1105.

For Mode 1103, data was collected when the full-scale structures had signals with vented backplates and the arms pointing southeast. Meanwhile, Mode 1105 was conducted while the signals had regular backplates and with the arms pointing southeast and having damping plates. Otherwise, both modes were conducted with the same experimental setup as discussed in the original report. Like before, the anemometer was oriented so that positive u and v were measured as shown on Figure 1, with w being the vertical component which is positive going upwards. Also shown on Figure 1 is the angle of attack sign convention.

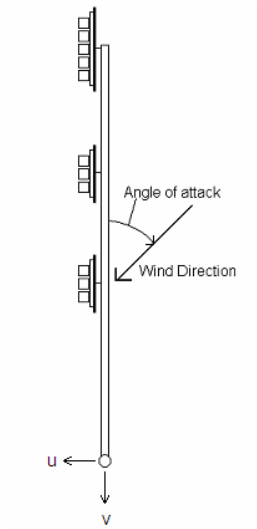

Figure E. 1. Anemometer Orientation and Angle of Attack Sign Convention

E. 2 Mode 1103

From March to June 2007, data was collected under Mode 1103 with the arm pointing southeast and the signals having vented backplates. The vented backplates are similar to the regular backplates used in Mode 1100, except that these backplates have louvers. During this period, 2613 hours of data were collected for TS1 and 2481 hours were collected for TS2. As usual, all the data was analyzed by dividing the long time histories into 2-minute segments, calculating summary statistics for different measured parameters, and plotting graphs. The graphs for TS1 are presented here as Figures 2 to 11, while the graphs for TS2 are presented as Figures 12 to 21. Outlying data points have been retained for completeness and have not been individually validated.

Paying close attention to the vertical vibrations (Y) of the arm of TS1, it can be seen in Figures 3, 5, 7, 9, and 11 that there were very few occasions when the standard

deviation of Y was over 2 inches. Still, higher than average values of the standard deviation of Y were observed for the following conditions:

- When the mean of the u-component was about -10 mph (as shown in Figure 3).
- When the mean of the v-component was about 8 mph (as shown in Figure 5).
- When the mean of the total wind speed was about 12 mph (as shown in Figure 9).
- When the mean wind direction was about 300 degrees (as shown in Figure 11).

For the case of TS2, there were a few more instances of the standard deviation of Y being over 2 inches, but there were no discernible patterns.

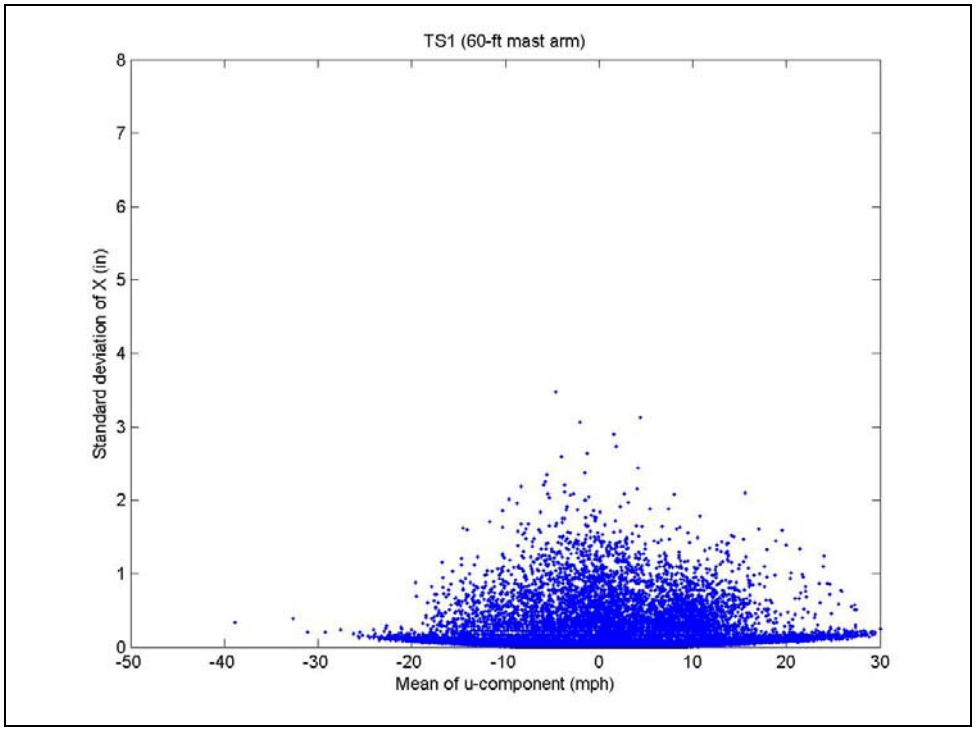

Figure E. 2. Effect of u-component on horizontal vibrations of TS1 with vented backplates

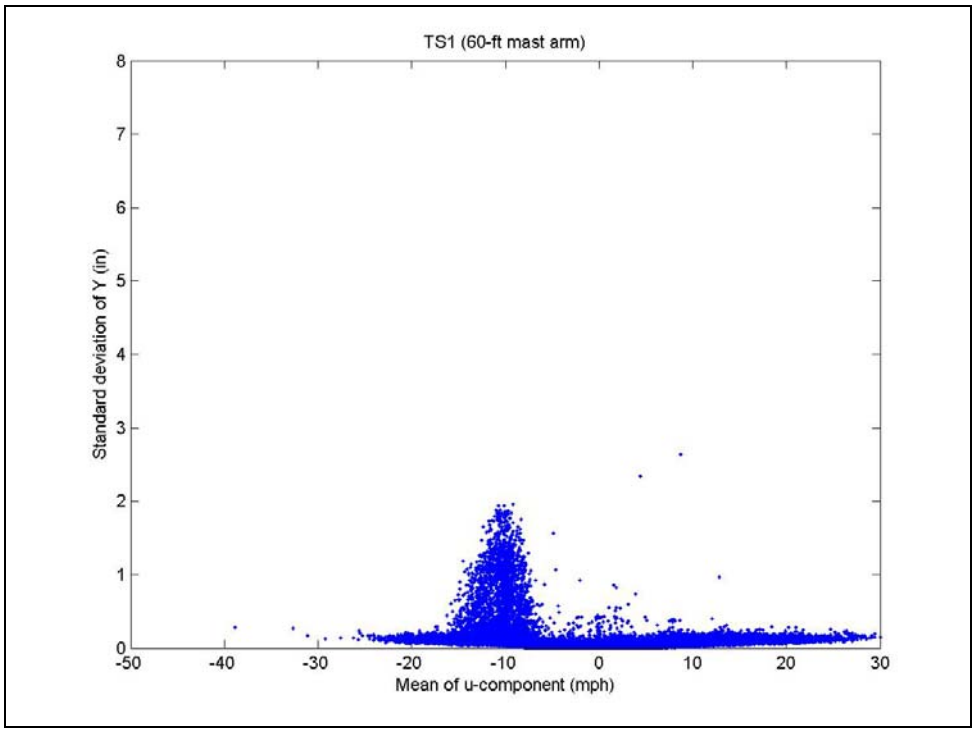

Figure E. 3. Effect of u-component on vertical vibrations of TS1 with vented backplates

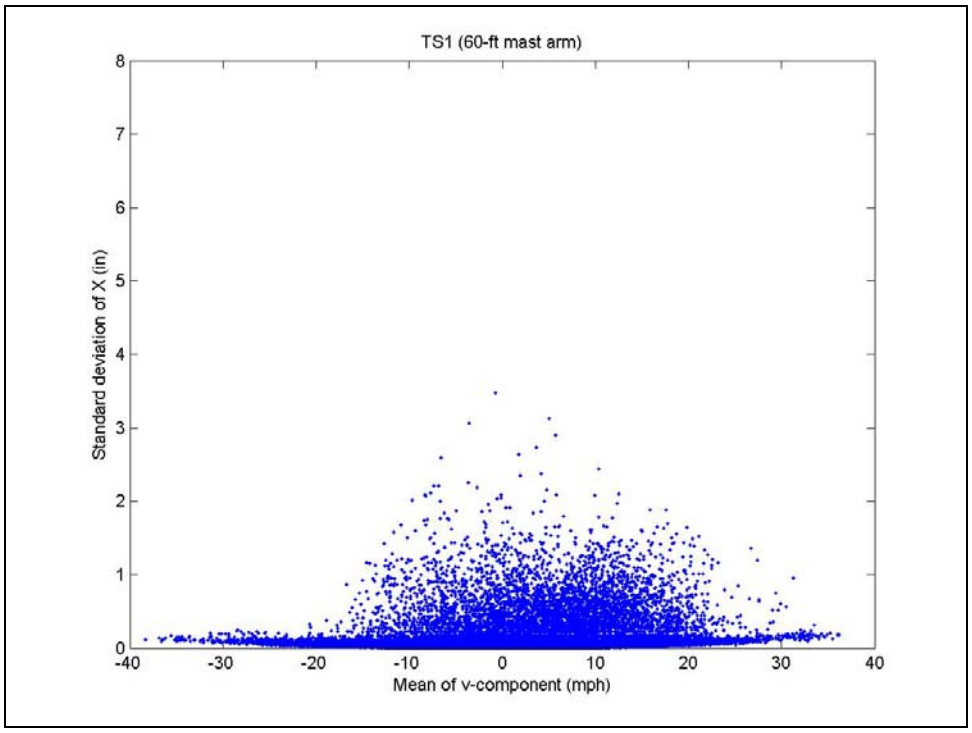

Figure E. 4 Effect of v-component on horizontal vibrations of TS1 with vented backplates

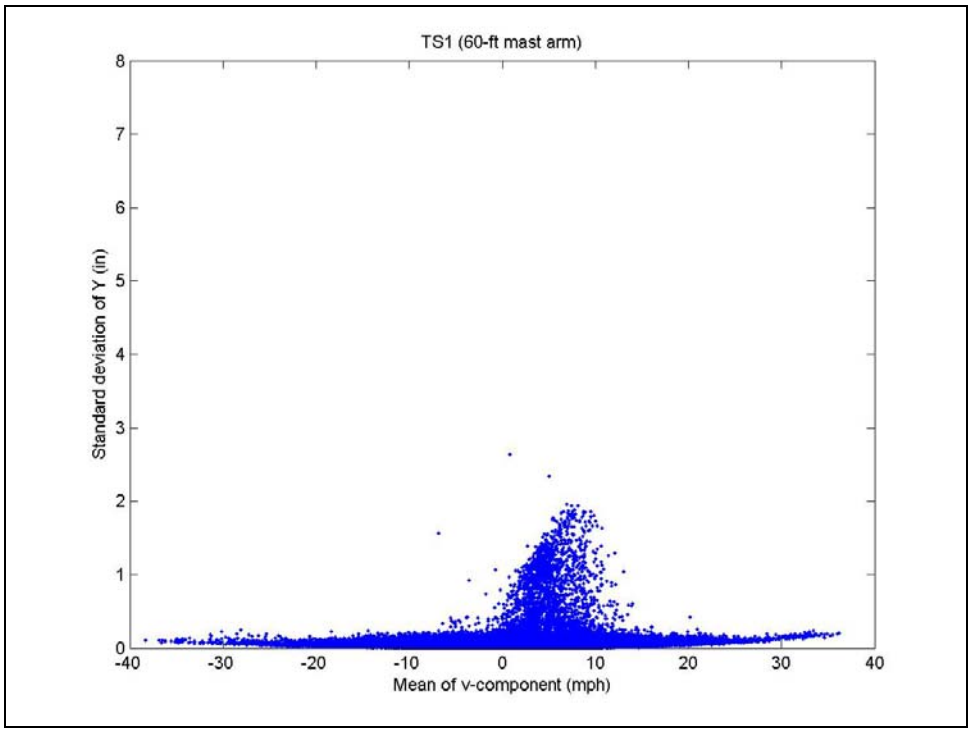

Figure E. 5 Effect of v-component on vertical vibrations of TS2 with vented backplates

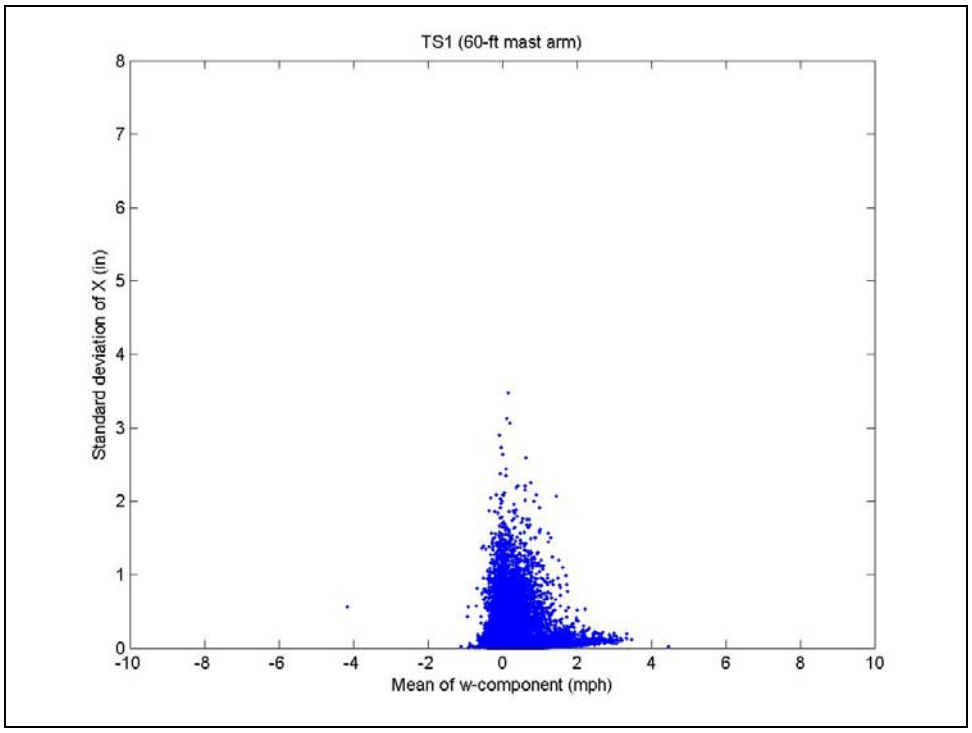

Figure E. 6 Effect of w-component on horizontal vibrations of TS1 with vented backplates

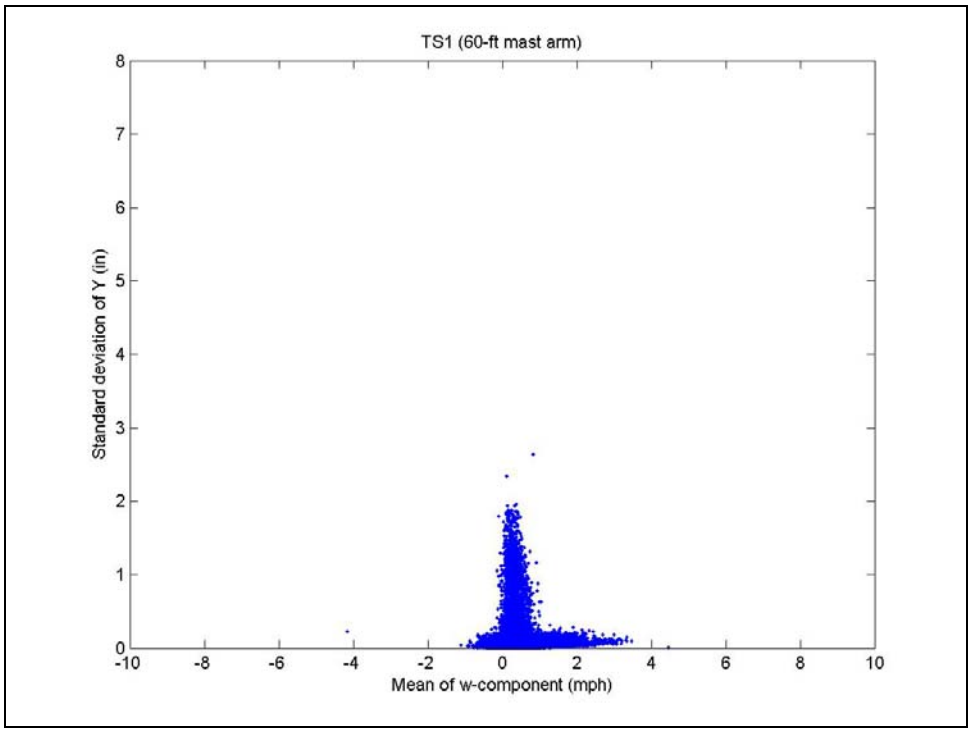

Figure E. 7 Effect of w-component on vertical vibrations of TS1 with vented backplates

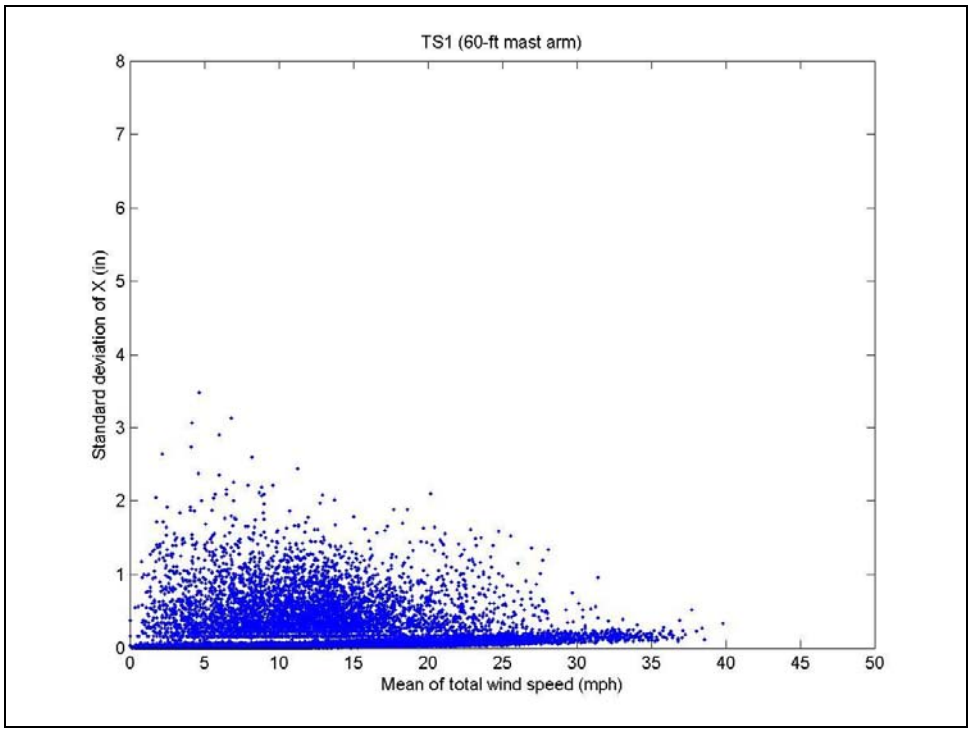

Figure E. 8 Effect of total wind speed on horizontal vibrations of TS1 with vented backplates

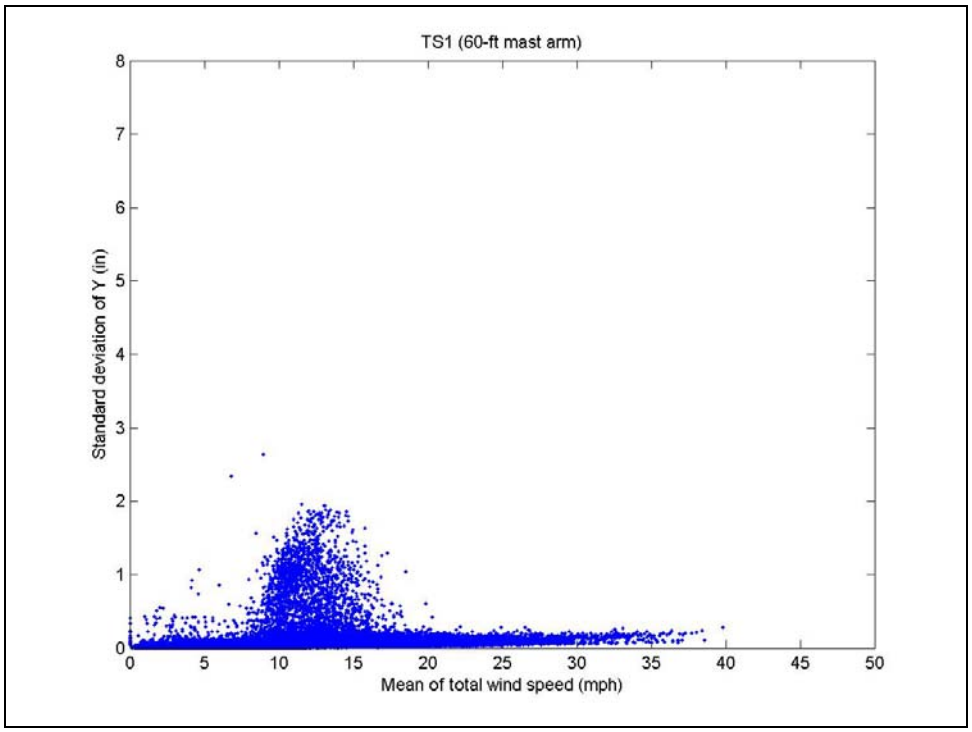

Figure E. 9 Effect of total wind speed on vertical vibrations of TS1 with vented backplates

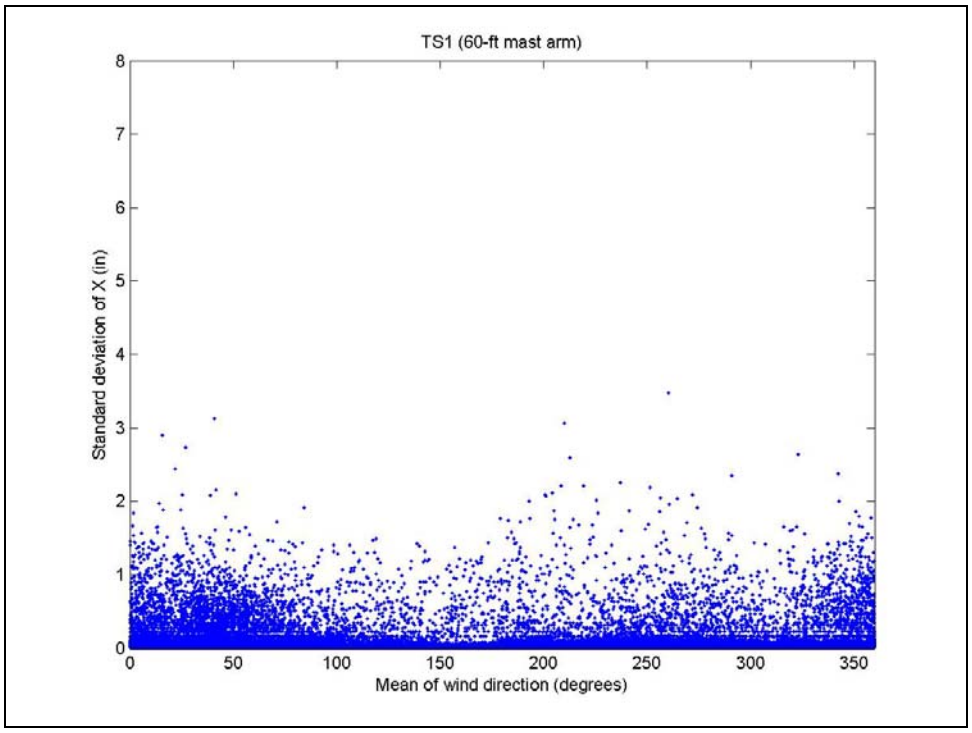

Figure E. 10 Effect of wind direction on horizontal vibrations of TS1 with vented backplates

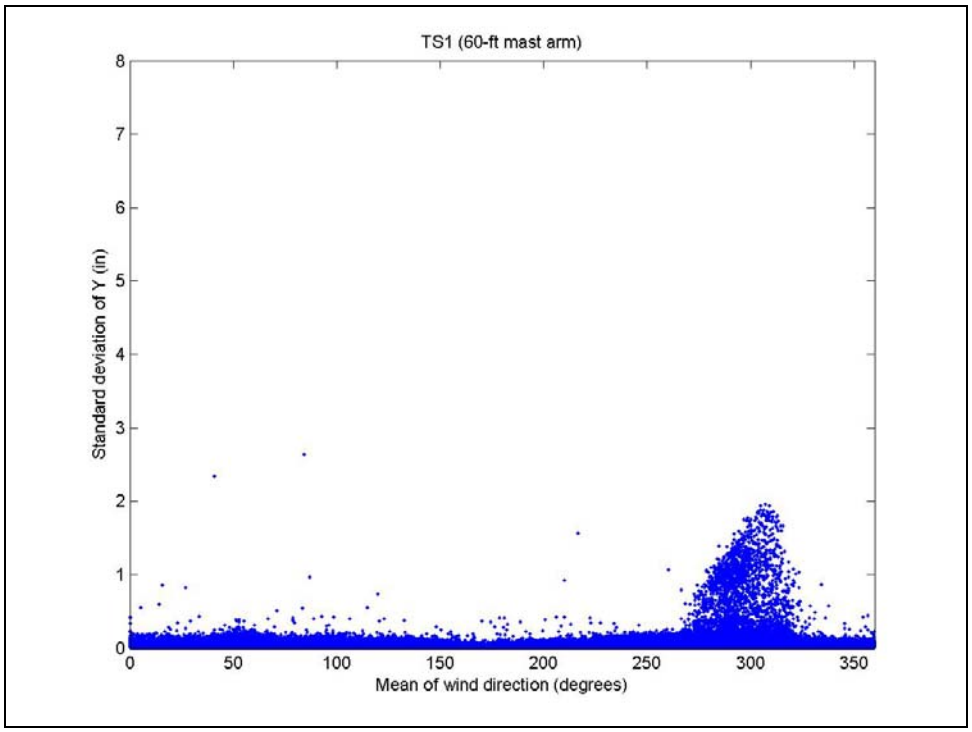

Figure E. 11 Effect of wind direction on vertical vibrations of TS1 with vented backplates

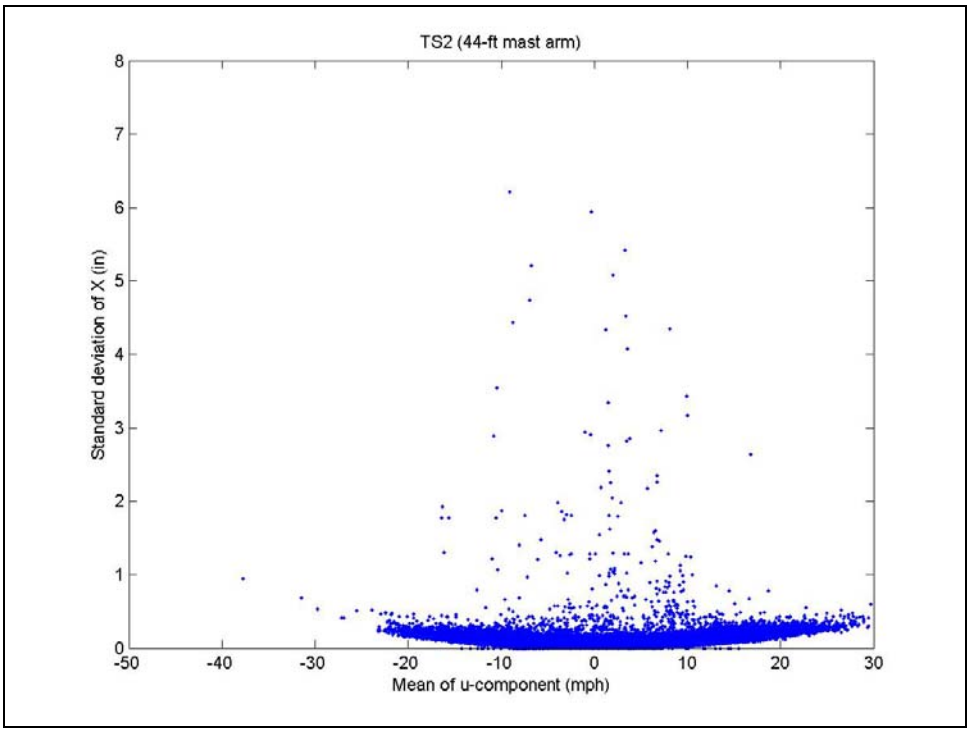

Figure E. 12 Effect of u-component on horizontal vibrations of TS2 with vented backplates

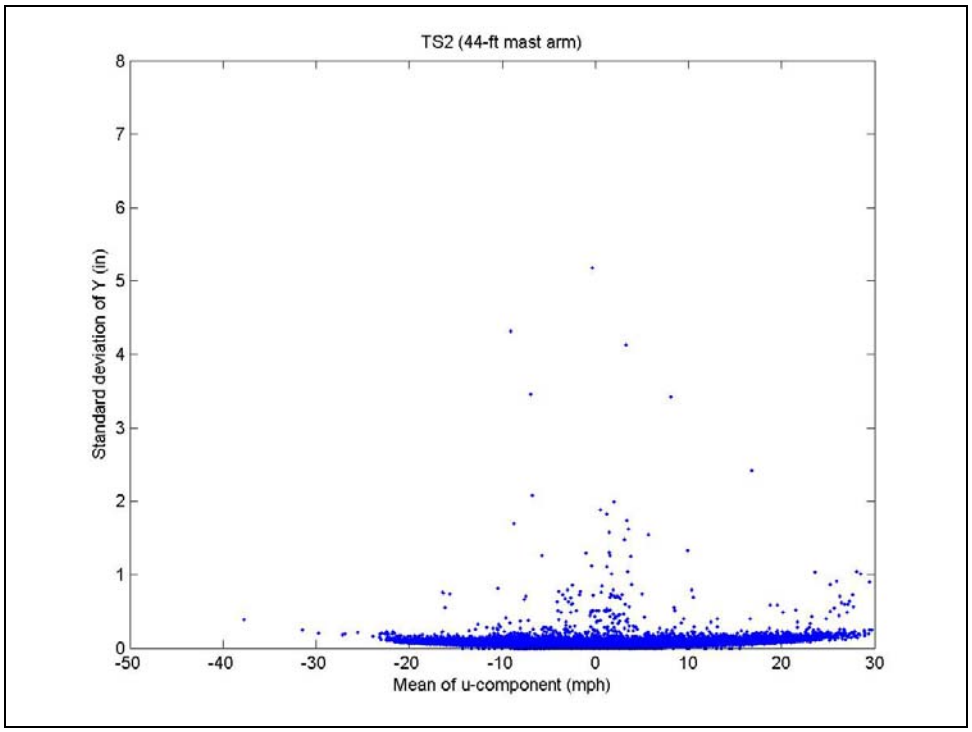

Figure E. 13 Effect of u-component on vertical vibrations of TS2 with vented backplates

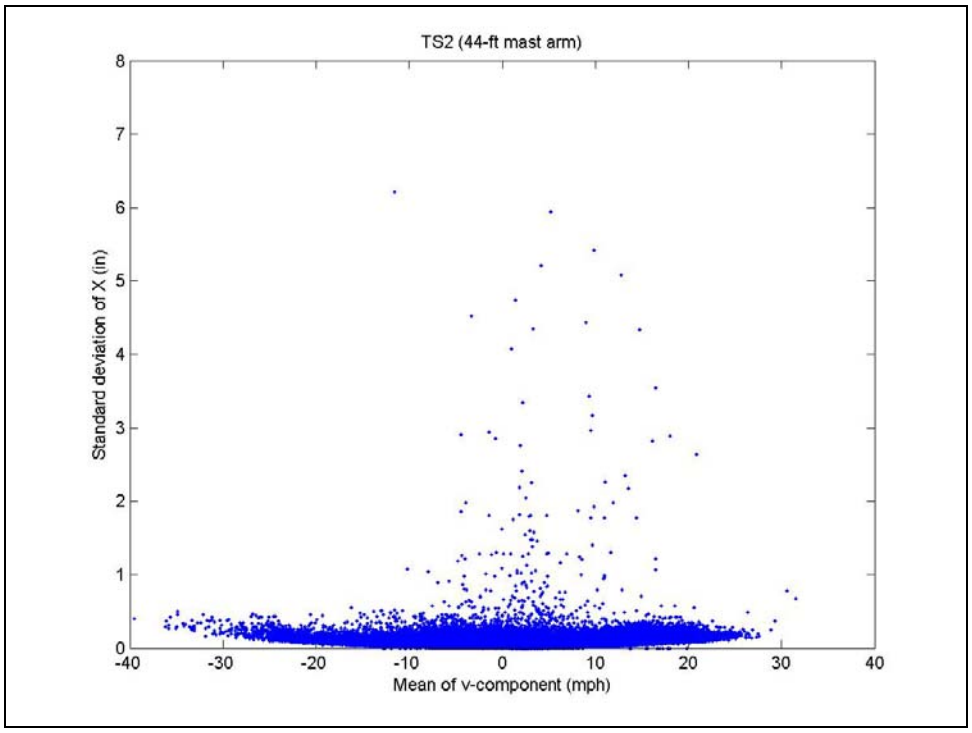

Figure E. 14 Effect of v-component on horizontal vibrations of TS2 with vented backplates

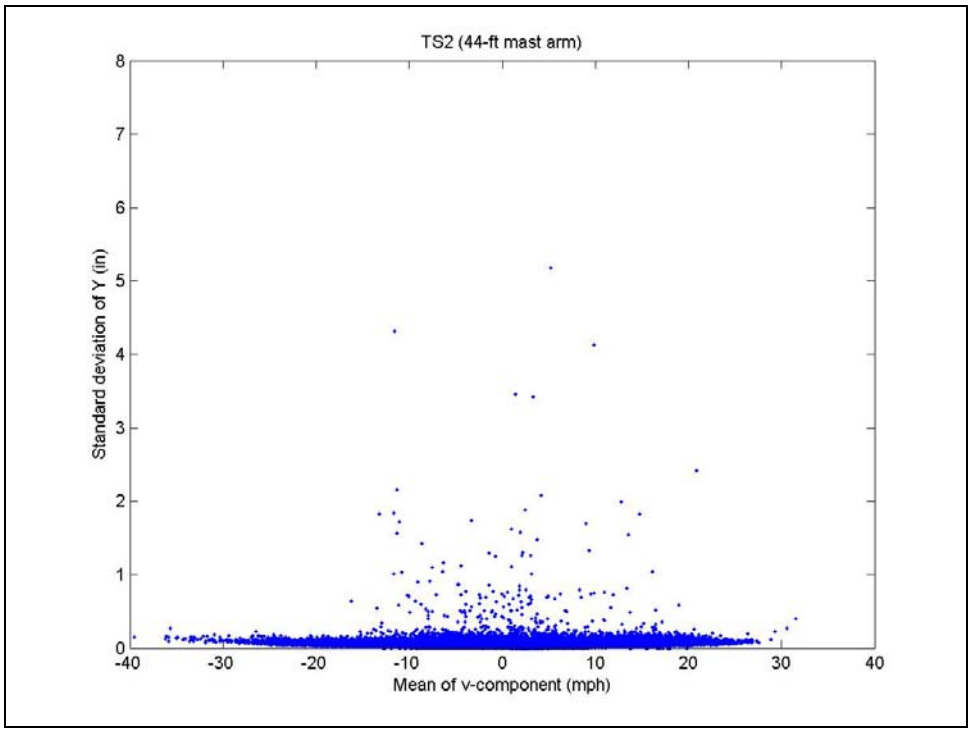

Figure E. 15 Effect of v-component on vertical vibrations of TS2 with vented backplates

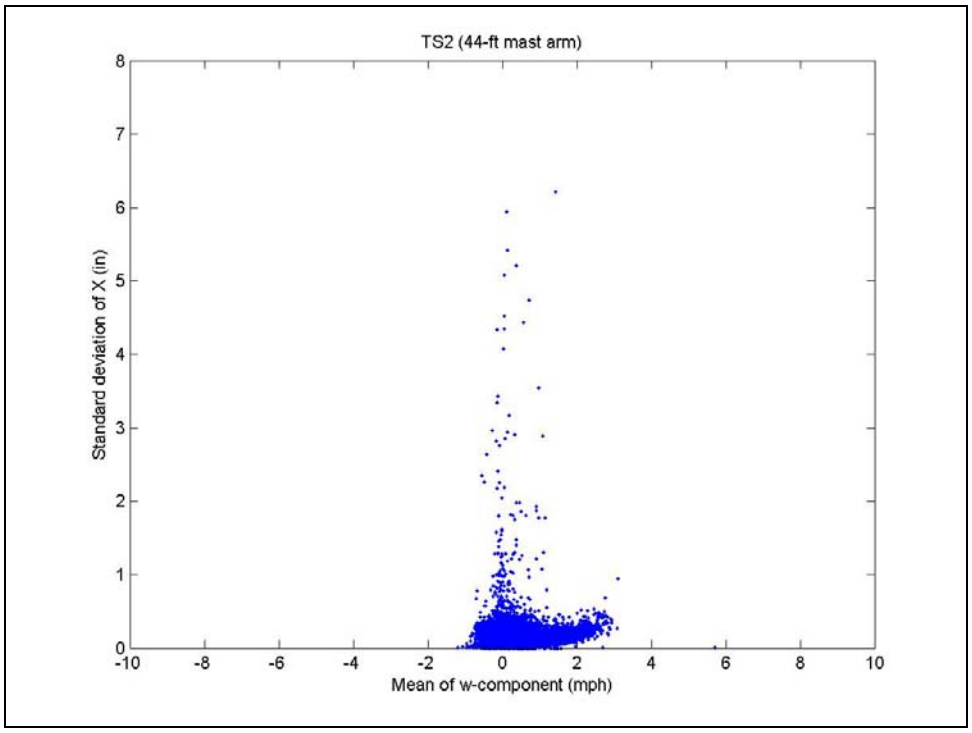

Figure E. 16 Effect of w-component on horizontal vibrations of TS2 with vented backplates

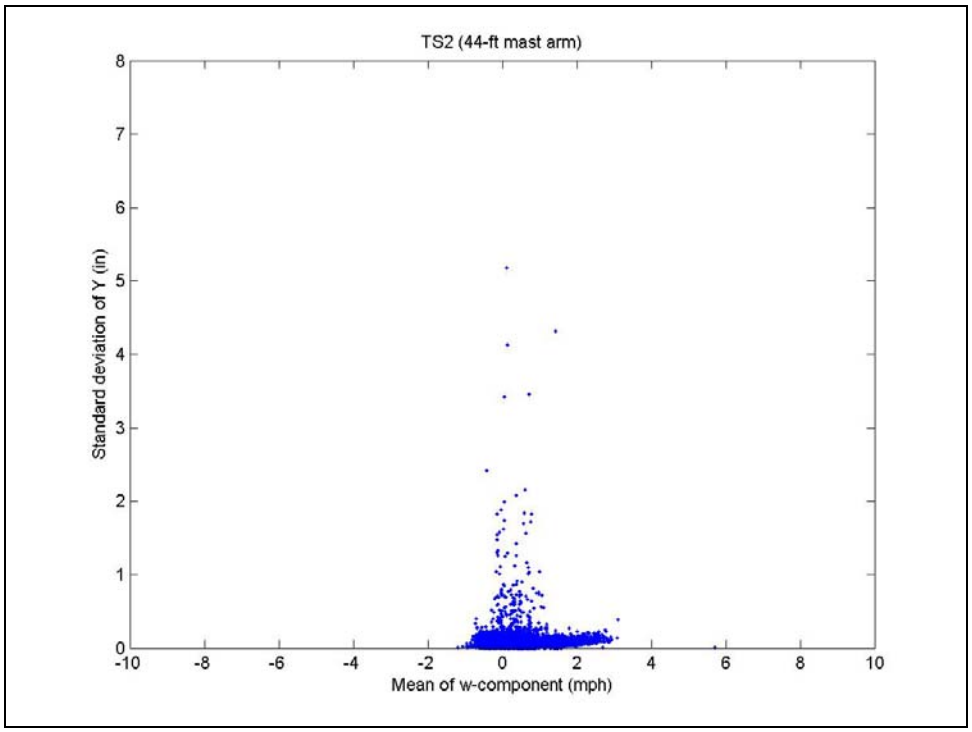

Figure E. 17 Effect of w-component on vertical vibrations of TS2 with vented backplates

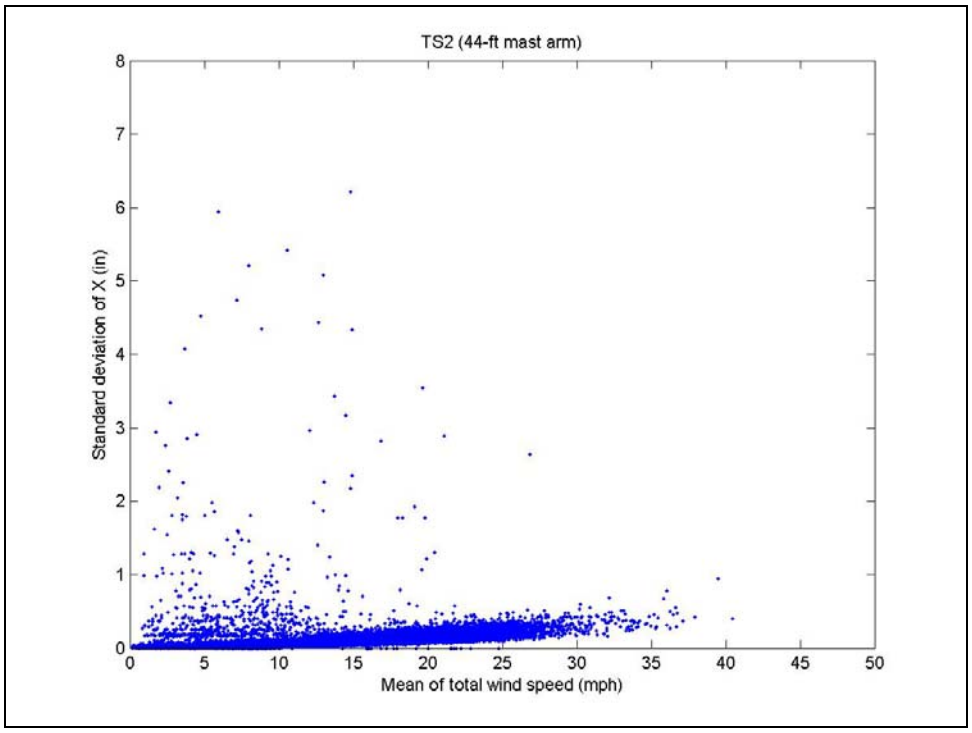

Figure E. 18 Effect of total wind speed on horizontal vibrations of TS2 with vented backplates

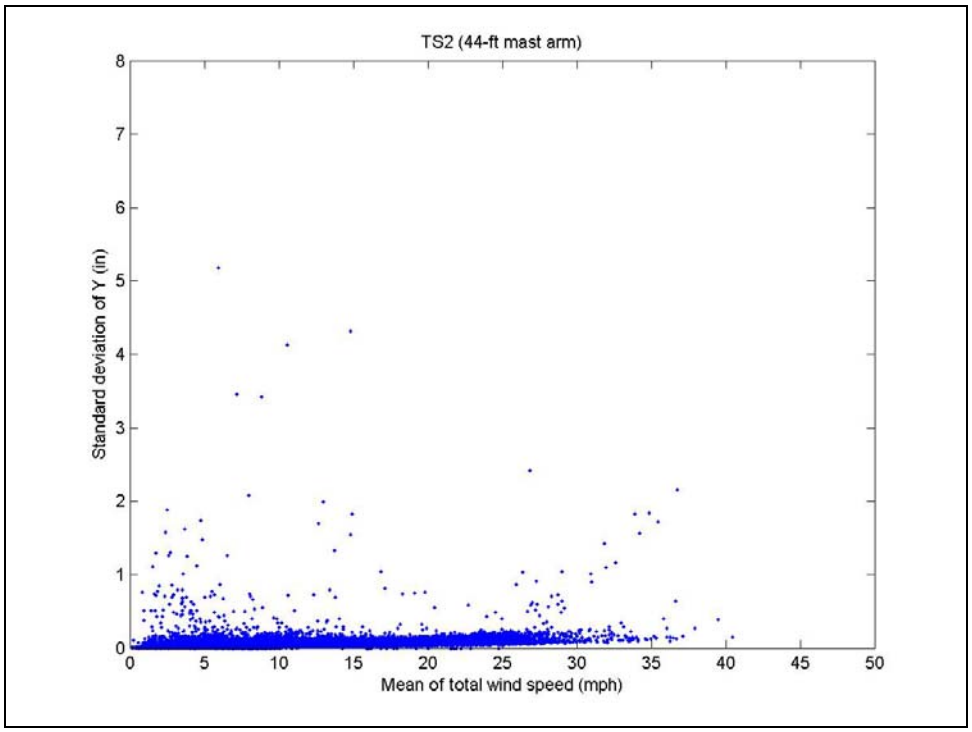

Figure E. 19 Effect of total wind speed on vertical vibrations of TS2 with vented backplates

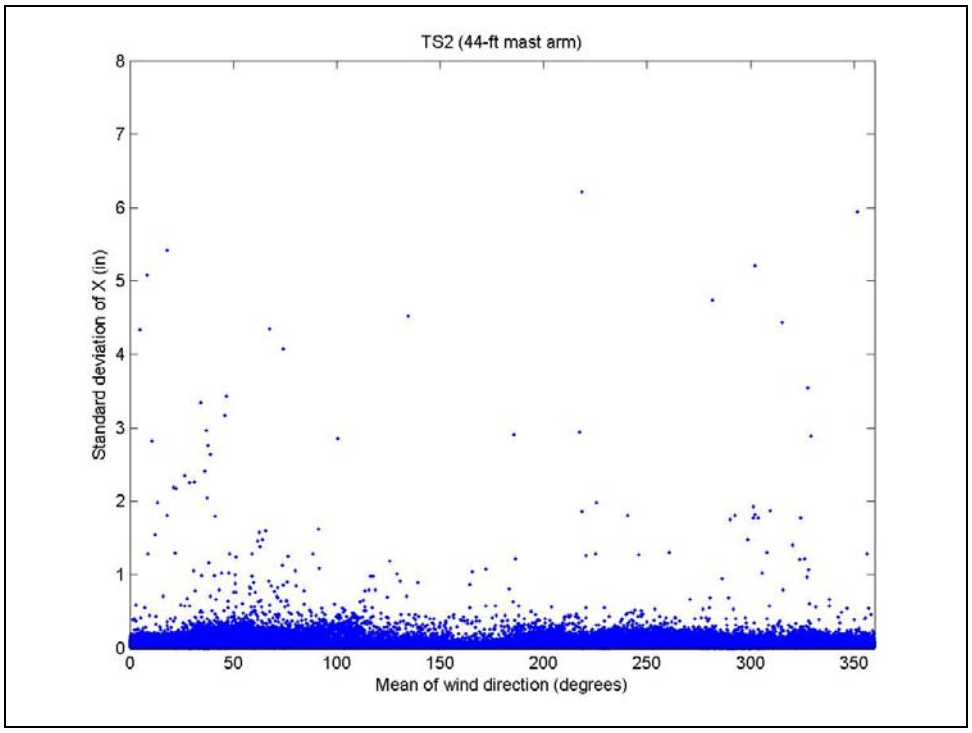

Figure E. 20 Effect of wind direction on horizontal vibrations of TS2 with vented backplates

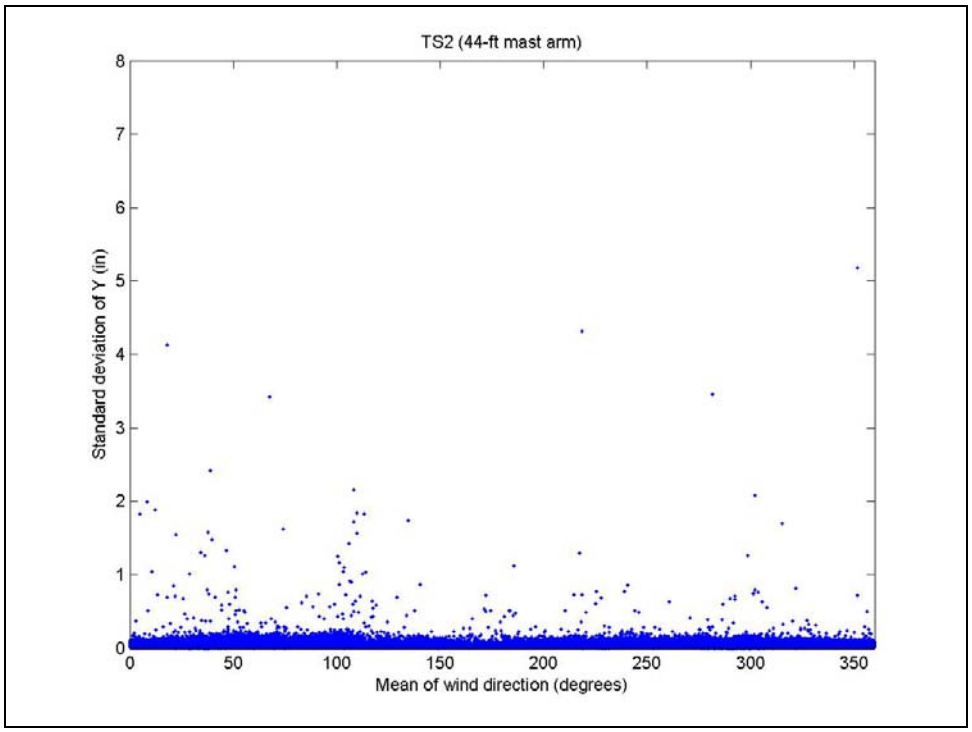

Figure E. 21 Effect of wind direction on vertical vibrations of TS2 with vented backplates

Figure E 22 compares the vertical vibrations results of Modes 1100 (signals with regular backplates) and 1103 (signals with vented backplates). For this figure, the data of Mode 1103 was plotted on top of the Mode 1100 data. It is apparent from this figure that the 44-ft structure did not vibrate much under either regular or vented backplates. Meanwhile, the vented backplates appeared to be effective in reducing the amplitude of vibrations of the 60-ft mast arm, at least when the angle of attack was away from 300 degrees. It should be kept in mind that only 2613 hours of data were collected for the 60-ft arm under Mode 1103 versus 4858 hours recorded under Mode 1100. It is possible that with more hours recorded under Mode 1103, larger vibrations could be observed.

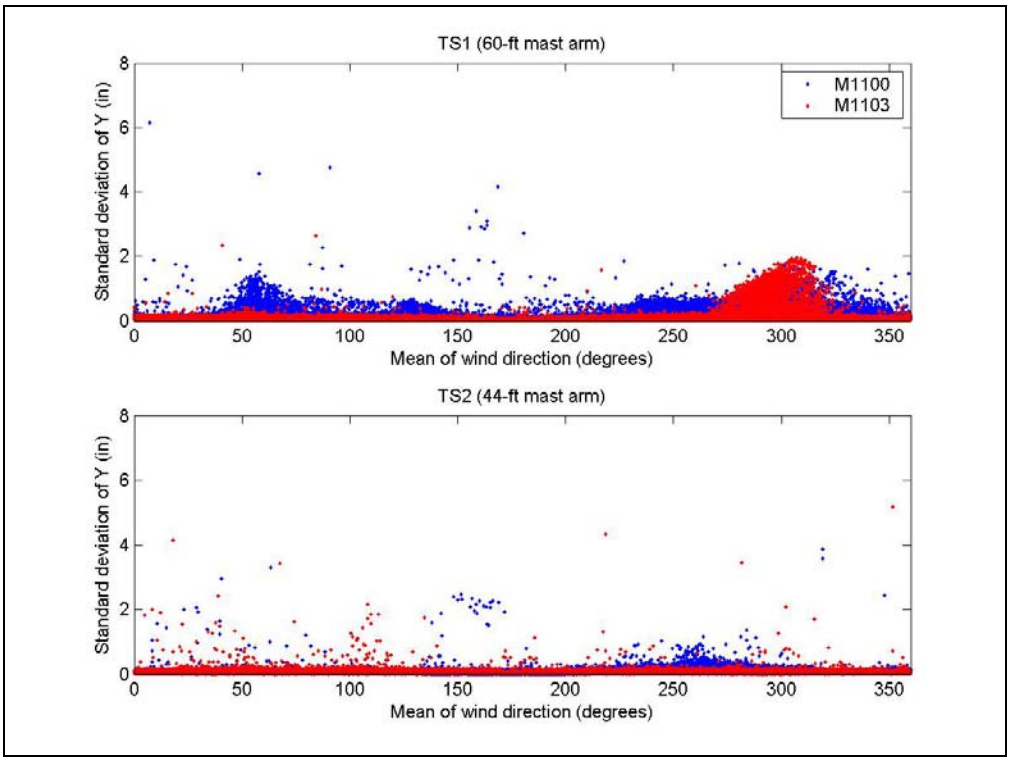

Figure E. 22 Comparison between Modes 1100 and 1103

E. 3 Mode 1105

From July to September 2007, data was collected under Mode 1105 with the arms pointing southeast and the signals having regular backplates. In addition, each arm had a plate installed as a damping device, as shown in Figure 23. Each plate was 60-inches by 16-inches and was located 5½ inches on top of the mast arm. For TS1, the center of the plate was located 86½ inches from the tip of the arm, while for TS2, the center of the plate was located 84 inches from the tip of the arm.

During this mode, 1175 hours of data were collected for both TS1 and TS2. As before, all data was analyzed by dividing the long time histories into 2-minute segments, calculating summary statistics for different measured parameters, and plotting graphs. All

the plotted graphs are presented here as Figures 24 to 43. Outlying data points have been retained for completeness and have not been individually validated.

Figure E. 23 Mast arm with damping plate

Paying close attention to the vertical vibrations of the arm of TS1, it can be seen in Figures 25, 27, 29, 31, and 33 that rarely was the standard deviation of Y over 1 inch. It appears that the plate was an effective damping device for this structure. This is not the case for TS2 for which several cases of the standard deviation of Y being over 2 inches. These cases were observed mostly under the following conditions:

- When the mean of the u-component was about 5 mph (as shown in Figure 35).
- When the mean of the v-component was about 3 mph (as shown in Figure 37).
- When the mean of the total wind speed was about 6 mph (as shown in Figure 41).

- When the mean wind direction was about 50 degrees (as shown in Figure 43).

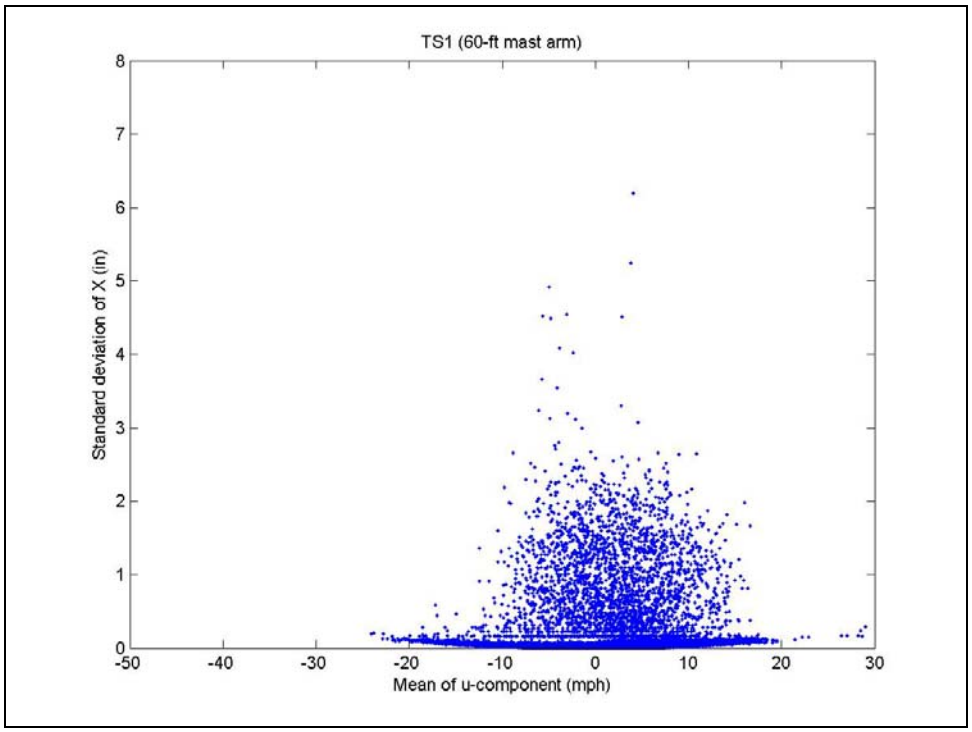

Figure E. 24 Effect of u-component on horizontal vibrations of TS1 with damping plate

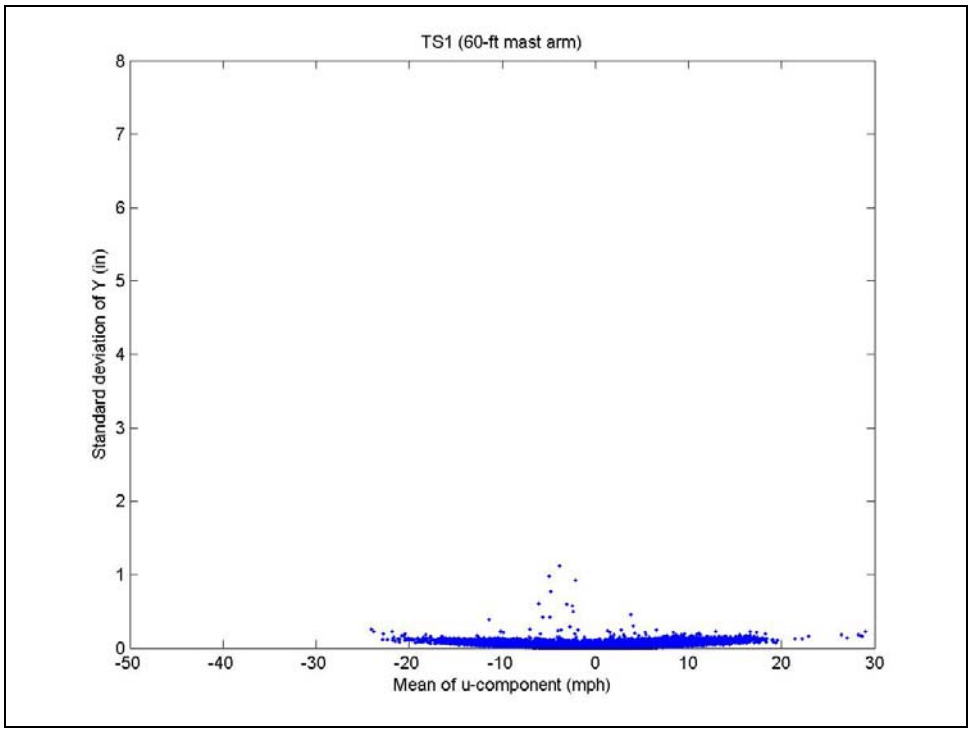

Figure E. 25 Effect of u-component on vertical vibrations of TS1 with damping plate

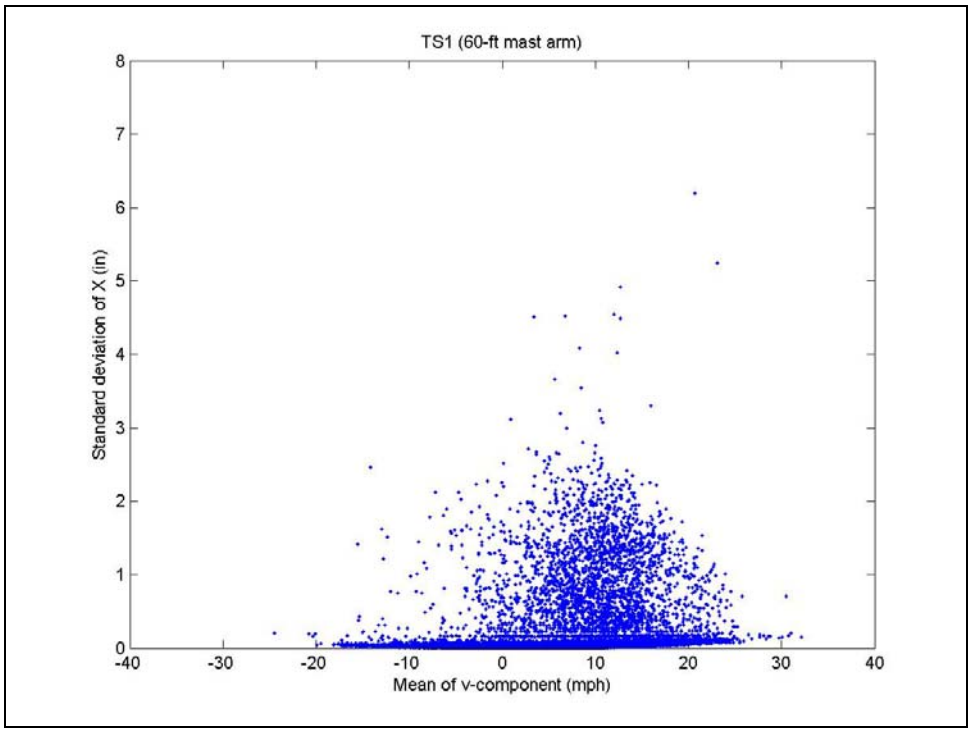

Figure E. 26 Effect of v-component on horizontal vibrations of TS1 with damping plate

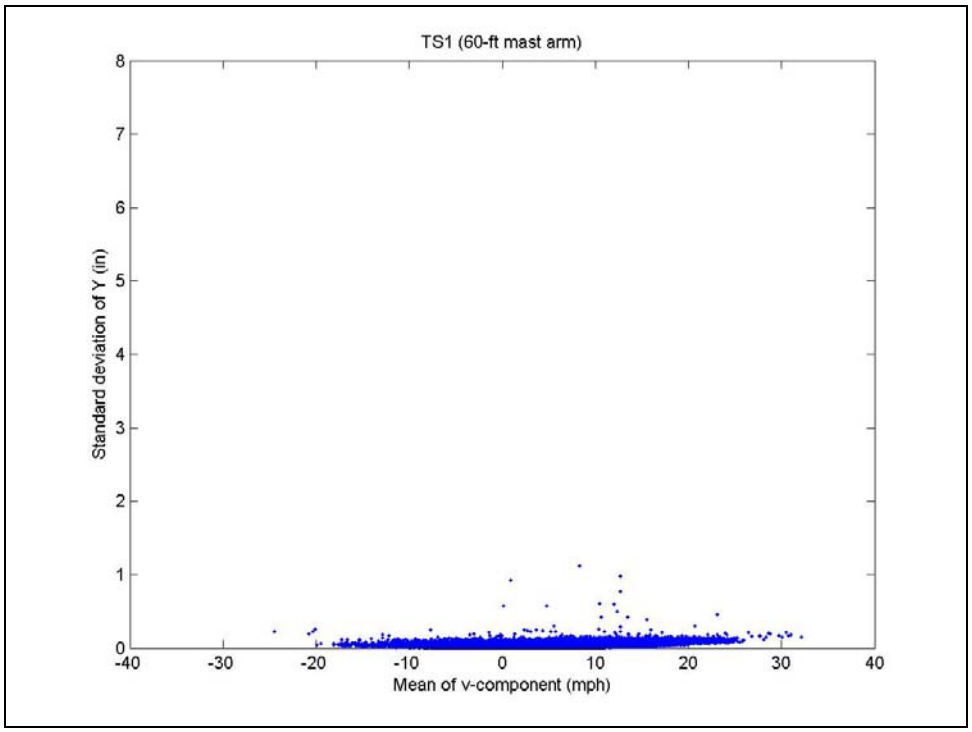

Figure E. 27 Effect of v-component on vertical vibrations of TS2 with damping plate

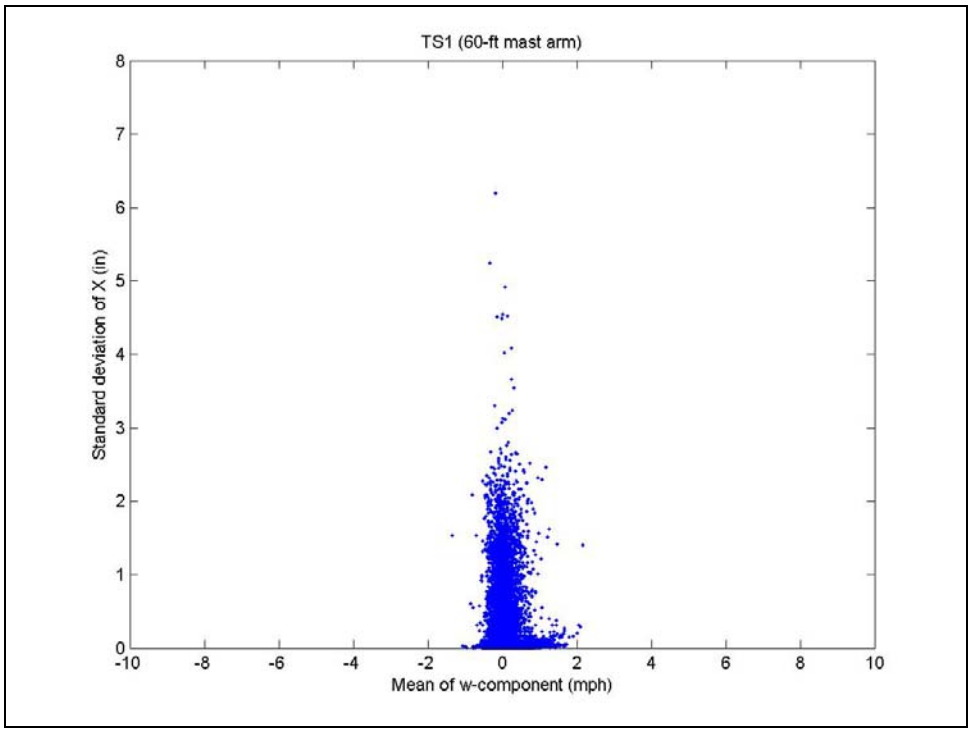

Figure E. 28 Effect of w-component on horizontal vibrations of TS1 with damping plate

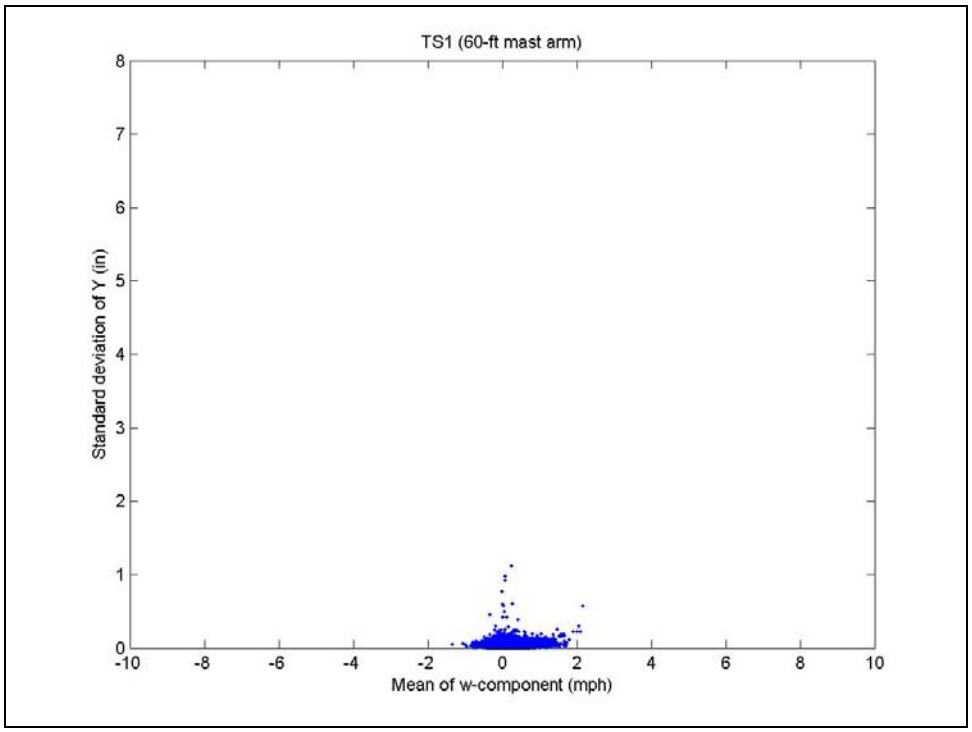

Figure E. 29 Effect of w-component on vertical vibrations of TS1 with damping plate

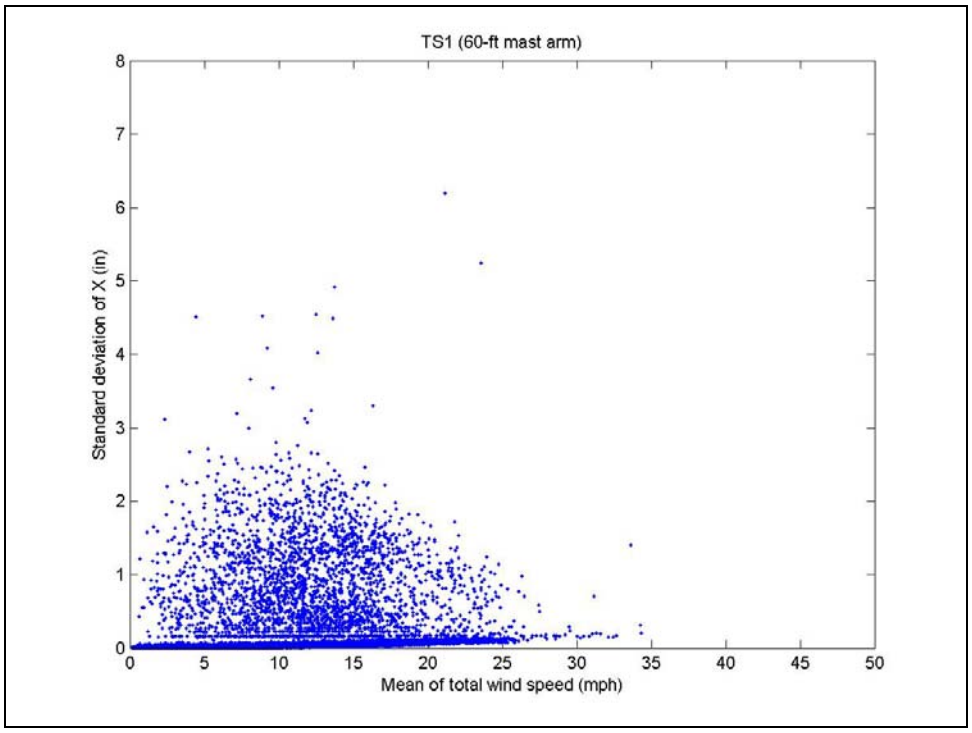

Figure E. 30 Effect of total wind speed on horizontal vibrations of TS1 with damping plate

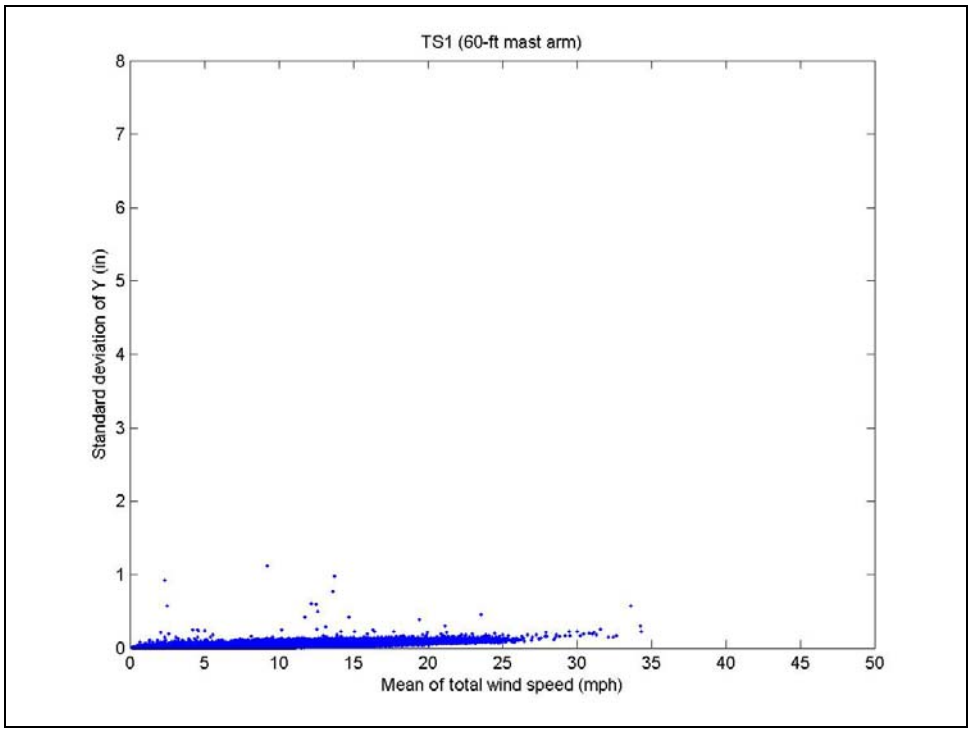

Figure E. 31 Effect of total wind speed on vertical vibrations of TS1 damping plate

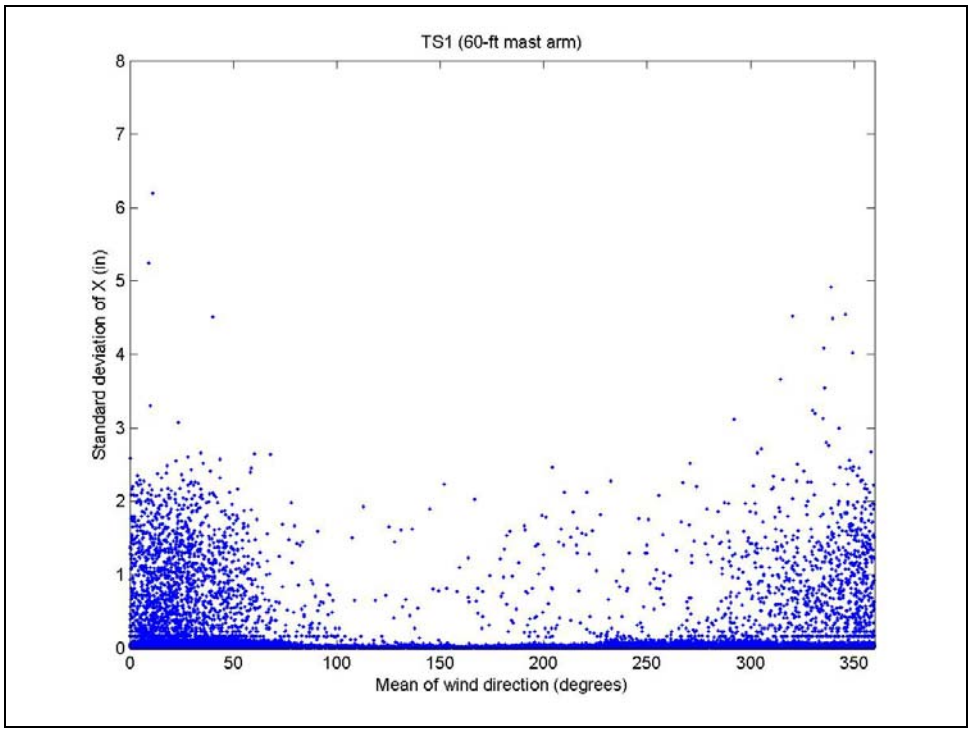

Figure E. 32 Effect of wind direction on horizontal vibrations of TS1 with damping plate

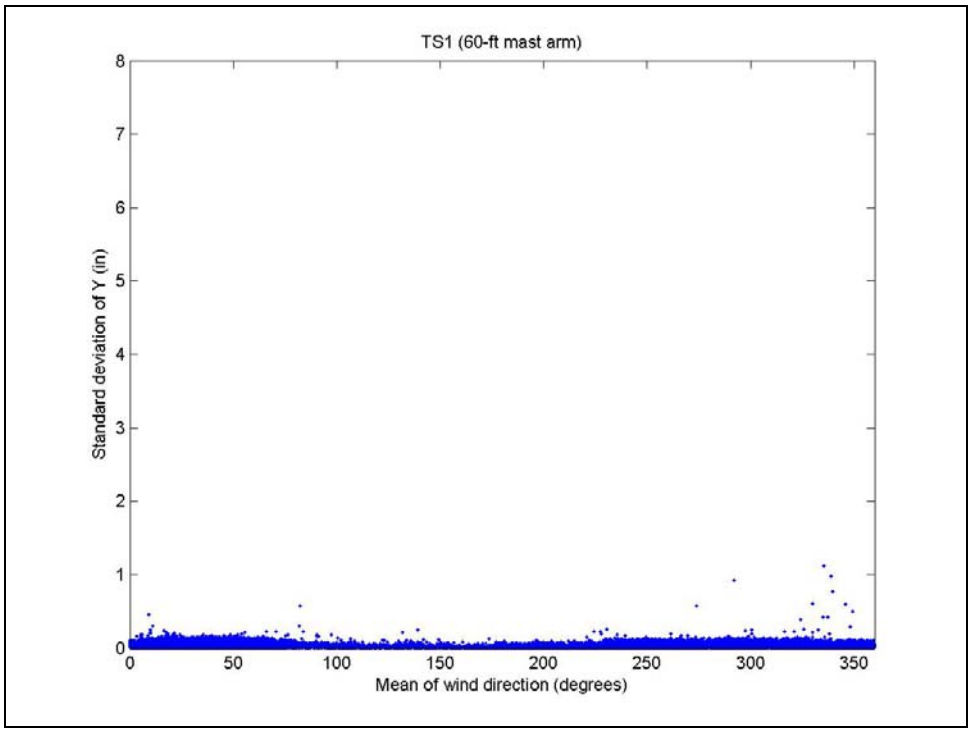

Figure E. 33 Effect of wind direction on vertical vibrations of TS1 with damping plate

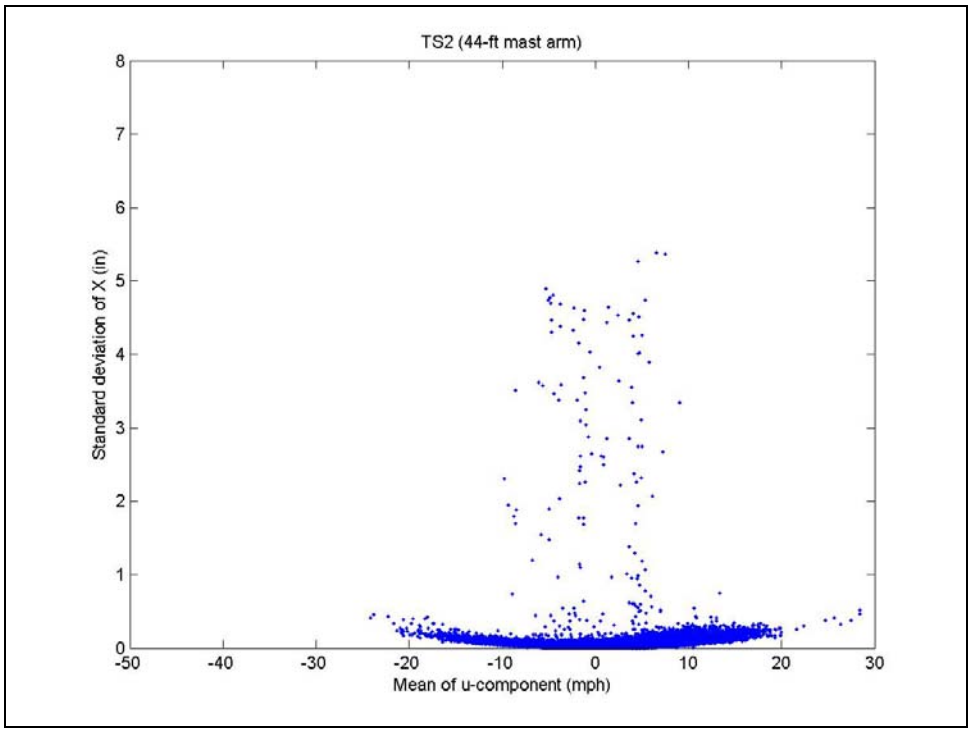

Figure E. 34 Effect of u-component on horizontal vibrations of TS2 with damping plate

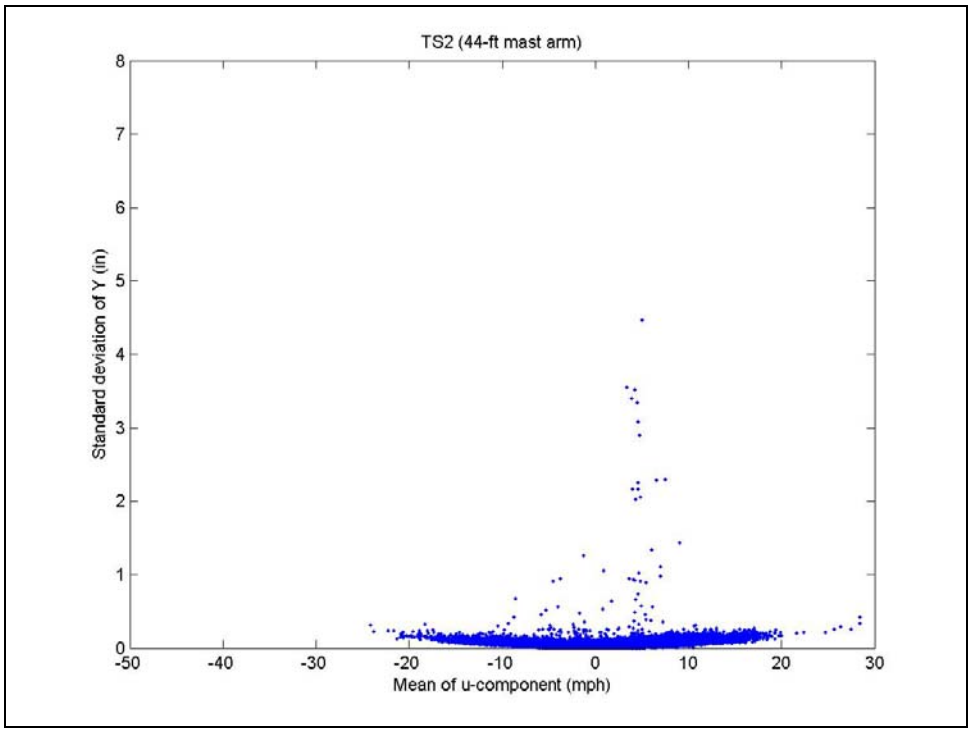

Figure E. 35 Effect of u-component on vertical vibrations of TS2 with damping plate

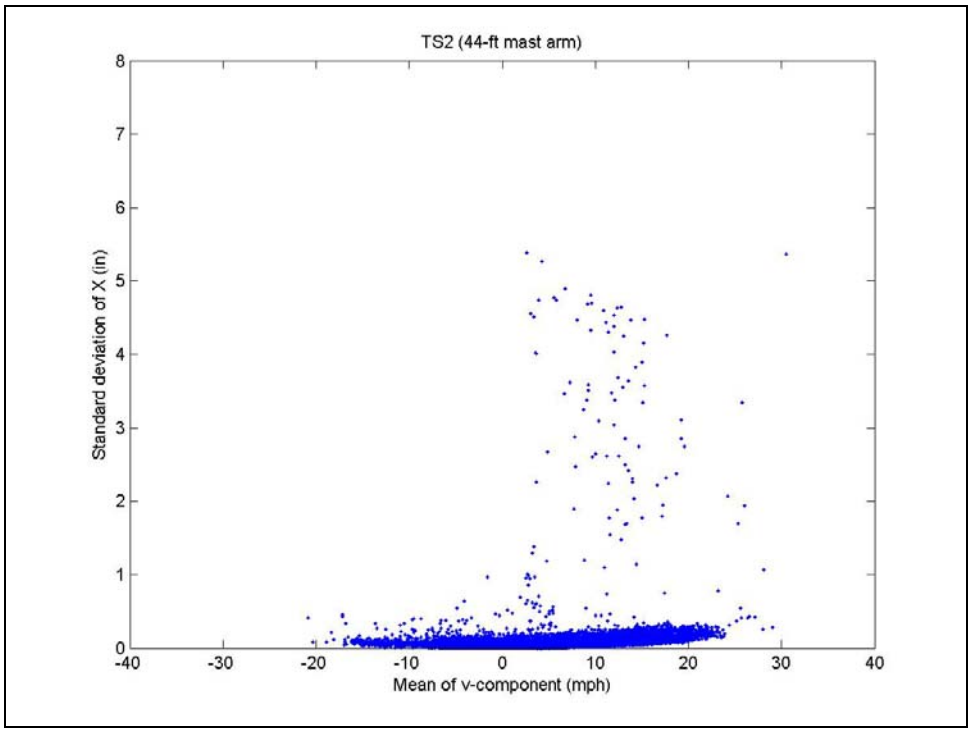

Figure E. 36 Effect of v-component on horizontal vibrations of TS2 with damping plate

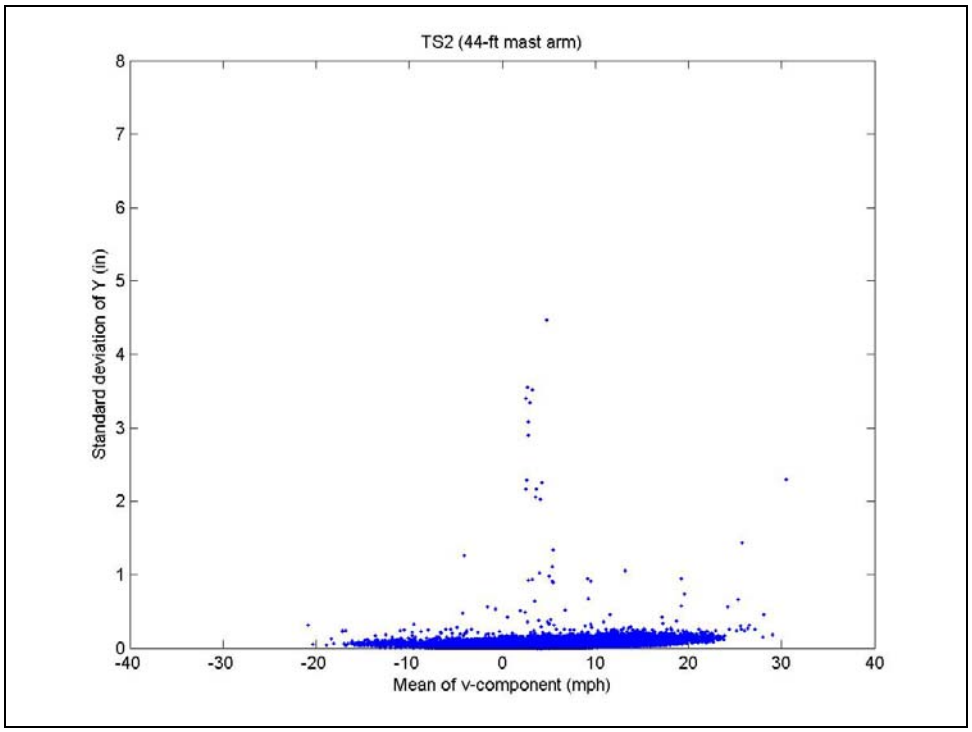

Figure E. 37 Effect of v-component on vertical vibrations of TS2 with damping plate

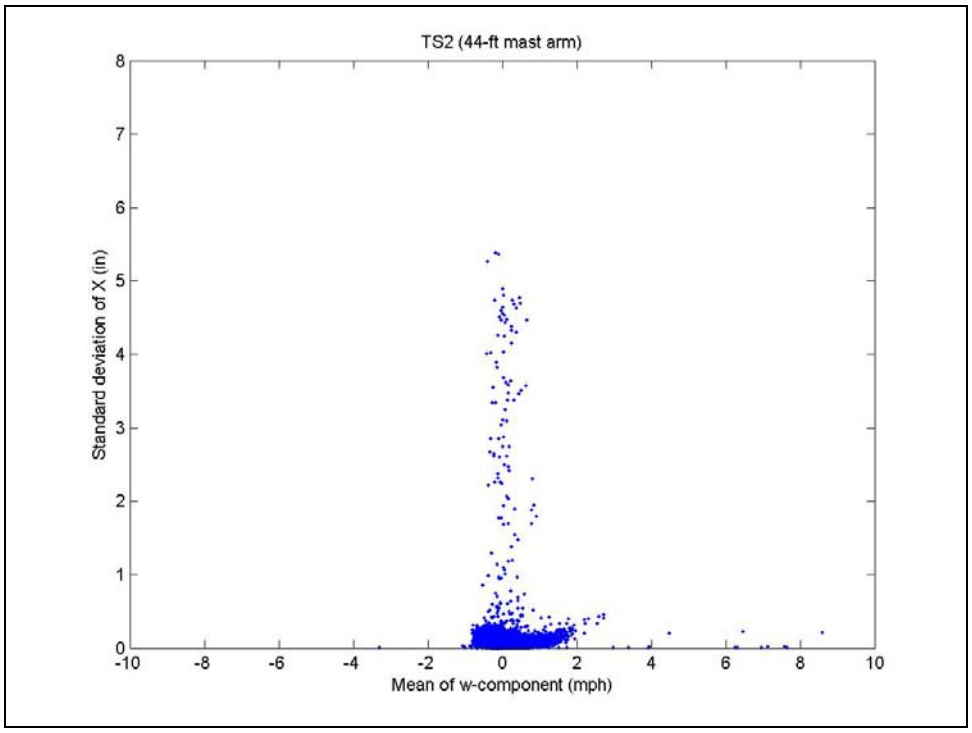

Figure E. 38 Effect of w-component on horizontal vibrations of TS2 with damping plate

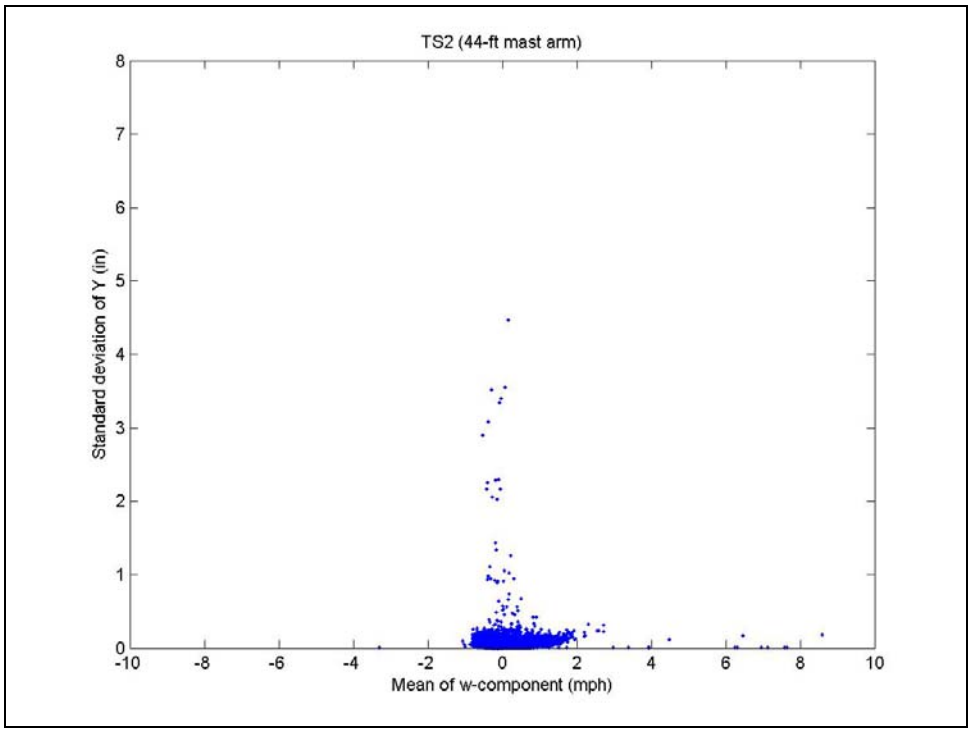

Figure E. 39 Effect of w-component on vertical vibrations of TS2 with damping plate

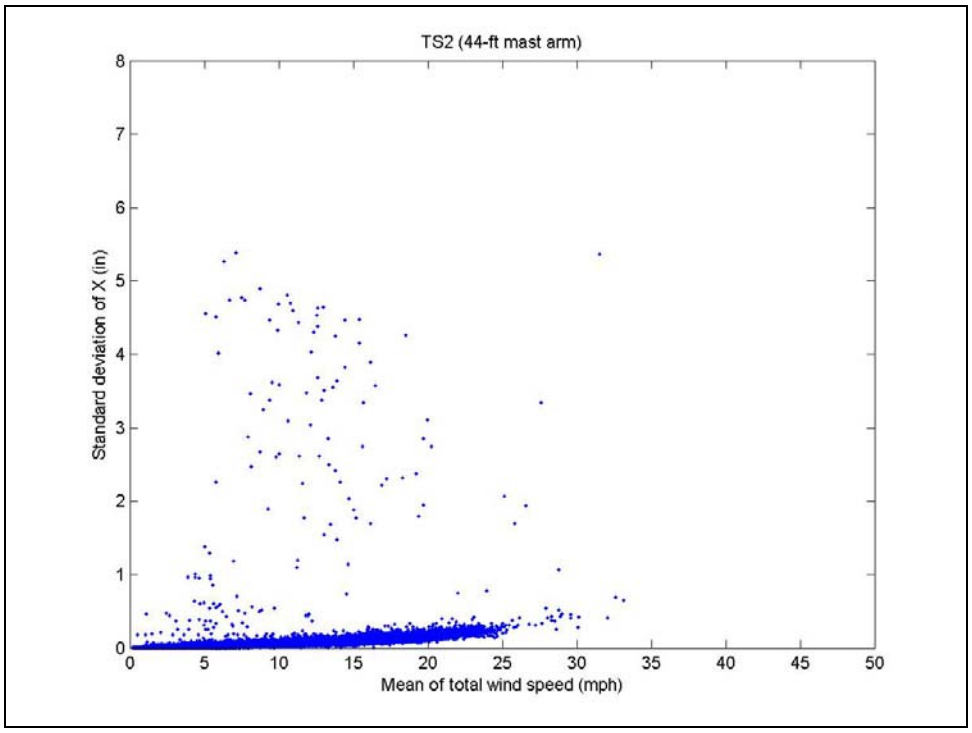

Figure E. 40 Effect of total wind speed on horizontal vibrations of TS2 with damping plate

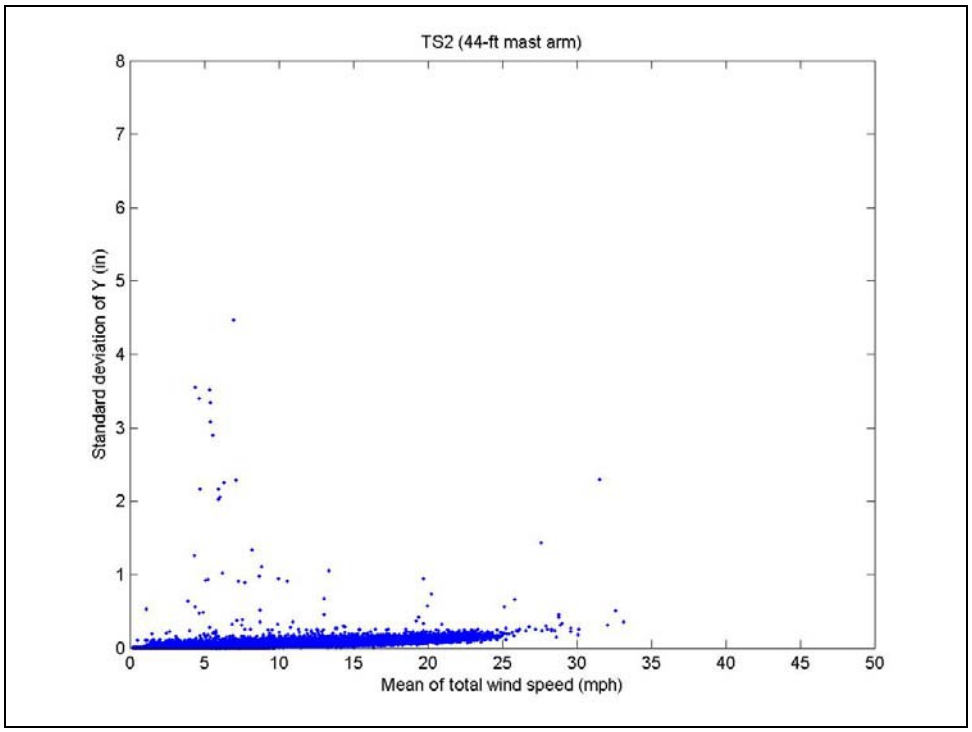

Figure E. 41 Effect of total wind speed on vertical vibrations of TS2 with damping plate

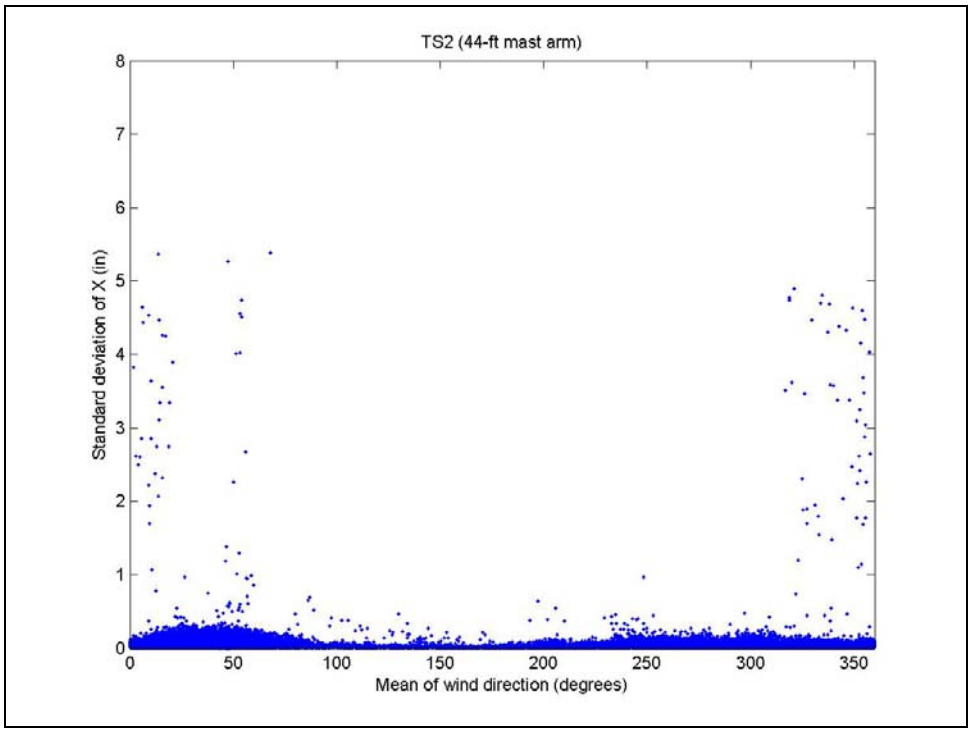

Figure E. 42 Effect of wind direction on horizontal vibrations of TS2 with damping plate

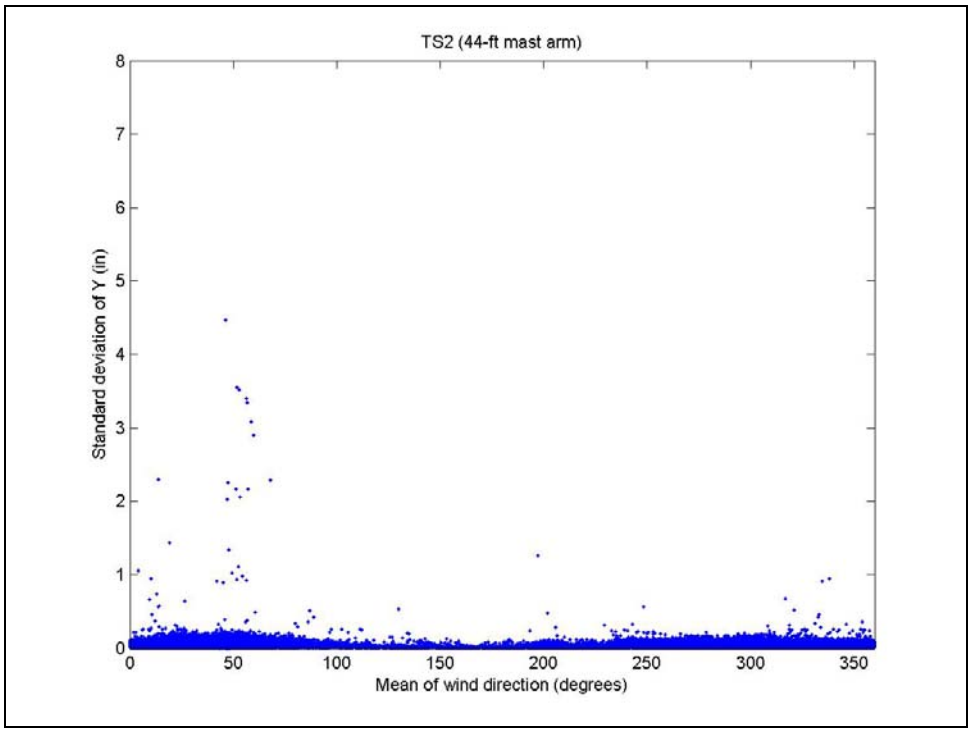

Figure E. 43 Effect of wind direction on vertical vibrations of TS2 with damping plate

Figure E 44 compares the vertical vibrations results of Modes 1100 (signals with backplates) and 1105 (signals with backplates and arms with damping plate). For this figure, the data of Mode 1105 was plotted on top of the Mode 1100 data. It is apparent from this figure that the damping plate was effective in minimizing the amplitude of vibrations of the 60-ft arm, but it was not very effective in minimizing them for the 44-ft arm.

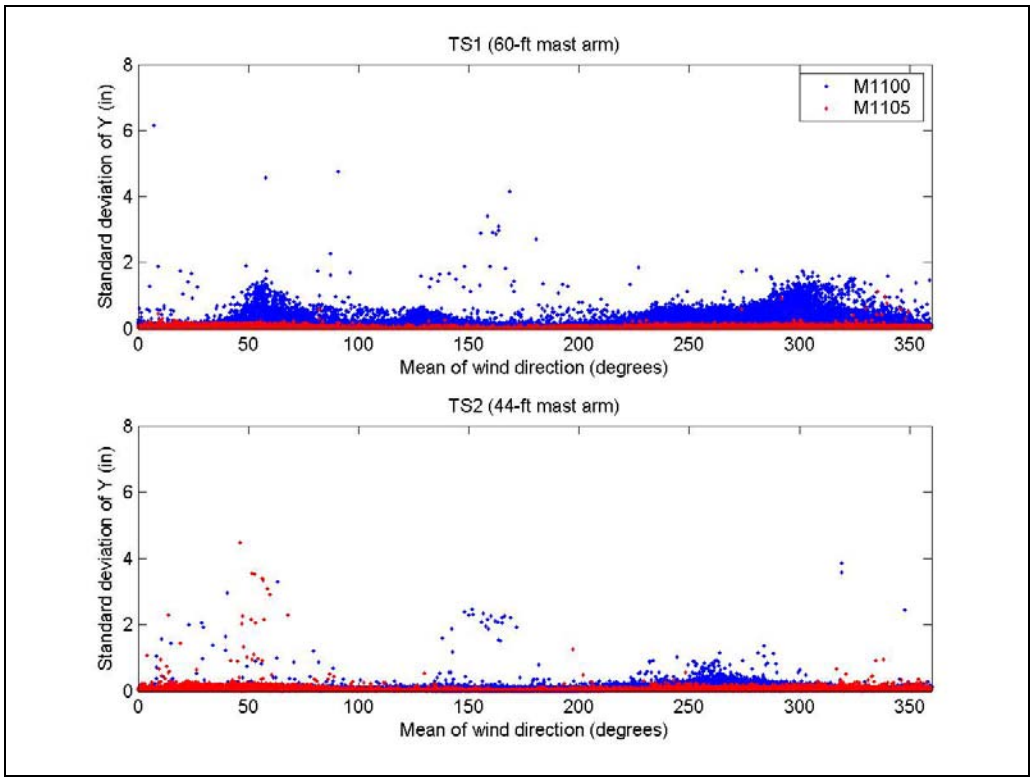

Figure E. 44 Comparison between Modes 1100 and 1105

E. 5 Conclusions

Two methods to minimize the amplitude of the vertical vibrations were tested in the full-scale experiments: (1) the vented backplates and (2) the damping plate. In the case of the 60-ft arm, the damping plate appeared to be effective in minimizing the amplitude of vibrations, but the vented backplates appeared to make the arm susceptible to vibrate at certain conditions, like when the mean wind direction is close to 300 degrees. Meanwhile, the vented backplates appeared to minimize the amplitude of vibrations of the 44-ft arm, but the damping plate to be ineffective in minimizing them.

TEXAS TECH UNIVERSITY
Multidisciplinary Research in Transportation

Texas Tech University | Lubbock, Texas 79409
P 806.742.3503 | F 806.742.4168